2006 Annual Report

Summer Research Institute
Interfacial and Condensed Phase Chemical Physics

October 2006

DISCLAIMER

This report was prepared as an account of work sponsored by an agency of the United States Government. Neither the United States Government nor any agency thereof, nor Battelle Memorial Institute, nor any of their employees, makes **any warranty, express or implied, or assumes any legal liability or responsibility for the accuracy, completeness, or usefulness of any information, apparatus, product, or process disclosed, or represents that its use would not infringe privately owned rights**. Reference herein to any specific commercial product, process, or service by trade name, trademark, manufacturer, or otherwise does not necessarily constitute or imply its endorsement, recommendation, or favoring by the United States Government or any agency thereof, or Battelle Memorial Institute. The views and opinions of authors expressed herein do not necessarily state or reflect those of the United States Government or any agency thereof.

PACIFIC NORTHWEST NATIONAL LABORATORY
operated by
BATTELLE
for the
UNITED STATES DEPARTMENT OF ENERGY
under Contract DE-AC06-76RL01830

This document was printed on recycled paper

2006 Annual Report

Summer Research Institute Interfacial and Condensed Phase Chemical Physics

October 2006

Pacific Northwest National Laboratory
Richland, Washington 99354

Executive Summary

The Pacific Northwest National Laboratory (PNNL) hosted its third annual Summer Research Institute in Interfacial and Condensed Phase Chemical Physics from May through September 2006. During this period, twenty PNNL scientists hosted twenty-seven scientists from twenty-five different universities. Of the twenty-seven participants, one was a graduating senior; twenty-one were graduate students; one was a postdoctoral fellow; and four were university faculty members.

Table of Contents

Acknowledgments

Even a modest-sized program such as this one would not happen without the assistance of many people. This year¹s scientific oversight committee consisted of Drs. Donald R. Baer, FSD, L. Rene Corrales, FSD and Stephan E. Barlow, EMSL. Ms. Nikki B. Avery was our administrator in 2006 and played the key role in ensuring the institute ran smoothly. Ms. Cynthia A. Irwin, Operations Administrator for Chemical Structure and Dynamics, and Ms. Susan M. Finch of Chemical Sciences provided financial and budgetary support

We also acknowledge Ms. Rebecca J. Janosky of PNNL¹s Science and Engineering Education Office. She handled a myriad of details associated with appointments, including awards, agreements and disbursements, while dealing with a major reorganization. We also wish to acknowledge Ms. Carol A. Elledge, Publications Design Group, Ms. Cori C. Blake, Web Ops, Mr. Mark D. Bayless, Rich Interaction Environments, and Ms. Rose M. Watt, Graph and Multimedia Design Group, respectively, for their expertise and timeliness in creating and developing the institute¹s website, application website and finalizing the institute¹s brochure. Mr. David Spiel provided expert photography support.

Special and belated acknowledgement is owed to my wife, Mrs. Janice Barlow. She initiated the Summer Institute barbeques that have become something of a tradition. Each year we have hosted, and deeply enjoyed two of these get-togethers at our home.

This year we inaugurated a collaboration with the National Science Foundation (NSF), discussed below. However here we need to acknowledge the roles of Dr. Katherine Covet of the NSF and Dr. Allison A. Campbell and Ms. Terry J. Law of EMSL in making this happen.

Finally, we wish to acknowledge the U.S. Department of Energy¹s Office of Basic Energy Sciences from whom we received the guidance to initiate the Summer Research Institute in Interfacial and Condensed Phase Chemical Physics and from whom support was ultimately derived.

The real stars of the Interfacial and Condensed Phase Chemical Physics Research Institute were our participants. The remainder of this document is largely devoted to them.

Stephan E. Barlow
Director, ICPCPSRI
October 2006

Summary

PNNL's Management and Operations Contract with the U.S. Department of Energy (DOE)[1] identified an Office of Basic Energy Science (BES) Mission Stretch Goal: "To establish PNNL in a national leadership role in the area of theoretical and experimental condensed phase and interfacial chemical physics research." Successful achievement of a national leadership role will be evidenced by: "Establishment of a summer school (at least two weeks in duration) to educate graduate students and young scientists in state-of-the- art theory, simulation, and experimental measurement, with a total attendance of at east 60 over the contract period."

Interfacial and Condensed Phase Chemical Physics is not so much a field of study as it is a cross cutting concept. Important issues exist in nearly every scientific discipline from Astronomy to Zoology that fall with the purview of this concept. Likewise all of the technology and engineering of the modern world and hopes for future development depend to one degree or another on our ability to understand and manipulate condensed phases and interfacial processes.

The guidance from DOE HQ Office of Science gave us considerable latitude in implementing the institute's advanced program that focuses on graduate students, postdoctoral fellows and university faculty. The institute caters to more senior people than generally accommodated by PNNL's summer internship programs. We believe that the best education people at this level can receive is to actively engage in research that is relevant to their own career development goals. To accomplish this objective, the institute has a different character and puts different requirements on its participants than do either the standard internship programs or other institutes, workshops, etc. Perhaps the best overall description of the institute is a "visiting scientist program for early career researchers." In this spirit, each young scientist's particular program was individually tailored. The descriptions given below are generally true for most of the young scientists but may or may not apply to any particular individual.

Participants and the Institute Structure

Prospective visitors applied electronically at the Summer Research Institute's web site: www.pnl.gov/si/. Submission of applications, screening and correspondence were all handled online. This greatly facilitated the review and screening process as well as record keeping. Preliminary screening was handled by the Director of the Institute who acknowledged receipt of the applications and informed the candidates of any additional information or actions that were necessary to complete the application process. A number of candidates were found to be unsuited to participate in the institute and they were informed as quickly as that determination could be made. Reasons for rejection at this stage included:

---

[1] Appendix H of Contract Number: DE-AC06-76RL01830, Modification M375.

♦ Candidate's area of interest was outside of the scope of the program, e.g., high energy physics or genetics.
♦ Prospective PNNL hosts were already committed or unavailable.
♦ Candidate was finishing a Masters or PhD degree and did not have a new position.
♦ Candidate failed to finish the application process.

Candidates who passed this first series of hurdles and who identified a willing PNNL host were then required to submit a summary of proposed research or activity that they would conduct at PNNL during the summer. Normally, this proposal was prepared with the assistance of both the PNNL host and the candidate's academic advisor (as appropriate). Once the application deadline had passed, all completed applications were reviewed by a PNNL science panel consisting of Dr. Donald R. Baer and Dr. L. Rene Corrales of PNNL's Fundamental Science Directorate and Dr. Stephan E. Barlow of PNNL's Environmental Molecular Sciences Laboratory (EMSL). All successful candidates received the unanimous approval of the panel. Individual acceptance and rejection letters were prepared and distributed by the Director. Interestingly, all of the candidates who were accepted agreed to come. Table 1 provides some statistics on applications and acceptances.

Table 1. 2005 Participant Numbers	
Applications and inquiries	58
Acceptances	29
Participants	27
Graduating Seniors	1
Graduate Students	21
Postdoctoral Fellows	1
Junior Faculty	1
Senior Researchers	3
US Citizens/Foreign National	8/19
PNNL Hosts	21
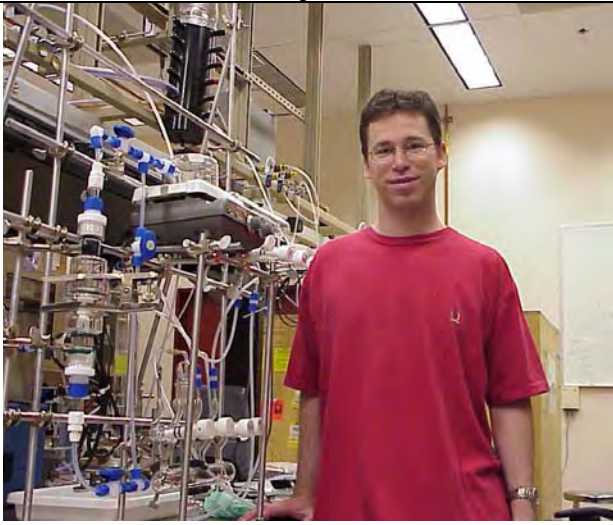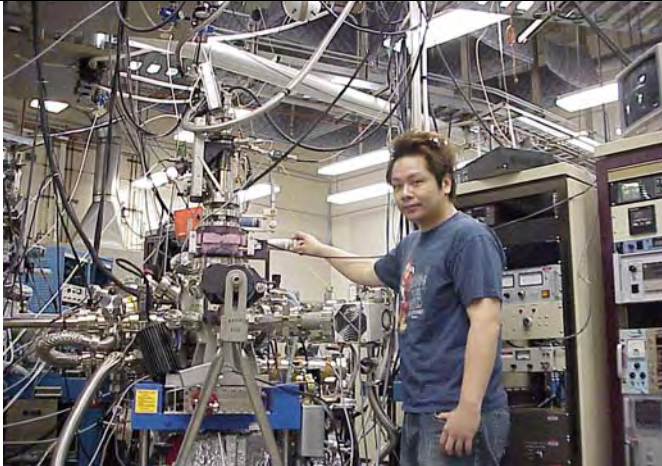
The application and acceptance procedure requires participation from all concerned parties: the PNNL hosts, the visitors and the visitors' supervisors at his or her home institution (if applicable). Further, PNNL hosts were expected to provide appropriate mentoring for the visitors as well as ensure all necessary resources were available to accomplish the proposed work. The visitors bear the bulk of the application responsibility in order to come to PNNL for an extended time away from home. The visitors' supervisors were expected to continue financial support during this visit to PNNL since the Summer Research Institute only covered travel to and from PNNL and partial living expenses.

Each visitor had a specific program tailored around his or her schedule and research goals. To accommodate individual schedules, the 2006 summer appointments began in early May and the final appointment concluded in September. Prior to their arrival, each participant was paired with a PNNL host and worked out a research program for the visit.
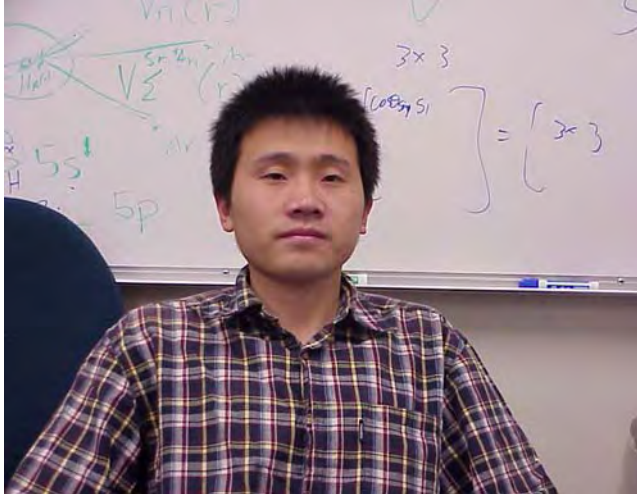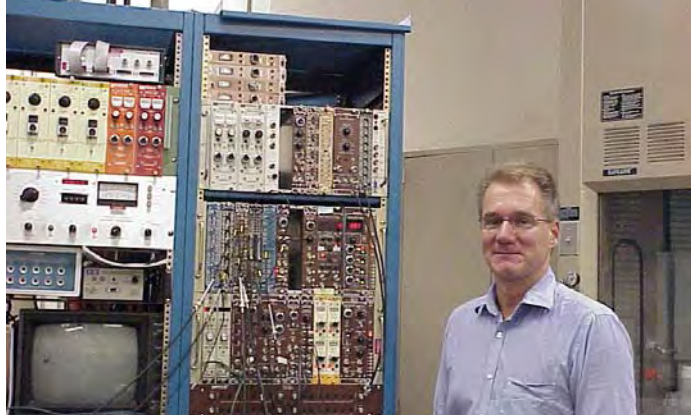
All of this activity was coordinated with the visitor's supervisor. Most often, our visitor was playing a role in a collaboration or prospective collaboration between the PNNL host and his or her supervisor. (For the cases of graduating seniors or faculty members slightly different procedures apply.) Table 2 lists our visitors, PNNL hosts and home institution supervisors. Table 3 shows the University Statistics

Table 2. Interfacial and Condensed Phase Chemical Physics Summer Research
Institute PNNL visitors, academic advisors, PNNL hosts
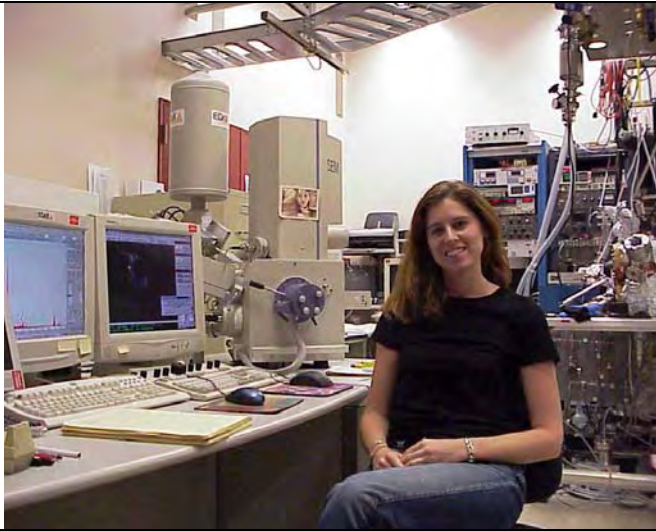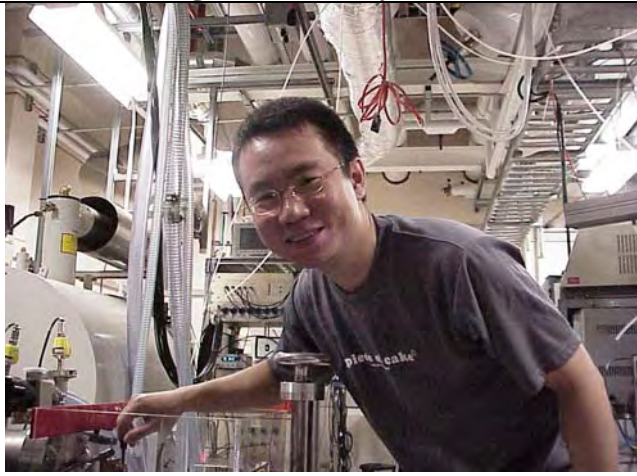
Visitors
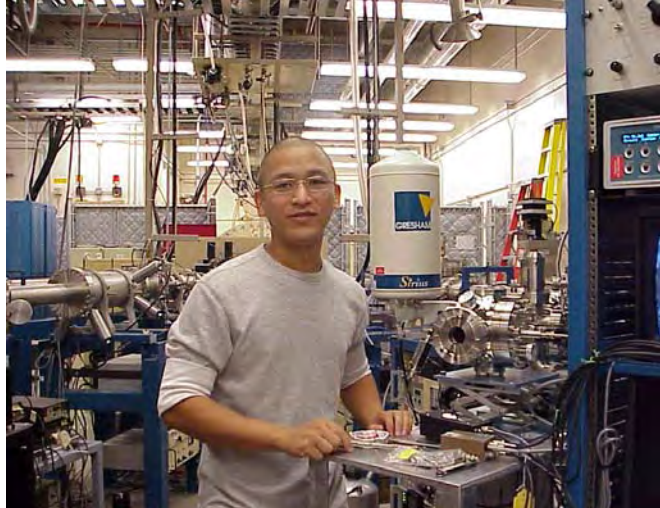
Jeremy Cain	
	Mechanical Engineering University of Southern California Los Angeles, CA jcain@usc.edu **University Advisor:** Prof. Hai Wang Department of Aerospace and Mechanical Engineering haiw@usc.edu **PNNL Host:** Dr. Alexander Laskin, EMSL alexander.laskin@pnl.gov
Chia-Lin Chang	
	Applied Physics Harvard University Cambridge, MA clchang@fas.harvard.edu **University Advisor:** Prof. Shriram Ramanathan Material Sciences Group shriram@deas.harvard.edu **PNNL Host:** Dr. Shuttha Shutthanandan, EMSL shuttha@pnl.gov
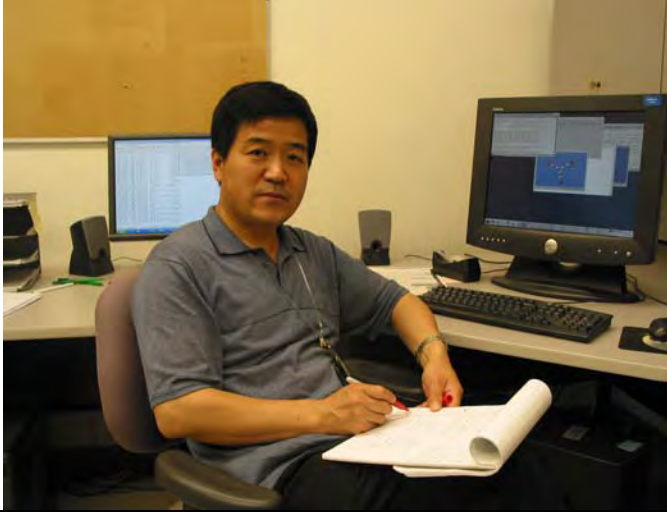
Chan Lan Chun	
	Environmental Engineering University of Minnesota Minneapolis, MN chun0157@umn.edu **University Advisor:** Prof. William A. Arnold Dept. of Civil Engineering arnol032@umn.edu **PNNL Host:** Dr. Don Baer, EMSL don.baer@pnl.gov
Luis Cuadra-Rodriguez	
	Chemistry University of Colorado at Boulder Boulder, CO luis.cuadra-rodriguez@colorado.edu **University Advisor:** Prof. Barney Ellison Department of Chemistry and Biochemistry barney@jila.colorado.edu **PNNL Host:** Dr. Alla Zelenyuk, FSD alla.zelenyuk@pnl.gov
Jun Cui	
	Chemistry University of Pittsburgh Pittsburgh, PA Jun_cui@hotmail.com **University Advisor:** Prof. Kenneth Jordan Department of Chemistry jordan@pitt.edu **PNNL Host:** Dr. Vanda Glezakou, FSD vanda.glezakou@pnl.gov

Shiyu Du	
	Chemistry Purdue University West Lafayette, Indiana dus@purdue.edu **University Advisor:** Prof. Joseph Francisco Department of Earth & Atmospheric Sciences jfrancis@purdue.edu **PNNL Host:** Dr. Greg Schenter, FSD greg.schenter@pnl.gov
Debamitra Dutta	
	Materials Engineering University of Florida Gainesville, FL ddutta@erc.ufl.edu **University Advisor:** Prof. Brij Mougil Department of Materials Science & Engineering bmoudgil@erc.ufl.edu **PNNL Host:** Dr. SK Sundaram, ETD sk.sundaram@pnl.gov
Dr. Mikael Elfman	
	Engineering Nuclear Physics Research Scientist, Lund Institute of Technology, University of Lund Lund, Sweden Mikael.Elfman@nuclear.lu.se **PNNL Host:** Dr. Yanwen Zhang, EMSL yanwen.zhang@pnl.gov
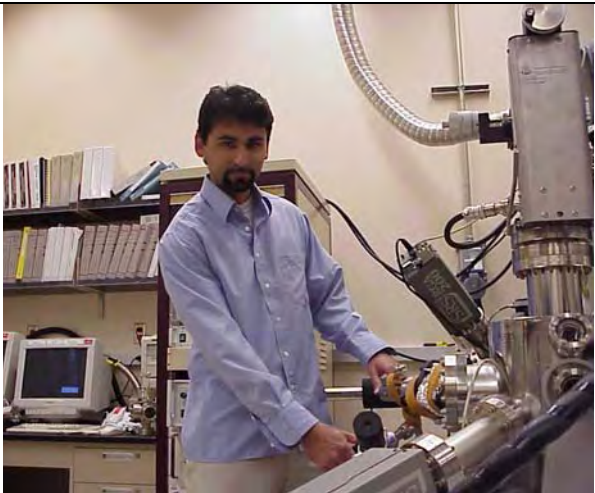
Diego E.B. Gomes	
	Biophysics Universidad Federal do Rio De Janeiro, Rio De Janeiro. Brazil diego@biof.ufrj.br **University Advisor:** Prof. Pedro Geraldo Pascutti Institute of Biophysics pascutti@biof.ufrj.br **PNNL Host:** Dr. Thereza Soares, C&ISD tasoares@pnl.gov
Rodrigo Gonzalez	
	Environmental Engineering Autonomous Metropolitan University Mexico City, Mexico rqga3@yahoo.com.mx **University Advisor:** Prof. Luisa Molina Molina Center for Strategic Studies in Energy and the Environment ltmolina@MIT.EDU **PNNL Host:** Dr. Alexander Laskin, EMSL alexander.laskin@pnl.gov
Matteo Guglielmi	
	Chemistry Ecole Polytechnique Federale De Lausanne, Lausanne, Switzerland matteo.guglielmi@epfl.ch **University Advisor:** Prof. Ursula Roethlisberger Laboratory of Computational Chemistry and Biochemistry at the Swiss Federal Institute of Technology **PNNL Host:** Dr. Roberto Lins Neto, C&ISD roberto.lins@pnl.gov

Dr. Rebecca Hopkins	
	Chemical Sciences Lawrence Berkeley National Laboratory Berkeley, CA RJHopkins@lbl.gov **Supervisor:** Dr. Mary K. Gilles Chemical Sciences **PNNL Host:** Dr. Alexander Laskin, EMSL alexander.laskin@pnl.gov
Kirsten Johnson	
	Physical Chemistry Massachusetts Institute of Technology Cambridge, MA kirstenj@mit.edu **University Advisor:** Prof. Mario Molina Professor of Chemistry and Professor of Earth, Atmosphere, and Planetary Sciences mmolina@mit.edu **PNNL Host:** Dr. Alexander Laskin, EMSL alexander.laskin@pnl.gov
Ngor wai (Corey) Lam	
	Chemistry The University of Hong Kong Pokfulam, Hong Kong lamnw@hkusua.hku.hk **University Advisor:** Prof. Ivan Chu Department of Chemistry ivankchu@hku.hk **PNNL Host:** Dr. Julia Laskin, FSD julia.laskin@pnl.gov

Vu Lam	
	Electrical Engineering University of Central Florida Orlando, FL organic@gmail.com **University Advisor:** Prof. Kalpathy Sundaram School Electrical Engineering and Computer Science sundaram@mail.ucf.edu **PNNL Host:** Dr. Theva Thevuthasan, FSD theva@pnl.gov
Christopher Lane	
	Physical Chemistry Georgia Institute of Technology, School of Chemistry and Biochemistry Atlanta, GA Christopher.lane@chemistry.gatech.edu **University Advisor:** Prof. Thomas Orlando Department of Chemistry & Biochemistry thomas.orlando@chemistry.gatech.edu **PNNL Host:** Dr. Greg Kimmel, FSD greg.kimmel@pnl.gov
Chan-Woo Lee	
	Materials Science and Engineering University of Florida Gainesville, FL cwandtj@ufl.edu **University Advisor:** Prof. Susan Sinnott Department of Materials Science and Engineering ssinn@mse.ufl.edu **PNNL Host:** Dr. Ram Devanathan, FSD ram.devanathan@pnl.gov

Prof. Jiangyu Li	
	Dept. of Mechanical Engineering University of Washington, Seattle, WA jjli@u.washington.edu **PNNL Host:** Dr. Leonard Fifield, ETD leonard.fifield@pnl.gov
Prof. Si-Dain Li	
	Department of Chemistry Xinzhou Teachers University, Shanxi, PRC lisidian@yahoo.com **PNNL Host:** Prof. Lai-Sheng Wang, Washington State University and PNNL ls.wang@pnl.gov
Suiqiong Li	
	Materials Engineering Auburn University Auburn, AL lisuiqi@auburn.edu **University Advisor:** Prof. Zhongyang Cheng Department of Materials Engineering chengzh@eng.auburn.edu **PNNL Host:** Dr. Chongmin Wang, EMSL chongmin.wang@pnl.gov

Julie Lloyd	
	Analytical Chemistry University of Delaware Newark, DE jlloyd@udel.edu **University Advisor:** Prof. Murray V. Johnston Dept. of Chemistry and Biochemistry mvj@udel.edu **PNNL Host:** Dr. M. Lizabeth Alexander, EMSL Lizabeth.alexander@pnl.gov
Rebecca Lowton	
	Inorganic Chemistry University of Oxford, Worcester College, Oxford, England Rebecca.lowton@worc.ox.ac.uk **University Advisor:** Prof. Peter Edwards Inorganic Chemistry Laboratory peter.edwards@chem.ox.ac.uk **PNNL Host:** Dr. Thomas Autrey, FSD tom.autrey@pnl.gov
Wagner Lucena	
	Biology Embrapa Algodao Recife, Brazil wagner@cnpa.embrapa.br **PNNL Host:** Dr. Roberto Lins Neto, C&ISD roberto.lins@pnl.gov

Amir Saheb	
	Chemistry Georgia Institute of Technology Atlanta, GA gtg563a@mail.gatech.edu **University Advisor:** Prof. Jiri Janata Dept. of Chemistry and Biochemistry jiri.janata@chemistry.gatech.edu **PNNL Host:** Dr. Don Baer, EMSL don.baer@pnl.gov
Prof. Andrzej Sobolewski	
	Professor of Physics Institute of Physics, Polish Academy of Sciences Warsaw Poland sobola@ifpan.edu.pl **PNNL Host:** Dr. Sotiris Xantheas, FSD Sotiris.xantheas@pnl.gov
Jennie Thomas	
	Chemistry University of California, Irvine, California jenniet@uci.edu **University Advisor:** Prof. Barbara Finlayson-Pitts Professor, Chemistry School of Physical Sciences bjfinlay@uci.edu **PNNL Host:** Dr. Liem Dang, FSD liem.dang@pnl.gov

Guanjun Wang	
	Physical Chemistry Fudan University Fudan, PRC 031022047@fudan.edu.cn **University Advisor:** Dr. Mingfei Zhou Department of Chemistry mfzhou@fudan.edu.cn **PNNL Host:** Dr. Lai-Sheng Wang, FSD ls.wang@pnl.gov

Table 3. 2005 University Statistics	
Auburn University, Auburn, AL, USA	1
Autonomous Metropolitan University, Mexico City, MEXICO	1
Ecole Polytechnique Federale De Lausanne, SWITZERLAND	1
Embrapa Algodão, Campina Grande, BRAZIL	1
Fudan University, Fudan, PRC	1
Georgia Institute of Technology, Atlanta, GA, USA	2
Harvard University, Cambridge, MA, USA	1
Institute of Physics, Polish Academy of Sciences, Warsaw, POLAND	1
Lawrence Berkeley National Laboratory, Berkeley, CA, USA	1
Lund Institute of Technology, Lund SWEDEN	1
Massachusetts Institute of Technology, Cambridge, MA, USA	1
University of Oxford, Worcester College, Oxford, ENGLAND	1
Purdue University, West Lafayette, IN, USA	1
The University of Hong Kong, Pokfulam, HONG KONG	1
University of Central Florida Orlando, Orlando, FL, USA	1
Universidad Federal do Rio De Janeiro, BRAZIL	1
University of California, Irvine, Irvine, CA, USA	1
University of Colorado at Boulder, Boulder, CO, USA	1
University of Delaware, Newark, DE, USA	1
University of Florida, Gainesville, FL, USA	2
University of Minnesota, Minneapolis, MN, USA	1
University of Pittsburgh, Pittsburgh, PA, USA	1
University of Southern California, Los Angeles, CA, USA	1
University of Washington, Seattle, WA, USA	1
Xinzhou Teachers University, Shanxi, PRC	1

27

Benefits

As described above, participation in the Summer Research Institute required a significant investment on the part of all parties involved. The only reason that a young scientist, PNNL host, or academic advisor would be involved is if they believed that their investment would be of benefit. We believe that the institute's structure promoted the likelihood of that success. PNNL is in a rather remote location far from major urban centers and large academic institutions, and these visitors were a real treat at the laboratory. Their inquisitiveness, creativity and energy helped stimulate PNNL staff to think in new, creative ways.

New in FY 2006

For readers familiar with the Interfacial and Condensed Phase Chemical Physics Summer Research Institute, most of the procedures and the underlying philosophy are unchanged. However, several important details are new. Some of these changes have been motivated by financial constraints; while other changes were driven by new state laws and federal regulations. New opportunities have also opened up.

This year, all of the participants came to PNNL with support from their home institutions. We can no longer offer "fellowships" or other forms of full support. It is a testimony to our growing reputation, however, that we had no shortage of qualified applicants and therefore nearly doubled the number of visitors that we hosted.

We also received assistance from the NSF, which supported seven of our visitors. We coordinated this assistance with the help of Dr. Katherine Covert of the NSF and the EMSL management. The NSF program was originally set-up by Dr. Covert and Dr. Allison Campbell, the EMSL director, for NSF grant holders to perform on-site work at EMSL. By mutual agreement, SRI participant, who were working in EMSL received the same level of support (travel and housing) as non-NSF supported visitors.

Dr. Rebecca Hopkins, a postdoctoral fellow from Lawrence Berkeley National Laboratory was the summer institute's first non-academic participant. She was also the first SRI participant from another national lab.

FY 2006 saw the inauguration of a new lecture series. The inaugural lecture was given by Prof. John Wheeler of UCSD. We hope in the future to expand this to several talks throughout the summer.

Three of our visitors did not fit into the "graduate student or young scientist" category. Dr. Michael Elfman of the Lund Institute of Technology is an expert in PIXIE and accelerator mass spectroscopy. Prof. Si-Dain Li is a computational chemist from Xinzhou Teachers University, Shanxi, PRC; he is also president of Xinzhou Teachers University. Prof. Andrzej L Sobolewski, is an associate professor of physics at the Physics Institute of the Polish Academy of Sciences and an expert in photophysics. These visitors were sponsored on a "resource available" basis. Their presence here in no

way took resources from junior researchers. Except for their more senior status, they otherwise met all of the requirements for participation in the Summer Institute.

Measures of Success

This is an educational and research enterprise. As such, its real success will only become apparent in the coming years and decades. Further, the relatively short time that our visitors were here can only be a small part of the story. We can already point, however, to a few early successes. First, although applicant pool was limited, we did receive twenty-nine outstanding applications. Twenty-seven of these candidates actually came to PNNL to participate in the institute. Second, all of the candidates, PNNL mentors and academic advisors expressed enthusiasm about the institute at the outset and were generally more enthusiastic by the end of the respective summer appointments. In several cases, plans are being readied for return visits to PNNL, independent of the summer program. Numerous presentations and manuscripts are being readied for submission to peer-reviewed journals.

2004 Follow-up

In last year's report, we stated that at least half-dozen papers were being prepared for publication as a result of the research performed at PNNL by Summer Institute participants. Currently, (October 2006) there are still four to six manuscripts in various stages of preparation as a consequence of the work in 2004, but sixteen papers, listed in Table 4 have already been published in the peer-reviewed literature. At least thirteen presentations at national or international meetings were also produced—see Table 5. In addition, numerous internal PNNL reports have been generated.

The author lists from 2004 (see Table 4 and 5) also point to an additional and somewhat unexpected benefit of the Summer Research Institute. Those visitors doing laboratory work in EMSL were extremely facile in harnessing internal collaborative opportunities and resources. Thus many of the papers included unanticipated participation by non-host PNNL staff members.

Table 4. Peer Reviewed Publications from 2004 work through August 2006
Jormarie Alvarez,[a] R. Graham Cooks,[c] S. E. Barlow, Daniel J. Gaspar, Jean H. Futrell, and Julia Laskin,[b] "*Preparation and in Situ Characterization of Surfaces Using Soft Landing in a Fourier Transform Ion Cyclotron Resonance Mass Spectrometer,*" Anal. Chem., **77** (2005), 3452-3460
Bogdan Gologan, Jason R. Green, Jormarie Alvarez,[a] Julia Laskin[b] and R. Graham Cooks,[c] "*Ion/surface reactions and ion soft-landing,*" Phys. Chem. Chem. Phys., **7** (2005) 1490–1500.
Yingge Du,[a] Y, S Atha, R Hull, James F Groves,[c] Igor V Lyubinetsky,[b] and Donald R Baer, "*Focused-Ion-Beam Directed Self-Assembly of Cu₂O Islands on SrTiO₃(100), Applied Physics Letters* **84** (2004) 5213-5215
Anita Lagutschenkov,[a] George S. Fanourgakis, Gereon Niedner-Schatteburg,[c] and Sotiris S. Xantheas,[b] "*The spectroscopic signature of the "all-surface" to "internally solvated" structural transition in water clusters in the n=17–21 size regime,*" J. Chem. Phys., **122** (2005) 194310
Fung Suong Ou[a], Laxmikant V. Saraf, and Donald R. Baer,[b] "*Use of Hydrogen Bubble to Direct Pattern Microstructures of Porous Silicon*" Appl. Phys. Lett., (submitted 2005)
JA Lloyd, Jeffrey M Spraggins,[a] Murray V Johnston,[c] and Julia Laskin,[b] "*Peptide Ozonolysis: Product Structures and Proposed Mechanisms for Oxidation of Tyrosine and Histidine*" J. Amer. Soc. Mass Spectrom. (submitted)
Steven L. Tait,[a] Zdenek Dohnálek.[b] Charles T. Campbell[c] and Bruce D. Kay, "*n-alkanes on MgO100. I. Coverage-dependent desorption kinetics of n-butane,*" J. Chem. Phys., **122** (2005) 164707.
Steven L. Tait,[a] Zdenek Dohnálek.[b] Charles T. Campbell[c] and Bruce D. Kay, "*n-alkanes on MgO100. II. Chain length dependence of kinetic desorption parameters for small n-alkanes,*" J. Chem. Phys., **122** (2005) 164708
Yiguang Wang,[a] L Zhang, Y Fan, J. Luo, DE McCready, CM Wang,[b] and L An,[c] "*Synthesis, Characterization, and Optical Properties of Pristine and Doped Yttrium Aluminum Garnet Nanopowders*" J. Am. Ceram. Soc., **88** (2005) 284–286
Jormarie Alvarez[a], JH Futrell, and Julia Laskin[b]. 2006. "*Soft-Landing of Peptides onto Self-Assembled Monolayer Surfaces.*" Journal of Physical Chemistry A 110(4):1678-1687. doi:10.1021/jp0555044
Hyun-shik Chang[a], Gregory V. Korshin,[c] Zheming Wang[b], and JM Zachara. 2006. "*Adsorption of Uranyl on Gibbsite: A Time-Resolved Laser-Induced Fluorescence Spectroscopy Study.*" Environmental Science and Technology 40(4):1244-1249.
Yingge Du[a], Igor V Lyubinetsky[b], DR Baer, and James F Groves[c]. 2006. "*Formation of Cu2O Quantum Dots on SrTiO₃ (100): Self-Assembly and Directed Self-Assembly." Journal of Applied Physics*. [In Press]
Alan G. Joly[b], JR Williams, SA Chambers, G Xiong, WP Hess, and David M Laman[a]. 2006. "*Carrier Dynamics in a-Fe₂O₃ (0001) Thin Films and Single Crystals Probed by Femtosecond Transient Absorption and Reflectivity.*" Journal of Applied Physics 99(5): Article: 053521 (6 pages).

Howard L Heinisch[b], HL, F Gao, RJ Kurtz, and Edward A Le[a]. 2006. "*Interaction of Helium Atoms with Edge Dislocations in Alpha-Fe*." Journal of Nuclear Materials 351(1-3):141-148. doi:10.1016/j.jnucmat.2006.02.02

Fung S Ou[a], Laxmikant V Saraf[b], and DR Baer. 2006. "*Patterned Regions of Porous Silicon through Trapped Hydrogen Bubbles*." Applied Physics Letters 88(14):143113 (3 pages). doi:10.1063/1.2188039

Lloyd JA, Jeffrey M Spraggins[a], Murray V Johnston[c], and Julia Laskin[b]. 2006. "*Peptide Ozonolysis: Product Structures and Relative Reactivities for Oxidation of Tyrosine and Histidine Residues*." Journal of the American Society for Mass Spectrometry 17(9):1289-1298. doi:10.1016/j.jasms.2006.05.009

a) 2004 ICPCPSRI Visitor b) PNNL Host c) Supervisor

Table 5 Presentations/Conference Papers from 2004 work though August 2006:
Fung Suong Ou[a], Laxmikant V. Saraf, and Donald R. Baer,[b] "*Site-specific formation of nanoporous silicon on micro-fabricated silicon surfaces,*" Presented by Fung Suong Ou at MRS 2004 Fall Meeting, Boston, MA on December 1, 2004. PNNL-SA-42481, Pacific Northwest National Laboratory, Richland, WA
CH Henager, Jr.,[b] EA Le[a], and RH Jones. 2004. "*A Model Stress Analysis of Swelling in SiC/SiC Composites as a Function of Fiber Type and Carbon Interphase Structure*." In the *11th International Conference on Fusion Reactor Materials in JOURNAL OF NUCLEAR MATERIALS*, no. Pt A, ed. Kohyama, A., **329-333** (2005) 502 - 506. Elsevier, Amsterdam, Netherlands
Julia Laskin[b], O Hadjar, P Wang, JH Futrell, Jormarie Alvarez[a], Jason R Green[a], and R.Graham Cooks[c]. 2006. "*Soft Landing of Peptide Ions on Surfaces*." Presented by Julia Laskin (Invited Speaker) at Isolated Biomolecules and Biomolecular Interactions (IBBI), Trest Castle, Czech Republic on May 10, 2006. PNNL-SA-48630
Julia Laskin[b], Jormarie Alvarez[a], R Graham Cooks[c], SE Barlow, and JH Futrell. 2004. "*Novel Techniques for Studying Ion-Surface Interactions in FT-ICR MS*." Presented by Julia Laskin (Invited Speaker) at ASMS Conference, Nashville, TN on May 24, 2004. PNNL-SA-40658.
Julia Laskin[b], Jormarie Alvarez[a], R Graham Cooks[c], JH Futrell, and SE Barlow. 2005. "*Collisions of Peptide Ions with Surfaces Studied Using FT-ICR MS*." Presented by Julia Laskin at 53rd ASMS Conference on Mass Spectrometry, San Antonio, TX on June 7, 2005. PNNL-SA-45421.
Yingge Du[a], S Atha, R Hull, James F Groves[c], Igor V Lyubinetsky[b], and DR Baer. 2004. "*Guided Control of Cu_2O Nanodot Self-Assembly on $SrTiO_2$ (100)*." Materials Research Society Symposia Proceedings 811:451-456.
Fanourgakis GS, Anita Lagutschenkov[a], K Kowalski, Gereon Niedner-Schateburg[b], and Sotiris S Xantheas[b]. 2005. "*Structural, spectral and excited state features of water hydrogen bonding networks: Results of ab-initio calculations and interaction potentials*." Presented by Sotiris S. Xantheas (Invited Speaker) at American Chemical Society, San Diego, CA on March 13, 2005. PNNL-SA-43386.

Fanourgakis GS, Anita Lagutschenkov[a], Gereon Niedner-Schateburg[b], and Sotiris S Xantheas[b]. 2005. "*Structural and spectral features of size selected water clusters in the n=7-21 regime: Results from electronic structure calculations and empirical potentials*." Presented by Sotiris Xantheas (Invited Speaker) at Symposium on Size Selected Clusters, Brand, Austria on February 28, 2005. PNNL-SA-4383
Anita Lagutschenkov[a], GS Fanourgakis, Gereon Niedner-Schateburg[b], and Sotiris S Xantheas[b]. 2005. "*The Spectroscopic Signature of the "All-Surface" to "Internally Solvated" Structural Transition in Water Clusters in the n=17-21 Size Regime*." Presented by Sotiris S. Xantheas (Invited Speaker) at EMSI International Workshop on Ions and Molecules at Aqueous Interfaces, Prague, Czech Republic on June 27, 2005. PNNL-SA-44788.
Alan G. Joly[b], WP Hess, G Xiong, David M Laman[a], JR Williams, and SA Chambers. 2005. "*Carrier Lifetimes and Dynamics in Epitaxial Grown Fe_{2O3}/Cr_{2O3} Thin Films Measured by Femosecond Transient Reflectivity and Absorption*." Presented by Gang Xiong (Invited Speaker) at APS Meeting, Los Angeles, CA on March 21, 2005. PNNL-SA-42076.
Fung S Ou[a], Laxmikant V Saraf[b], DR Baer, Z Wang, and MH Engelhard. 2004. "*Use of Hydrogen Reactivity During Chemical Etching to Achieve Site-Specific Nano-Porosity*." Presented by Don Baer at Micro Nano Breakthrough Conference, Portland, OR on July 28, 2004. PNNL-SA-42111.
Jeffrey M Spraggins[a], Julia Laskin[b], and Murray V Johnston[c]. 2005. "*Ozonated Peptides: Insight Into Structure and Fragmentation Energetics Using SID FT-ICR MS*." Presented by Julia Laskin (Invited Speaker) at 53rd ASMS Conference on Mass Spectrometry, San Antonio, TX on June 8, 2005. PNNL-SA-45420.
Liu Y, Zhiwei Yang[a], PL Gassman, Hai Wang[c], and Alexander Laskin[b]. 2006. "*Probing Deliquescence, Efflorescence and Hygroscopic Growth of Aerosols Using Micro-FTIR Spectroscopy*." Presented by Yong Liu at AGU Meeting, San Francisco, CA on December 12, 2006.

a) 2004 ICPCPSRI Visitor **b)** PNNL Host **c)** Supervisor

2005 Follow-up

As we noted above, one year is a fairly short time for scientific research to be performed, the results digested, written-up and published. None-the-less work from the summer of 2005 has already produced three refereed publications (Table 6) and fifteen presentations (Table 7). There is every reason to expect this number to rise substantially in FY 2007.

Last year we noted that Mr. Anoop M. Mayampurath had been offered employment at PNNL. In the intervening year he has become a very productive and respected member of the EMSL's Instrument Development Lab. We also noted that Dr. Zhenrong Zhang's visit in Bruce Kay's lab has been extended. Since that time, she has become a postdoctoral fellow at PNNL.

Table 6 Publications from 2005 work through August 2006
Gutowska A, L Li, Y Shin, CM Wang, XS Li, JC Linehan, RS Smith, BD Kay, Benjamin A Schmid[a], WJ Shaw, MS Gutowski, and Thomas Autrey[b]. 2005. "*Nano-Scaffold Mediates Hydrogen Release and Reactivity of Ammonia Borane*." Angewandte Chemie International Edition 44(23):3578-3582.
Zhenrong Zhang[a], O Bondarchuk, John M White[c], BD Kay, and Zdneek Dohnalek[b]. 2006. "*Imaging Adsorbate O-H Bond Cleavage: Methanol on TiO$_2$(110)*." Journal of the American Chemical Society 128(13):4198-4199
Yiguang Wang[a], Linan An[c], Y Fan, L Zhang, Sarah D Burton[b], and Z Gan. 2005. "*Oxidation of Polymer-derived SiAICN Ceramics*." Journal of the American Ceramic Society 88(11):3075-3080. doi:10.1111/j.1551-2916.2005.00542.x

Table 7 Presentations and Conference Proceedings of 2005 work through August 2006
Julia Laskin[b], and Ivan K Chu[a]. 2006. "*Fragmentation Energetics of Peptide Radical Cations from Time-and Energy-Resolved Surface-Induced Dissociation Studies*." Presented by Julia Laskin at ASMS Conference on Mass Spectroscopy, Seattle on May 29, 2006. PNNL-SA-48918.
Julia Laskin[b], and Ivan K Chu[a]. 2006. "*Fragmentation Energetics of Peptide Radical Cations from Time-and Energy-Resolved Surface-Induced Dissociation Studies*." Presented by Julia Laskin (Invited Speaker) at 4th International UPPSALA Conference, Hong Kong, Hong Kong on December 14, 2006. PNNL-SA-48918.
Lam C, G Orlova, Julia Laskin[b], and Ivan K Chu[a]. 2006. "*Facile Generation and Characterization of Cationic Radical Peptides: Ligand Effect and Peptide Structures*." Presented by Julia Laskin at ASMS Conference on Mass Spectroscopy, Seattle, WA on May 29, 2006. PNNL-SA-48953.
Futrell JH, Ivan K Chu[a], and Julia Laskin[b]. 2006. "*Collisional Activation and Dissociation of Even- and Odd-Electron Peptide Cations*." Presented by Jean Futrell (Invited Speaker) at 24th Informal Meeting on Mass Spectrometry, Ustron, Poland on May 14, 2006. PNNL-SA-50638.
Bauder LM, S Thevuthasan, S Kuchibhatla, and YJ Kim. 2006. "*Growth and Characterization of Samaria Doped Ceria for the Application of Fuel Cell Electrolytes*." Presented by Lilyann Bauder (Invited Speaker) at PNNL Student Poster Session, Richland, WA on August 4, 2006. PNNL-SA-51244.
Satyanarayana Kuchibhatla[a], OA Marina, CM Wang, BW Arey, V Shutthanandan, MH Engelhard, LV Saraf, DW Matson, Sudipta Seal[c], Donald R Baer[b], and S Thevuthasan. 2005. "*Fabrication of Gadolinia and Samaria Doped Ceria and Zirconia Vertical Layered Nanostructures for Solid Oxide Fuel Cell Applications*." Presented by Satyanarayana Kuchibhatla at 2005 MRS Fall Meeting, Boston, MA on November 29, 2005. PNNL-SA-45945.

Donald R Baer[b], MH Engelhard, AS Lea, DJ Gaspar, KH Pecher, CM Wang, JE Amonette, AA El-azab, Satyanarayana Kuchibhatla[a], and Sudipta Seal[c]. 2006. "*The Secret Life of Nanoparticles: characteristics of nanoparticles and nanostructured materials that are frequently forgotten or ignored.*" Presented by D.R. Baer (Invited Speaker) at 2006 TMS Annual Meeting & Exhibition, San Antonio, TX on March 12, 2006. PNNL-SA-46479.

Gutowska A, Benjamin A Schmid[a], L Li, RS Smith, BD Kay, JC Linehan, WJ Shaw, NJ Hess, Y Shin, MS Gutowski, and Thomas Autrey[b]. 2005. "*Hydrogen Storage in HNBH Systems.*" Presented by Tom Autrey (Invited Speaker) at 3rd International Conference on Materials for Advanced Technologies 2005, Singapore, China on July 5, 2005. PNNL-SA-44161.

Smith RS, Benjamin A Schmid[a], NJ Hess, BD Kay, and Thomas Autrey[b]. 2005. "*Mechanistic studies of molecular hydrogen formation from borane ammonia complexes.*" Presented by Tom Autrey at PacifiChem 2005, Honolulu, HI on December 16, 2005. PNNL-SA-44791.

Benjamin A Schmid[a], A Gutowska, L Li, WJ Shaw, JC Linehan, NJ Hess, LL Daemen, C Brown, E Mamontov, and and Thomas Autrey[b]. 2005. "*Novel hybrid materials for hydrogen storage: using mesoporous scaffolds to enhance the reactivity and selectivity of hydrogen release from ammonia borane.*" Presented by Tom Autrey at PacifiChem 2005, Honolulu, HI on December 19, 2005. PNNL-SA-44871.

Smith RS, BD Kay, LL Daemen, C Brown, E Mamontov, NJ Hess, WJ Shaw, JC Linehan, Benjamin A Schmid[a], AC Stowe, MS Gutowski, and and Thomas Autrey[b]. 2005. "*Spectroscopic Studies of Hydrogen Formation From Amineborane Complexes.*" Presented by Tom Autrey at 230th National American Chemical Society Meeting, Washington, DC on August 28, 2005. PNNL-SA-45354.

Hartl MA, LL Daemen, Thomas Autrey[b], JC Linehan, NJ Hess, AC Stowe, MS Gutowski, C Brown, E Mamontov, and Benjamin A Schmid[a]. 2005. "*Methyl Torsion Dynamics in Methyl Borate - An Inelastic Neutron Scattering Study.*" Presented by Monika A. Hartl at 230th National American Chemical Society Meeting, Washington, DC on August 28, 2005. PNNL-SA-45356.

Thomas Autrey[b], M Bowden, T Kemmitt, WJ Shaw, NJ Hess, JC Linehan, MS Gutowski, and Benjamin A Schmid[a]. 2006. "*Mechanistic Studies of Hydrogen Release from Solid Amine Borane Materials.*" Presented by Mark Bowden at Materials Research Society, San Francisco, CA on April 18, 2006. PNNL-SA-49481.

Wei Wei[a], Y Sun, John M White[c], G Xiong, AG Joly, Kenneth M Beck[b], and Wayne P Hess[b]. 2006. "*Real Time Study of Cu Diffusion Through a Ru Thin Film by Photoemission Electron Microscopy (PEEM).*" In The Materials Research Society. PNNL-SA-49613, Pacific Northwest National Laboratory, Richland, WA.

Zhenrong Zhang[a], O Bondarchuk, John M White[c], J Kim, BD Kay, and Zdenek Dohnalek[b]. 2006. "*Surface Reactions of Alcohols on TiO$_2$(110) Investigated by in situ Scanning Tunneling Microscopy.*" Abstract submitted to ACS National Meeting, San Francisco, CA.

Participant Survey

The questionnaire in the Appendix survey was sent to all of the summer program participants (visitors, hosts and advisors). From these, approximately seventy individuals we received thirty-two replies. I also attempted to conduct exit interviews with all of the visitors and actually met with all but three. Further, I have had informal discussions with visitors and PNNL hosts/mentors. Even though the Summer Institute is a scientific program, we have made no attempt to be "scientific" about the survey. The survey serves three distinct purposes. First, it helps to identify problems and weaknesses. Second, we also attempt to identify the "really" good things that need to be retained. And third, it helps to provide guidance for future program improvements.

General Impressions

Overall, the results of our survey and other inquiries produced very similar results to previous years' feedback. That is, most participants—visitors, hosts and home institution supervisors—were more enthusiastic about the program after participating in it than before. I received both written and verbal comments to the effect that the program should be continued into the indefinite future and suggestions that the program should be expanded in several ways.

Praise was universal for the smooth operation of the summer program. Credit for this goes primarily to our administrator, Ms. Nikki Avery. Not only did she organize things to run as smoothly as possible, when the inevitable problem did arise, she was able to resolve them quickly. On the one or two occasions where problems became more protracted, the difficulties could generally be traced to people not contacting her promptly---in future years, our visitors and hosts need to be more aware of this avenue.

Comments that elicited narrative responses are given in the appendix and arranged according to the role of the respondent—Academic Supervisor, PNNL host, visitor.

Difficulties

Most of the difficulties experienced by our visitors fell into two broad categories: those associated with PNNL and those associated with Richland. Lab-level problems and difficulties mostly arise from our visitors' unfamiliarity with the national lab work environment and PNNL's own idiosyncratic features. Most of these problems required the visitor to become more familiar with PNNL, while others required Nikki Avery's intervention. Future visitors will be explicitly reminded to contact Nikki or the SRI Director when as soon as problems arise.

The most irksome problem confronted our foreign national visitors, who generally cannot get 24/7 access to EMSL laboratories. This is an EMSL management policy that was implemented for reasons of safety and security. Most SRI visitors came by my office at the beginning of their stay and I informed them of this policy. This seemed to reduce the frustration levels that were evident in earlier years.

Other difficulties experienced by our visitors are simply the result of the physical location of the laboratory on the outskirts of Richland, WA. Housing and transportation can be challenging. Nikki arranged for all of our visitors from outside the US to stay at PNNL's guesthouse. A number of participants from inside the US also stayed there. All were pleased with the accommodations; however it is difficult get from there to local stores without a car. Similarly those staying in town had a three to five mile commute to the lab. The housing and transportation problems have improved somewhat over the last few years, but still remain a challenge.

There were two cases where the PNNL host appeared to be over committed and either did not have enough physical space—a serious problem across PNNL—or was engaged in extensive travel and did not have adequate time. All would be hosts and mentors need to be reminded of their obligations in both of these areas. It is better not to host a summer visitor than to be unable to provide the resources necessary for a successful experience. With that said, the Summer Institute's general experience with PNNL hosts has been very positive.

Future Improvements

Publicity

In FY 2006, we substantially increased our publicity efforts, and as reported above nearly doubled our participation. It will be important to maintain this effort and expand it if possible in 2007. Publicity of the very best sort is of course "word of mouth" that is spreading from participants. We now appear in the American Chemical Society's list of summer research opportunities. We should endeavor to reach out to other profesional societies and groups. Further, we need to refine and expand our annual mailing list. We also need to look into getting listed on the DOE educational opportunities website.

Participation and Continuity

Several participants recommended that the program be both expanded and extended pass the FY 2007 stretch goal year. This year's small experience with more senior visitors indicates that there is a real need for a program similar to this one to serve that group. At this juncture, simply expanding the scope of the ICPCPSRI program may be a viable approach as the marginal costs would be small.

Other Iprovements

Several comments were received to the effect that more activities to promote interactions among the Summer Institute's participants are needed. Currently the two barbeques are the only such avenue. In the future, we would like to expand the lecture program, possibly by collaborating with the distinguished visitor program. Whatever is done in this regard, it must not place an undue burden on our participant's limited time at PNNL. Currently the only activity mandated by the Summer Institute is the preparation of a final report—this should remain unchanged.

Technical Reports

The remainder of this document is devoted to the technical reports provided by each young scientist. As noted above, some of these are single paragraph abstracts and, therefore, have rather limited content. Other reports, however, are nearly complete papers. These documents are "as received," apart from minor formatting changes in some cases. We have made no effort to edit or evaluate these reports. Given the limited distribution intended for this report, none of the results in these reports should be considered "published" by virtue of appearing here.

Heterogeneous Reaction Kinetics of NaCl+HNO$_3$*

Jeremy Cain and Hai Wang
Department of Aerospace and Mechanical Engineering
University of Southern California
Los Angeles, CA
and
Dr. Yong Liu and Dr. Alexander Laskin
Pacific Northwest National Laboratory
Richland, WA

Previous investigations into heterogeneous reaction kinetics of NaCl[1] and a variety of atmospheric particles[2] have been performed in a reaction chamber depicted in Figure 1(a). In this reactor setup, aerosol samples are deposited on TEM grids supported by a grid holder, and the holder is placed in a circular chamber with diluted gaseous reactants flowing at a constant flow rate. Even though measurements of reaction parameters have been performed successfully using this configuration, a detailed knowledge of the effects of fluid flow on the reaction kinetics is not known. Laskin et al.[1] recognized that gaseous diffusion of the reactant to the substrate surface is an important factor in the determination of fundamental reaction rate parameters. In order to obtain accurate rate measurements, it is necessary to control the diffusion boundary layer thickness. For this reason, a new reaction chamber was designed and implemented, as seen in Figure 1(b). The new reactor is based on the concept of stagnation flow, i.e., an axi-symmetric flow of diluted reactant gas jet impinging on the TEM grids fixed atop the grid holder. This design is expected to give desirable flow field and uniform diffusion boundary layer thickness, as well as allow for flow variables to be easily manipulated.

TEM Grid Holder
(a) Old reactor design
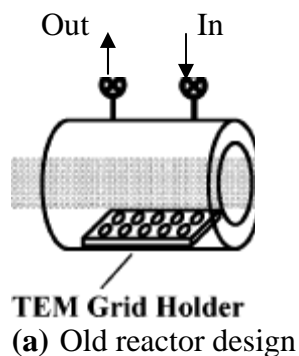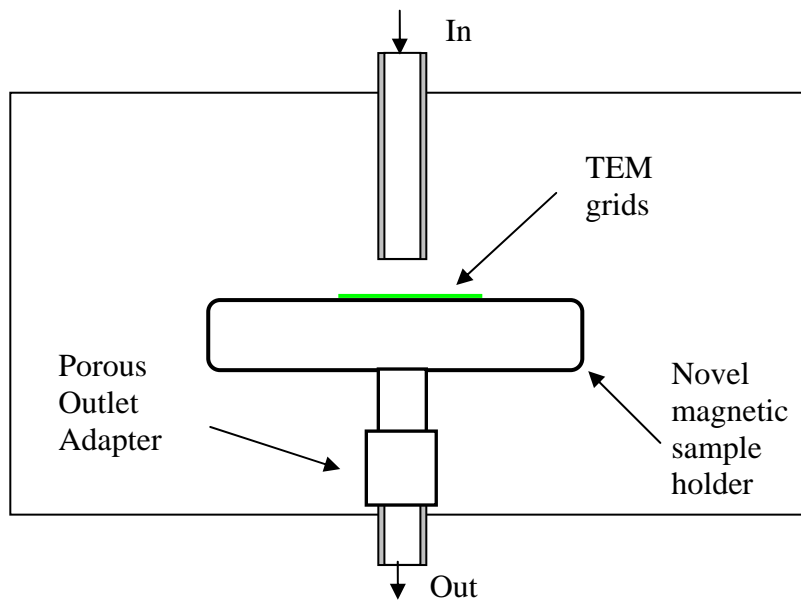
(b) New reactor design using stagnation flow
Fig. 1 – Different reaction chamber designs

The primary purpose of my Summer Institute Study at EMSL was to examine the new reactor, which was designed by computational fluid dynamics (CFD), and apply the knowledge gained from the CDF simulations in both testing the reactor and improving upon its design. Modeling the fluid flow in FLUENT,[3] a CFD solver, allowed for detailed information such as spatial variations in species concentration like that of Figure 2(a) to be obtained. It was determined through numerical modeling how the transport of reacting gas species would be affected by changes in certain parameters (e.g., tube diameter and velocity). Upon examination of model results, optimal operating conditions were determined, as seen in Figure 2(b), and used in heterogeneous reaction experiments. In the limiting case of complete surface coverage, the diffusion boundary layer thickness increases and concentration gradient decreases radially, with the latter being a much stronger function of radial co-ordinate than the former. The key parameters which change the boundary layer profile are velocity (V), tube offset height (L), and tube inner diameter (d). Numerical simulations are able to tell us the changes in concentration gradient with those in L and d, as shown in Figure 2(b). Thus, for a desirable concentration gradient tolerance we know how many grids can be tested and under what conditions they may be tested.
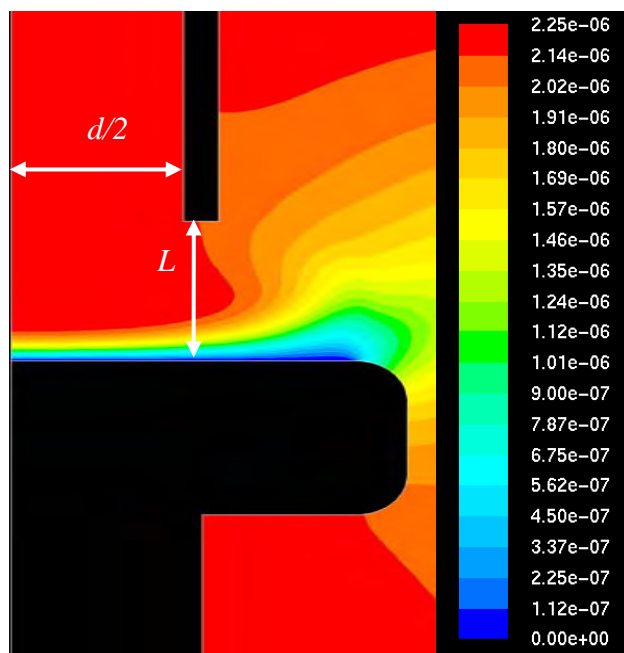
(a) HNO_3 mass fraction contours for 2-D axi-symmetric stagnation flow
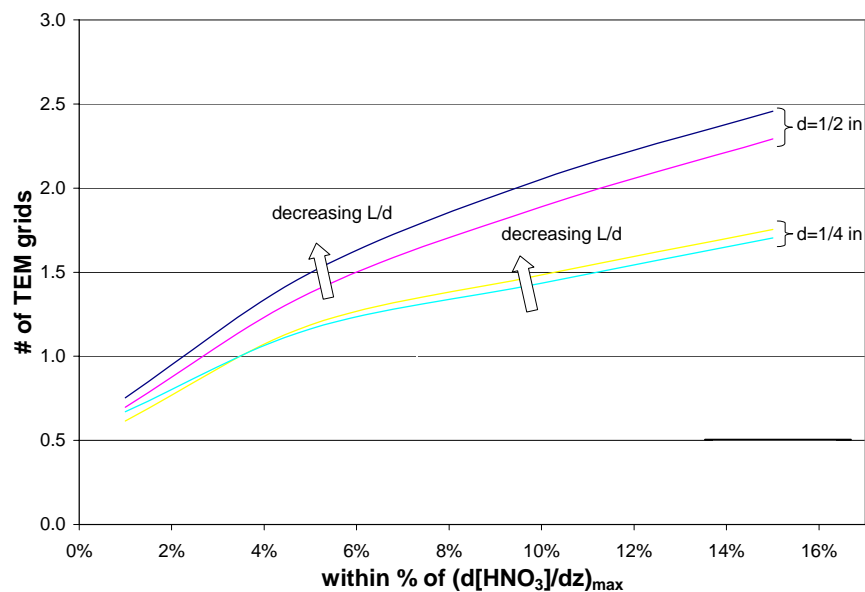
(b) Reactor operating conditions for varying parameters (V = 4L/min)
Fig. 2 – Sample computational modeling results

The new reactor design was then used to study the heterogeneous reaction kinetics of NaCl with HNO_3 at the relative humidity RH = 80%. Experimental results obtained thus far show the expected dependency of pseudo-first order rate constant as a function of number density of particles on grid surface, as seen in Figure 3. Based on a diffusion-kinetic analysis[1], we have

$$\frac{[HNO_3]_\infty}{k_I} = a + bN_s$$

$$= \frac{1}{k_{II}}(1+\delta k_s) + \left[\delta[Cl^-]_{d,0}\, e^{-k_I t}\left(\frac{4}{3}\pi r_d^{\,3}\right)\right]N_s$$

A fit to the data gives the intrinsic second-order rate constant $k_{II} = 5.5\times10^{-15}$ (cm^{-3}s) with an uncertainty factor equal to about 2.4. The reaction uptake coefficient is then calculated from

$$\gamma_{net} = \frac{4k_{II}[Cl^-]_d V_d}{\bar{c}_{HNO3} S_d}\ .$$

Assuming that the droplets are spherical, we obtain $\gamma_{net} = 0.06$ ($\times$/ $\div 2.4$). This value is in a close agreement with the recently report value of 0.05 at RH = 85% by Saul et al.[3] who studied the same reaction kinetics in a substrate-free laminar flow reactor. The close agreement suggests that the current reactor design is valid and is expected to give quantitative heterogeneous kinetic data. Validating the design through conformation of experimental results is necessary before moving to systems which have not been studied before, such as heterogeneous reactions of reactive free radicals with soot.
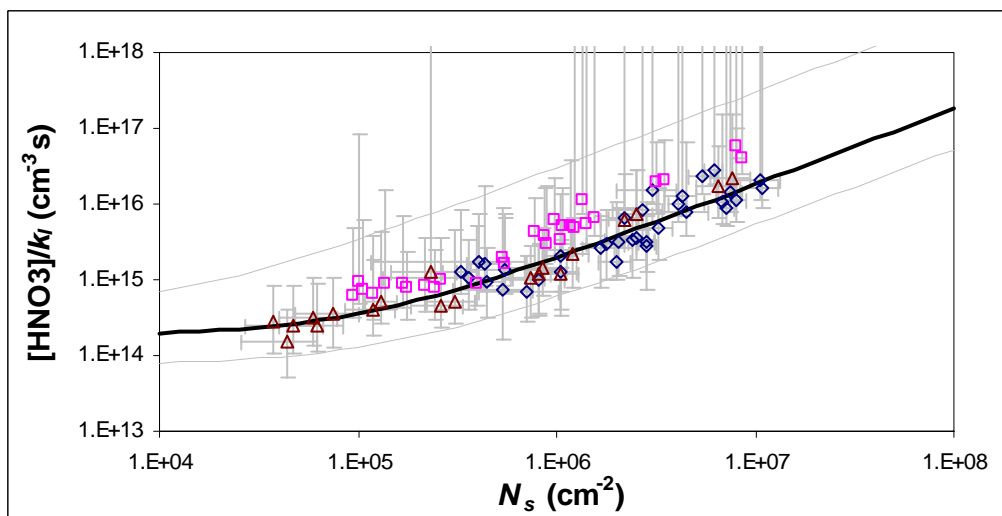
Fig. 3 – Variation of pseudo-first order rate constant as a function of NaCl particle number density on the substrate surface

References:

1. Laskin, A.; Wang, H.; Robertson, W.H.; Cowin, J.P.; Ezell, M.J.; Finlayson-Pitts, B.J. *J. Phys. Chem. A* 2006, 110, 10619.
2. Krueger, B.J.; Grassian, V.H.; Iedema, M.J.; Cowin, J.P.; Laskin, A. *Anal. Chem.* 2003, 75, 5170.
3. Saul, T.D.; Tolocka, M. P.; Johnston, M. V. *J. Phys. Chem. A.* 2006, 110, 7614.

In-situ studies of initial oxidation of bare InAs surfaces and oxide/InAs interfaces

C.L. Chang, S. Ramanathan
Division of Engineering and Applied Sciences,
Harvard University, Cambridge, MA 02138
and
V. Shutthanandan,
Pacific Northwest National Laboratory,
Richland, WA

The scaling of MOSFET (metal-oxide-semiconductor field effect transistors) has become aggressive due to the need for higher performance and integration density in nano-electronic devices [1]. A major effort is to replace SiO_2 with higher-dielectric (high-k) constant oxide films as the gate dielectric in future transistor application due to its high leakage currents and intrinsic reliability concerns [2]. Thus integration of high-k dielectrics into CMOS processes is a major challenge. Beyond the substitution of conventional SiO_2 by high-k dielectrics for geometric scaling, another avenue to overcome the issue of surface mobility degradation is to use substrates with higher hole and electron mobility instead of silicon. Also, high mobility channel layers could alleviate the saturation of Si MOSFET drain current upon dimension shrinkage by providing a higher source injection velocity. InAs is a good candidate worthy of further investigation for this purpose.

Interface between high-k dielectrics and the substrate is of concern since unwanted interface layers with lower permittivity will degrade the device performance. The purpose of annealing in oxygen environment is to let the oxygen vacancies within the dielectrics be filled to reduce the leakage current. But it could be possible that introduced oxygen will not only fill up anion vacancies, but also diffuse deeper toward the oxide/InAs interface to form undesired oxide interfacial layers. To confirm the oxygen diffusion mechanism during the annealing process, two experiments with yttria-doped zirconia (YDZ) grown on InAs and bare InAs have been annealed in oxygen at various temperatures and studied.

YDZ films were grown by electron beam evaporation method on InAs substrate at room temperature. High resolution Rutherford backscattering spectrometry (RBS) and nuclear reaction analysis (NRA) measurements were carried out in random geometries at the Environmental Molecular Science Laboratory (EMSL) accelerator facility, Pacific Northwest National Laboratory (PNNL). Both *in situ* NRA and RBS measurements are performed after annealing experiments. ^{18}O is introduced at a pressure of 2×10^{-6} Torr during heat treatment at five different temperatures: 200°C, 300°C, 400°C, and 500°C for 30 minutes. SIMNRA [3] was used to simulate the experimental RBS spectra as shown in Fig. 1, and the total anion concentration is 3.15×10^{17} cm^{-2}. NRA data on an as-loaded sample shows that the as-deposited YSZ film a small fraction of vacancies. In table 1 it shows that some ^{16}O leaves the YDZ film until 200°C, but is similar from 200°C to 500°C. Whereas ^{18}O increases proportional to the rising temperature above 200°C as in table 1. Beyond 200°C ^{16}O doesn't appear to exchange with ^{18}O as the results suggest. The oxygen occupancy ratio is defined as total oxygen areal density (^{16}O and ^{18}O) divided by the total anion sites; and oxygen occupancy ratio reaches unity at 500°C.

Annealing Condition	^{16}O NRA $(Nt)_i$ (atoms/cm^2)	^{18}O NRA $(Nt)_i$ (atoms/cm^2)	Occupancy ratio
As-loaded	3.05E+17	0	96.7%
200ºC	2.72E+17	5.76E+14	86.5%
400ºC	2.72E+17	1.78E+16	92.1%
500ºC	2.88E+17	2.88E+16	100%

Table 1. Comparison of ^{16}O and ^{18}O by NRA as a function of annealing temperature.
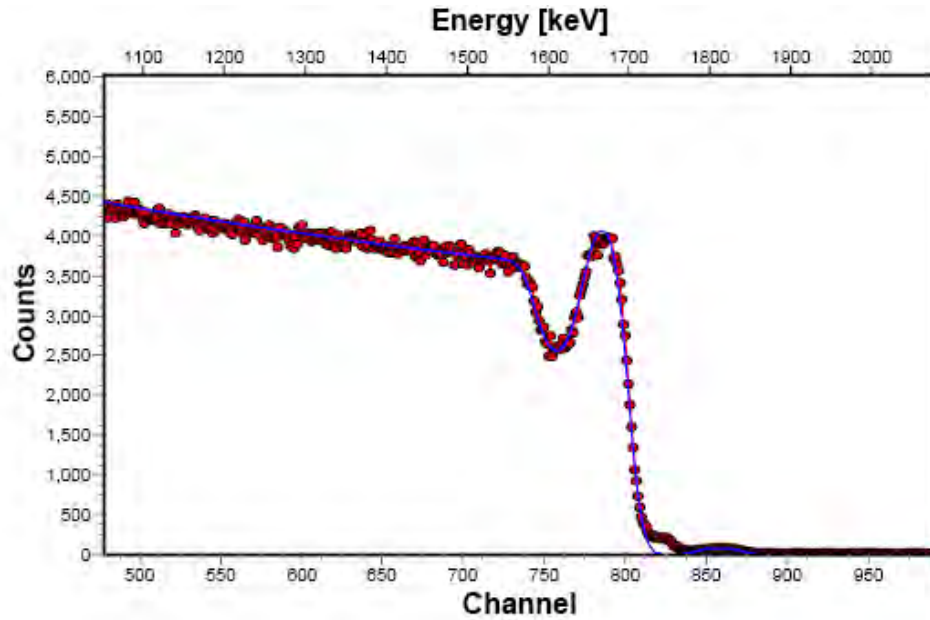
Fig. 1 RBS spectrum for YDZ on InAs simulated by SIMNRA[3].
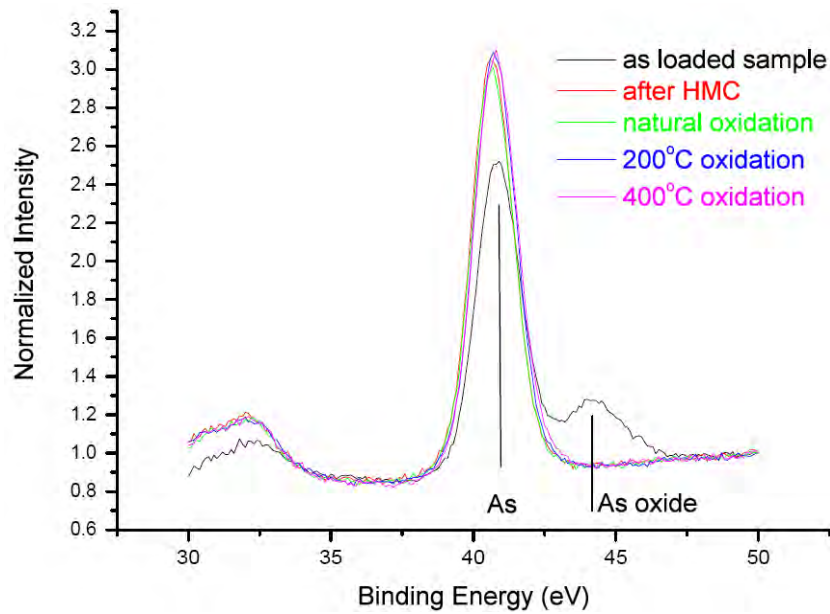
Fig. 2 (a) XPS for arsenic.
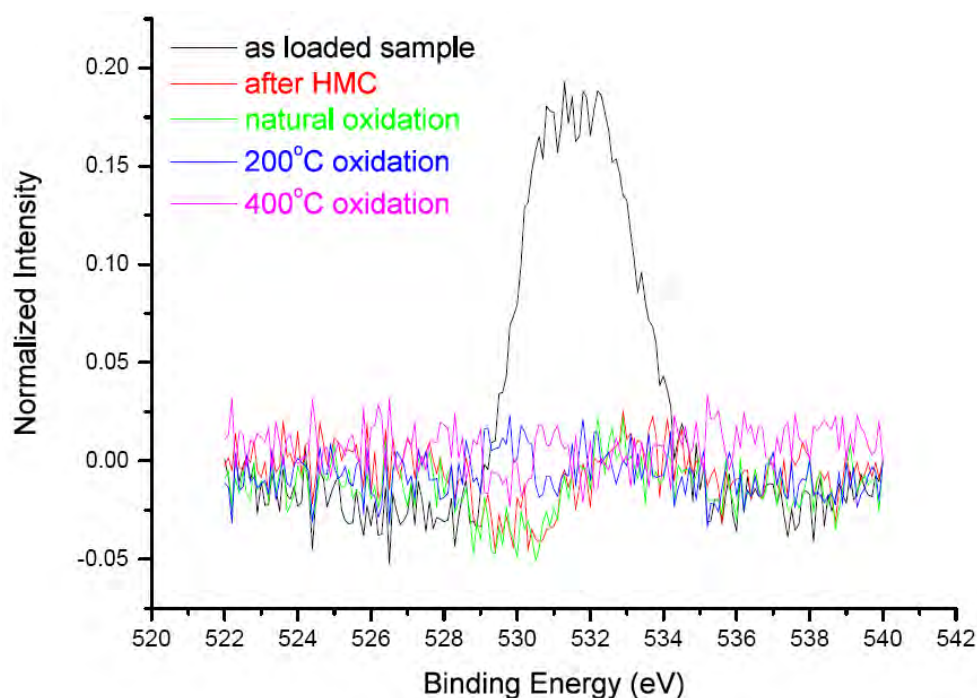
Fig. 2(b) XPS for oxygen

Furthermore, the oxidation of InAs bare substrates under identical annealing conditions has also been investigated. Both *in situ* XPS and NRA measurements are carried out to acquire information on the surface oxide. After the complete removal of native oxide on InAs by HMC (Hydrogen Molecule Method), the XPS shows no oxide formed on InAs surface as seen in Fig. 2(a) for arsenic and in Fig. 2(b) for oxygen peak. Following the HMC, the same annealing conditions as above are performed. No oxide peak shows up as we can see in Fig. 2(a) and the amount of oxygen is not increasing as temperature is increasing up to 500°C. The oxygen concentration information from NRA measurement confirms this result. This supplementary experiment tells the information that under the same oxygen annealing condition the bare InAs is resistant to oxidation. From this information we could infer that during annealing, oxygen will fill up the anion vacancies instead of diffusing deeper toward YSZ/InAs to form the undesired interfacial oxide layers.

Both oxygen diffusion mechanism for YSZ on InAs and bare InAs in oxygen annealing are characterized and studied by *in situ* high resolution RBS, NRA and XPS measurements. The result suggests the oxygen will fill up the anion vacancies instead of forming the unwanted oxide interfacial layers between YSZ and InAs.

1. Y. Taur, "CMOS design near the limit of scaling," *IBM Journal of Research & Development*, 40 (2002), 213-222.
2. M. K. Weldon et al., "The surface science of semiconductor processing: gate oxides in the ever-shrinking transistor," *Surface Science*, 500 (2002), 859-878.
3. *SIMNRA User's guide*, edited by M. Mayer, Max-Planck-Institut fur Plasmaphysik, Germany.

Metal-doped iron particles

Chan Lan Chun and William A. Arnold
University of Minnesota
Minneapolis, MN
and
Don Baer, EMSL
Pacific Northwest National Laboratory
Richland, WA

Report:

1. Major routes of particle synthesis
- Solution based synthesis (Starting material: dry Toda iron): Chanlan Chun in EMSL
- Sputtering based synthesis: Samples from Dr. Qiang group (U of Idaho)
- Hydrogen-reduction process (Starting material: 6-line ferrihydrite): Dean Matson and Chanlan Chun in PSL

2. Samples (√ : completely done, W: waiting list, and N/A: not applicable)

Process	Sample ID	Description (washing)	Synthesis	ICP	TEM	XRD	XPS	4-Cl-NB
Solution (Toda iron)	DT-UT	Untreated Toda iron	√		√	√	√	√
	C-M	Toda iron w/o dopants after Milli-Q washing	√	√		√	√	
	S-M-Cu-1	0.17 % Cu-doped Toda iron (Milli-Q water)	√	√		√		√
	S-M-Cu-10	0.62 % Cu-doped Toda iron (Milli-Q water)	√	√		√		√
	S-M-Ni-1	0.12 % Ni-doped Toda iron (Milli-Q water)	√	√		√	√	√
	S-M-Ni-10	0.43 % Ni-doped Toda iron (Milli-Q water)	√	√	√	√	√	√
	S-M-Pd-1.5	0.08 % Pd-doped Toda iron (Milli-Q water)	√	√	√	√		√
	C-A	Toda iron w/o dopants after acid washing	√	√	√	√	√	
	S-A-Cu-1	0.12 % Cu-doped Toda iron (Acid)	√	√		√		
	S-A-Cu-10	0.75 % Cu-doped Toda iron (Acid)	√	√	√	√	√	
	S-A-Ni-1	0.19 % Ni-doped Toda iron (Acid)	√	√		√	√	
	S-A-Ni-10	0.62 % Ni-doped Toda iron (Acid)	√	√	√	√	√	
	S-A-Pd-1.5	0.07 % Pd-doped Toda iron (Acid)	√	√		√	√	
Hydrogen Reduction	HR-Fe	Iron without dopants	√	√	√	√	W	√
	HR-FePd0.5	0.5 % Pd-doped iron	√	√	√	√	W	√
	HR-FePd1	1 % Pd-doped iron	√	√	√	√	W	√
	HR-FePd2	2 % Pd-doped iron	√	√	√	√	W	√
	HR-FeCu0.5	0.5 % Cu-doped iron	√			√		
	HR-FeCu1	1 % Cu-doped iron	√			√		
	HR-FeCu2	2 % Cu-doped iron	√			√	W	
	HR-FeNi0.5	0.5 % Ni-doped iron	√			√		
	HR-FeNi1	1 % Ni-doped iron	√			√		
	HR-FeNi2	2 % Ni-doped iron	√			√	W	
Sputtering	SP-FeCu2	Uniformly 2 % Cu-doped iron	√	N/A	√		√	
	SP-FeCu5	Uniformly 5 % Cu-doped iron	√	N/A			√	
	SP-FeCu15	Uniformly 15 % Cu-doped iron	√	N/A	√		√	
	SP-FeNi2	Uniformly 2 % Ni-doped iron	√	N/A	√		√	
	SP-FeNi5	Uniformly 5 % Ni-doped iron	√	N/A	√		√	
	SP-FeNi15	Uniformly 15 % Ni-doped iron	√	N/A	√		√	

Section 1. Metal-doped iron produced by solution process

Synthesis of metal-doped irons

- Synthesis of metal-doped irons was performed in an anoxic chamber using deoxygenated Milli-Q water at 22 ± 2 °C.
- Dry Toda iron was used as a starting material.
- Toda iron was washed with deoxygenated Milli-Q water or 0.01 N H_2SO_4 solution before metal doping process
- Metal plating solutions were prepared by dissolving metal sulfates in 0.01 N H_2SO_4 solution. The initial concentrations of metal solution were ranged from 0.6 to 10 μM.
- After doping, particles were flash dried using acetone.
- Sample description

ID	Description
C-M	Toda iron washed using Milli-Q water (sonication)
C-A	Toda iron washed using 0.01 N H_2SO_4 solution
S-M-Cu-10	Toda iron doped with Cu (high concentration, $CuSO_4$) after Milli-Q water washing
S-A-Cu-10	Toda iron doped with Cu (high concentration) after acid washing
S-M-Cu-1	Toda iron doped with Cu (low concentration) after Milli-Q water washing
S-A-Cu-1	Toda iron doped with Cu (high concentration) after acid washing
S-M-Ni-10	Toda iron doped with Ni (high concentration, $NiSO_4$) after Milli-Q water washing
S-A-Ni-10	Toda iron doped with Ni (high concentration) after acid washing
S-M-Ni-1	Toda iron doped with Ni (low concentration) after Milli-Q water washing
S-A-Ni-1	Toda iron doped with Ni (low concentration) after acid washing
S-M-Pd-1.5	Toda iron doped with Pd (high concentration, $PdSO_4$) after Milli-Q water washing
S-A-Pd-1.5	Toda iron doped with Pd (high concentration) after acid washing

Materials Characterization
- The materials were characterized using inductively coupled plasma (ICP), X-ray diffraction (XRD), and transmission electron microscopy (TEM). X-ray photoelectron spectroscopy (XPS) analysis is not scheduled yet.
- ICP samples were prepared by dissolving the solid particles in a solution of 3.6 % HNO_3 and 5.3 % HCl, followed by dilution in Milli-Q water. The diluted solutions were analyzed for Fe, Pd, Ni, Cu, and S using Perkin-Elemer Optima 3000DV.
- XRD was performed using a PANalytical X'pert MPD diffractometer equipped with an X'Celeator detector and cupper source. Each sample was protected from oxygen by applying a few drops of 50 % glycerol and 50 % methanol. Data was collected over the range of 5-80° 2θ α at a scan rate of 2°/min.
- High-resolution TEM was performed using a JEOL JEM 2010F operated at 200 kV. All images were digitally collected using CCD camera and were analyzed using Gatan Digital Micrograph 3.3.1. Samples were mounted on carbon-coated TEM grids which were then mounted on airtight TEM sample holder in the anoxic glove box for minimizing oxygen exposure during transfer from the anoxic chamber to the microscope.

Results and Discussion
ICP Analysis
- The amount of metal present in the final solid was low in comparison with materials synthesized by other processes (hydrogen reduction and sputtering process) This is because of high surface area of dry Toda iron and low solubility of metals in 0.01 N H_2SO_4.
- The amount of metal deposited on iron is below monolayer (0.02ML ~ 0.16ML)

Table 1. Metal content onto dry Toda iron

Metal Additive	ID	Plating Solution Concentration[a] (mM)	Deposited Metal Mass[b] (μmoles/g Fe)	Deposited Metal Content[c] (mol %)	Relative concentration to monolayer(ML)[d]
Copper	S-M-Cu-1	1.40	17.4	0.17	0.04ML
	S-M-Cu-10	7.20	89.6	0.62	0.13ML
	S-A-Cu-1	1.40	17.4	0.12	0.03ML
	S-A-Cu-10	7.20	89.6	0.75	0.16ML
Nickel	S-M-Ni-1	2.02	18.7	0.12	0.02ML
	S-M-Ni-10	10.19	62.9	0.43	0.09ML
	S-A-Ni-1	2.02	20.8	0.19	0.04ML
	S-A-Ni-10	10.19	70.0	0.62	0.12ML
Palladium	S-M-Pd-1.5	0.58	7.23	0.077	0.02ML
	S-A-Pd-1.5	0.58	7.22	0.071	0.02ML

a. Aqueous metal concentration used in doping process
b. Deposited additive mass resulting from displacement plating

$$= \frac{\text{Initial Plating Solution Concentration} - \text{Plating Solution Concentration after Displacement}}{\text{Toda Iron Mass}} \times \text{Volume of Plating Solution}$$

c. Content of metal present in each sample determined by dissolving the solid particles in a solution of 3.6 % HNO_3 and 5.3 % HCl, followed by ICP analysis
d. Amount of deposited atom equivalent to a single monolayer was calculated: 4.76 mol % Cu; 5.00 mol % Ni; and 4.10 mol % Pd. (See Appendix)

XRD

- XRD patterns show that the materials are composed of magnetite and iron. In addition, no significant difference in the degree of crystallinity, which would be detected by changes in peak broading and relative intensity, were apparent between samples. (Figure 1)
- According to peak areas of iron (220) face and magnetite (440) face, the ratio of magnetite/iron in metal-doped irons are usually lower than that in untreated Toda iron (Table 2). A possible explanation is that iron oxide may be dissolved more than metal iron by washing process because metal iron was protected from iron oxide shell. This led to change ratio of magnetite to iron.
- No significant difference was found in XRD patterns between Milli-Q water washing and acid washing.
- Glycerol coating did not make a difference for most of samples except for three samples (written in red in Table 2). Those three samples caught a fire while transferred to sample holder, suggesting they are much more likely to start reacting in air in comparison with the undoped material.
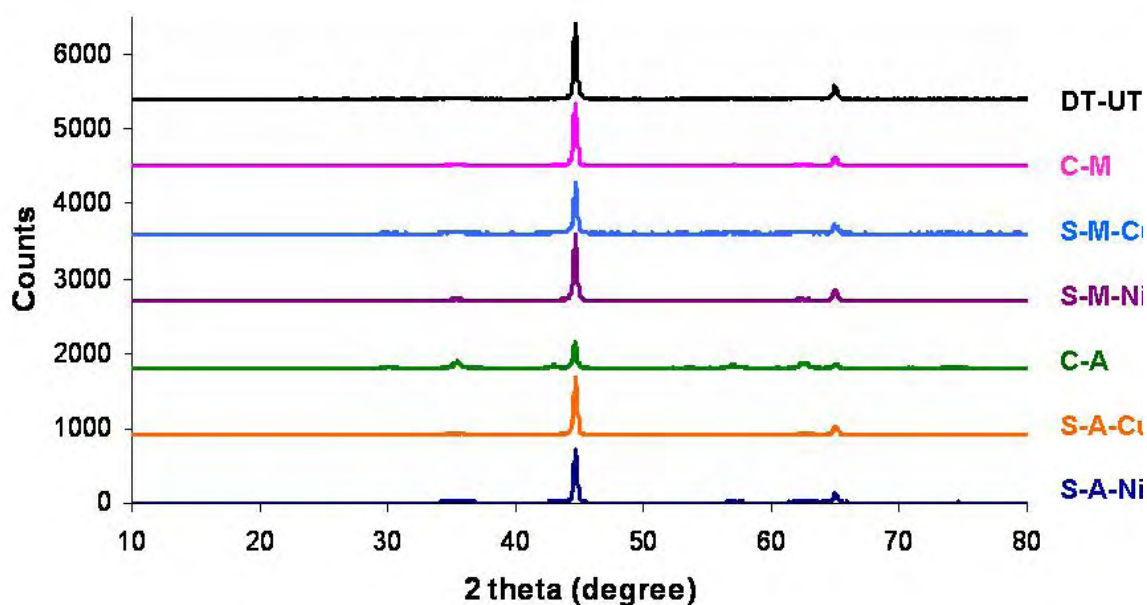
Figure 1. XRD patterns of the metal-doped irons.

Table 2. Ratio of Magnetite/Fe

ID	Milli-Q water washing		ID	Acid washing	
	Mag/Fe[a]	Fe as Mag[b].		Mag/Fe	Fe as Mag.
C-M	0.28	0.12	C-A	0.62	0.23
S-M-Cu-1	0.16	0.07	S-A-Cu-1	0.24	0.11
S-M-Cu-10	0.24	0.11	S-A-Cu-10	0.20	0.09
S-M-Ni-1	0.25	0.11	S-A-Ni-1	0.31	0.13
S-M-Ni-10	0.23	0.10	S-A-Ni-10	0.26	0.11
S-M-Pd-1.5	0.64	0.24	S-A-Pd-1.5	0.33	0.14

[a]Ratio of magnetite/Fe calculated using XRD peak area (Untreated Dry Toda iron: 0.40)
[b]Fraction of Fe atom as magnetite phase(Untreated Dry Toda iron: 0.28)

TEM Images

- Metal-doped Toda irons consist of aggregation of small irregular particles which consist of a single crystal Fe^0 core with an oxide shell in a similar to untreated Toda iron.
- However, oxide shells of metal-doped Toda irons became rougher and thicker in comparison of those of untreated one. Such changes are due to washing process given that metal-doped irons have similar morphology with Toda iron solely after washing process (Figure S1). Acid washing makes more dramatic change on morphology than Milli-Q washing.
- TEM images of metal-doped irons do not show the location where metals are deposited on iron surfaces, suggesting metal dopants may be incorporated with iron oxide shell during plating process.
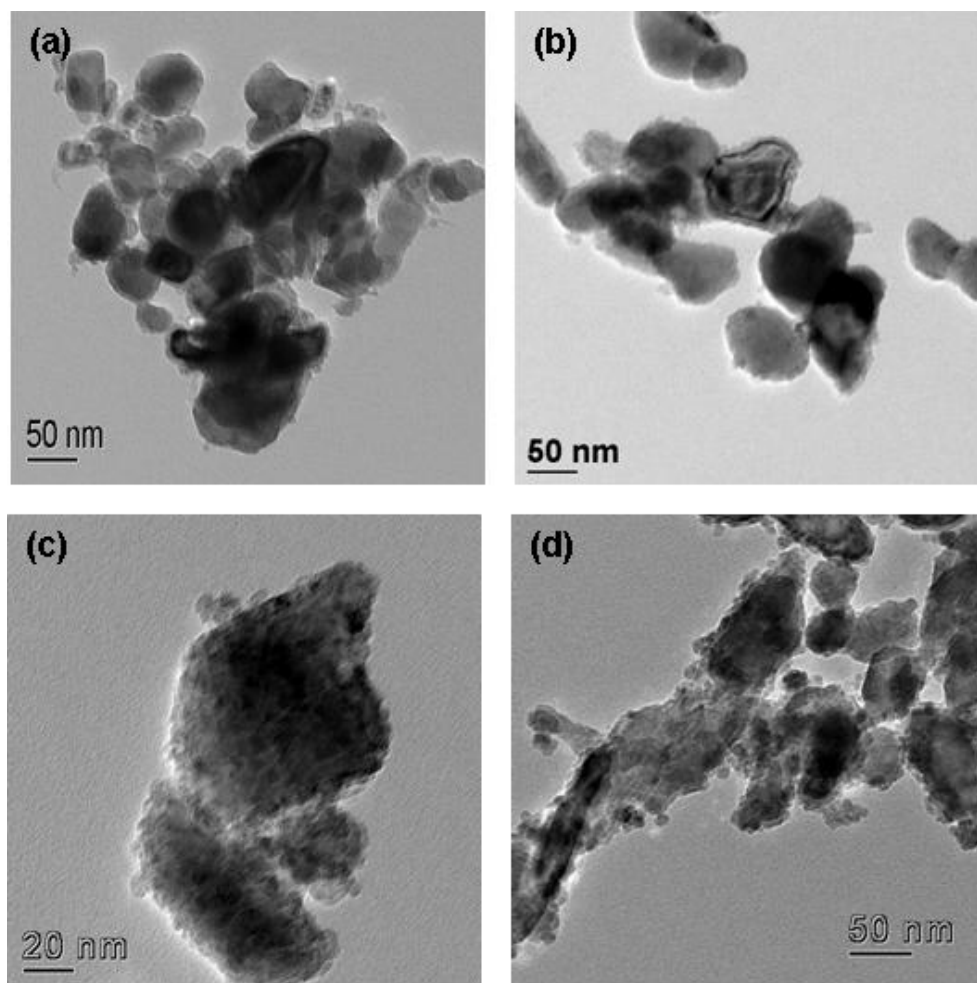
Figure 2. TEM images of (a) untreated dry Toda iron, (b) 0.43 % Ni-doped Toda iron after Milli-Q water washing (S-M-Ni-10), (c) 0.62 % Ni-doped Toda iron after acid washing (S-A-Ni-10), and (d) 0.75 % Cu-doped Toda iron after acid washing (S-A-Cu-10)

Reactivity Test

- In order to test reactivity of metal-doped iron, kinetic experiments were performed using 4-chloro-1-nitrobenzene (4-Cl-NB). 4-Cl-NB has been used as a model compound of insecticide and herbicide. It can be reduced to 4-chloroaniline (4-Cl-An) in the presence of reductants such as reduced iron or iron oxides.
- Batch experiments were carried out in 74 mL serum bottles containing a 0.4 g/L mineral suspension buffered at pH 7 with deoxygenated 25 mM bistripropane (BTP). Initial concentration of 4-Cl-NB was 100 µM. Samples were withdrawn at selected intervals using a two-syringe technique involving simultaneous injection of deoxygenated BTP buffer to avoid the introduction of headspace. The samples were filtered though 0.2 µm PTFE Gelman Acrodisk syringe tip filter to stop the reaction and to remove mineral particles.
- 4-Cl-NB and 4-Cl-An were analyzed using High Pressure Liquid Chromatography (Agilent 1100 Series) equipped with a C_{18} column (Model?).

The injection volume was 20 µL and the detector wavelength was 245 and
276 nm for 4-Cl-NB and 4-Cl-An, respectively. The mobile phase was 5 mM pH
7 phosphate buffer/acetonitrile (2/3 v/v) at a flow rate of 1 mL/min.

- Figure 3 shows that all metal dopants (Cu, Ni, and Pd) promoted reduction rates
  of 4-Cl-NB. Cu-doped iron (S-M-Cu-1) have higher reactivity than Ni-doped one
  (S-M-Ni-1) even though they have similar deposited metal mass of ~18 µmoles/g
  Fe (Note that this observation is different from results obtained by David
  Cwiertny). Pd-doped iron (S-M-Pd-1.5) has relatively low deposited metal mass
  (~ 7 µmoles/g Fe) but its reactivity is similar with Ni-doped ones.

- Similar reactivity between S-M-Cu-1 (17.4 µmoles/g Fe) and S-M-Cu-10
  (89.6 µmoles/g Fe) reveals that increasing the mass of Cu deposited on the dry
  Toda iron does not affect reactivity. Likewise, it is true for Ni-dopes irons (S-M-
  Ni-1 and S-M-Ni-10).
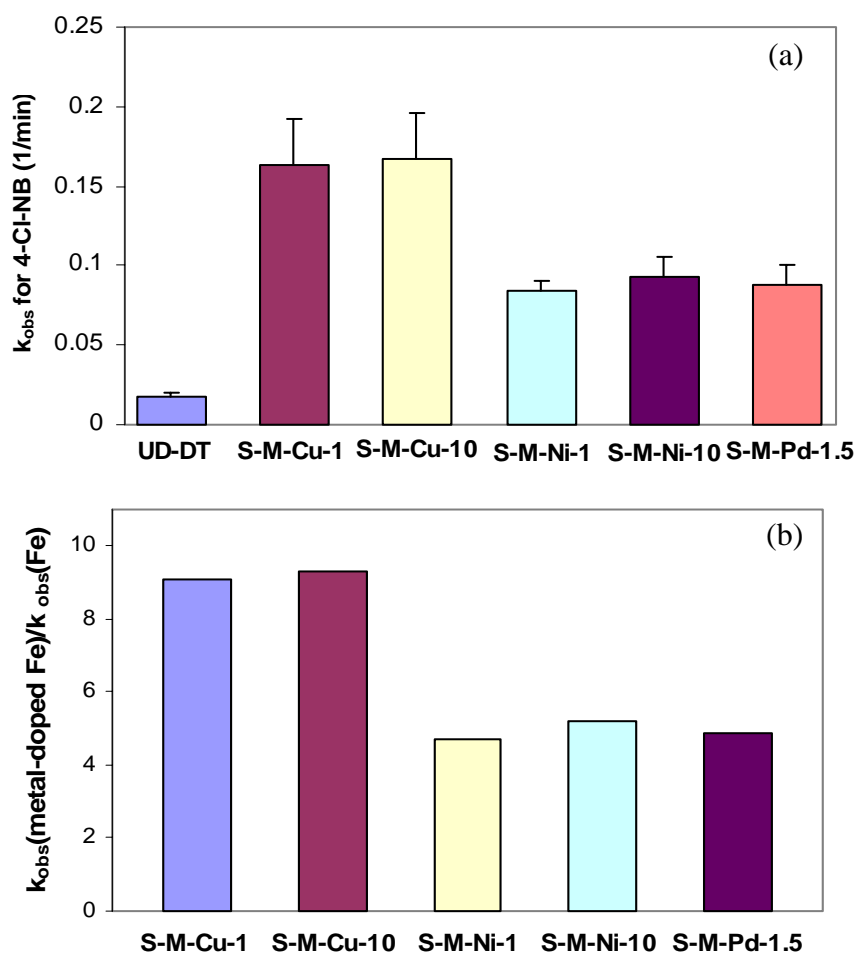
Figure 3. (a) Pseudo-first-order-reduction rate constants of 4-Cl-NB in the presence of
dry Toda iron or metal-doped dry Toda irons and (b) rate enhancement provided by
metal-doping

Iron Corrosion Test

- Aqueous Fe concentration generated over time was measured for the rate of iron corrosion in metal-doped iron/water system.
- Batch reactors were prepared in the similar manner to reactivity experiment. Reactors were filled with deoxygenated 25 mM BTP buffer (pH 7) and a mineral mass loading of 2.5 g/L. Multiple, identical batch reactors were prepared for each sample and reaction vials were scarified at certain time interval. Iron concentration was analyzed using ICP (Perkin-Elemer Optima 3000DV)
- There is no significant difference on both the amount of Fe(II) generated over 24 h and corrosion rate among metal-doped dry Toda irons
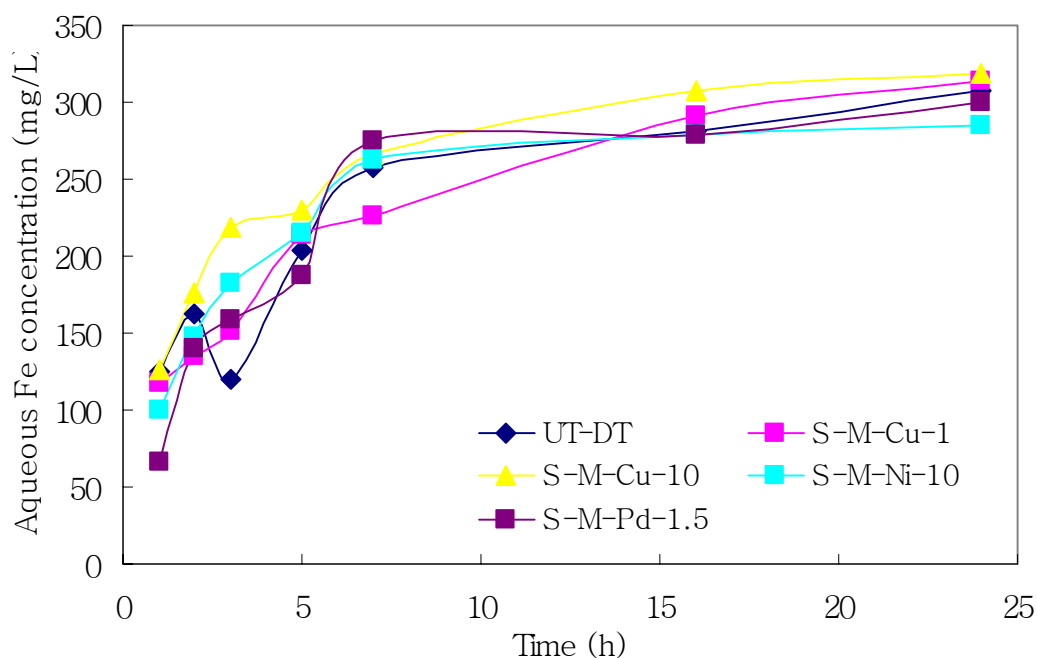
Figure 4. Aqueous Fe concentration as a function of time in metal-doped dry Toda iron/water batch system

Appendix

<div style="border:1px solid;">A Single Monolayer Equivalent of Metal Atoms</div>

Assumption
- The metal layer is dominantly in the lowest energy fcc (111) orientation
- BET surface area of Toda iron (SA) = 29 m²/g

FCC(111) area = equilateral triangle with the side equal to 4r

4r

Surface Area of Unit Cell (SA-UC)

$$= 4 \cdot \sqrt{3} \cdot r^2$$

Shared by 6 units

Shared by 2 units

Each FCC(111) unit surface has 2 atoms … $3 \times \dfrac{1}{6} + 3 \times \dfrac{1}{2} = 2$
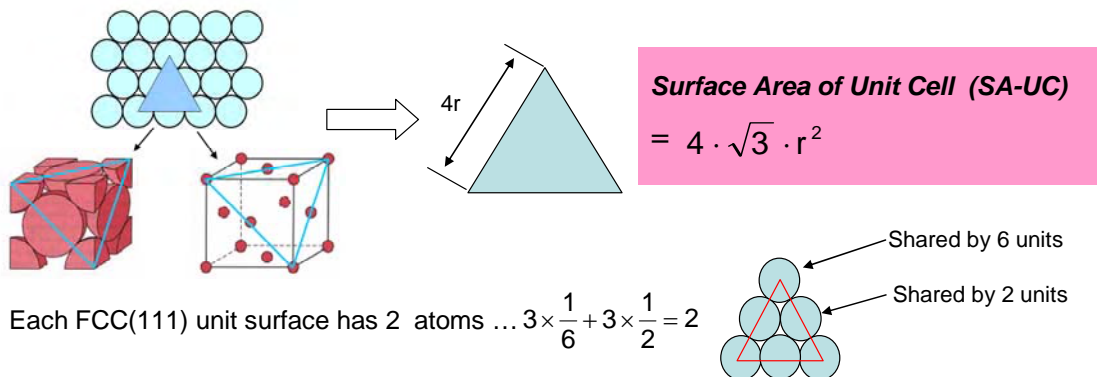
A Single Monolayer Equivalent of Metal Atoms

$$= \frac{SA\ m^2}{g - Fe} \left| \frac{unit\ cell}{SA - UC\,m^2} \right| \frac{2\,atoms}{unit\ cell} \left| \frac{mol - metal}{6.02 \times 10^{23}\ atoms} \right.$$

Surface area of Toda iron (m²/g)	29		
Dopant	Ni	Cu	Pd
Atomic mass	58.7	63.5	106.4
Density of Atom (g/ml)	8.9	8.96	12
Radius of Atom (nm)	0.125	0.128	0.138
Surface area of Unit Cell (m²)	1.076E-19	1.129E-19	1.311E-19
Metal mass for monolayer (μmol/g)	895.007	853.129	734.770
Metal/Fe for monolayer (mol %)	5.00	4.76	4.10
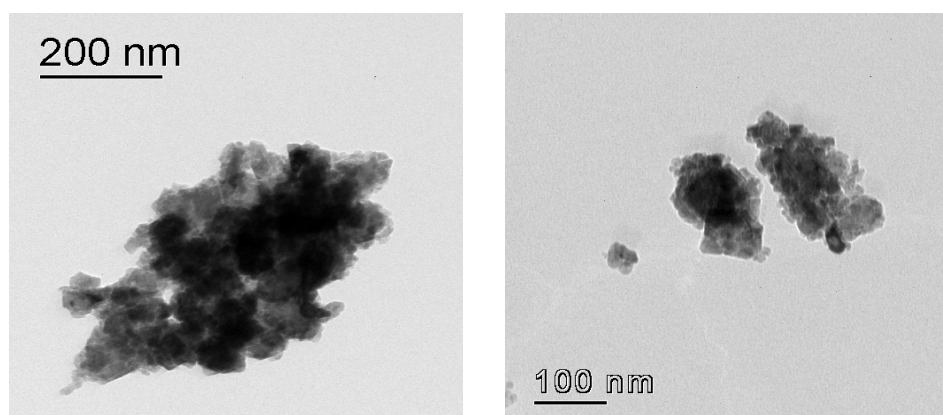
Figure S1. TEM images of dry Toda iron after acid washing

Section 2. Pd-doped iron produced by hydrogen reduction

Synthesis of Pd-doped Iron

- Ferrihydrite nanoparticles were prepared using a method adopted from Matson et al. (1994)
- The dried ferrihydrite was heated at 330 °C in air for 30 minutes to form hematite.
- Sulfate was added to hematite in the form of H_2SO_4 (Water content is 10 μl/g)
- Four samples of hematite with various amounts of palladium doping (0, 0.5, 1.0, and 2.0% moles Pd/moles Fe) were prepared by adding a palladium(II) acetate dissolved in acetone.
- Pd-doped hematite was heated in a flow of H_2 (10 ml/min) at 450 °C for 2 hours.
- Sample description

Sample ID	Dean's label	Description
HR-Fe	58160-31-4	0 mol % palladium-doped iron
HR-FePd0.5	58160-31-1	0.5 mol % palladium-doped iron
HR-FePd1	58160-31-2	1 mol % palladium-doped iron
HR-FePd2	58160-31-3	2 mol % palladium-doped iron
Ferrihydrite	52654-90-1	Stating material
Hematite	-	Oxidized material of ferrihydrite (52654-90-1)

Materials Characterization

- The materials were characterized using inductively coupled plasma (ICP), X-ray diffraction (XRD), and transmission electron microscopy (TEM). X-ray photoelectron spectroscopy (XPS) analysis is not scheduled yet.
- ICP samples were prepared by dissolving the solid particles in a solution of 3.6 % HNO_3 and 5.3 % HCl, followed by dilution in Milli-Q water. The diluted solutions were analyzed for Fe, Pd, Ni, Cu, and S using Perkin-Elmer Optima 3000DV.
- XRD was performed using a PANalytical X'pert MPD diffractometer equipped with an X'Celeator detector and cupper source. Each sample was protected from oxygen by applying a few drops of 50 % glycerol and 50 % methanol. Data was collected over the range of 5-80° $2\theta \alpha$ at a scan rate of 2°/min.
- High-resolution TEM was performed using a JEOL JEM 2010F operated at 200 kV. All images were digitally collected using CCD camera and were analyzed using Gatan Digital Micrograph 3.3.1. Samples were mounted on carbon-coated TEM grids which were then mounted on airtight TEM sample holder in the anoxic glove box for minimizing oxygen exposure during transfer from the anoxic chamber to the microscope.

Results and Discussion

XRD Analysis

- XRD patterns show that the materials are composed of magnetite and iron. In addition, no significant difference in the degree of crystallinity, which would be detected by changes in peak broadening and relative intensity, were apparent between samples. (Figure 1)
- According to peak areas of iron (220) face and magnetite (440), the average ratio of magnetite/iron is 1.10 (0.40 for Toda iron) and the fraction of Fe atom in magnetite phase is 0.35.(0.28 for Toda iron)
- Unidentified peaks in the pattern of HR-Fe indicate the presence of other phases but those peaks do not match with peaks of possible iron oxides.
- XRD patterns of starting materials are shown in Fig S1.
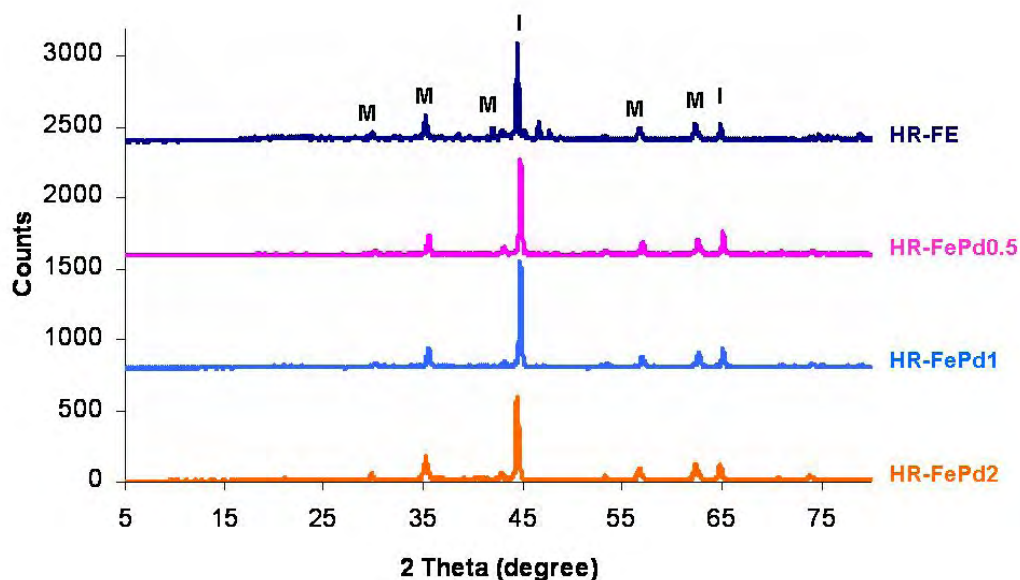
Figure 1. XRD patterns of the 0 %, 0.5 %, 1 %, and 2 % palladium-doped iron. I and M are used to label iron and magnetite peaks, respectively.

Composition of Pd-doped Iron

- ICP analysis shows that the amount of palladium present in each of the samples was consistent with the percentage of palladium in the hematite. The concentrations of other metals such as Cu, and Ni were found to be trace (Cu/Fe and Ni/Fe are less than 0.01 mol %). Sulfur concentration is below the detection limit.
- Quantitative EDX analysis shows that the atomic ratios of Pd/Fe are lower than ICP results.
- Pd doping does not make a difference in the ratio of magnetite/iron.

Table 1. Summary of Composition

ID	Pd Content[a] (mol %)	Pd Content[b] (atomic %)	Magnetite/Fe[c]	Fe as Magnetite[d]
HR-Fe	0.08	ND[e]	1.26	0.38
HR-FePd0.5	0.44	0.23	0.86	0.30
HR-FePd1	1.10	0.74	1.02	0.34
HR-FePd2	1.95	1.13	1.24	0.38

[a]Values were determined using ICP. [b]Values were quantified using TEM-EDX for three different locations. [c]Ratios of magnetite/iron were calculated using XRD peak areas; Fe(220) and Magnetite (440). [d]Fraction of Fe atoms as in magnetite phase [e]Not detectable.

TEM Analysis

- Figure 1a show that iron without Pd doping consists of aggregated of faceted plates and smaller irregular particles.
- The faceted plates are usually composed of a nearly single crystal Fe^0 core with a oxide shell (Figure 1c) but smaller irregular particles do not have oxide shell (Figure 1b and 1d).
- Particle size varies from 30 to 100 nm
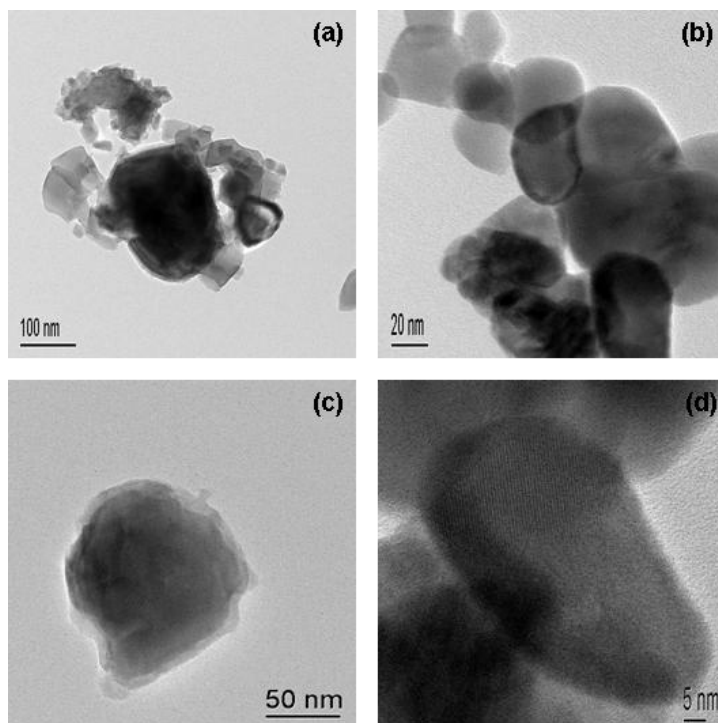
Figure 2. TEM images of iron particles without Pd doping: (a) Low magnification image of iron aggregates, (b) and (d) higher resolution images of irregularly shaped metal iron particles, and (c) higher resolution image of individual iron particle composed of Fe^0 core and oxide shell.

- TEM images of Pd-doped irons shows formation of smaller particles on iron particles. TEM-EDX verifies that such particles are Pd metal. The population of Pd particles increases with Pd loading (Figure 3a, 3b, and 3d). Pd particles are spherical and typically 2-10 nm in diameter.
- Pd deposition on iron particles is discontinuous and heterogeneous. Even Figure 3d and 3e are images of 2% Pd-doped iron, the region in Figure 3e appears virtually free of deposited Pd but the region in Figure 3d has lots of small Pd particles.
- Pd deposition occurred on iron metal surface as well as on iron oxide shell. However, Pd was deposited predominately on iron oxide shell (Figure 3d and 3f).
- Figure 3c shows that small Pd particles deposited on iron oxide shell also have oxide shell.
- TEM images of starting materials are presented in Figure S2.
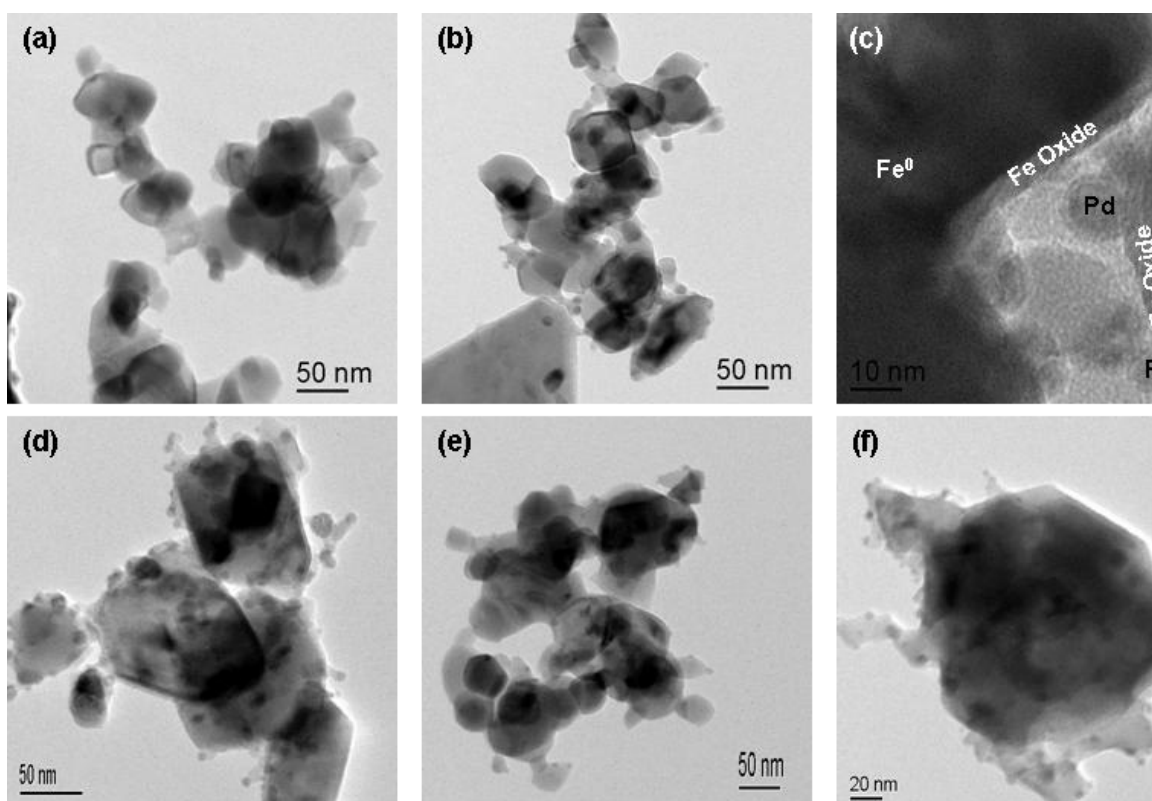
Figure 3. Representative TEM images of Pd-doped iron particles: (a) 0.5 % Pd; (b) and (c) 1 % Pd; (d), (e), and (f) 2 % Pd

Reactivity and Corrosion Test

- Reactivity was evaluated via kinetic batch experiment using 4-Cl-NB. A detailed description of the 4-Cl-NB batch systems used in this study is included in Section 1. One difference is that initial concentration of 4-Cl-NB was 400 μM.
- Iron produced by hydrogen process in PSL has much higher reactivity than dry Toda iron.

- Unlike metal-doped irons produced by solution process, no rate enhancement by metal additive was observed. Due to high reactivity, the observed rate constant is highly mass transfer limited. If that is the case, we cannot see the effect of metal doping on reactivity because the particle size of each sample is similar.
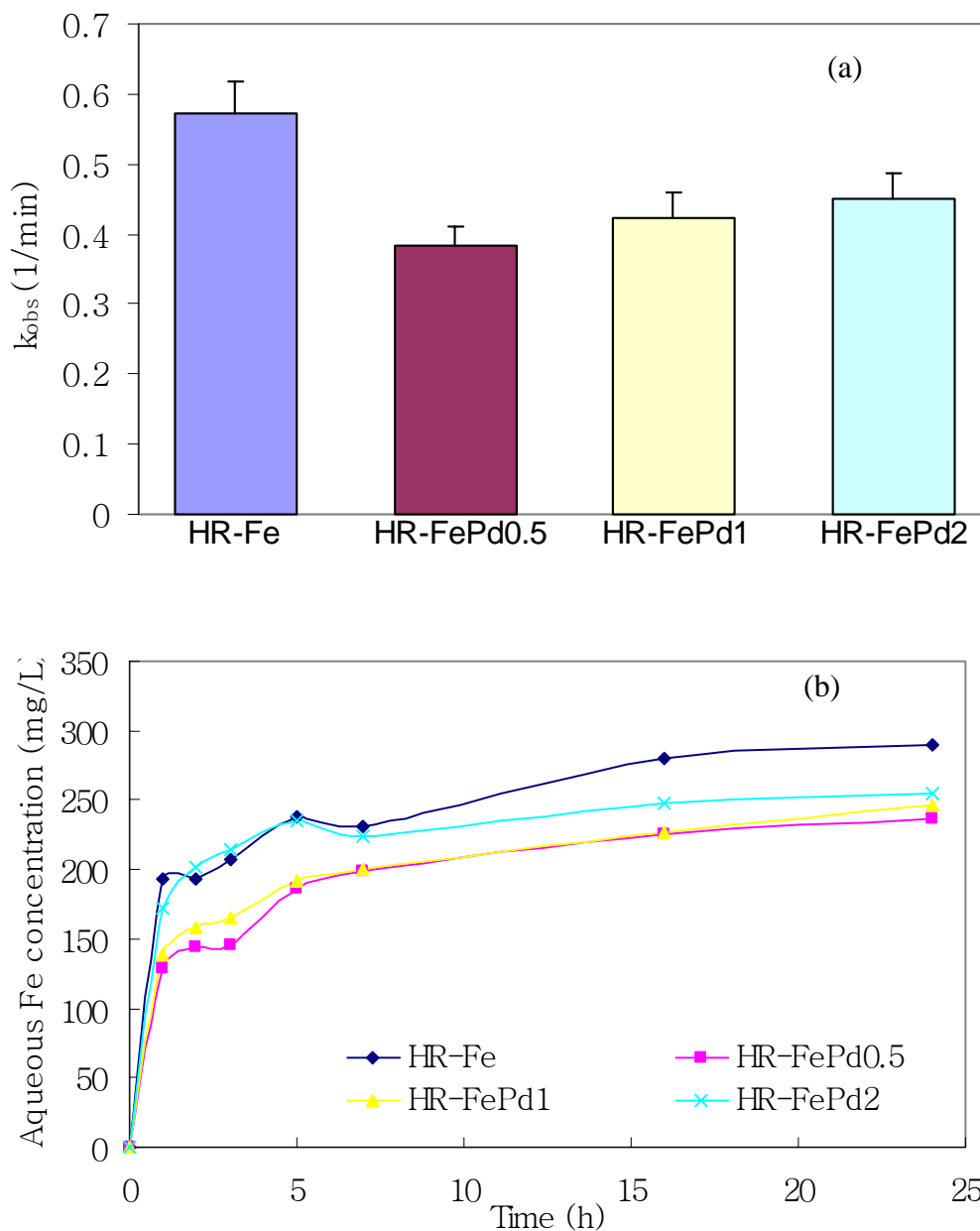
Figure 4. (a) Pseudo-first-order-rate constant of 4-Cl-NB by iron and Pd-doped irons and (b) aqueous Fe concentration as a function of time in iron/water batch systems.
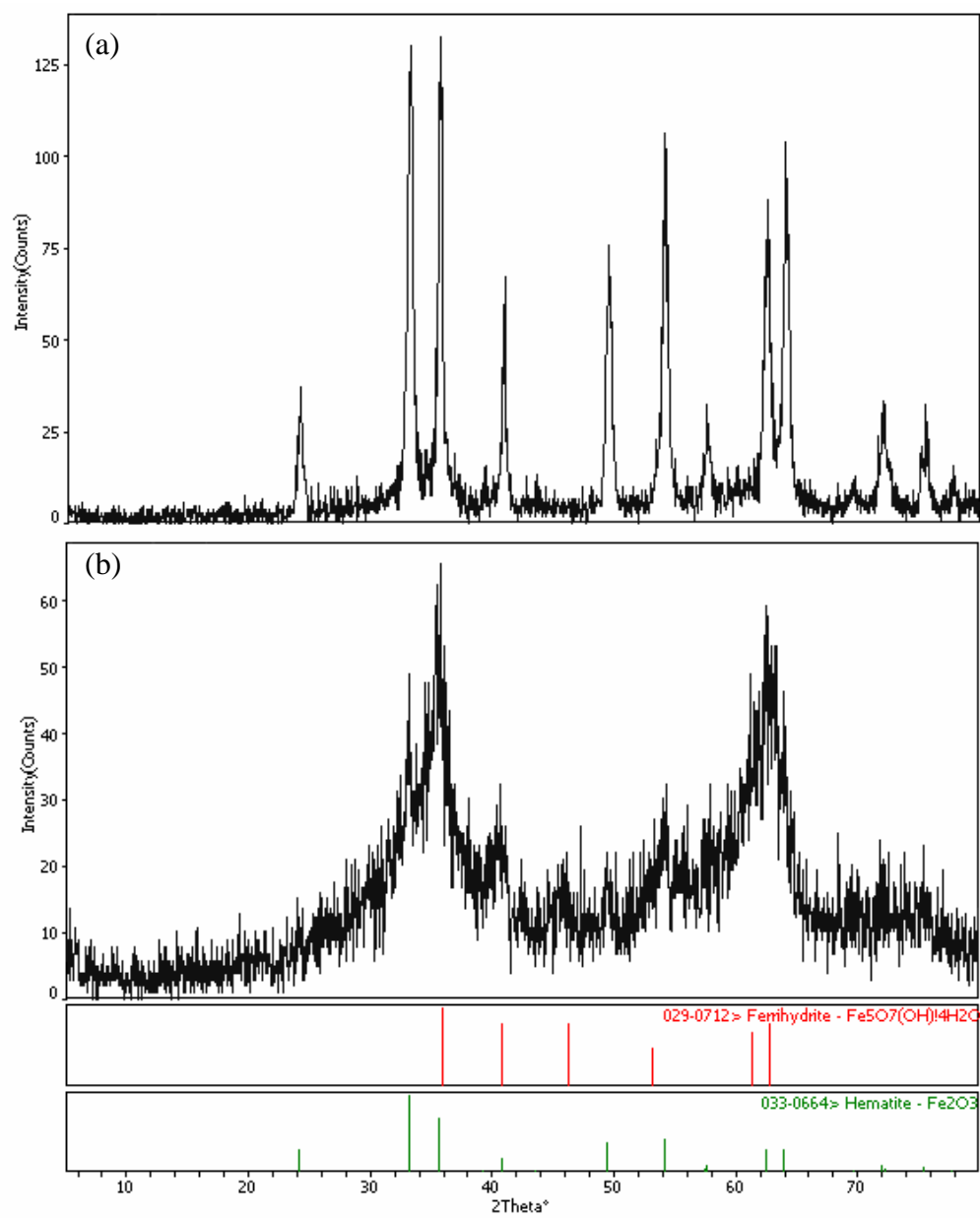
Figure S1. XRD patterns of (a) hematite and (b) ferrihydrite.
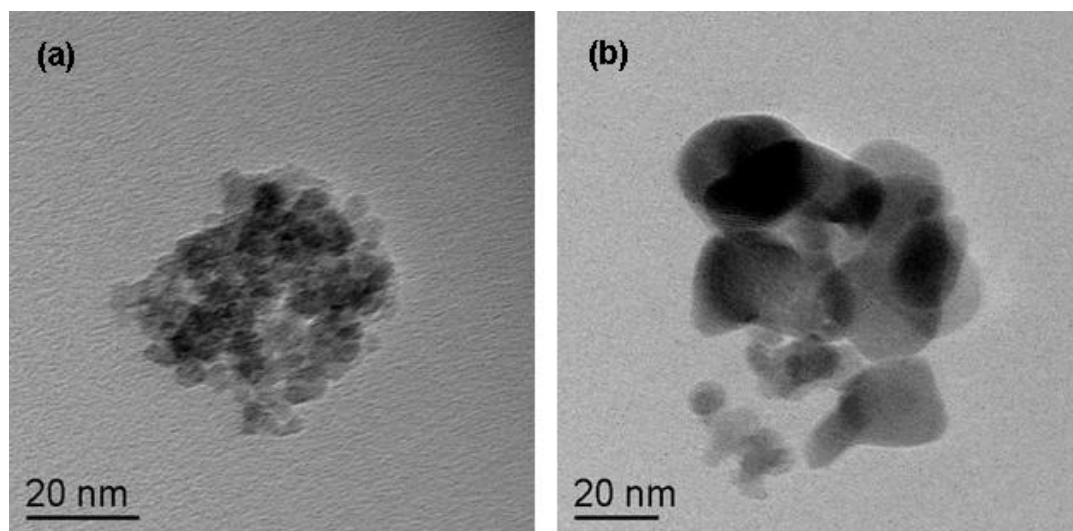
Figure S2. TEM images of (a) ferrihydrite and (b) hematite

Characterization of Aqueous Particles Internally Mixed With Surfactants

Luis A. Cuadra-Rodriguez and Barney Ellison
University of Colorado at Boulder,
Department of Chemistry and Biochemistry
Boulder, Colorado
and
Alla Zelenyuk
Pacific Northwest National Lab
Environmental Molecular Sciences Laboratory
Richland, WA

In the past few decades aerosols research has gained more attention due to aerosols' climate effect and temperature influence in the atmosphere. Many studies have shown that organic matter composed a significant amount of atmospheric particles. One interesting type of aerosol is the "inverted" micelle that consists of a water core with inorganic salts covered with surfactants. These surfactants matter can affect the chemical and physical properties particles. In this study we studied the effect of surfactants on aqueous particles at low relative humidity at different surfactants concentrations. Size resolved experiments were conducted using SMPS and SPLAT to get mobility and aerodynamic size distributions to get the effective densities of these particles. Both size distributions show that due to surfactants the particles are retaining water and as the surfactant concentration is increased the effective density decreases for a given mobility diameter. Qualitatively this is also confirmed by SEM pictures where as the surfactant concentration is increased more surfactant is associated to a NaCl particle, which explains the lower effective density. More work need to be done in order to estimate how much water is retained in these types of particles.

Introduction

Aerosols or particulate matter has gained attention in the last few decades. These can affect climate in different ways. Aerosols can act as cloud condensation nuclei (CCN) that increase the reflectivity of sunlight by clouds, which lead to lower earth temperature.[1-2] Also, the scattering and absorption of light by fine particles in the atmosphere can increase this cooling effect due to the change in physical and chemical properties of the aerosols. Many field studies have shown that organic compounds are a significant part of the total particulate matter in the atmosphere, accounting between 10%-70% of the fine particulate mass.[3]

Ellison *et al*. (1999) proposed a mechanism that account for the organic compounds in the aerosols, its reactivity and the effect in its CCN activity by the generation of nascent marine aerosols.[4] These aerosols are "inverted" micelles composed of a water core and inorganic salts covered with surfactants (hydrophobic tail with a polar head). These surfactants are believed to affect the chemical and physical properties of aqueous aerosols. Recently, Thornton *et al*.(2006) found that the reactive uptake of N_2O_5 by aqueous NaCl particles coated with sodium dodecyl sulfate is suppressed by a factor of 10 as the surfactant completely cover the aerosol surface.[5]

Even though chemical properties have been studied, almost no study has attempted to study the physical properties of these "inverted" micelles aerosols. In this study we show some physical properties (size distribution, effective density, SEM) for different aqueous aerosols covered with sodium dodecyl sulfate (SDS), sodium oleate (SO) and laurtrimonium chloride (LC). The measurements were done at low relative humidity and suggest that the particles retain water. The amount of water retained still a question that need to be addressed.

Experimental

Aerosols were generated by aerosolizing aqueous solutions with a TSI atomizer. The aerosol flow was 0.20-0.30 L min^{-1} and was used as the sampling flow to the Scanning Mobility Particle Sizer (SMPS), whose sheath flow was set to 4.0 L min^{-1}. All experiments were done at low relative humidity; therefore the SMPS was conditioned with dry air flow before and within measurements. This ensures a low relative humidity environment and cleanliness of the sampling lines. The aerosol flow was passed through two diffusion dryers in series and then into the SMPS. For each solution, mobility diameter size distribution measurements were carried out using the SMPS/CPC system. Subsequently, size selected particles from the SMPS were sampled by SPLAT to get the aerodynamic size distribution. SPLAT details are described in reference 6. In addition, Scanning Electron Microscopy (SEM) was used to further characterize the particles.

Sodium dodecyl sulfate (99% pure), sodium oleate (98% pure), laurtrimonium chloride (98% pure), sodium chloride (99.5% pure) were obtained from Sigma-Aldrich Co and used without further purification. Aqueous solutions were made using ultra pure deionized water.

Results and Discussion

Aqueous solutions. The behavior and properties of surfactants in aqueous particles internally mixed with surfactants was investigated. Aqueous solutions of sodium dodecyl sulfate (SDS), sodium oleate (SO) and laurtrimonium chloride (LC) were made in the 10^{-5}-10^{-1} M range. Mobility diameter size distribution measurements show that for SDS and SO the peak is broadening as the concentration is increased, whereas in LC no significant differences are observed (shown in Figure 1). This could be interpreted as having the particles coated with surfactants as expected, which presumably will increase particle diameter

and slow water evaporation. Although the measured vacuum aerodynamic diameter distribution for a given mobility diameter shows not many differences for SDS.
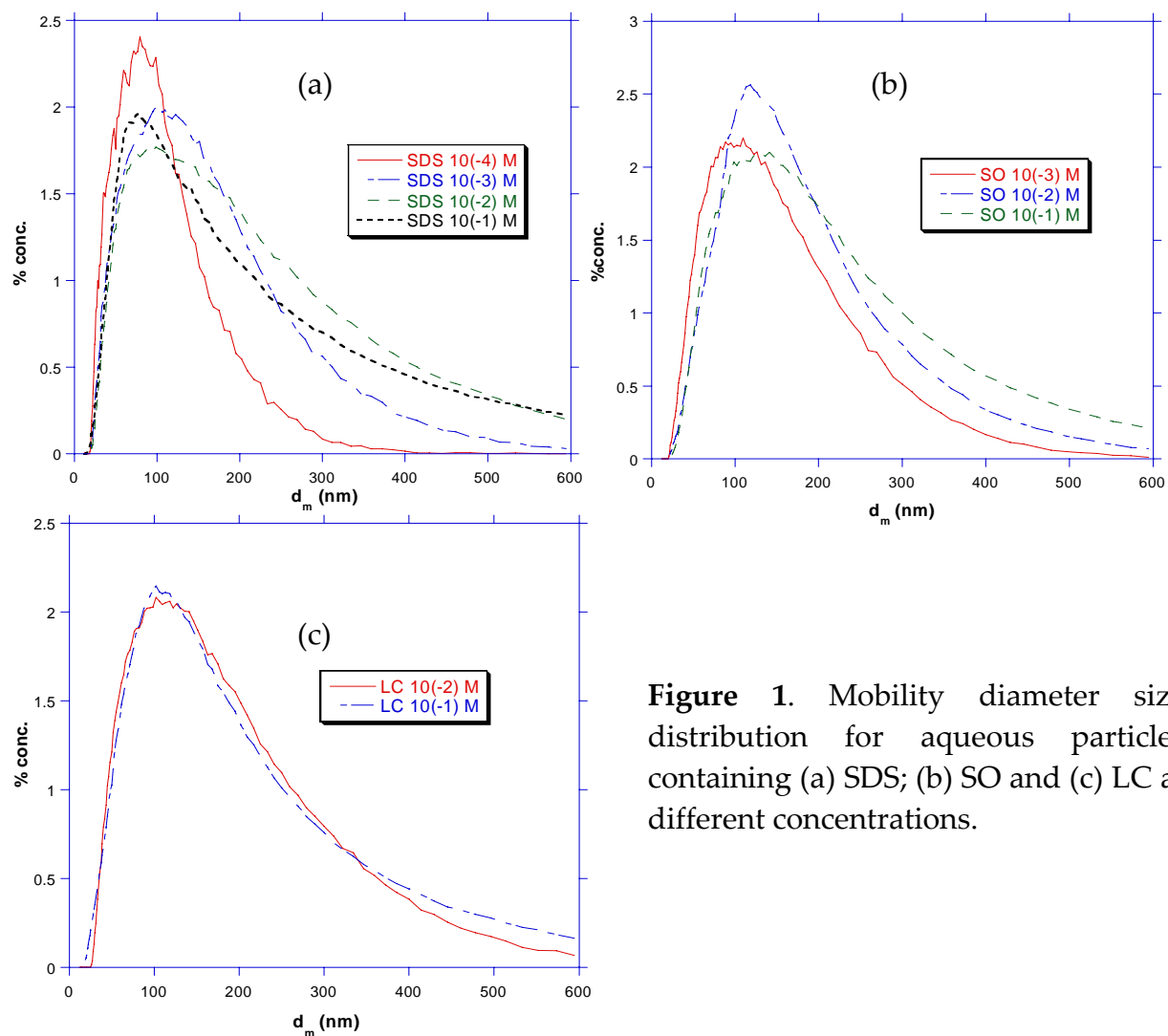
Figure 1. Mobility diameter size distribution for aqueous particles containing (a) SDS; (b) SO and (c) LC at different concentrations.

In Figure 2 it is shown the vacuum aerodynamic diameter distribution for SDS and SO for a mobility diameter of 508nm and different concentrations. The distribution for SDS does not differ as much as the one for SO as the concentration is increased. At low concentrations a tail appears in the distribution showing a "bimodal" or spread distribution, even though is the

same mobility diameter. Evaporation mechanisms and kinetics in the aerodynamic lens for wet particles could be complicated, possibly making particles lose water in different ways which is seen as a "bimodal" distribution. This is shown by Zelenyuk *et al.* (2006) for NaCl aqueous droplets.[7] In addition, the double bond in SO could affect how the particles are coated by the surfactant giving more room for water to evaporate at low concentrations. As the concentration is increased the bimodal feature disappears but still the peak broadens. The SO most intense peaks and SDS peaks show aerodynamic diameter differing by < 5%, whereas the SO smaller peak differs by 24%.
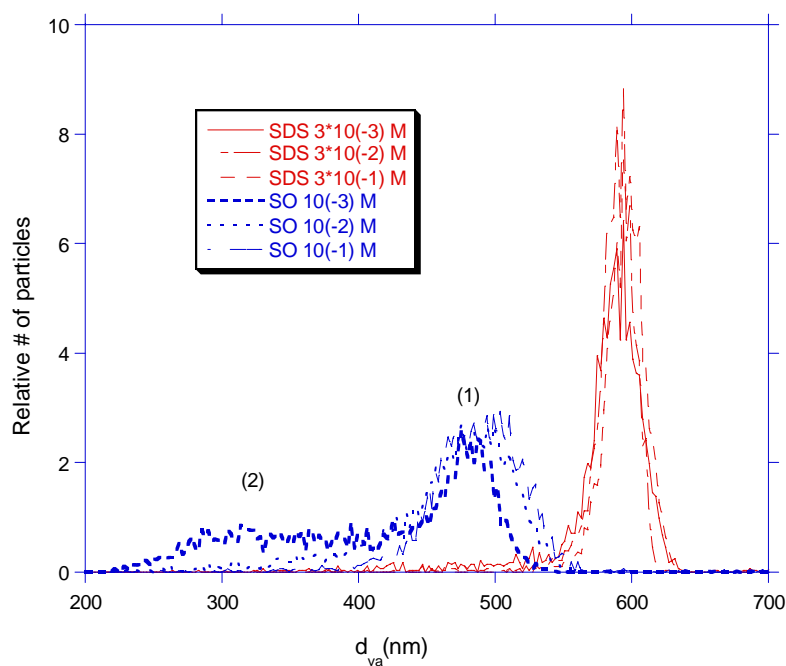
Figure 2. SDS and SO aerodynamic size distribution with a mobility diameter of 508nm

Furthermore the effective density, which is related to the ratio of d_{va} to d_m, also behaves differently for these two systems. Table 1 show d_{va}/d_m for the two systems at different concentrations for d_m = 508nm. Again, the main peak for both systems differ only by a few percent that is within experimental error except for second peak for SO. SDS has a bulk density of 0.37 g cm^{-3} and SO has a bulk

density of 1.02 g cm^{-3}. If substantial amount of water is retained due to surfactant coverage the effective density should resemble that of water. In the opposite case the effective density should reflect more likely the bulk density. Since SO and water have similar densities is difficult to get information about water retention in those particles. SDS density is significantly different from water. Based on the measured effective density, aqueous SDS particles retain water in the aerosol phase.

Table 1. Summary of d_{va}/d_m for SDS and SO for a mobility diameter of 508nm

	SDS			SO		
	3×10^{-3}M	3×10^{-2}M	3×10^{-1}M	1×10^{-3}M	1×10^{-2}M	1×10^{-1}M
d_{va}/d_m	1.16	1.17	1.18	0.95 (1) 0.72 (2)	0.96	0.97

NaCl. NaCl thermodynamic and particle shape information is known, therefore the effect of surfactants on these hygroscopic particles was studied. Solutions of NaCl ~0.05M containing SDS and NaCl ~0.1M containing SO were analyzed in the range 0 M-10^{-5} M for surfactants concentration. The mobility size distribution follow the same trend as for the aqueous solutions; as the surfactant concentration is increased from 10^{-5} M to 10^{-2} M the peak broadens to higher sizes. NaCl measured effective density also represents what has been measured[8] before including dynamic shape factors. An interesting observation is that SDS changes the particle effective density more than SO; what was expected due to their bulk densities. This is shown in Figure 3, where the d_{va}/d_m is plotted as a function of d_m for SDS and SO in the 0 M-10^{-5} M surfactant concentration range. Although NaCl concentration is different in each surfactant solution, the NaCl effective density for both concentrations is measured to be close and within experimental error. In addition, several runs of SDS in NaCl ~0.1 M follow the

same trend and fit perfectly when the NaCl:Surfactant ratio is considered. Despite that, this behavior cannot be explained completely by simple means of bulk densities as is the case for inorganic salts aerosols.[8]
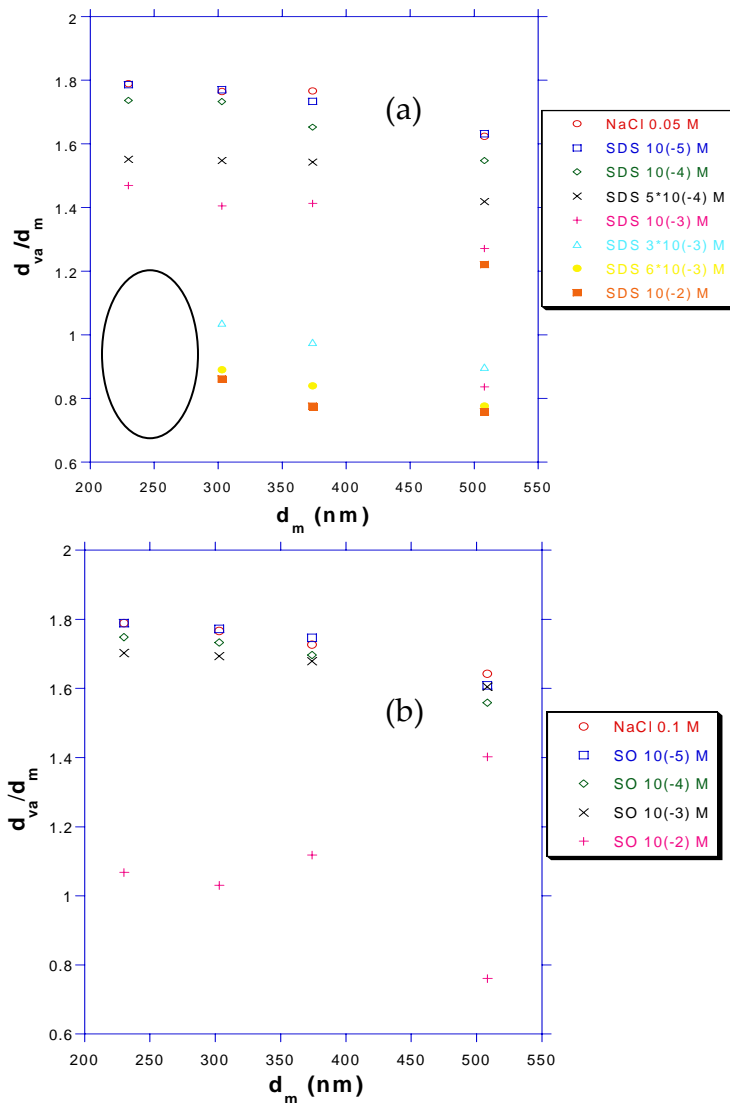
Figure 3. dva/dm as a function of dm for (a) SDS and (b) SO at different concentrations

Moreover, for SDS as the concentration is increased smaller particles "disappeared", marked as a black circle in Figure 3. Again the aerodynamic size distribution changes from resolved peaks for NaCl solution to almost converging, broad peaks as the surfactant concentration approaches 10^{-2} M

(figure not shown). This behavior is similar to the aqueous solutions bimodal behavior but in this case the size resolution for multiple charged particles is lost and only one broad peak is observed for every mobility diameter selected.

Scanning Electron Microscopy was used to understand what happened to small particles and also to have another mean to characterize the particles. Mobility diameter of 500nm was selected, sample and analyzed using SEM for particles containing NaCl with $1x10^{-4}$ M, $1x10^{-3}$ M and $6x10^{-3}$ M SDS. The same was done for a mobility diameter of 224nm. In Figure 4, the SEM picture is shown for d_m = 224nm and [SDS] = $6x10^{-3}$ M. Particularly interesting is the fact that large particles are present even though small were selected, which is something we don't understand. But there are not as many as small ones. In this picture is clear that small particles are present, but they seem too small to be detected by SPLAT. Another important feature is that many NaCl are associated with a "wet mark" around it, implying that the particles were deposited wet on the substrate. This is observed more and more at high concentration of surfactants, which explain the lower effective densies at those concentrations and the water retention.
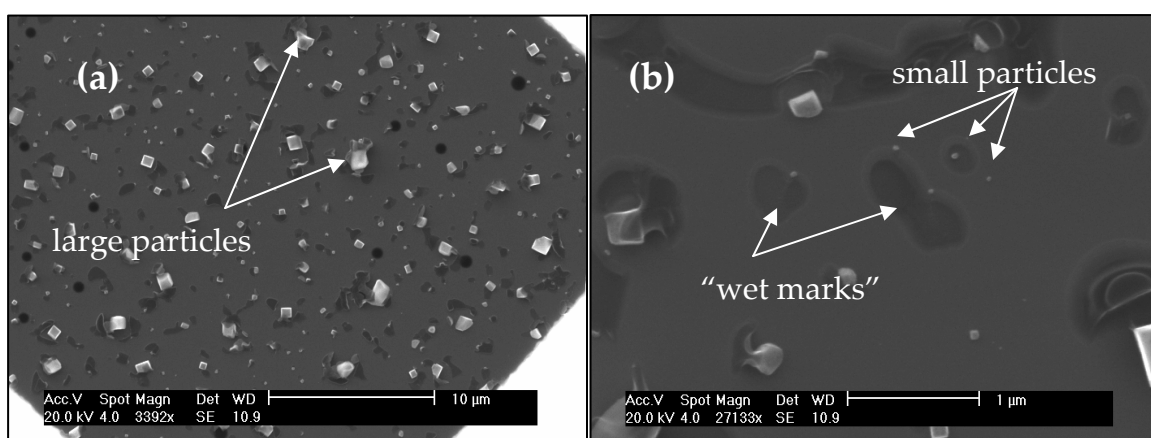
Figure 4. SEM pictures for particles containing NaCl and [SDS] = $6x10^{-3}$ M with mobility diameter, d_m of 224nm. (a) 3392x magnification and (b) 27133x magnification.

Conclusion

Here we have studied the physical properties of aqueous particles internally mixed with different surfactants. All measurements were conducted at low RH and show that every surfactant behaves differently and don not follow a particular trend. Aerodynamic size distribution shows that the particles lose water in different ways for SO when compare to SDS because of the peak broadening at low surfactant concentration. The surfactant surface coverage and structure may play a role in the suppression of water loss. Effective density measurements, mobility size distribution and SEM pictures show that the different systems retain water even though effective density could not be explain by simple means as other systems. SEM pictures help explain qualitatively the effective densities for SDS in aqueous NaCl and the particles' morphology. An interesting observation is that many NaCl particles are associated with a "wet mark" that implies the particles were deposited wet on the substrate. Despite all that, the amount of water retain or lose by these type of particles still a challenge that need more measurements to start understanding the "inverted" micelle system.

References

1) Cruz, C.N.; Pandis, S.N. *Atmospheric Environment.* **1997**, 31 (15): 2205-2214.
2) Penner, J.E.; Hegg, D.; Leaitch, R. Unraveling the role of aerosols in climate change *Environmental Science and Technology*. August 1, **2001**, pp 333 A- 340 A.
3) Tolocka,M.P.; Solomon, P. A.; Mitchell, W.; Gemmill, D.; Wiener,R. W.; Homolya, J.; Natarajan, S.; Vanderpool, R. W. *Aerosol Sci.Technol.* **2001**, *34*, 88-96.
4) Ellison, G. B.; Tuck, A. F.; Vaida, V. *J. Geophys. Res.-Atmos.* **1999**, *104*, 11633-11641.
5) Mcneill, V.F.; Patterson, J.; Wolfe, G.M.; Thornton, J.A. *Atmos. Chem Phys.,* **2006**, 6, 1635-1644.
6) Zelenyuk, A.; Imre, D. *Aerosol Science Tech.* **2005**, 39, 1-15.
7) Zelenyuk, A.; Imre, D.; Cuadra-Rodriguez, L.A. *Analytical Chem.* 2006, ASAP article; DOI: 10.1021/ac061184o
8) Zelenyuk, A.; Cai, Y.; Imre, D. *Aerosol Science Tech.* **2006**, 40, 197-217.

I. Theoretical characterization of H_3O^+ at the water/methanol – vapor interface

II. Theoretical characterization of $NaClO_4/H_2O$ solutions

Jun Cui, and K.D. Jordan
Department of Chemistry, University of Pittsburgh
Pittsburgh, PA
and
L.X. Dang, C. Wick, V. Glezakou,
Pacific Northwest National Laboratory
Richland, WA

Proton transport plays an important role in biochemistry, chemistry, and many other fields. Proton transport in methanol/water solution can serve as a valuable model system for understanding proton transport in mixed hydrophobic and hydrophilic environments, thus provide insight into proton transport in biological systems. During my stay in PNNL, I used molecular dynamics simulations to study proton behavior at methanol/water solution – vapor interface. In the simulations, three solutions with varying concentration of methanol were used: 1 M HCl/water, 0.25 M methanol/1 M HCl/water, 0.5 M methanol/1 M HCl/water. The Dang-Chang force field[1] was used for water and the AMBER force field[2] for methanol. The Dang-Chang model was modified to account for the H_3O^+ ions. The modified model puts a -0.42 Coulomb point charge on O atom, a 0.47 Coulomb point charge on each of the three H atoms. Periodical boundary conditions were applied in all three directions. A box consisting of 1000 molecules was placed into the simulation cell with dimensions 28×28×157 Å. AMBER 7 software package was adopted for molecular dynamics simulation. The initial coordinates were produced using the Monte Carlo simulated annealing method. It was found that the

simulations had difficulty in equilibrating. Ab inito calculations revealed that the proton

on H_3O^+ tends to transfer to the O atom of a methanol molecule. This strong interaction

caused the problems in the Monte Carlo simulations.

During my study at PNNL, I also started simulations aimed at understanding the
experimental finding that the folding/unfolding temperatures of model proteins depend
sensitively on the perchlorate concentration. We wanted to examine the idea that the main
influence of the perchlorate is on the structure of the water. I started molecular dynamics
simulations of NaClO$_4$/water solution, studying the hydration structure of ClO$_4^-$. As
described above, the AMBER and Dang-Chang force fields were used for the ions and
water respectively. All the simulations were carried out in an isobaric-isothermal (NPT)
ensemble at 1 atm and 298 K. The radial distribution functions of three solutions (0.5 M,
0.83 M, 1.0 M NaClO$_4$ in water) are displayed in the following figures. Figure 1 shows
the Cl-Cl radial distribution function change with perchlorate concentrations. Figure 2 is
the perchlorate concentration dependence of perchlorate Cl-water oxygen. Work on this
project is continuing.

References

(1)   Dang, L. X.; Chang, T.-M. *J. Chem. Phys.* **1997**, *106*, 8149.
(2)   Cornell, W. D.; Cieplak, P.; Bayly, C. I.; Gould, I. R.; Merz, K. M.; Ferguson, D. M.; Spellmeyer, D. C.; Fox, T.; Caldwell, J. W.; Kollman, P. A. *J. Am. Chem. Soc.* **1995**, *117*, 5179.
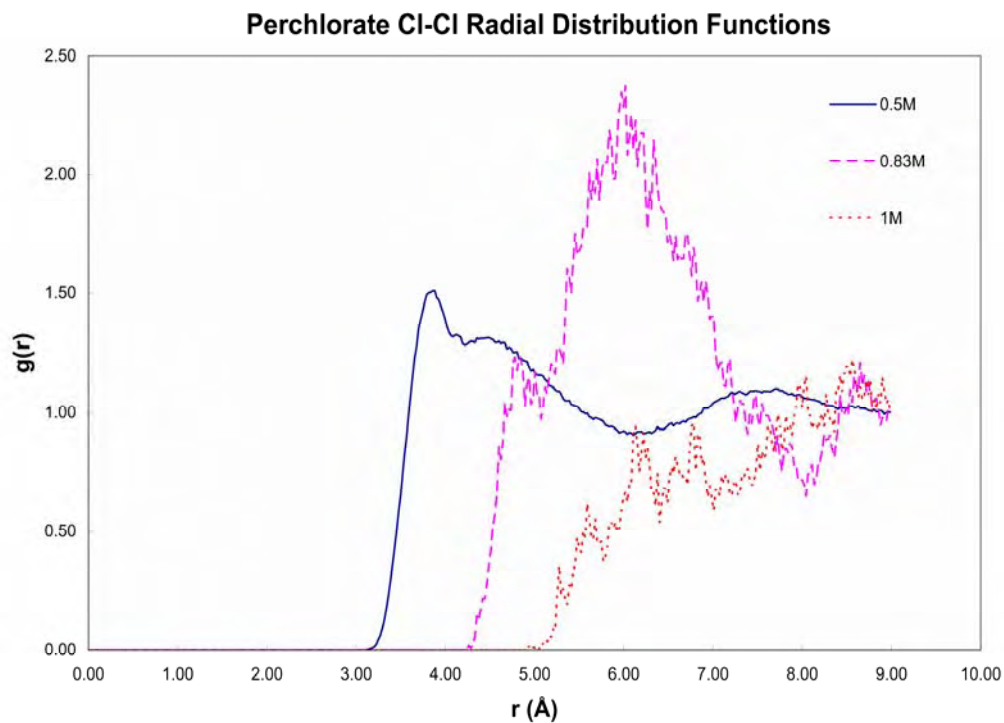
Figure 1. NaClO$_4$ concentration dependence of radial distribution functions between perchlorate chlorine.
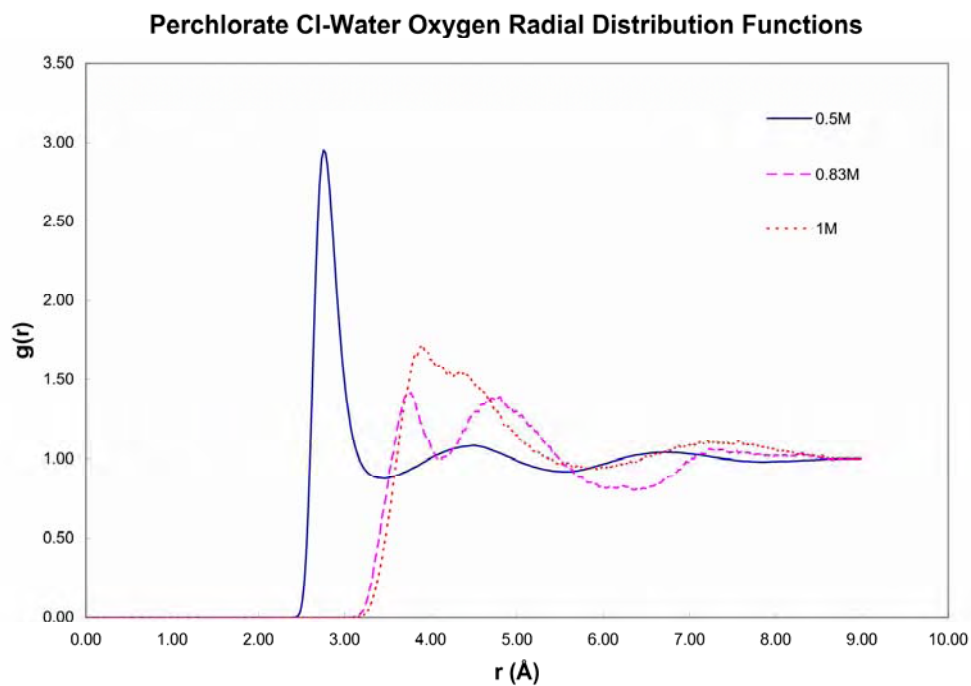
Figure 2. NaClO$_4$ concentration dependence of radial distribution functions between perchlorate chlorine and water oxygen.

OCl Radical – H$_2$O interaction: ab initio calculation and the development of empirical potential

Shiyu Du and Prof. Joseph Francisco
Department of Chemistry
Purdue University
West Lafayette, Indiana USA 47907-1393
and
Gregory K. Schenter and Bruce Garrett
Chemical Science Division
Pacific Northwest National Laboratory
Richland, WA 99352

Abstract

In the ozone removal processes in the atmosphere, the ClO free radical is found to act in an important role in recent years. In this work, we present our Potential Energy Scan of the H$_2$O•OCl system with high level ab initio methods. Because of the existence of low-lying excited states of the H$_2$O•OCl complex, and their potential impact on the chemical behavior of the OCl radical in the atmosphere, we perform a Potential Energy Surface (PES) scan at CCSD(T)/aug-cc-pVTZ level of both the first excited and ground states in order to model the physics of the unpaired electron in the OCl radical. Empirical rigid potentials for both ground and excited states were built based on a Thole Type Model. The two minimums of the H$_2$O•OCl complex are recovered by the empirical potential.

Introduction

Free radicals are well known to be the most reacting species in the atmosphere. The hydrogen bonding effect is considered as one of most important association processes in the chemical transformations and more and more hydrogen-bonded complexes are found by both experimental and theoretical studies[1-11]. A better understanding of the reactions, bonding characters, energies and roles of the complexes formed between water molecules and reacting free radicals are worth pursuing.

In the ozone removal processes in the atmosphere, ClO free radical is found to play an important role[12-15] in recent years. It has been proposed[12-16] that the critical steps in some mechanisms in the ozone removal process are that a ClO dimer is formed and then it is photodecomposed. For the formation of ClO dimer, Francisco et al.[11,16,] by *ab initio* study, found a water-ClO complex of a skewed nonplanar structure which is proposed to be the chaperone in the dimer formation process. Fu at el.[17] found other stationary points in the ClO·H$_2$O complex potential energy surface for both of the A' and A'' states and studied the corresponding vibrational frequencies with Density Functional Theory[18,19] and the Moller-Plessett Perturbation method[20-22]. All the previous studies concentrated on the stationary points. However, as one of the most atmospherically important species, these studies are far from enough because a complete study of the potential energy surface and high level calculations are needed in order to model the chemical process of this radical in the atmosphere and other surroundings in the liquid phase by molecular dynamics simulation. It is also necessary to obtain an empirical potential for the ClO·H$_2$O system.

In this work, we report the potential energy surface scan for both the ground and first excited state by locating the single electron on different orbitals with a high level calculation at the level of couple cluster involving single and double excitations with a perturbation estimation of the triple excitations [CCSD(T)][23-26] with the basis set of the family of augmented correlation-consistent basis sets of triple zeta quality (aug-cc-pVTZ). This approach has been shown to be large enough to converge in a previous related study[27] and a fitted empirical interaction potential we modified from the rigid potential between water molecules "Thole-type" model (TTM)[28-31] for H$_2$O·OCl

(mTTMC) to the binding energy by *ab initio* calculations. With the consideration of the single electron effect, we obtain a well behaved empirical potential.

Method

A. Computational Details

The ground state and first excited state electronic energy of the $ClO \cdot H_2O$ system were both scanned. In order to characterize the potential energy surface, we locate the ClO radical on different configurations relative to the water molecule. Our ab initio calculations are all at the level of CCSD(T)/aug-cc-pVTZ. In each potential energy scan, we calculate approximately 30~40 points. The interaction energy of any configuration is calculated from the difference between the corresponding $ClO \cdot H_2O$ complex energy and the monomer energies in their optimized geometries at the level of CCSD(T)/aug-cc-pVTZ. All the *ab initio* calculations were performed with the Molpro 2002 suite of programs[32] at EMSL[33].

B. Empirical Models

In this work, we reparameterize the TTM[28-31] among recently established models[34-37] because by modifying this model, we have successfully established an empirical potential for the $OH \cdot H_2O$ system. A great similarity between the $ClO \cdot H_2O$ and the $OH \cdot H_2O$ potentials[16] is found.

In the TTM model, as discussed in detail in the literature[28-31], the interactions between two molecules are decomposed by Lennard-Jones type attractive-repulsive interaction energy (U^{pair}), the induction energy (U^{ind}) and the electrostatic energy (U^{elec}). Since the interaction between water molecules has been well parameterized, we keep all the parameterizations for H_2O-H_2O interaction unchanged. As we have found in the potential surface fitting for the $OH \cdot H_2O$ system, it is possible to model the single occupied orbital by setting the three diagonal elements of the polarizability tensors (α_{xx}, α_{yy}, and α_{zz}) for the Cl and O atoms in the ClO radical. And another important feature of this model is the introduction of the "M-site" which is a hypothetical site where the electrostatic interaction is located and has been successfully used to obtain good H_2O-H_2O and $OH \cdot H_2O$ interaction energies. In our mTTMC model, we also add an "M-site" for the

ClO·H$_2$O complex between the two atoms in ClO radical besides the one which has been set up for water molecules. One difference between this potential and the OH·H$_2$O system is that we introduce the Lennard-Jones type interaction between the Cl atom and the H atom in the water molecule.

Computaional Results

A. Sampling of Potential Energy Surface

In the sampling of the ClO·H$_2$O Potential Energy Surface (PES), the coordinate for OCl radical monomer is shown in **Fig 1** and that for H$_2$O is the same as previous work.[28-31] For the complex, we adopt the same spherical coordinate system that was used for the H2O·OH complex. As shown in **Fig 2**, the water molecule is set in the plane perpendicular to the z-axis. The O atom (O1) in H$_2$O is placed at the origin and one of the O-H bonds is located in the positive direction on the x-axis. The coordinate of the other H atom can be calculated from the rigid bond angle θ_w and OH bond length r^w_{OH} of the water molecule that are optimized at the level of CCSD(T)/aug-cc-pVTZ. The bond distance of ClO radical, r_{OCl} is also optimized at the same level of theory. Since TTM in this work is a rigid model, we fixed the values of θ_w, r^w_{OH} and r_{OCl} to the values shown in **Table 1**. The coordinate of the O atom (O2) in ClO can be determined by the distance between the two oxygen atoms (one of which is in the origin point) R_{OO}, and the two spherical coordinates θ and φ. The coordinates of the Cl atom can be obtained similarly by first calculating the relative coordinate to O2 by the O-Cl bond distance, and two spherical coordinate θ' and φ' corresponding to O2 and then adding the coordinate of O2 relative to the origin point (O1). So the rectangular coordinates of the five atoms are calculated as follows:

O1 (in H$_2$O): (0, 0, 0)

H1 (in H$_2$O): (r^w_{OH}, 0, 0)

H2 (in H$_2$O): ($r^w_{OH}\cos\theta_w$, -$r^w_{OH}\sin\theta_w$, 0)

O2 (in ClO): ($R_{OO}\cos\theta\cos\varphi$, $R_{OO}\cos\theta\sin\varphi$, $R_{OO}\sin\theta$)

Cl (in ClO): ($R_{OO}\cos\theta\cos\varphi+r_{OCl}\cos\theta'\cos\varphi'$, $R_{OO}\cos\theta\sin\varphi+r_{OCl}\cos\theta'\sin\varphi'$, $R_{OO}\sin\theta+r_{OCl}\sin\theta'$)

The PES is totally determined by five variables, R_{OO}, θ, φ, θ' and φ' for both the ground state and the first excited state.

The PES scans for the ground state and first excited state are shown in **Fig 3**- **Fig 9** corresponding to all the five variables as listed in **Table 2**. R_{OO} is scanned more than others because it is the main parameter to determine the long range interaction. The reason we made PES scans for both states is that because of the existence of the single occupied orbital, the excited state obtained by exchanging the appropriate double occupied orbital and the single occupied orbital that is sometimes very close in energy with the ground state. This implies that the excited states can be a very important factor in determining the behavior of ClO·H_2O. For the same reason, as in our study of the H_2O·OH system, we also have considered both states. In this work, the first three scans are for R_{OO} and the other four scans are for φ, θ, φ' and θ' respectively.

As shown in **Fig 3**, the potentials are obtained by scanning the interaction energy as a function of R_{OO} with the configuration as pictured in the insert. The angle of Cl-O2-O1 is kept 70° which is the minimum obtained from scan # 4. In this configuration, the ground and excited states have A" and A' symmetry respectively and it is consistent with the corresponding H_2O·OH potential. This is probably because the complex in the A" state has larger orbital overlapping on the molecular plane than A'. The binding energies of the two states at the minimum are 3.03 (at R_{OO} = 3.05 Å) and 1.53 (at R_{OO} = 3.20 Å) kcal/mol respectively and are consistent with those optimized at the MP2 level by Fu et al[17]. The energy difference of the two states is lager than those of H_2O·OH (3.51 and 1.41 kcal/mol) at the corresponding geometries, but the equilibrium R_{OO} values are quite similar with those of H_2O·OH which are 3.00 and 3.20 Å respectively. The energy differences of the A' and A" states decrease when R_{OO} increases and are lower than 0.5 kcal/mol when R_{OO} is larger than 4.0 Å.

The second R_{OO} scan (scan #2) is performed for the configuration at which the Cl atom in OCl radical forms a weak bond with the O atom in water molecule as **Fig 4** illustrates. The angle formed by the OCl radical and the water molecular plane is 87°, which is the lowest in energy among all angles. The Cl-O1 distances at equilibrium are 2.81 Å and 2.86 Å for the ground state (A') and excited state (A") respectively and the ClH distance of A' state is calculated to be 3.48 Å, which is consistent with Fu et al.[17]'s result. The binding energies of the two states are 3.39 and 3.09 kcal/mol. And we find that the energy gap between the two states is less than 0.5 kcal/mol when R_{OO} is larger than 4.2

Å. The equilibrium distance is much larger and the bonding energy is also lower when comparing to those of $H_2O\cdot OH$. These differences are probably due to the much larger electron density on Cl atom than the H atom in OH.

Our last R_{OO} scan (scan #3) is plotted in **Fig 5**, where OCl radical is positioned on the bisector of the H-O-H angle of water molecule. This configuration belongs to C_{2v} point group. The binding energy for ground state B_2 and excited state B_3 are 1.76 (at R_{OO} = 3.05 Å) and 1.28 (at R_{OO} = 3.20 Å) kcal/mol. When comparing these results with the $H_2O\cdot OH$ complex, the binding energy is about 0.2-0.4 kcal/mol less but the equilibrium geometries are very close. These are consistent with what is revealed from the calculations for scan # 1. This implies that the interaction radius for O2 and H atom are close to that of $H_2O\cdot OH$ although the interaction energy is lowered. This is probably a result that O2 has a lower electron density because of much larger electronegativity of chlorine than that of hydrogen. Another interesting fact is that the equilibrium R_{OO}, in this configuration correspnonds to a transition state in $H_2O\cdot OH$. With further calculations, we will see that this is probably also true for $H_2O\cdot OCl$.

The angular potential scans are plotted for **Fig 6** to **Fig 9** which correspond to the scans of the four angular variables respectively. In **Fig 6**(scan #4), the interaction energies of the ground state A" and excited state A' are calculated by changing the φ' from -90° to 90° as shown in the insert. The calculations show that the energy difference between the two states is less than 0.5 kcal/mol when φ' is in the [-30°, 27°] range. As seen from the figure, there are two minimums (φ' = ±70°) and one maximum (φ' = -3°) on PES for the ground state, whose binding energies are correspondingly 2.98, 2.65 and 1.80 kcal/mol. However, for the excited state, only one minimum (φ' = 30°) is found with a binding energy of 1.75 kcal/mol. This is quite different from the similarity of the A' and A" states on the PES of $H_2O\cdot OH$ at the analogous geometry.

The potential scan with θ' as the variable (scan #5) is given in **Fig 7**. The OCl radical is positioned on the opposite side to the H atoms of the water molecule. The angle of ·OCl to the water molecule plane is set 87° with R_{OO}=4.4 Å as in scan #2 which results in the approximate symmetry of the potential curves for both states. The energy splitting is less than 0.5 kcal/mol except when θ' is ranged from θ'=100° to 150° kcal/mol with a maximum of 0.88 kcal/mol when θ'= 120°. The energy of the ground state A' has a

binding energy 3.39 kcal/mol when θ' is 93° and this exactly matches the minimum configuration of scan #2.

The next angular scan is the binding energy as a function of φ (scan #6) as graphed in **Fig 8**. The R_{OO} is fixed to be 3.15 Å. The H atom is kept collinear with the two O atoms all through the scan. The most important feature about this scan is that the energy splitting of the ground (A") and excited (A') states is all less than 0.5 kcal/mol, which means the excited state is significant to predict the chemical behavior of the structure with the rotation of the OCl radical. The two minima appear when the OCl radical is near collinear to the two OH bonds in the water molecule which gives a binding energy 1.82 and 1.69 for the two states. The two maxima are found when the OCl radical is on the bisector of H-O-H angle in the water molecule or its extension. This result is consistent with the study of the $H_2O \cdot OH$ potential energy surface.

The last potential scan is a θ scan (scan #7) as shown in **Fig 9**. The OCl radical is rotating along the plane passing the bisector of the water molecule and perpendicular to it. The R_{OO} is set as 3.05 Å, the minimum of scan #3. As we see from the figure, the binding energy decreases with the increasing θ value and reaches the minimum when θ=90° and all the atoms are coplanar. The energy of A' state is more stable than A" state but their difference is less than 0.5 kcal/mole when θ<75°. A point worthy of noting is that if we consider the results of scan #3, scan #6 and this scan, the minimum of scan #7 or scan #3 is probably corresponding to a first order stationary point or a transition state which resembles the potential energy surface of $H_2O \cdot OH$.

So with the above calculations, we obtained the potential energy surface of $H_2O \cdot OCl$, we find the PES resembles that of $H_2O \cdot OH$ in some of the configurations. And as expected, the excited states of both of the two complexes have a energy difference less than 0.5 kcal/mol from the ground states, namely, very important in determining their chemical behaviors.

B. The description of the empirical potentials

All the fitted parameters for the $ClO \cdot H_2O$ complex in mTTMC are listed in **Table 3** and **Table 4** for the ground and first excited states respectively. All the parameters are for the OCl radical since we use the same parameterizations for the water molecule as that in

TTM2-R[28-31] model. The OCl bond length is set as the CCSD(T) optimized geometry. As shown in the tables, the charges on the Cl atom and O atom of the OCl radical are $\pm 3.22 \times 10^{-20}$ C and $\pm 4.58 \times 10^{-20}$ C for the ground and excited states respectively. This is smaller than those of the OH radical. The ground state dipole moment is calculated as 1.14 D, comparable to our CCSD(T) prediction 1.23 D and the experimental value 1.24 D.[38] These results are reasonable because the Cl atom has a much higher electronegativity. The polarizability of the O atom has a larger component than the other two directions for the ground state, which is similar to that of the OH radical. But for the excited state, the x and z components are dominant. We find that the Cl atom has a much larger polarizabilty with main component in x direction for both states. The difference of the Cl atomic polarizability between the two states is in that the excited state has a much lower y component. The ground state molecular polarizability is estimated to be 3.02 Å^3 by averaging the diagonal components of the polarizability tensors and it is in excellent agreement with the estimation of 3.04 Å^3 at the level of CCSD(T)/aug-cc-pVTZ. As for the Lennard-Jones potential, we include all the possible combinations between the two bodies. The powers for the O-O interaction are fixed to be 12 and 6, and this interaction shows a consistent σ value with that in the $H_2O \cdot OH$ potential and a lower ε than $H_2O \cdot OH$ potential. The O1-Cl4 interaction is calculated to be stronger than O-O interaction for both states, which indicates a strong chemical bonding effect between the two atoms. The O2-H2(3) interaction is much stronger in the ground state than in the excited state. Their magnitudes suggest that the chemical bonding between them only occurs when the system is in the ground state. In this potential, the H2(3)-Cl4 interaction is also considered since the Cl atom has a large van der Waals radii. The data show that this interaction has large σ values but very small ε values. This means that there is an additional repulsion to reproduce the PES of the $H_2O \cdot OCl$ system.

The empirical potentials for scan #1 shown in **Fig 3** are consistent with the ab initio values. The fitted ground state energy is 2.92 kcal/mol at the minimum of R_{OO}= 3.00 Å, with a deviation of 0.1 kcal/mol in binding energy and -0.05 Å in geometry. The energies of fitted excited state also well resemble the A' state, whose minimum is predicted to be R_{OO}=3.10Å, 0.1 Å shorter than the CCSD(T) prediction. The energy difference between

the ab initio and fitted values is less than or very slightly above 0.3 kcal/mol when $R_{OO} >$ 3.2 Å.

The mTTMC model prediction for scan #2 is also satisfactory as shown in **Fig 4**. The energy deviations of the empirical potential for the states A' and A'' at the minimum are only 0.03 kcal/mol with R_{OO} errors 0.0 Å and -0.1 Å respectively. When $R_{OO} > 4.2$ Å, the energy errors from the quantum chemical calculations are below 0.1 kcal/mol for the ground state and 0.5 kcal/mol for the excited state.

The performance of the current OCl potentials on the transition state (scan #3 in **Fig 5**) is also in good agreement with the ab initio results. The deviation of the empirical potential is less than 0.15 kcal/mol when $R_{OO} > 3.0$ Å for both A' and A'' states. At the minimum points, the prediction error of the parameterized potential is only -0.05 and -0.10 Å in R_{OO} for the ground and excited states respectively and approximately 0.01 kcal/mol in binding energy for both.

Our new OCl potential also gives satisfactory prediction on the angular scans.

As shown in **Fig 6**, the two states of the empirical potential correctly separate in scan #4. For the ground state, the empirical potential gives two minimums with binding energies of 2.52 and 3.29 kcal/mol located at φ'= -70° and 80° (beyond the range of the figure) respectively. These results resemble the ab initio calculations which predict -70° and 70° as two minimums as observed in the figure. As for the excited state, the empirical potential has a binding energy of 1.92 at the minimum, which agrees very well with the CCSD(T) prediction although the φ' angle has a 30 degrees difference. When φ' is in the range of [-40°, 30°], the energy deviation of both of the two fitted states is less than 0.2 kcal/mol.

Scan #5 plotted in **Fig 7** is also fitted with good accuracy. The energy splitting is well mimicked by the Thole Type model. The deviations are less than 0.3 kcal/mol when θ' is in the range of [0º, 30º], [78º, 108º] and [156º, 180º]. The minimum point θ'=93° and the minimum point θ'=0° are both correctly located with binding energy error no more than 0.07 kcal/mol for both of the A' and A'' states.

The φ scan is well fitted with the mTTMC model for both A' and A'' states as seen in **Fig 8**. The maximum and minimum points found by the empirical potential are consistent with the prediction of the quantum chemical calculations for both states except a -10°

error for the ground state at φ=270°. The prediction fitted ground state has a maximum deviation of 0.15 kcal/mol at φ =0°, which is probably due to the difficulty in fitting the flatness of the CCSD(T) PES when OCl is collinear to the OH bond of the water molecule. But with φ in the range of 20° to 230°, the binding energy deviation is lower than 0.1 kcal/mol. In contrast, the excited state is better fitted when 260°<φ<360° with deviation within 0.1 kcal/mol. The error for the excited state is all less than 0.30 kcal/mol.

For the last scan (scan #7 in **Fig 9**), the results of the mTTMC prediction are also satisfactory. Both empirical potentials show a minimum at θ=90° as the CCSD(T) potential with an error of 0.02 kcal/mol and 0.01 kcal/mol respectively for A' and A" states respectively. The error is lower than 0.24 kcal/mol all over the potential scan for both states.

As discussed above, by reparameterization of the modified TTM potential, we obtained empirical potentials of $H_2O \cdot OCl$ system with rather good quality. The overall comparison of the empirical potential and the *ab intio* results are shown in **Fig 10** and **Fig 11** for ground and excited states respectively. In these figures, we show the energy difference by $\triangle E = E^{ab\ initio} - E^{TTM}$ for all the scans. As seen from the curve, the perturbation of the energy error mostly occurs around 0 for both states. The ground state energy shows a better accuracy except only one point of the repulsive wall in Scan #1. When the binding energy is around -2 kcal/mol, some negative error can be seen in Scan #5 for the ground state. The error of the excited state also behaves very reasonably and all the error is in the range of ±1 kcal/mol. The figures illustrate that the performance of our parameterization is satisfactory in predicting the stabilization of the complex.

In order to quantitatively show the error of the mTTMC potential, we summarize the average difference ($\overline{\Delta E}$), average of the absolute difference ($\overline{|\Delta E|}$), the variance of the signed difference ($\sigma(\Delta E)$), and the maximum difference ($\max(\overline{|\Delta E|})$) between the CCSD(T) calculation results and the mTTMC potentials as shown in **Table 5.** The overall average errors are both very close to 0 for ground and excited states. The average absolute error is only 0.09 kcal/mol for the ground state when the interaction energy is less than -3 kcal/mol. The corresponding variance of the error with the same cutoff

energy is also the least, which is 0.12 kcal/mol. This is an indication that the minimum points of the ground state are well reproduced by the mTTMC potential. The largest $\sigma(\Delta E)$ value of 0.25 kcal/mol and a 0.17 kcal/mol of $\overline{|\Delta E|}$ can be found when the interaction energy is below -2 kcal/mol, which reflect the error in Scan #5 as shown in **Fig 10**. Approximately 180 points of the ground state potential energy surface are in the range of -2 to 0 kcal/mol. The $\overline{|\Delta E|}$ in this range is only 0.13 kcal/mol, showing very good accuracy. For the excited state, the predicted absolute error can be found slightly larger than the ground state. The largest absolute error, which is 0.94 kcal/mol, in the excited state is found in Scan #4. The distribution of the points for excited state is also most in the range of -2 and 0 kcal/mol (up to 206 points). The $\sigma(\Delta E)$ value of the excited state is about 0.3 kcal/mol.

The comparison of the above results with those that we obtained from the mTTM potential for the $H_2O \cdot OH$ system show that the newly fitted modified TTM potential for the $H_2O \cdot OCl$ is more accurate. This indicates that the TTM functional form with anisotropic polarizabilities behaves better for $H_2O \cdot OCl$ than $H_2O \cdot OH$.

With the newly built potential, we performed energy minimization of the $H_2O \cdot OCl$ complex. Two minima are obtained. The global minimum is predicted to be the one by Fu. et al.[17] in **Fig 12**. And the local minimum is close to the geometry calculated by Francisco et al.[11,16], but with a planar structure as in **Fig 13**. We reoptimized the two minima of the complex at the level of CCSD(T)/aug-cc-pVTZ. The geometry parameters are shown in **Fig 12** and **Fig 13**. The binding energy of the global and local minimums are predicted to be 3.42 kcal/mol and 3.22 kcal/mol and their corresponding dipole moments are 5.01 D and 1.18 D respectively. The closeness of the two minima strongly suggests that both of the two $H_2O \cdot OCl$ complex configuration may exist with a significant population. This conclusion is in very good agreement with the prediction by our mTTMC model since the energy difference of the local minimum from the global minimum predicted by our empirical potential is lower than 0.02 kcal/mol. This finding may have significant implication for the experimental study of the interaction between the OCl radical and water.

Conclusion

In this work, we performed ab initio calculations on the PES of the $H_2O•OCl$ system at the level of CCSD(T)/aug-cc-pVTZ. From the computational results, we find that it is in good comparison with that of the $H_2O•OH$ complex. The empirical potential has been constructed with the TTM functional form. Our fitted empirical potentials well resemble the ab initio results and the optimized structures of the $H_2O•OCl$ complex also agrees well with previous predictions.

References

1. Stumm, W.; Morgan, J.J. *Aquatic Chemistry*; Wiley; New York, 1996

2. R. L. Mauldin III, S. Madronich, S. J. Flocke, and F.L. Eisele, G.J. Frost, and A.S.H. Pervot, Geophys. Res. Lett. **24**, 3033 (1997)

3. M. Poeselova, P. Jungwirth, D. J. Tobias, and R. B. Gerber, J. Phys. Chem. B. **107**, 12690 (2003)

4. P. Cabral do Couto, R. C. Guedes, and B. J. Costa Carbral, J. Chem. Phys., **119**, 7344 (2003)

5. A. C. Legon, and D. J. Millen, Chem. Rev. **86**, 635 (1986)

6. S. A. Cooke, G. K. Gorlett, C. M. Evans, and A. C. legon, Chem. Phys. Lett. **272**, 61 (1997)

7. P. Hobza, J. Sponser, and T. Beschel, J. Comput. Chem. **16**, 1315 (1995)

8. A. C. Legon, and D. J. Millen, Acc. Chem. Res. **20**, 39 (1987)

9. J. Lundell, and Z. Latajka, J. Phys. Chem. **101**, 5004 (1997)

10. A. C. Legon, Chem. Phys. Lett. **237**, 291 (1995)

11. Y. Li, and J. S. Francisco, J. Chem. Phys. **115**, 8381 (2001)

12. R. A. Cox, and G. D. Hayman, Nature **332**, 796 (1988)

13. L. T. Molina, and M. J. Molina, J. Phys. Chem. **91**, 433 (1987)

14. M. J. Molina, Science **238**, 1253 (1987)

15. S. P. Sander, R. R. Friedl, and Y. L. Yung, Science **245**, 1095 (1989)

16. J. S. Francisco and S. P. Sander J. Am. Chem. Soc. **117**, 9917 (1995)

17. H. Fu, Z. Zhou, and X. Zhou, Chem. Phys. Lett., **382**, 466 (2003)

18. A. D. Becke, J. Chem. Phys. **98**, 5648 (1993)

19. C. Lee, W. Yang, and R. G. Parr, Phys. Rev. B **37**, 785 (1988)

20. M. J. Frisch, M. Head-Gordon, and J. A. Pople, Chem. Phys. Lett. **166**, 281 (1990)

21. M. Head-Gordon and T. Head-Gordon, Chem. Phys. Lett. **220**, 122 (1994)

22. C. Moeller and M. S. Plesset, Phys. Rev. **46**, 618 (1934)

23. C. Hampel and H. -J. Werner, J. Chem. Phys. **104** 6286 (1996);

24. M. Schütz and H.-J. Werner, J. Chem. Phys. **114**, 661 (2001);

25. M. Schütz and H.-J. Werner, Chem. Phys. Lett. **318**, 370 (2000);

26. M. Schütz, J. Chem. Phys. **113**, 9986 (2000).

27. D. P. Schofield and H. G. Kjaergaard, J. Chem. Phys. **120**, 6930 (2004)

28. C. J. Burnham, J. C. Li, S. S. Xantheas, and M. Leslie, J. Chem. Phys. **110**, 4566 (1999)

29. C. J. Burnham and S. S. Xantheas, J. Chem. Phys. **116**, 1479 (2002)

30. S. S. Xantheas, C. J. Burnham, and R. J. Harrison J. Chem. Phys. **116**, 1493 (2002)

31. C. J. Burnham and S. S. Xantheas, J. Chem. Phys. **116**, 1500 (2002)

32. R. D. Amos, A. Bernhardsson, and A. Berning, et al. MOLPRO, a package of ab initio programs

33. See http://www.emsl.pnl.gov for more information

34. M. W. Mahoney and W. L. Jorgensen, J. Chem. Phys. **114**, 363 (2001)

35. A. Glattli, X. Daura, and W. F. van Gunsteren, J. Chem. Phys. **116**, 9811(2002)

36. H. Yu, T. Hansson, and W. F. van Gunsteren, J. Chem. Phys. **118**, 221(2003)

37. H. Yu and W. F. van Gunsteren, J. Chem. Phys. **121**, 9549(2004)

38. NIST webbook. See http://webbook.nist.gov/chemistry/form-ser.html.

Table 1. The geometry of CCSD(T)/aug-cc-pvtz optimized H_2O and OCl.

r^w_{OH} (Å)	θ_w (degrees)	r_{OCl} (Å)
0.9616005	104.186	1.5936

Table 2. The variables and parameters of CCSD(T)/aug-cc-pVTZ PES scan of $H_2O \cdot OH$.

Scan #	R_{OO} (Å)	θ (degrees)	φ (degrees)	θ' (degrees)	φ' (degrees)
1	Variable	90	0	90	70
2	Variable	87	128	3	52
3	Variable	90	-52	90	-52
4	3.15	90	0	90	Variable
5	4.40	87	128	Variable	-52
6	3.15	90	Variable	90	$= \varphi$
9	3.05	Variable	-52	$= \theta$	-52

Table 3. Parameterization of the OCl radical in empirical ground state potential.

Q_{Cl} (electronic charge)	3.216×10^{-20} C	Q_O (electronic charge)	-3.216×10^{-20} C
$\alpha_{O,xx}$ (Å^3) 0.074	$\alpha_{O,yy}$ (Å^3) 1.477	$\alpha_{O,zz}$ (Å^3)	0.074
$\alpha_{Cl,xx}$ (Å^3) 4.446	$\alpha_{Cl,yy}$ (Å^3) 2.848	$\alpha_{Cl,zz}$ (Å^3)	0.148
σ_{OO} (Å) 2.986	ε_{OO} (kcal/mol) 0.186	M-O distance in OH (Å)	0.407
σ_{O1Cl4} (Å) 2.567	ε_{O1Cl4} (kcal/mol) 0.961	n, m*	10.35, 4.00
σ_{O2H3} (Å) 2.001	ε_{O2H3} (kcal/mol) 0.193	n, m*	9.00, 4.00
σ_{Cl4H3} (Å) 3.295	ε_{Cl4H3} (kcal/mol) 0.050	n, m*	9.01, 5.61

*n and m are the exponential numbers in the Lennard-Jones Potential $U^{pair} = \Sigma\varepsilon[(\sigma/r)^n - (\sigma/r)^m]$.

Table 4. Parameterization of the OCl radical in empirical first excited state potential.

Q_{Cl} (electronic charge)	4.582×10^{-20} C	Q_O (electronic charge)	-4.582×10^{-20} C
$\alpha_{O,xx}$ (Å^3) 0.593	$\alpha_{O,yy}$ (Å^3) 0.074	$\alpha_{O,zz}$ (Å^3)	0.593
$\alpha_{Cl,xx}$ (Å^3) 4.446	$\alpha_{Cl,yy}$ (Å^3) 0.297	$\alpha_{Cl,zz}$ (Å^3)	0.148
σ_{OO} (Å) 2.981	ε_{OO} (kcal/mol) 0.216	M-O distance in OH (Å)	0.635
σ_{O1Cl4} (Å) 2.713	ε_{O1Cl4} (kcal/mol) 0.542	n, m*	13.16, 8.78
σ_{O2H3} (Å) 1.810	ε_{O2H3} (kcal/mol) 0.031	n, m*	10.40, 6.00
σ_{Cl4H3} (Å) 3.338	ε_{Cl4H3} (kcal/mol) 0.043	n, m*	13.57, 4.80

*n and m are the exponential numbers in the Lennard-Jones Potential $U^{pair} = \Sigma\varepsilon[(\sigma/r)^n - (\sigma/r)^m]$.

E_{cut} (kcal/mol)	Ground State					Excited State				
	$\overline{\Delta E}$ (kcal/mol)	$\overline{|\Delta E|}$ (kcal/mol)	$\sigma(\Delta E)$ (kcal/mol)	$\max(|\Delta E|)$ (kcal/mol)	$N(E_{cut})$	$\overline{\Delta E}$ (kcal/mol)	$\overline{|\Delta E|}$ (kcal/mol)	$\sigma(\Delta E)$ (kcal/mol)	$\max(|\Delta E|)$ (kcal/mol)	$N(E_{cut})$
-3	-0.02	0.09	0.12	0.29	20	0.10	0.11	0.13	0.31	7
-2	0.00	0.17	0.25	0.73	69	0.08	0.31	0.35	0.51	26
-1	-0.05	0.15	0.22	0.74	154	-0.04	0.21	0.30	0.94	121
0	-0.07	0.13	0.19	0.74	243	-0.03	0.19	0.28	0.94	232
1	-0.06	0.13	0.20	1.13	251	-0.03	0.19	0.28	0.94	249
3						-0.03	0.19	0.28	0.94	251

Table 5. Average error $\overline{\Delta E}$, average unsigned error $\overline{|\Delta E|}$, variance of the average error $\sigma(\Delta E)$, and the maximum unsigned error $\max(|\Delta E|)$ in the mTTM fit to the CCSD(T)/aug-cc-pVTZ predicted ground and excited states of the H$_2$O·OCl complex. The results are obtained corresponding to the number of points $N(E_{cut})$ with cutoff energy E_{cut}.
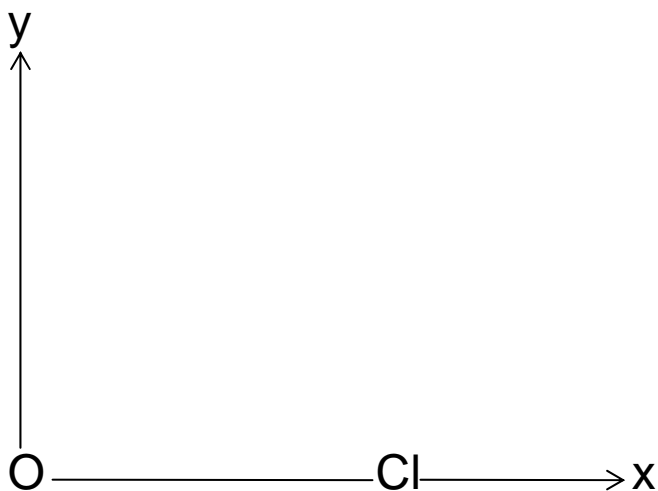
Fig 1. The coordinate setup fro the OCl radical monomer
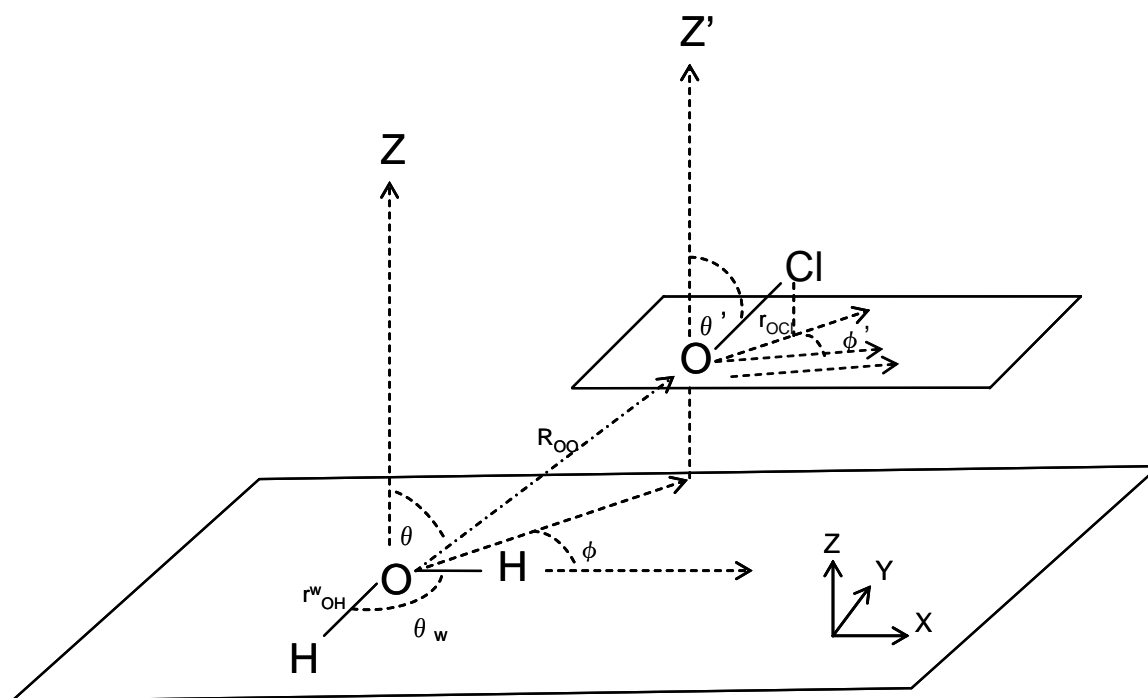
Fig 2. The coordinate setup for the $H_2O \cdot OCl$ complex
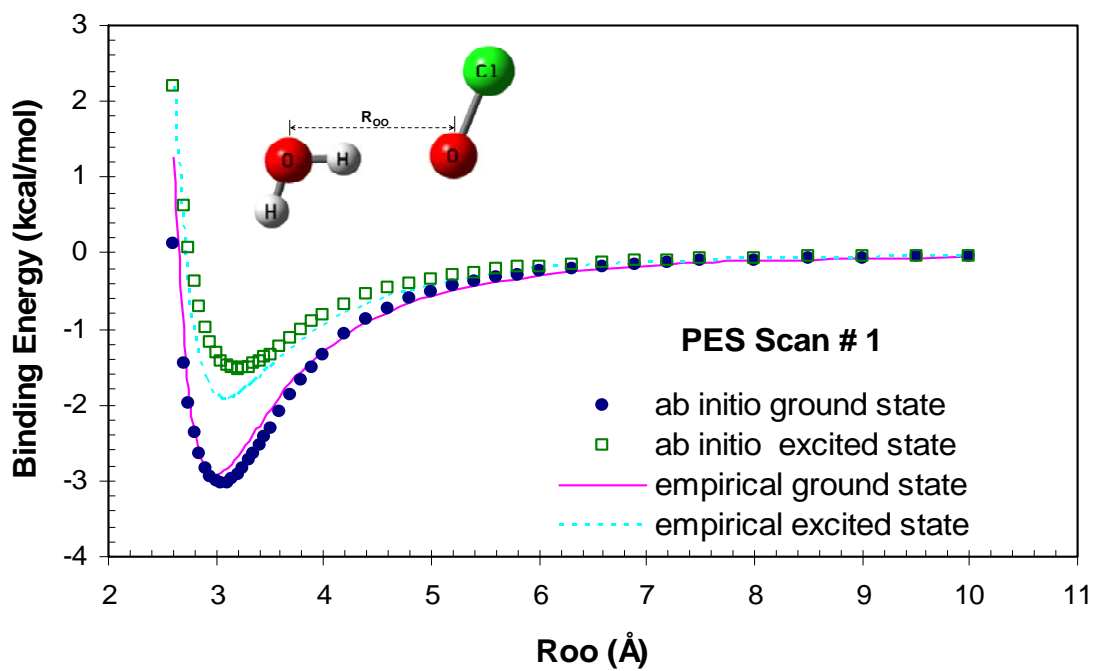
Fig 3. Potential Scan #1. Interaction energy vs R_{OO} for the ground and excited states predicted by CCSD(T) calculations and mTTMC potential.
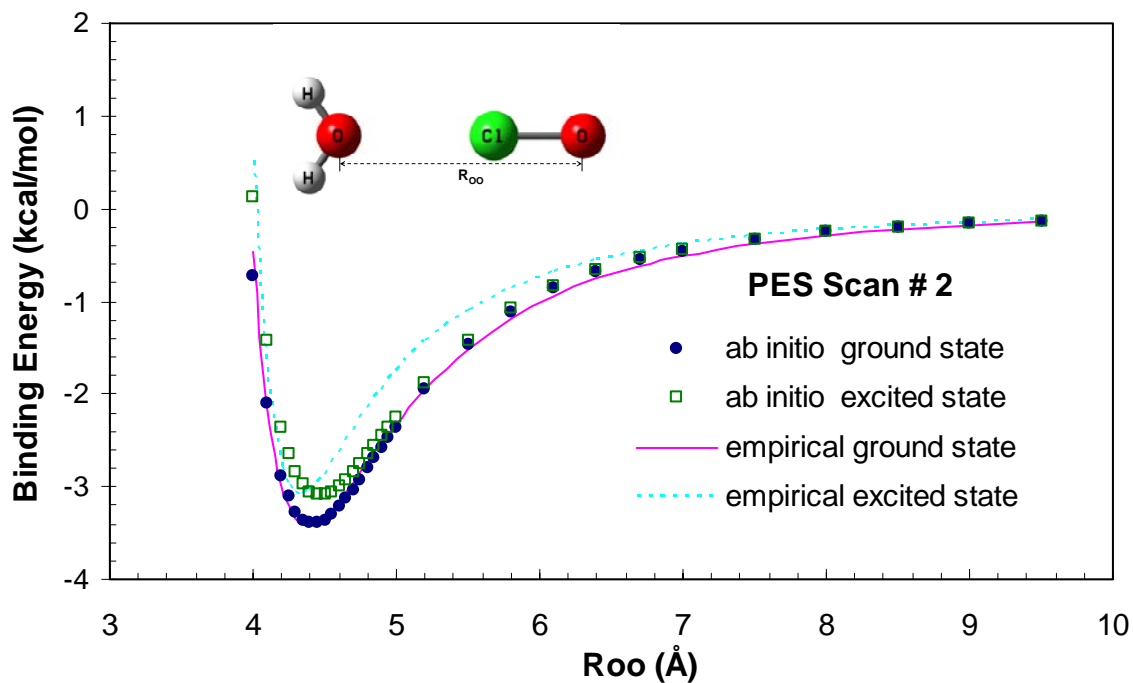
Fig 4. Potential Scan #2. Interaction energy vs R_{OO} for the ground and excited states predicted by CCSD(T) calculations mTTMC potential.
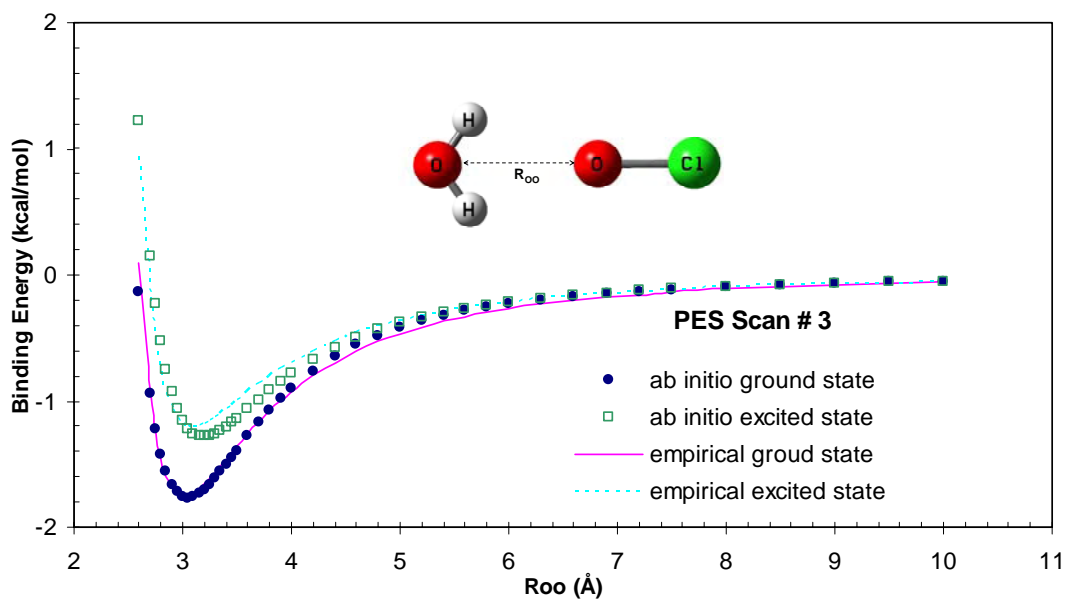
Fig 5. Potential Scan #3. Interaction energy vs R_{OO} for the ground and excited states predicted by CCSD(T) calculations and mTTMC potential.
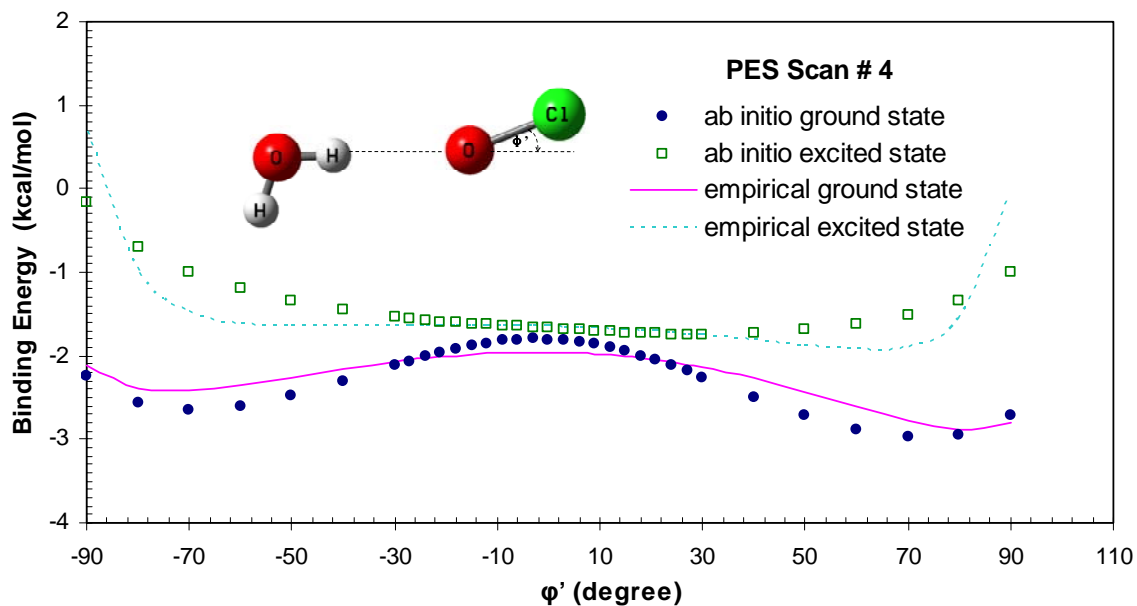
Fig 6. Potential Scan #4. Interaction energy vs φ' for the ground and excited states predicted by CCSD(T) calculations and mTTMC potential.
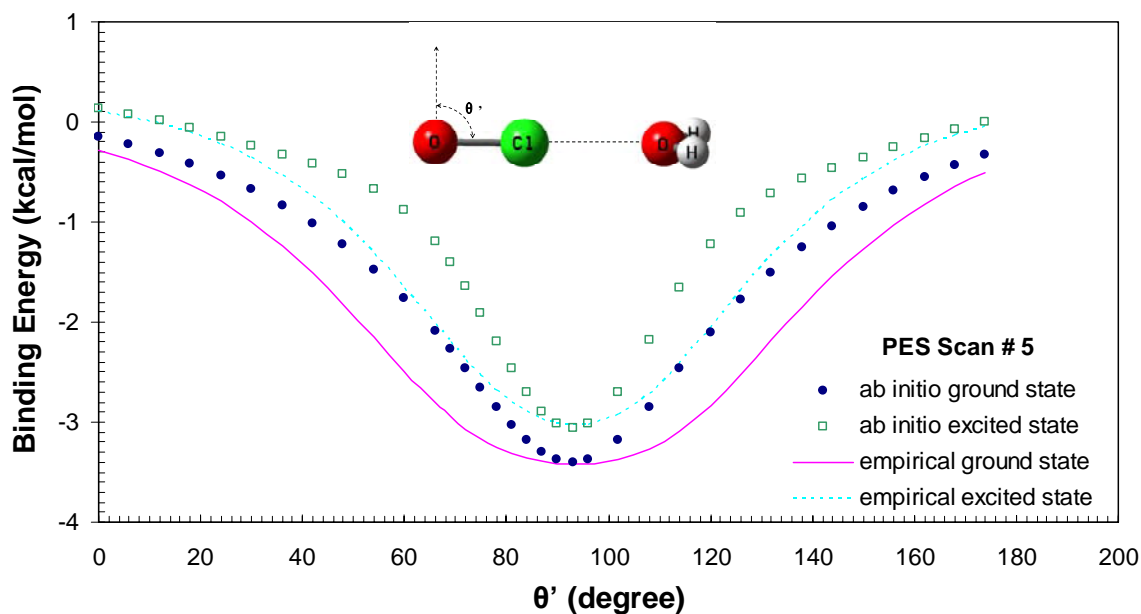
Fig 7. Potential Scan #5. Interaction energy vs θ' for the ground and excited states predicted by CCSD(T) calculations and mTTMC potential.
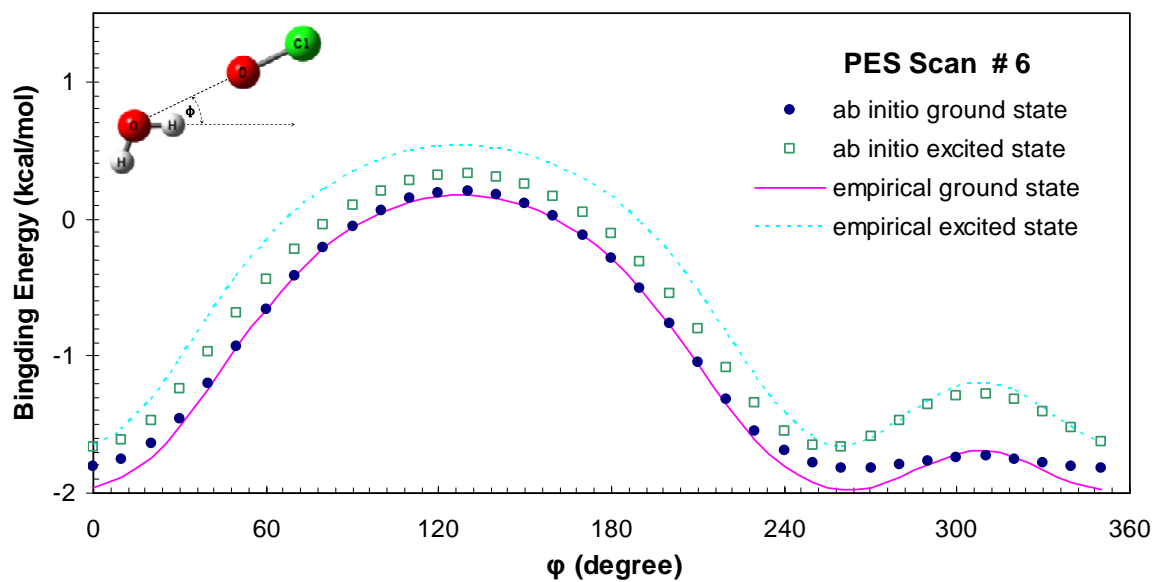
Fig 8. Potential Scan #6. Interaction energy vs φ for the ground and excited states predicted by CCSD(T) calculations and mTTMC potential.
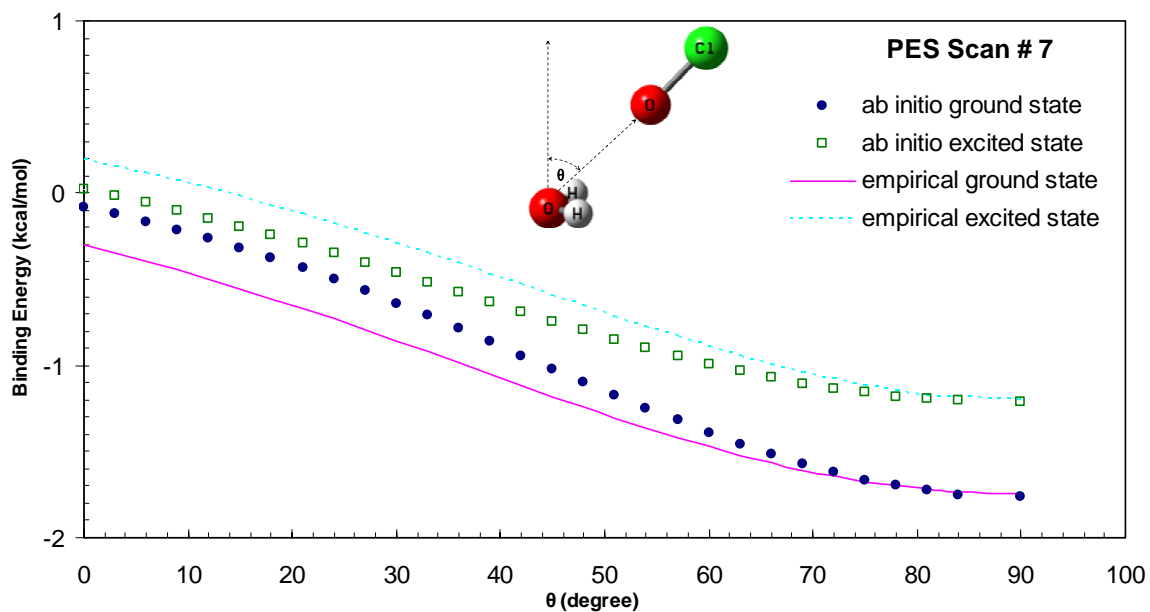
Fig 9. Potential Scan #7. Interaction energy vs θ for the ground and excited states predicted by CCSD(T) calculations and mTTMC potential.
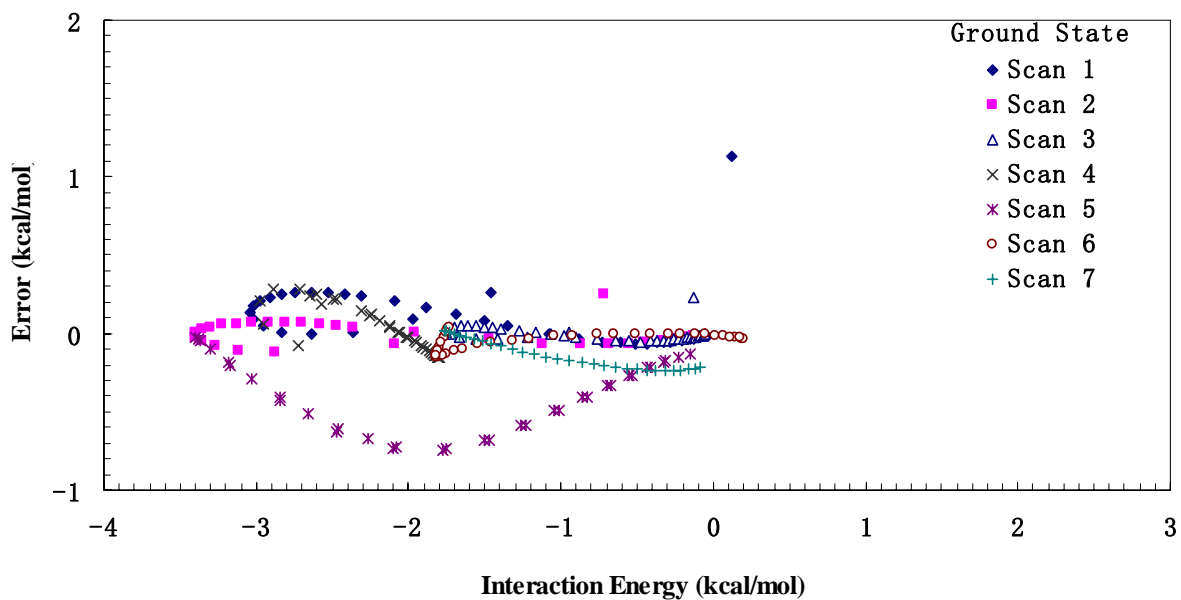
Fig 10. Errors in parameterized ground state potential as a function of the CCSD(T) energy for the PES scans.
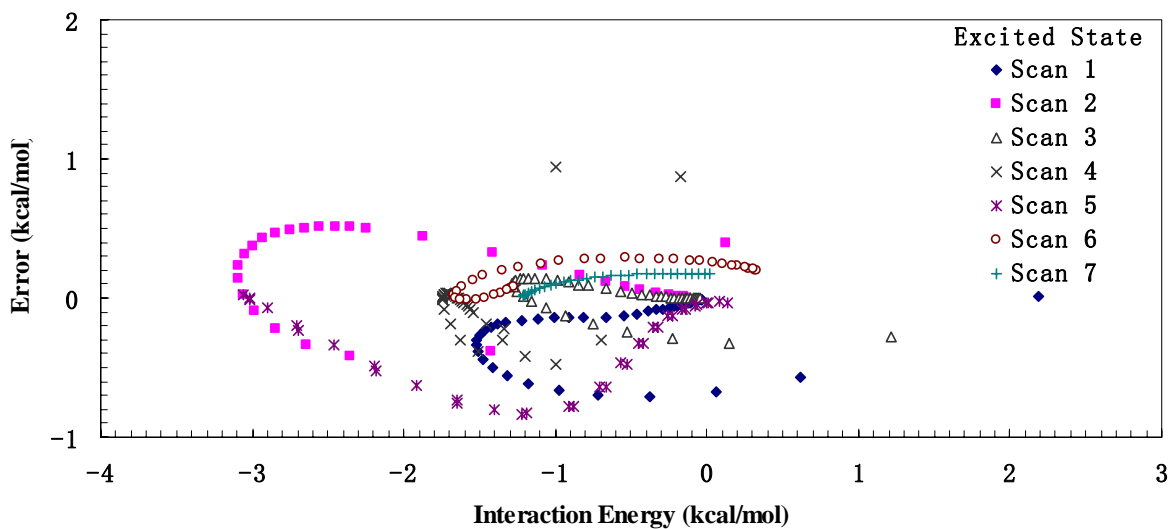
Fig 11. Errors in parameterized excited state potential as a function of the CCSD(T) energy for the PES scans.
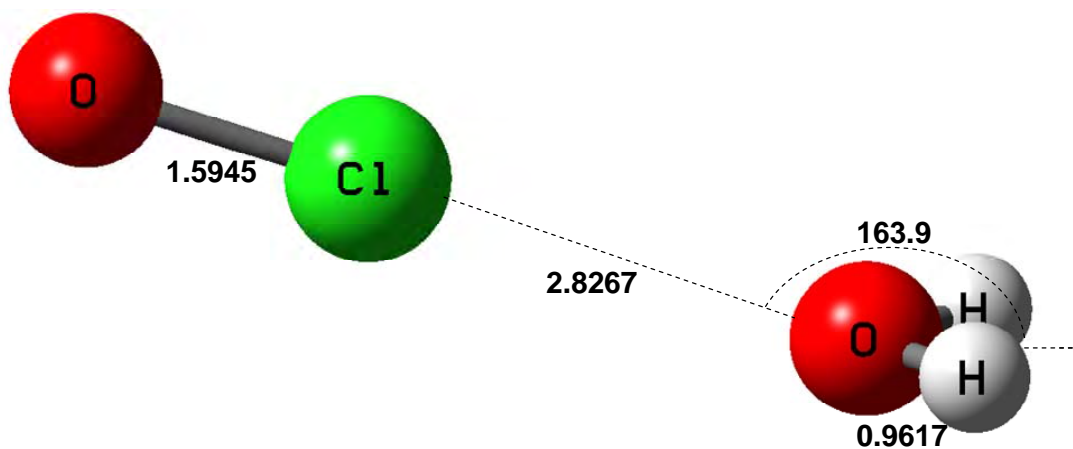
Fig 12. The geometry of the global minimum of H$_2$O·OCl predicted by the mTTMC empirical potential. Distances are in angstroms and angles are in degrees.
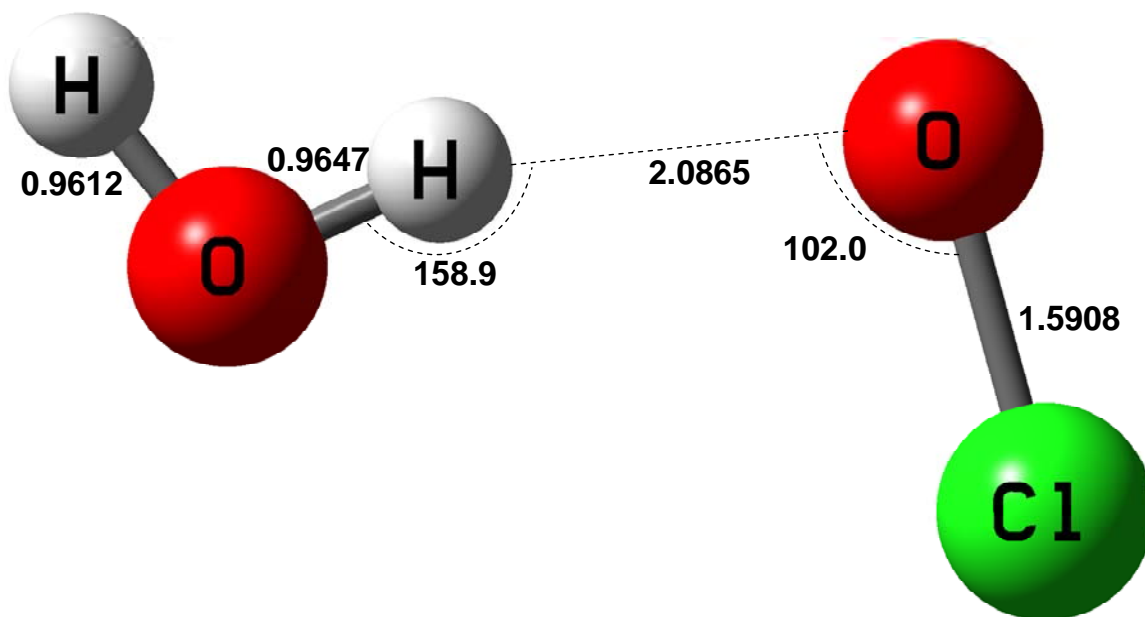
Fig 13. The geometry of the local minimum of H$_2$O·OCl predicted by the mTTMC empirical potential. Distances are in angstroms and angles are in degrees.

Study of the inflammatory responses of Single-Walled Carbon Nanotubes (SWCNTs) On Murine Macrophage Cells (RAW 264.7)

Debamitra Dutta and Prof. Brij Mougil

Materials Engineering

University of Florida

Gainesville, FL

and

Dr. SK Sundaram

Pacific Northwest National Laboratory

Richland, WA

1. Introduction

Carbon nanotubes (CNTs) have been shown to possess some unique mechanical, physical and chemical properties that show potential for electronics, optics and biomedical applications [1-3]. Among the two types of carbon nanotubes, single-walled carbon nanotubes (SWCNTs) and multi-walled carbon nanotubes (MWCNTs), SWCNTs have drawn a lot of attention due to strong Van der Waals forces and self organizing properties [4, 5] that can give rise to 'rope like structures'. SWCNTs generally have a diameter between 0.5-2 nm with varying lengths that can be many thousand times larger than the diameter. Due to its excellent conductivity, SWCNT have become the candidate materials for future electronic miniatures smaller than micro-electromechanical devices.

It is obvious that the use of carbon nanotubes in the future can have a terrific impact on our society in every sphere of life. But before we move ahead from the stage of possibilities and potentials, it is imperative that we understand the effect of these amazing objects created by accident on our cells, organelles and tissues. It is important for us to study the potential hazards of inhalation and all other effects of the nanotubes in the physiological environment. Research approaches in the past decade have developed covalent and non-covalent methodologies to functionalize the insoluble nanotubes to solve the major problems of solubility [6, 7]. Although this has led to enhanced biocompatibility, a still better understanding of the toxicological aspects is necessary to realize the long-term fate of the nanotubes inside the living body.

Existing literature data on biological activity and toxicity assessments of carbon nanotubes are ambiguous. On one hand, there are several reports stating that purified CNTs when functionalized appropriately [1, 8, 9] are completely non-toxic and can preserve the functionality of immune cells [10] and carbon nanotubes filled with DNA or peptide molecules can be utilized for molecular therapeutic applications [11-14]. These nanotubes have also been used to fabricate nanomotors for disease treatments. Cui et al have also shown that SWCNTs can induce the down-regulation expression of adhesion associated proteins and up-regulation of apoptosis related genes[15]. Various benefits and challenges associated with

the manufacture of biocompatible carbon nanotubes has been discussed [16-18] to give insights to potential biological applications [19-22].

On the other hand, several investigators have reported the adverse effects of CNT on keratinocyte cells [23-26], growth inhibition behavior in the neuron cells of an embryonic rat brain [27], and granuloma formation in the mouse lung [4, 28-30]. The method of synthesizing the SWCNTs has a profound effect on the biological properties. For example, the presence of catalyst elements in SWCNTs like iron [4, 9, 31, 32] can result in inducing toxicity. Also, the presence of organics is associated with oxidative stress and the generation of free radicals. So organics if present in appreciable quantities, can interact with enzymes in the lung resulting in oxidative stress [33] via the production of superoxides [34] and finally lead to release of proinflammatory cytokines [35].

2. Objective

In the present study, we have examined the *in vitro* inflammatory behavior of SWCNTs (at concentrations < 100 μg/ml and incubation period of 24 hours) in murine macrophage cells (RAW 264.7) by studying the iNOS and COX-2 activity using western blotting techniques. Commercially available SWCNTs, containing impurities like nickel and yttrium were dispersed in cell media and added to the cells to stimulate any inflammatory reactions.

In a second phase, the goal of the research work was to study the effects of sonicating the dispersion medium (cell media) and attribute a mechanism to explain the variations in inflammation behavior. Experiments were designed to highlight the differences in the cytotoxic behavior of SWCNTs in presence and absence of sonication.

3. Definitions

It is important for us to know and understand the meaning of some biological terminologies that are associated with the current research work. As my major of study, was a non-biological one, and I have been involved in interdisciplinary subjects at every step of my work, I had to look up the internet to have a better understanding of these terms and then design experiments according. So I felt it might benefit readers in a similar situation, if these terminologies are explained before we proceed.

Immunoblotting or what is more popularly known as ***Western Blot technique (WB)*** is a powerful tool for protein characterization. It detects a wide range of proteins in samples of tissues, homogenates or extracts using gel electrophoresis technique to separate the denatured proteins on the basis of mass. It makes use of specific primary (1°) and secondary (2°) antibodies to detect proteins (antigen) immobilized on a matrix. It is customary to precede the process of detection by transfer onto a membrane to make even the smallest amount of proteins easily detectable. Additionally, it is also easier to handle membranes as compared to the gels. During migration through the gel, the proteins are separated on the basis of size and charge. The proteins having a smaller size are characteristically able to migrate faster than larger proteins through the gel.

Next, a monoclonal or polyclonal antibody capable of recognizing the protein of interest is chosen and can be either directly labeled or itself probed with a 2° linked to a marker protein. For protein detection, the primary antibody is added at an appropriate dilution and incubated with the membrane. The specific antibody for a particular protein is directed towards the blotted protein and bind to it while other antibodies get washed away at the end of incubation. A secondary antibody - anti-immunoglobulin antibodies coupled to a reporter group is added to detect the bound antibodies which have bound. The excess secondary antibody is finally washed free of the membrane and a substrate is added that reacts with the conjugate and precipitates to give a visible band in the area where the primary antibody bound to the protein. We studied COX-2 and INOS protein expressions as stimulated by SWCNTs (any dose-dependent behavior) using western blot techniques and attempted to relate a potential biochemical mechanism to explain the observed activity in the cells.

Cyclooxygenase (COX) is an enzyme [36] in the metabolic pathway responsible for the formation of important biological mediators called prostanoids (including the prostaglandin, prostacyclin and thromboxane). There are two isoforms of COX, namely COX-1 and COX-2 [37]. COX-1 is a constitutive

housekeeping gene found abundantly in most mammalian cells whereas COX-2 is a cytokine inducible isoform occurring abundantly in stimulated macrophages and other sites of inflammation. An increase in COX-2 expression has been associated with diseases like rheumatoid arthritis, seizures, ischemia and colon cancer.

An early immune response by the macrophages towards any foreign materials is generally associated with the production of nitric oxide (NO). NO plays an important role in signaling [38, 39] to different organelles and also functions as a regulatory molecule to generate immune response. It is generated by a soluble enzyme, *inducible nitric oxide synthase (INOS)* following exposure to certain cytokines. Apart from the immune system, INOS is also found in the cardiovascular system. In the last decade, there has been a lot of data generated on INOS expression in chronic inflammatory diseases of the human airways, kidney, heart, skin and teeth. Although sometimes the INOS reactivity is associated locally to macrophage cells, but more commonly it is related to the epithelial cells around the foci of inflammation. Thus, it has been argued that INOS expression is a secondary phenomenon indicative of an inflammatory disease. This essentially serves as an excellent biomarker for immune responses *in vitro* as well as *in vivo* instead of measuring the relative expression levels of numerous other cytokines.

Receptors are proteins found on the surface of the cell membrane or occurring within the cell nucleus or cytoplasm. It binds to a specific molecule called ligands (e.g. hormones) and initiates a cellular response in the system. A group of such receptors having the function of recognizing negatively charged macromolecules , and participating in the removal of any waste molecules from the body are referred to as *scavenger receptors* [40]. It has been shown that macrophage cells expressing scavenger receptors on their plasma membrane is able to uptake the low density lipoproteins deposited in the inner and outer linings of blood vessels and attain a foamy structure. During the uptake process, they also secrete a lot of inflammatory cytokines that lead to the development of atherosclerosis. A *scavenger receptor antagonist (SRA)* binds to the receptor and works to inhibit its normal physiological functioning.

Macrophages, being antigen presenting cells in living systems, primarily guard against all foreign body materials. Whenever these macrophage cells encounter any alien material like particulate matter or pathogens etc, they get activated and immediately phagocytose the foreign material and extrude certain chemical mediators of inflammation. In case of environmental particles [41], alveolar macrophages and the epithelial cells in the airway get stimulated to inhale the particles and trigger the release of reactive oxygen species. The *RAW 264.7 murine macrophage cell line*, an appropriate model in studying the macrophage signaling behavior was used in this research.

A *dose-response curve* is plotted for a system to express the correlative relationship between the exposure-characteristics and the spectrum of effects on the system due to the exposure. It is the most basic and integral concept in the science of toxicology. The shape of the dose-response curve has many implications in toxicity assessments of a system.

Glyceraldegyde 3-phsphate dehydrogenase (GAPDH) is an important enzyme used in glycolysis. Levels of GAPDH in the western blot experiment represent an internal control for the COX-2 and INOS bands.

Potentially toxic, natural compounds found inside pathogens like bacteria are known as *endotoxins.* Generally, the biological activity of endotoxin can be related to the *lipopolysaccharide (LPS).* The lipid component imparts toxicity while the polysaccharide components contribute towards immunogenicity.

4. Materials and Methods

4.1 Materials
The SWCNTs used for this study were purchased from Sigma-Aldrich Co. (Prod. No.519308). Bacterial LPS was purchased from Sigma Chemical (St Louis, MO). RPMI 1640, sodium pyruvate, FBS, L-glutamine, peniclillin and streptomycin were purchased from Invitrogen (Carlsbad, CA). All other chemicals used were purchased of cell-culture grade and better.

4.2 SEM-EDS Analysis

Non-functionalized as-received SWCNTs were studied on a scanning electron microscope in energy dispersive spectrometry (EDS) mode to detect the compositional elements present along with the nanotubes. Aluminum stubs were smeared with silver paint, the nanotubes placed on the stubs and attached to copper tapes to make them conductive. The metallic stubs were then placed on the holder and introduced into the instrument at a vacuum of 10 kV.

4.3 TEM Imaging

Transmission Electron Microscopy (TEM) was used for the size measurement of SWCNTs. The images were taken on a Hitachi H-7000 microscope (Japan). TEM samples were prepared by placing a drop of SWCNTs solution (in denatured ethanol) directly onto a carbon-coated copper grid (200 mesh) and imaging was done at 10kv.

4.4 Cell Culture

The cell line (American Type Culture Collection, Manassas, VA) used for this study was RAW 264.7 (murine macrophage cells). The cells were grown in RPMI 1640 supplemented with 10% fetal bovine serum, 2mM glutamine, 1mM sodium pyruvate and 100 U/ml penicillin and 0.1 mg/ml streptomycin in a humidified air containing 5% CO_2, 95% air at 37 ^{o}C. Cells were cultured in cell culture dishes (60 cm diameter) (Fisher Scientific) and passaged using a cell scraper upon reaching 60-70% confluency. The cell culture medium was exchanged once in two days.

For exposure to SWCNTs, cells were seeded into smaller cell culture dishes (30 cm diameter) at a seeding density of $4.2x10^5$ cells per dish in a final volume of 3 ml, 24 hrs prior to addition of nanoparticles and incubated in humidified air containing 5% CO_2, 95% air at 37 ^{o}C. Prior to use on the next day, the culture medium was replaced with fresh media containing the added nanoparticles at the predefined concentrations. After incubation, the cells were washed 3 times with sterile PBS to remove all non-associated nanoparticles from the cellular environment.

Two stock solutions of SWCNTs (at 1 mg/ml) were prepared in sterile cell-media and sterile PL-127 (emulsifying agent) respectively. Pre-determined concentrations of the experimental SWCNT solutions at 25 to 100 μg/ml solution were prepared from the stock solution (either prepared normally or by serialized dilution method) using cell culture media, either sonicated or non-sonicated depending on the experimental sample. For sonicated samples, the cell culture media used for dilution was put into the ultra-sonication bath for a period of 15 minutes. An equal quantity of cell culture media (without any sample) sonicated for 15 minutes was treated as a control. All solutions (SWCNTs and controls) were vortexed well for one minute for better dispersion.

4.5 Dose-Response Curves

In order to generate a dose-response curve for the SWCNTs, macrophage cells were plated at the above-mentioned seeding density to a final volume of 3 ml per cell culture dish and incubated with SWCNTs at predetermined doses (at 25 to 100 μg/ml) for 24 hours.

Upon removal, the dishes were washed 3 times with ice-cold PBS. After the final wash, 1 ml of sterile PBS was added and the cells were scraped carefully to remove all live cells. The cell-suspension (~ 1ml in volume) was placed in centrifuge tubes. The number of live cells in each tube was then counted using a Coulter Cell Counter,   utilizing dynamic light scattering principles.

A dose-response curve was generated by plotting the concentration of nanoparticles added, in the abscissa and the number of live cells counted, on the ordinate. The concentration range at the central portion of the dose response curve was selected to dose the macrophage cells in Western blot experiments.

4.6 Western blot (WB) Analysis

Raw 264.7 cells were plated and exposed to SWCNTs in cell-media and PL-127 (sonicated and non-sonicated) for 24 hours in the incubator similar to the experiments mentioned in the previous section (generation of dose-response curves). Upon removal, the dishes were washed with ice-cold sterile PBS and stored in the freezer at -80°C for future processing. In due course of time, the cells were taken out and placed on a box of ice and 150 μl ice-cold lysis buffer was added. The cells were then immediately scraped using a cell scraper and transferred to a homogenization assay and homogenized. 0.5 μl spermine was added to the lysate (to prevent the formation of a viscous clump), transferred into an eppendorf vial and centrifuged at 4°

C, 18000 G (rcf*) for 5 minutes. After centrifugation, the supernatant was taken out very carefully and placed into freshly labeled eppendorf vials for the Protein Assay.

4.6.1 Protein Assay

The supernatant of the cell lysates prepared above were assayed for total protein content using the BSA protein assay at 582 nm in a multi-plate spectrophotometer against a BSA standard curve. Calculations were done to find the final concentration and quantity of sample that has to be loaded for gel-electrophoresis. The samples were then prepared using relevant amounts of 4X and 1X loading buffers and stored at room temperature for 1-d gel Electrophoresis.

4.6.2 1-d gel Electrophoresis

The different parts of a box for 1-d gel Electrophoresis are made to fit correctly and two 10 ml SDS acrylamide gels (10 wells with 1.5 mm spacer) are taken out from the refrigerator. The cover is removed carefully along with the comb. The gels are then placed in the correct position inside the box. A buffer solution is prepared beforehand by adding 25 ml a 20 X buffer (NU PAGE MES SDS Running Buffer - 20X) to 475 ml DI water. It is stirred for homogenizing the solution and poured into the inside chamber and made sure that the level comes to the very top. 50 µl or some pre-decided quantities of the samples prepared above are loaded into each well. The See blue Plus 2 standard is loaded at the extreme left and the samples are placed to the right. The gel is then run on POWER PAC 300 till all bands are seen at the bottom.

While the gel is running, sufficient quantity of the transfer buffer is poured in 3 dishes to immerse the gel later. Once the gel is formed the POWER PAC 300 is put off and the buffer is emptied into the sink. The white box is unlocked and the rivets are broken using a scalpel. The side where the gel sticks at the bottom is placed below and the tip of the well and the portion where tape was removed is cut-off. The gel is submerged into the dish with transfer buffer and equilibrated for 10 – 15 minutes.

4.6.3 Preparing the membrane

A nitrocellulose membrane (to drive the protein bands onto) is taken along with a pair of white PVDF filter papers. Some methanol is taken in a square plastic dish, into which the membrane is placed (using forceps) for a few seconds to make it hydrophobic. In the mean time, the WB membrane is placed into some transfer buffer, taken in a large plastic dish. The membrane is taken out of the methanol and placed onto the filter paper. The gel is then placed on it and sandwiched using the other filter paper and the whole set up is placed on the POWER/PAC 1000 machine for transfer, which generally takes between 60 -70 minutes.

4.6.4 Blocking Buffer Using Carnation Milk

The membrane is removed and washed in PBST solution twice with intermittent rocking for 5 minutes. The gel is then left to soak in a blocking buffer (5% Carnation milk in PBS Tween Solution) prepared beforehand for one hour. After one hour, the gel is again washed three times using PBST and buffer equilibration and left for overnight rocking inside the cold storage.

4.6.5 Conjugation of Primary (1°) and Secondary (2°) Antibodies

The sample is taken out and all expient liquid is aspirated out. 8 ml western blot buffer solution (50 ml 10X Tris Buffer Saline Solution + 450 ml water + 10 g (2%) BSA + 100 mg thimorosol (antibacterial) + 5 ml (10%) Tween 20 (detergent and wetting agent)) is then added to the samples. The pre-selected 1° antibody is added at the necessary dilutions and the sample is left to rock at slow speeds for an hour for continuous mixing, after which the membrane is washed using PBST for three times with intermittent rocking of 5 minutes each. The 2° antibody (at correct dilution) is similarly added followed by four PBST solution washes. The detection agent (using West Pico Chemiluminescent solution) is prepared beforehand and the membrane is read on the Chemiluminescent instrument.

4.7 Fluorescent Microscopic Imaging

Cells were imaged using fluorescence microscopy to study the effect of scavenger receptor antagonists on the macrophage-uptake of SWCNTs. A thin monolayer of cells were plated in 4-well chamber slides (at approx. 3×10^3 cells per well) to a final volume of 500 µl cell media. Prior to nanoparticle addition, the cell media was exchanged with serum free media and the cells were then exposed to alexafluor tagged SWCNTs at predetermined doses for 15 minutes. Upon removal, the dishes were washed with ice-cold PBS, fixed using glutaldehyde and watched using a fluorescent microscope at 647 nm.

5. Experiments Performed

Samples and the number of live cells counted on the Coulter Cell Counter for each sample in the dose-response curve experiments and details of samples used for the western blot experiments performed is given below.

5.1 Dose-Response Curves

As mentioned before, dose-responses curves were generated to study the effect of SWCNTs on murine macrophage cells. A representative curve for the dose-response curves generated has been shown in **Figure 4**. *[Note: Dose-response curves for each Experiment have been recorded in the Laboratory Notebook at PNNL and a soft copy is available with Dr Thomas Weber at 331 Building, PNNL, Richland].*

In order to generate a dose-response curve for cells incubated with cell media containing SWCNTs, an experiment (**dose-response experiment I**) was designed with particle concentrations from 12.5 to 100 μg/ml. As observed (**Figure 4)** there was a remarkable decrease in number of living cells with a decrease in particle concentration from 25 μg/ml to 12.5   μg/ml. The next experiment (**dose-response experiment II**) was designed with particle concentrations varying between 12.5 to 25 μg/ml (12.5, 15, 20 and 25 μg/ml) to magnify any observed effects on the cell viability. Results (**Table 2**) indicated a slow decrease in cell growth with increasing particle concentration. The experiment was repeated for reproducibility (**dose-response experiment III**).

At this point, we realized the practical problem of not being able to re-use any leftover SWCNTs dispersed in the cell media for the subsequent experiment. It is known that cell media contains an enormous quantity of proteins which have a finite lifetime. Even cell media stored in the refrigerator at -25 ^{0}C is not recommendable for use after a period of one week. In order to reduce the wastage of the SWCNTs, we decided to use PL-127 an emulsifying agent as the dispersion medium. Previous investigators have reported the advantages of the use of pluronic (1% **Pluronic** F108) to stabilize and disperse single-walled nanotubes in toxicity studies [10].

In order to study any toxic effect of the emulsifier (pluronic PL-127) on the RAW 267.4 macrophage cells. So in the following experiment (**dose- response experiment IV**), we incubated the macrophage cells with sonicated and non-sonicated pluronic at emulsifier concentrations ranging from 0.25 to 1 %.

We concluded that there was no substantial toxic effect of the pluronic in the cells up to a pluronic concentration of 1%. The nanotubes were observed to be more stable and better dispersed in 1% PL-127 as compared to the use of cell media as the dispersion medium. A stock solution of 1 mg/ml of nanotubes in the emulsifier (1%) was prepared and stored in the refrigerator for an indefinite period of time. In subsequent experiments, pre-determined concentrations of nanotubes were prepared from the stock solution using cell-media as the diluent. Depending on the description of the sample desired, the diluent (cell-media) was sonicated (for SCM – sonicated cell media samples) for a period of 15 minutes on the ultra-sonication bath or not (for NSCM - non-sonicated cell-media samples).

In **dose- response experiment V**, toxicity tests to study the differences in effect of SWCNTs in PL-127 and cell media (sonicated and non-sonicated) were conducted. The effect of sonicating the cell media is observed in **Table 5.** In general, the number of cells counted in dishes containing samples in sonicated cell media was visibly higher than in non-sonicated cell media.

5.1.1 Experiments with SWCNTs
5.1.1.1 Dose-Response Experiment I

Table 1: Experimental results of dose-response experiment I

	Sample Details	No. of live cells	Avg. # live cells	SWCNTs Conc
1	Naïve Control	35751 35012	34884	-
2	Sonicated Media	33888 29644 27935	31074	-
3	12.5 µg/ml SWCNT	35642 42580 39581	33452	12.5 µg/ml
4	25 µg/ml SWCNT	18196 13727 10724	11562	25 µg/ml
5	50 µg/ml SWCNT	10234 12140 11394	10877	50 µg/ml
6	75 µg/ml SWCNT	9097 8875 19311	12059	75 µg/ml
7	100 µg/ml SWCNT	7992 11786 11338	11562	100 µg/ml

5.1.1.2 Dose-Response Experiment II
Table 2: Experimental results of dose-response experiment II

Sl No	Sample Details	No. of live cells (Reading 1)	No. of live cells (Reading 2)	Avg. # live cells	SWCNT Conc
1	Sonicated Media	23138 27387 24116	23104 26707 23990	24740	-
2	12.5 µg/ml SWCNT	21506 22621 21726	21876 22257 21691	21946	12.5 µg/ml
3	15 µg/ml SWCNT	20289 21594 21893	20349 21785 21854	21294	15 µg/ml
4	20 µg/ml SWCNT	18547 20771 21279	18596 20501 21661	20226	20 µg/ml
5	25 µg/ml SWCNT	20457 21463 16993	20271 20042 16849	19346	25 µg/ml

5.1.1.3 Dose-Response Experiment III

Table 3: Experimental results of dose-response experiment III

Sl No	Sample Details	# of live cells	Avg. # live cells	SWCNTs Concentration
1	Naïve Control (NSCM)	15086 19127 20636	18283	-
2	12.5 µg/ml SWCNT in NSCM	17093 16611 16120	16608	12.5 µg/ml
3	25 µg/ml SWCNT in NSCM	16168 14864 16645	15892	25 µg/ml
4	50 µg/ml SWCNT in NSCM	14808 15846 15156	15270	50 µg/ml

5.1.2 Experiments with PL-127

5.1.2.1 Dose-Response Experiment IV

Table 4: Experimental results of dose-response experiment IV

Sl No	Sample Details	# live cells Reading 1	# live cells Reading 2	Avg. # live cells	Concentration PL-127
1	Naïve Control	678 543 643	662 539 648	619	-
2	0.25 % PL-127 NSCM	966 764 504	832 781 513	727	0.25 %
3	0.5 % PL-127 NSCM	770 812 807	794 772 854	802	0.5 %
4	0.75 % PL-127 NSCM	587 733 826	581 767 765	710	0.75 %
5	1.0 % PL-127 NSCM	694 847 734	652 853 700	747	1.0 %
6	0.25 % PL-127 SCM	523 557 530	524 589 493	536	0.25 %
7	0.5 % PL-127 SCM	575 582 763	626 566 756	645	0.5 %
8	0.75 % PL-127 SCM	664 656 757	696 635 695	684	0.75 %
9	1.0 % PL-127 SCM	737 609 558	715 627 538	631	1.0 %

5.1.2.2 Dose-Response Experiment V

Table 5: Experimental results of dose-response experiment V

Sl No	Sample Details	# live cells Reading 1	# live cells Reading 2	Avg. # live cells	SWCNTs Concentration
1	Naïve Control	38964 69404 33891	39874 69662 34266	36749	-
2	PL-127 NSCM	14039 55358 41929	13882 56455 36746	47622	-
3	25 µg/ml SWCNT in PL-127 in SCM	31005 30709 32114	29558 30319 31836	30924	25 µg/ml
4	50 µg/ml SWCNT in PL-127 in SCM	14370 14375 15950	14398 14372 15783	14875	50 µg/ml
5	100 µg/ml SWCNT in PL-127 in SCM	25920 16155 19396	25710 15862 19512	20426	100 µg/ml
6	PL-127 sonicated	12115 9901 10569	12255 15862 19512	10801	
7	SCM	42028 24823 21216	41806 25151 20736	22982	
8	25 µg/ml SWCNT in SCM	13563 32230 12447	13500 32187 12405	12979	25 µg/ml
9	50 µg/ml SWCNT in SCM	14062 29786 38846	14798 29731 38727	34273	50 µg/ml
10	100 µg/ml SWCNT in SCM	12849 13463 10573	13103 13399 10673	12343	100 µg/ml

Use of sonication techniques was clearly having a negative effect on the toxicity studies of the system. In order to understand the effect of the contribution and understand the mechanism of action, further experiments with similar samples were conducted for western blot experiments.

5.2 Western Blot Experiments

Seven WB experiments (three different types) were conducted using SWCNT in PL-127 and two experiments were conducted using Scavenger receptor antagonists (Fucoidan and Polyinosinic Acid) to understand the mechanism of inflammation of SWCNT in the RAW 264.7 cells.

Details of all samples prepared for each western blot Experiment (using SWCNTs and SRA) is given in complete details below. Each western blot experiment was designed to get a better understanding of the activity of SWCNTs in the macrophage cells and its mechanism of action. Initially, a set of experiments, (enlisted below as ***Western Blot Experiment 5.2.1.1***) was performed to study any difference in inflammatory

behavior of SWCNTs in sonicated cell media as compared to the use of PL-127 as a dispersing media. The experiment was repeated nine times for reproducibility in results and we noticed the same trends in the protein up-regulation activity.

Thereafter, further experiments were designed to get a better understanding on the mechanism of action.

5.2.1 Experiments with SWCNTs

5.2.1.1 Type I (WB Experiment 2A, 3A, 6A, 6B, 6C)
Table 6: Details of samples for incubating macrophage cells for western blot experiments with SWCNTs Type I *(2A, 3A, 6A, 6B, 6C)*

Sl No.	Sample Details	RPMI 1640 (NSCM/ SCM)	LPS	PL-127	SWCNTs~10 mg/ml
1	Control (only cells)	3 ml NSCM			
2	1 % PL-127 (sonicated)	"		30 μl	
3	SCM	3 ml SCM			
4	1 ng/ml LPS	3 ml NSCM	3 μl		
5	1 ng/ml LPS + SCM	3 ml SCM	3 μl		
6	LPS + SWCNT in PL127	3 ml NSCM	3 μl		50 μl in PL-127
7	LPS+ SWCNT in SCM	3 ml SCM	3 μl		50 μl in SCM
8	SWCNT in PL-127	3 ml NSCM			50 μl in PL-127
9	SWCNT in SCM	3 ml SCM			50 μl in SCM

5.2.1.2 Type II (WB Experiment 4B)
Table 7: Details of samples in western blot experiment with SWCNTs/SRA Type II

Sl No	Sample Details	RPMI 1640 (NSCM/ SCM)	LPS	PL-127	Fucoidan Stock ~1mg/ml	SWCNTs Stock ~10mg/ml
1	Control (only cells)	3 ml NSCM				
2	1 % PL-127 (sonicated)	3 ml SCM		30 μl		
3	1 ng/ml LPS	3 ml NSCM	3 μl			
4	LPS + 50 μg/ml SWCNT	"	3 μl			50 μl
5	LPS + 25 μg/ml Fucoidan	"	3 μl		15 μl	
6	LPS + 25 μg/ml Fucoidan + 50 μg/ml SWCNT	"	3 μl		15 μl	50 μl
7	25 μg/ml Fucoidan + 50 μg/ml SWCNT	"			15 μl	50 μl
8	50 μg/ml SWCNT	"				50 μl

5.2.1.3 Type III (WB Experiment 7)

Table 8: Details of samples in western blot experiment with SWCNTs/SRA Type III

Sl No	Sample Details	RPMI 1640 (NSCM/ SCM)	LPS ~	Fucoidan Stock ~1mg/ml	SWCNTs Stock ~10mg/ml
1	Control (only cells)	3 ml NSCM			
2	1 ng/ml LPS	"	3 µl		
3	12.5 µg/ml Fucoidan	"		7.5 µl	
4	LPS + 12.5 µg/ml Fucoidan	"	"	7.5 µl	
5	50 µg/ml SWCNT in SCM	3 ml SCM			50 µl in PL-127
6	LPS + 50 µg/ml SWCNT in SCM	"	"		50 µl in SCM
7	LPS + 50 µg/ml SWCNT in SCM + 12.5 µg/ml Fucoidan	"	"	7.5 µl	50 µl in PL-127

5.2.2 Experiments with Scavenger Receptor Antagonists
5.2.2.1 Type I (WB Experiment 3B)

Table 9: Details of samples in western blot experiment with SRA Type I

Sample No.	Sample Details	RPMI 1640 (NSCM/ SCM)	LPS	PU Acid Stock ~1mg/ml	Fucoidan Stock ~1mg/ml
1	Control (only cells)	3 ml NSCM			
2	1 ng/ml LPS	"	3 µl		
3	LPS + 50 µg/ml Fucoidan	"	3 µl		30 µl
4	LPS + 50 µg/ml PU Acid	"	3 µl	30 µl	
5	50 µg/ml PU Acid	"		30 µl	
6	50 µg/ml Fucoidan	"			30 µl

5.2.2.2 Type II (WB Experiment 4A)
Table 10: Details of samples in western blot experiment with SRA Type II

Sample No.	Sample Details	RPMI 1640 (NSCM/ SCM)	LPS	Fucoidan Stock ~1mg/ml
1	Control (only cells)	3 ml NSCM		
2	1 ng/ml LPS	"		
3	50 µg/ml Fucoidan	"		30 µl
4	25 µg/ml Fucoidan	"		15 µl
5	12.5 µg/ml Fucoidan	"		7.5 µl
6	LPS + 50 µg/ml Fucoidan	"	3 µl	30 µl
7	LPS + 25 µg/ml Fucoidan	"	3 µl	15 µl
8	LPS + 12.5 µg/ml Fucoidan		3 µl	7.5 µl

To confirm the role of scavenger receptors in uptake process, experiments *(Experiment 5.2.1.2)* using SWCNTs in presence of SRAs (fucoidan and polyinosinic acid) were conducted to determine a more effective SRA (*Experiment 5.2.2.1)* and an optimum concentration of fucoidan (effective SRA) for complete inhibition activity. Finally, the COX-2 and INOS activity of SWCNTs in the presence of SRAs (fucoidan) on the cells were studied (*Experiment 5.2.1.2 and 5.2.1.3)*. Presence of antagonists successfully negated all antagonist effects of LPS mediated inflammatory responses for inflammatory responses (**Figure 12).**

6.1 Materials Analysis
Table 11: Composition of the SWCNTs as procured from Sigma-Aldrich observed on SEM-EDS at 10 kV potential.

Weight % by Element					
Element	C K	O K	Si K	Y L	Ni K
Wt % by element	77.65	2.04	0.12	2.9	17.29
Atomic % by Element					
Element	C K	O K	SiK	Y L	NiK
Atomic % by element	93.37	1.85	0.06	0.47	4.25

Figure 1: Spectroscopic analysis for composition of SWCNTs on SEM – EDS.
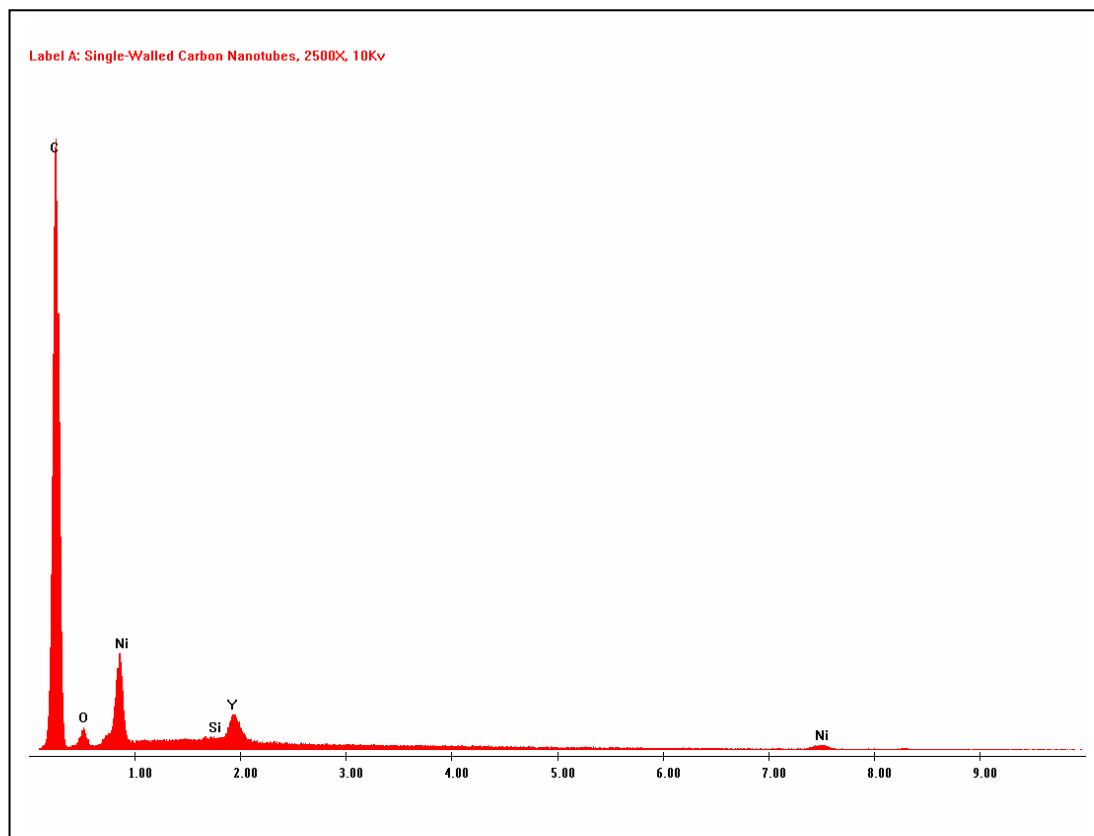
Table 12: Composition of white spots on SWCNTs structure observed on SEM EDS (10 kV potential).

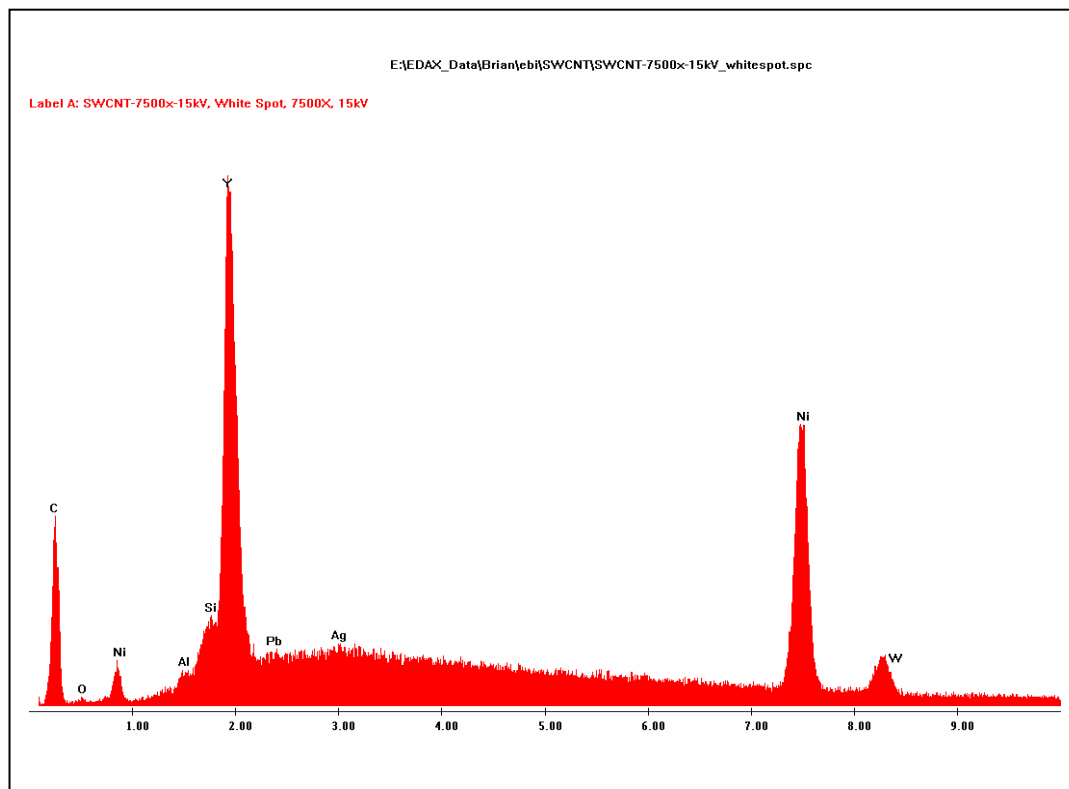| Weight % by Element					
Element	**C K**	**O K**	**Si K**	**Y L**	**Ni K**
Wt % by element	30.85	0.25	0.51	17.19	43.47
Atomic % by Element					
Element	**C K**	**O K**	**Si K**	**Y L**	**Ni K**
Atomic % by element	71.89	0.43	0.51	5.41	20.72

Figure 2: Spectroscopic analysis for composition of white spots of SWCNTs on SEM – EDS.
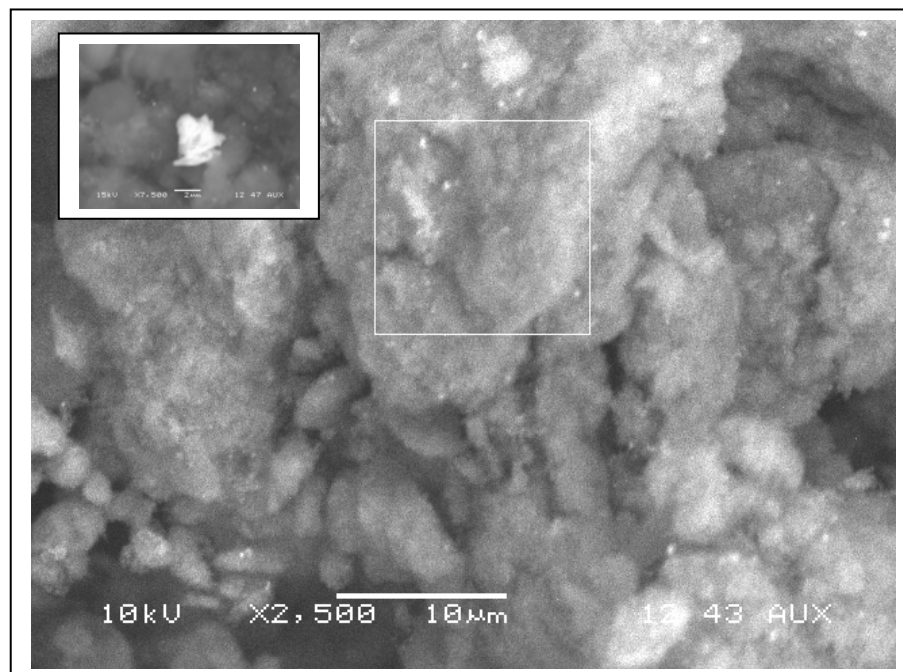
Figure 3: SEM image for SWCNTs and (inset)white spots observed on the structure of SWCNTs

6.2 Dose- response Curve
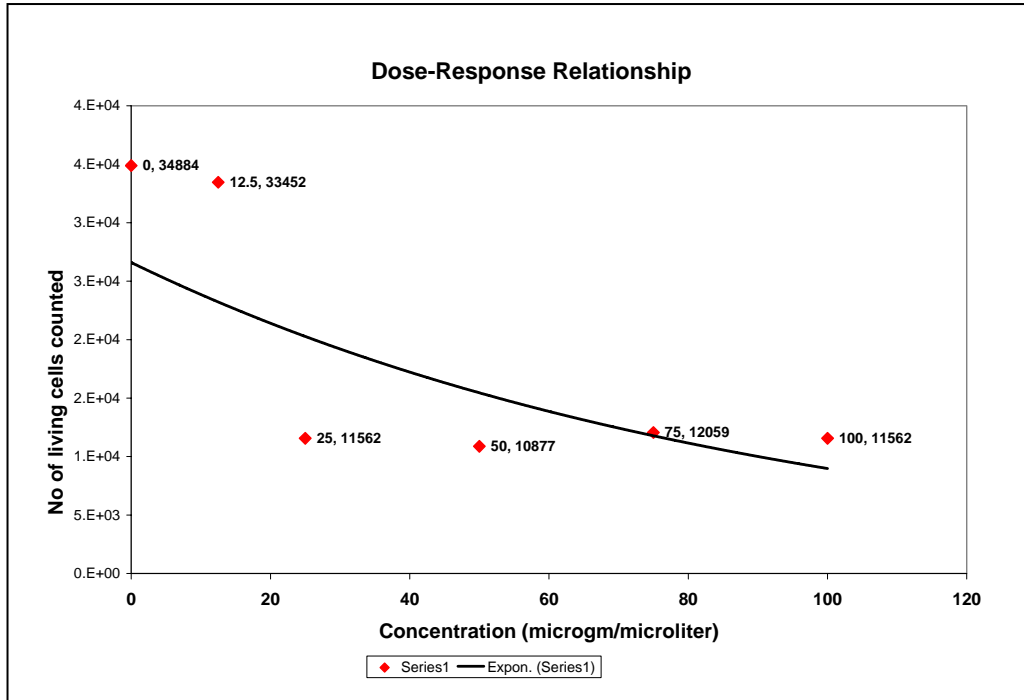
Figure 4: Representative Dose-Response Curve from Experiment 1

6.3 Western Blot Analysis
6.3.1 Histograms for western blot analysis

Figure 5: Histogram representing the iNOS activity of SWCNTs in Exp 5.2.1.1

Figure 6: Histogram representing the COX-2 activity of SWCNTs in Exp 5.2.1.1
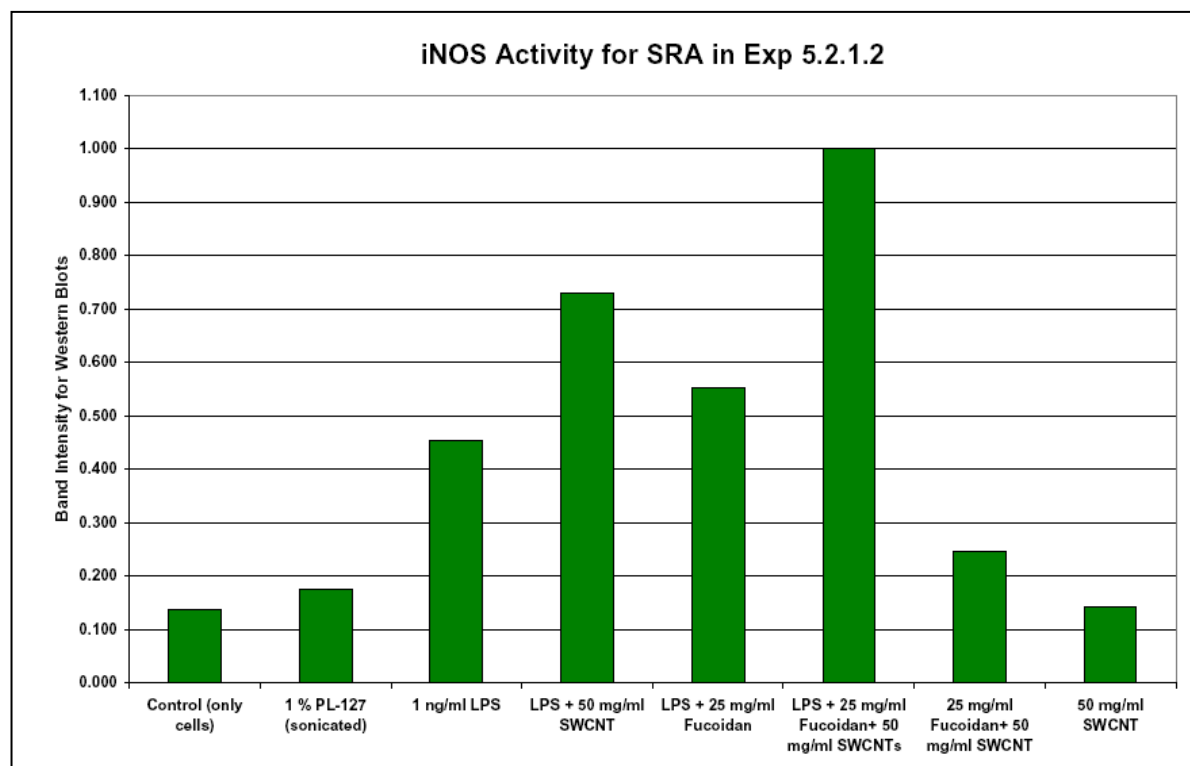
Figure 7: Histogram representing the iNOS activity of SWCNTs in Exp 5.2.1.2
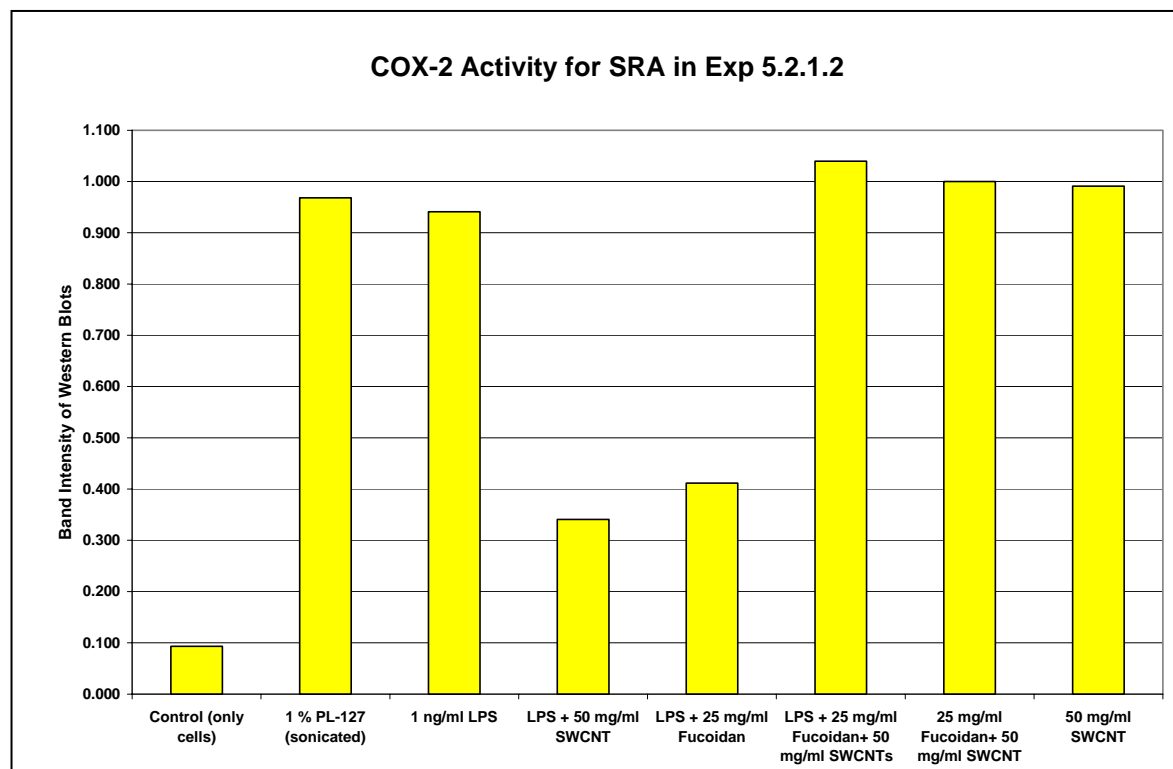
Figure 8: Histogram representing the COX-2 activity of SWCNTs in Exp 5.2.1.2
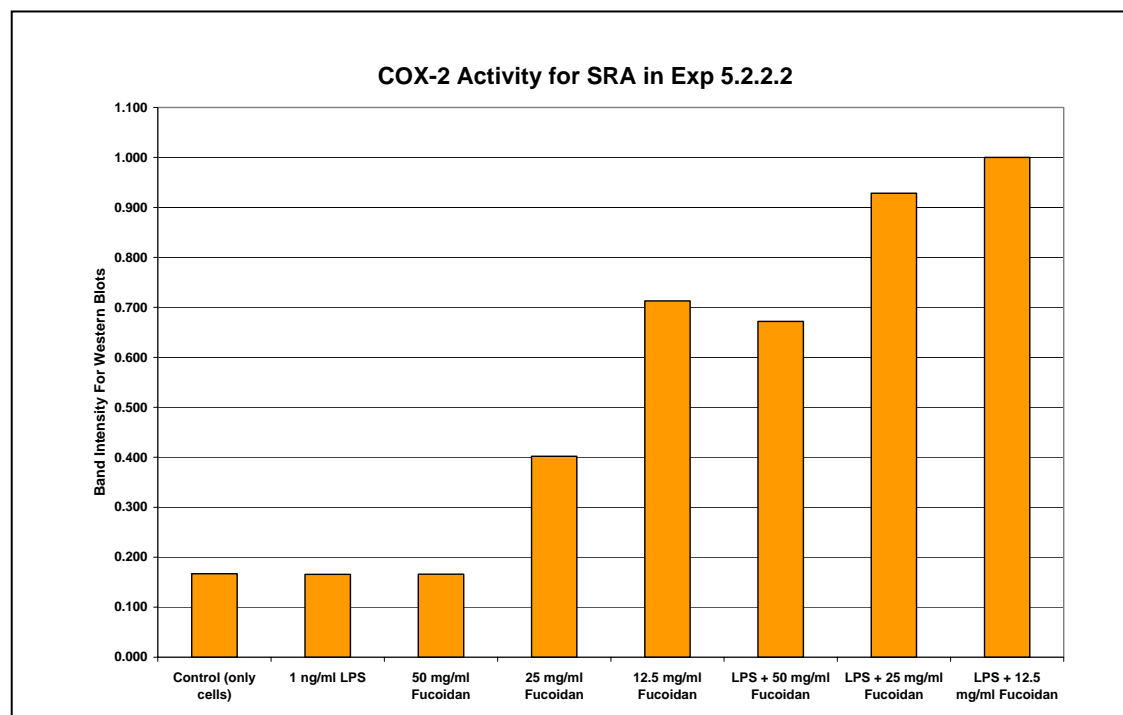
Figre 9: Histogram representing the iNOS activity of SRAs in Exp 5.2.2.2
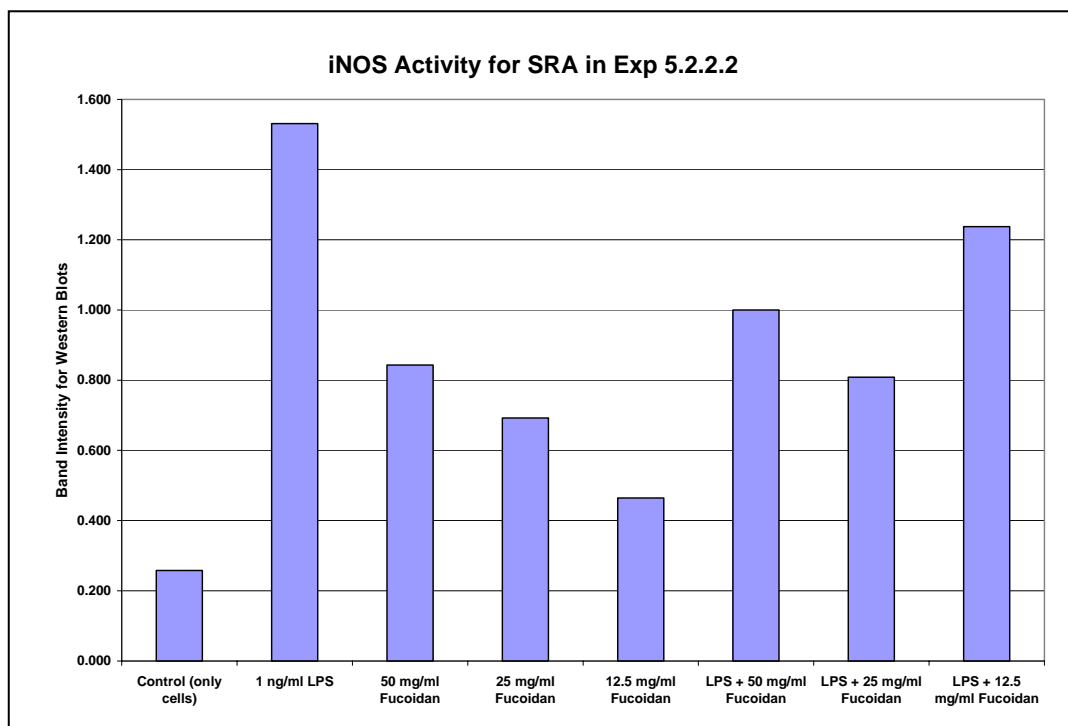
Figure 10: Histogram representing the COX-2 activity of SRAs in Exp 5.2.2.2

6.3.2 Bands for western blot analysis

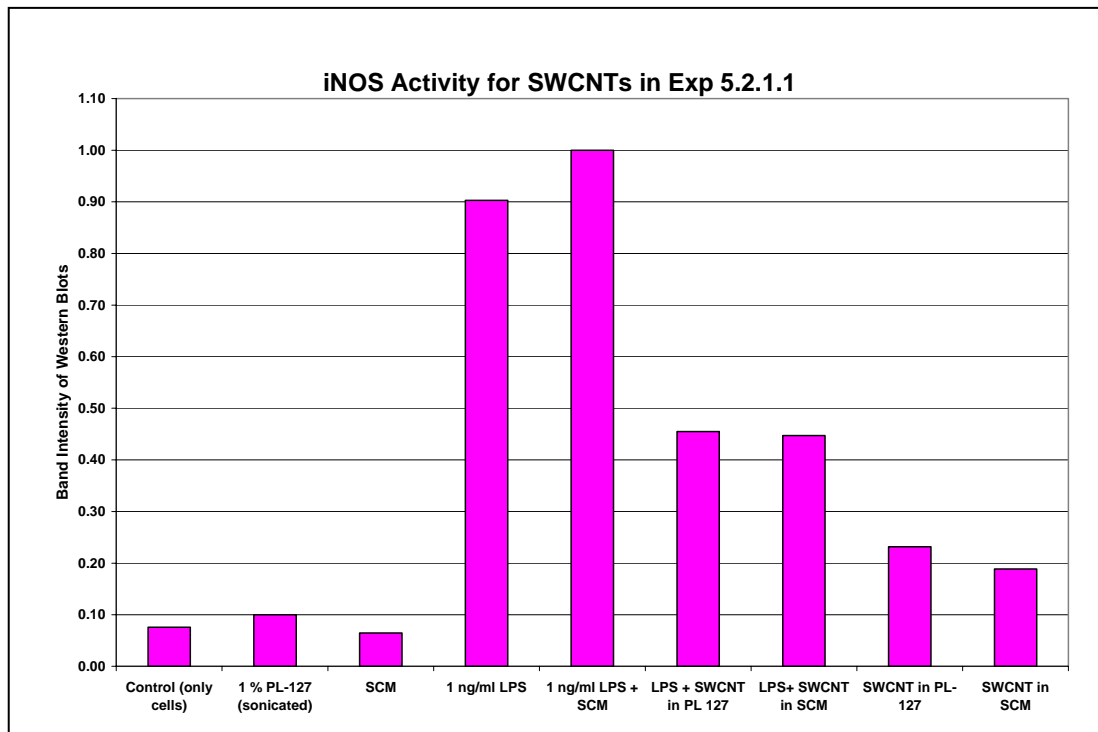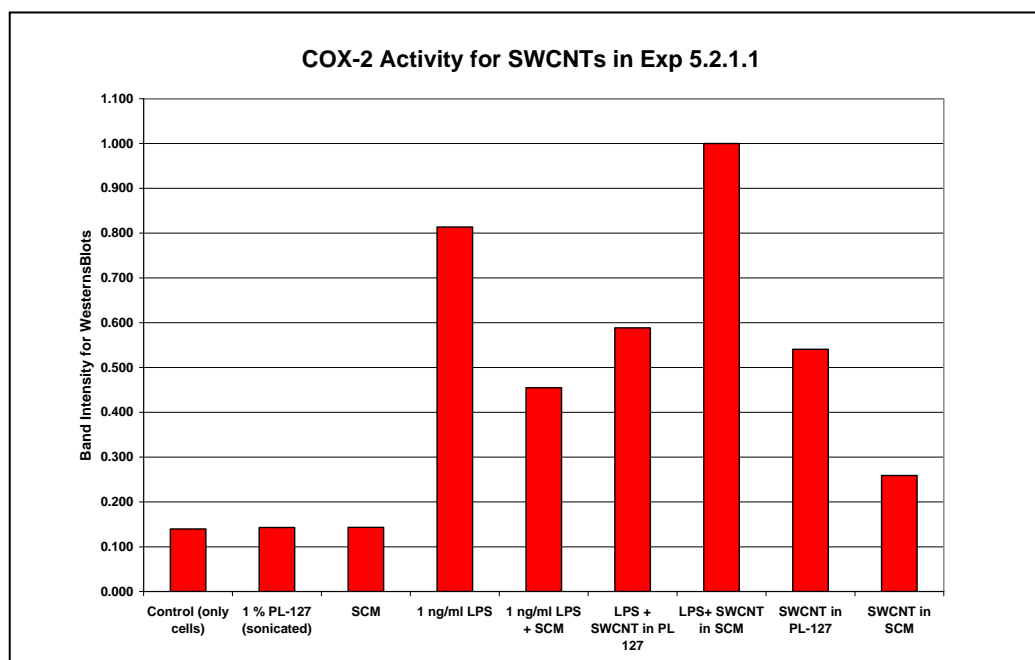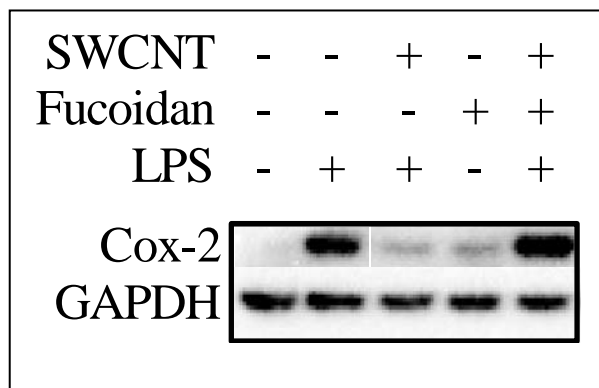**Figure 11:** Representative western blot bands to show the functional role of Scavenger Receptors in the pro-inflammatory behavior of SWCNTs
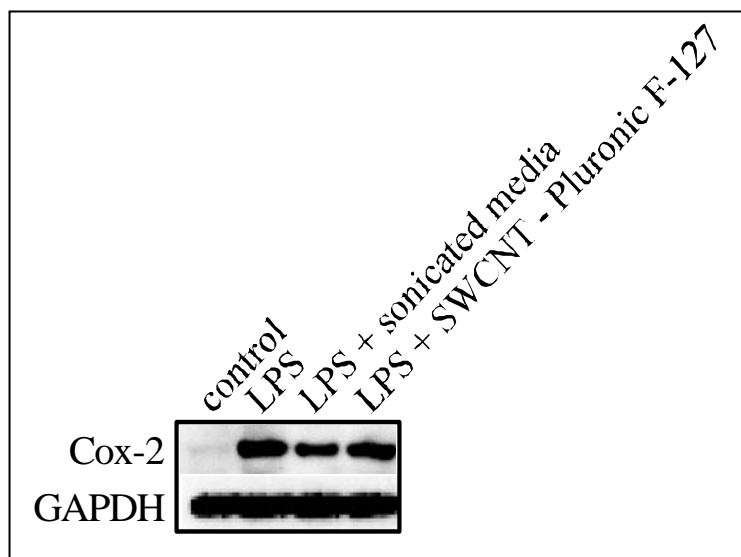
Figure 12: Western blot bands to show that the re-suspension of SWCNT in PL-127 does not cause any antagonism of LPS-Mediated Inflammatory Response

6.4 Fluorescence Microscopic Imaging
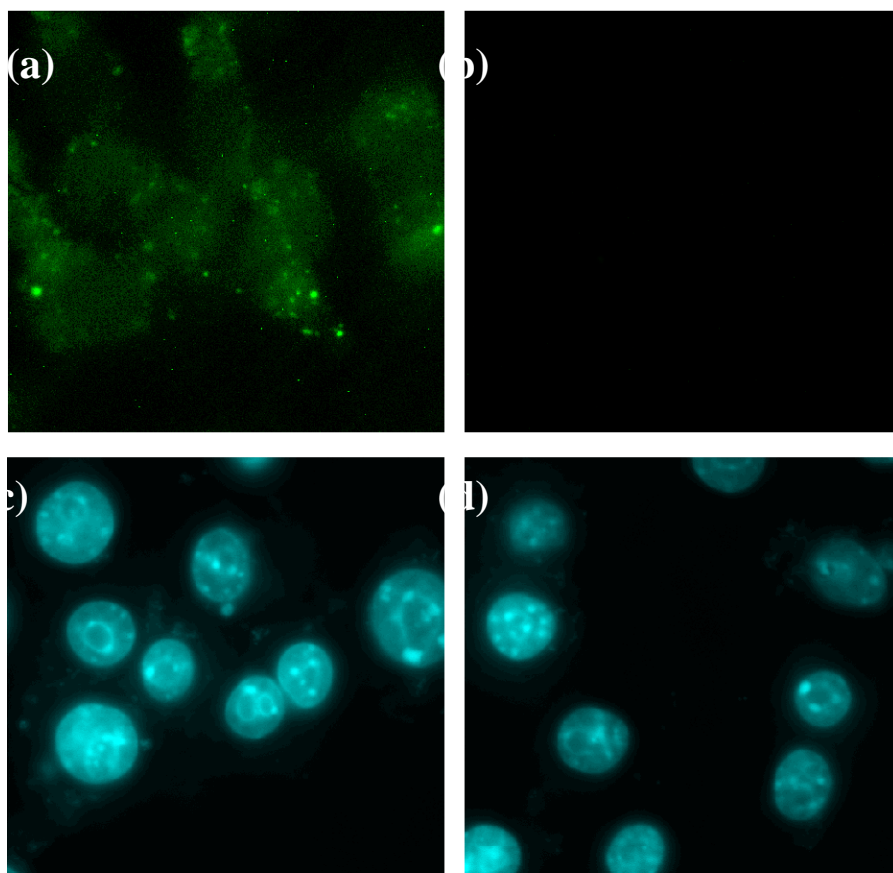
Figure 13: RAW 267.4 Cell experiment with SWCNTs. Fluorescent microscopic images of SWCNTs labeled with Alexafluor 647 in the **(a)** presence of Scavenger Receptor Antagonists (SRA) **(b)** absence of SRA **(c) and (d)** corresponding DAPI (to observe the nuclei) labeled cells for SWCNTs labeled with Alexafluor 647. Images clearly demonstrate the role of scavenger receptor in the SWCNTs uptake.

The non-functionalized SWCNT sample used contained nickel and yttria as impurities along with carbon as observed from SEM-EDS results (**Figure 1 and Table 11).** The presence of impurities may play an inflammatory role in the macrophage cells. It is important to take some adequate steps to remove these elements (acid leaching or using purer samples of SWCNTs synthesized using Laser Ablasion etc) and verify observed effects attributed to the behavior of SWCNTs. (*Note*: *This remained as incomplete work and is assigned as future work on this project).* Certain white spots observed on the structures were recognized in SEM-EDS as areas of high impurity. The composition analysis **(Figure 2 and Table 12)** shows that the nickel and yttria content of these regions are comparatively higher than other areas of the SWCNT structure. SEM image of the structure of SWCNTs is shown in **Figure 3** with a magnified image of the white spots on the SWCNT structure (inset).

Figure 4, as described before is the representative dose-response curve of Experiment 5.1.1. The points on the curve (representing the response of the cells to the nanotubes) indicate a drastic change in activity of cells for particle concentrations above12.5 µg/ml. At particle concentrations above 25µg/ml, the dose-response curve started attained a comparatively flat shape. To ensure that we were in the right window of concentration for dose-response analysis, we selected 25 and 50 µg/ml as the particle concentrations to dose the cells for western blot experiments.

Histograms in **Figures 5-10** show iNOS and COX-2 activity of the macrophage cells incubated with corresponding SWCNT samples in the different experiments.

Figures 11-12 show representative bands from the western blot experiments indicating the role of scavenger receptors in nanoparticle uptake and the contribution of ultra-sonication techniques on the inflammatory behavior of SWCNTs respectively.

Macrophage activation when exposed to bacterial endotoxin (LPS) initiates inflammatory responses that can be observed from western blot bands. As expected and shown in **Figure 11,** a positive COX-2 activity is present in cells that were incubated with LPS and a very minimal COX-2 activity was observed when cells were incubated with SWCNT, but there was no activity when SWCNTs were added along with LPS.

Previous investigators have reported that scavenger receptors on the surface of mouse peritoneal macrophage cells can effectively internalize superparamagnetic iron oxide nanoparticle [42, 43] and modulate the cellular responses. It is possible that the SWCNTs are delivered into the murine macrophage cells in a similar fashion. It has been reported that SWCNTs can behave as generic intra-cellular transporters to deliver various proteins like bovine serum albumin (BSA) and cytochrome c [44]. The SWCNT-protein conjugate was observed to be released into the cell cytoplasm from the lysosomes. It is possible, that the nanotubes get associated with pieces of damaged proteins/albumin created during ultra-sonication of the cell media. These pieces of damaged proteins enter the macrophage cells along with the SWCNTs, and exhibit an antagonistic effect of LPS mediated inflammatory (COX-2 and INOS) responses. As observed in **Figure 12,** re-suspending the SWCNTs in an emulsifying agent (PL-127) without any sonication exhibited no antagonism of LPS-mediated inflammatory responses in the cells.

The role of scavenger receptors in the uptake of SWCNTs was confirmed using fluorescent microscopy. Cells (DAPI labeled and non-labelled) were incubated with SWCNTs

(similar to experimental sample) labeled with Alexa Fluor 647 along with scavenger receptor antagonists (fucoidan). **Figure 13** shows the microscopic images of the the macrophage cells observed at 647 nm. The absence of any fluorescent particles in **Figure 13(b)** indicates that no uptake was possible due to the non-availability of the scavenger receptors in the presence of fucoidan. Thus the process ofuptake of the nanotubes is clearly a receptor-mediated endocytotic uptake and hence the toxicity behavior can be correspondingly manipulated depending on the application of the nanoparticulate system in consideration.

[Note: Individual COX-2 and INOS bands for each western Blot Experiment has been recorded in the Laboratory Notebook at PNNL and a soft copy of some western Blot bands are available with Dr Thomas Weber at 331 Building, PNNL, Richland].

8. Conclusions

We have shown that non-functionalized SWCNTs display a variation in the inflammatory responses in macrophage cells depending on the dispersion medium of the nanotubes. Use of sonicated media as a dispersing medium led to antagonism of LPS mediated inflammatory responses whereas use of an emulsifier to disperse the nanotubes did not do so. This difference in results has tremendous implications in toxicity determination in nanoparticulate materials.

In addition, we have also shown that scavenger receptors play a functional role in the process of nanotube uptake, where SWCNTS behave as intracellular transporters to 'piggy-back' proteins into the macrophage cells. By themselves, the SWCNTs to not show any substantial inflammatory effects, but in the presence of damaged proteins etc can exhibit COX-2 and INOS responses on the RAW 264.7 cells

Acknowledgments

References

1. Pantarotto, D., et al., *Translocation of bioactive peptides across cell membranes by carbon nanotubes.* Chemical Communications, 2004(1): p. 16-17.
2. Bianco, A. and M. Prato, *Can carbon nanotubes be considered useful tools for biological applications?* Advanced Materials, 2003. **15**(20): p. 1765-1768.
3. Baughman, R.H., A.A. Zakhidov, and W.A. de Heer, *Carbon nanotubes - the route toward applications.* Science, 2002. **297**(5582): p. 787-792.
4. Warheit, D.B., et al., *Comparative pulmonary toxicity assessment of single-wall carbon nanotubes in rats.* Toxicological Sciences, 2004. **77**(1): p. 117-125.
5. Warheit, D.B., *What is currently known about the health risks related to carbon nanotube exposures?* Carbon, 2006. **44**(6): p. 1064-1069.
6. Shim, M., et al., *Functionalization of carbon nanotubes for biocompatibility and biomolecular recognition.* Nano Letters, 2002. **2**(4): p. 285-288.
7. Bahr, J.L. and J.M. Tour, *Covalent chemistry of single-wall carbon nanotubes.* Journal of Materials Chemistry, 2002. **12**(7): p. 1952-1958.

8.   Dumortier, H., et al., *Functionalized carbon nanotubes are non-cytotoxic and preserve the functionality of primary immune cells.* Nano Letters, 2006. **6**(7): p. 1522-1528.

9.   Kam, N.W.S., et al., *Nanotube molecular transporters: Internalization of carbon nanotube-protein conjugates into mammalian cells.* Journal of the American Chemical Society, 2004. **126**(22): p. 6850-6851.

10.   Sayes, C.M., et al., *Functionalization density dependence of single-walled carbon nanotubes cytotoxicity in vitro.* Toxicology Letters, 2006. **161**(2): p. 135-142.

11.   Cui, D.X. and H.J. Gao, *Advance and prospect of bionanomaterials.* Biotechnology Progress, 2003. **19**(3): p. 683-692.

12.   Gao, H.J., et al., *Spontaneous insertion of DNA oligonucleotides into carbon nanotubes.* Nano Letters, 2003. **3**(4): p. 471-473.

13.   Cui D, O.C., Ravindran S, Kong Y, Gao H., *Encapsulation of pt-labelled DNA molecules inside carbon nanotubes.* Mech Chem Biosyst., 2004. **1**(2): p. 113-21.

14.   Kam, N.W.S., Z.A. Liu, and H.J. Dai, *Carbon nanotubes as intracellular transporters for proteins and DNA: An investigation of the uptake mechanism and pathway.* Angewandte Chemie-International Edition, 2006. **45**(4): p. 577-581.

15.   Cui, D.X., et al., *Effect of single wall carbon nanotubes on human HEK293 cells.* Toxicology Letters, 2005. **155**(1): p. 73-85.

16.   Rojas-Chapana, J.A. and M. Giersig, *Multi-walled carbon nanotubes and metallic nanoparticles and their application in biomedicine.* Journal of Nanoscience and Nanotechnology, 2006. **6**(2): p. 316-321.

17.   Murakami, H. and N. Nakashima, *Soluble carbon nanotubes and their applications.* Journal of Nanoscience and Nanotechnology, 2006. **6**(1): p. 16-27.

18.   Liopo, A.V., et al., *Biocompatibility of native and functionalized single-walled carbon nanotubes for neuronal interface.* Journal of Nanoscience and Nanotechnology, 2006. **6**(5): p. 1365-1374.

19.   Liu, G.D. and Y.H. Lin, *Carbon nanotube-tem plated assembly of protein.* Journal of Nanoscience and Nanotechnology, 2006. **6**(4): p. 948-953.

20.   Ni, Y.C., et al., *Chemically functionalized water soluble single-walled carbon nanotubes modulate neurite outgrowth.* Journal of Nanoscience and Nanotechnology, 2005. **5**(10): p. 1707-1712.

21.   Perez, B., et al., *Glucose biosensor based on carbon nanotube epoxy composites.* Journal of Nanoscience and Nanotechnology, 2005. **5**(10): p. 1694-1698.

22.   Sinha, N., J.Z. Ma, and J.T.W. Yeow, *Carbon nanotube-based sensors.* Journal of Nanoscience and Nanotechnology, 2006. **6**(3): p. 573-590.

23.   Service, R.F., *American Chemical Society meeting: Nanomaterials show signs of toxicity.* Science, 2003. **300**(5617): p. 243-243.

24.   Shvedova, A.A., et al., *Exposure to carbon nanotube material: Assessment of nanotube cytotoxicity using human keratinocyte cells.* Journal of Toxicology and Environmental Health-Part A, 2003. **66**(20): p. 1909-1926.

25.   Monteiro-Riviere, N.A., *Multi-walled carbon nanotube exposure in human epidermal keratinocytes: Localization and proteomic analysis.* Abstracts of Papers of the American Chemical Society, 2005. **229**: p. U911-U912.

26.   Monteiro-Riviere, N.A., et al., *Multi-walled carbon nanotube interactions with human epidermal keratinocytes.* Toxicology Letters, 2005. **155**(3): p. 377-384.

27.   Mattson, M.P., R.C. Haddon, and A.M. Rao, *Molecular functionalization of carbon nanotubes and use as substrates for neuronal growth.* Journal of Molecular Neuroscience, 2000. **14**(3): p. 175-182.

28. Chan, H.C., et al., *A phenylacetate derivative, SCK6, inhibits cell proliferation via G(1) cell cycle arrest and apoptosis.* European Journal of Pharmacology, 2003. **467**(1-3): p. 31-39.

29. Lam, C.W., et al., *Pulmonary toxicity of single-wall carbon nanotubes in mice 7 and 90 days after intratracheal instillation.* Toxicological Sciences, 2004. **77**(1): p. 126-134.

30. Maynard, A.D., et al., *Exposure to carbon nanotube material: Aerosol release during the handling of unrefined single-walled carbon nanotube material.* Journal of Toxicology and Environmental Health-Part A, 2004. **67**(1): p. 87-107.

31. Donaldson, K., P.H. Beswick, and P.S. Gilmour, *Free radical activity associated with the surface of particles: A unifying factor in determining biological activity?* Toxicology Letters, 1996. **88**(1-3): p. 293-298.

32. Ghio, A.J., et al., *Metals associated with both the water-soluble and insoluble fractions of an ambient air pollution particle catalyze an oxidative stress.* Inhalation Toxicology, 1999. **11**(1): p. 37-49.

33. Hiura, T.S., et al., *The role of a mitochondrial pathway in the induction of apoptosis by chemicals extracted from diesel exhaust particles.* Journal of Immunology, 2000. **165**(5): p. 2703-2711.

34. Kumagai, Y., et al., *Generation of reactive oxygen species during interaction of diesel exhaust particle components with NADPH-cytochrome P450 reductase and involvement of the bioactivation in the DNA damage.* Free Radical Biology and Medicine, 1997. **22**(3): p. 479-487.

35. Abe, S., et al., *Diesel exhaust (DE)-induced cytokine expression in human bronchial epithelial cells - A study with a new cell exposure system to freshly generated DE in vitro.* American Journal of Respiratory Cell and Molecular Biology, 2000. **22**(3): p. 296-303.

36. Mitchell, J.A., S. Larkin, and T.J. Williams, *Cyclooxygenase-2 - Regulation and Relevance in Inflammation.* Biochemical Pharmacology, 1995. **50**(10): p. 1535-1542.

37. Chien, P.S., O.T. Mak, and H.J. Huang, *Induction of COX-2 protein expression by vanadate in A549 human lung carcinoma cell line through EGF receptor and p38 MAPK-mediated pathway.* Biochemical and Biophysical Research Communications, 2006. **339**(2): p. 562-568.

38. Kroncke, K.D., K. Fehsel, and V. Kolb-Bachofen, *Inducible nitric oxide synthase in human diseases.* Clinical and Experimental Immunology, 1998. **113**(2): p. 147-156.

39. Chauhan, V., et al., *Effects of ambient air particles on nitric oxide production in macrophage cell lines.* Cell Biology and Toxicology, 2004. **20**(4): p. 221-239.

40. Furumoto, K., et al., *Hepatic uptake of negatively charged particles in rats: possible involvement of serum proteins in recognition by scavenger receptor.* Journal of Controlled Release, 2004. **97**(1): p. 133-141.

41. Nam, H.Y., et al., *The role of nitric oxide in the particulate matter (PM2.5)-induced NF kappa B activation in lung epithelial cells.* Toxicology Letters, 2004. **148**(1-2): p. 95-102.

42. Weissleder, R., et al., *Superparamagnetic Iron-Oxide - Enhanced Detection of Focal Splenic Tumors with Mr Imaging.* Radiology, 1988. **169**(2): p. 399-403.

43. Stark, D.D., et al., *Superparamagnetic Iron-Oxide - Clinical-Application as a Contrast Agent for Mr Imaging of the Liver.* Radiology, 1988. **168**(2): p. 297-301.

44. Kam, N.W.S. and H.J. Dai, *Carbon nanotubes as intracellular protein transporters: Generality and biological functionality.* Journal of the American Chemical Society, 2005. **127**(16): p. 6021-6026.

A Fast Screening Technique to Evaluate Si Detector Response to Ions

Mikael Elfman
Engineering Nuclear Physics Research Scientist, Lund Institute of Technology,
University of Lund
Lund, Sweden
and
Yanwen Zhang
Pacific Northwest National Laboratory
Richland, WA

National security issues have recently prompted an urgent need for improved radiation detector materials. Existing materials do not meet the stringent requirements of nuclear nonproliferation and homeland security applications. Accelerated materials discovery efforts are needed to develop the next generation radiation detector materials with excellent energy resolution at room temperature. Fast screening techniques are, therefore, required to investigate numerous candidate materials to provide quick information about material properties relevant to detector performance.

The response generated in detector materials by radiation energy deposition is the fundamental basis for understanding material functionality as a radiation detector. Energy resolution and detection efficiency can provide a critical basis for identification of possible candidate materials. The current work demonstrates a fast screening technique in obtaining relevant quantitative data on the response of a silicon detector, which is a benchmark material. The experimental approach used in this work can be applied to quickly evaluate the candidates of radiation detector materials.

Silicon detectors are widely used for determining energies of neutral and charged particles in various ion beam analysis (IBA) techniques, radioactive ion beam applications, and satellite experiments. Despite their extremely widespread use for over four decades [1] and limited approaches to calibration [2,3], there exist no predictive calibrations for ions with a wide range of atomic number and energies. Silicon detector response to ions and the pulse height defect (PHD) for heavy particles have been reported over the years. However, contributions to PHD, such as non-ionization energy loss and inefficient electron-hole (e-h) collection in the detector active volume, are not fully analyzed in a quantitative manner, and variation of the average energy, ε, required to produce an e-h pair remains controversial. In the current study, the pulse height defect in a Si detector was extensively investigated over a wide energy region using a time-of-flight (TOF) telescope, and fundamental understanding of Si detector response to ions is addressed.

The experimental setup is shown in Fig.1. Energetic ion beams produced using a tandem accelerator are forward scattered by a bulk Au target into the TOF telescope, which is followed by the Si detector of interest. The energy of scattered ions ranges from a few hundreds keV to a few tens MeV. The Si detector used in this study was an
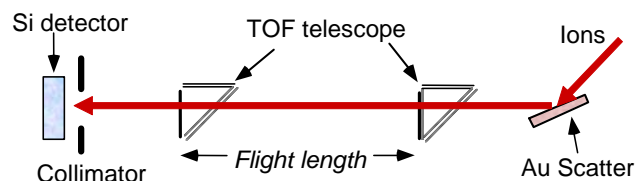

Fig. 1 Schematic diagram of the experimental

ORTEC ultra ion-implanted-silicon detector with entrance contact made by an extremely thin boron implantation. The detector response is simultaneously measured over a wide energy range, for which the energy is determined from the TOF and isotopic mass prior to impinging on the Si detector. During the measurements, the output signals from the timing detectors were recorded in an inverse start-stop mode to minimize the dead time, and the Si detector response is delayed in order to coincide with the TOF signal. For each ion, the energy is determined as

$$E(keV) = \frac{1}{2} M \cdot (\frac{L}{TOF})^2 - \Delta E_{foil} = slope \cdot E(ch) + offset \tag{1}$$

where M is the ion mass, TOF is the time for the ion to pass through the flight length (L), and ΔE_{foil} is the energy loss in traversing the carbon foil in the second timing detector. The time calibration of the TOF telescope was done using both the signals of the ions that are scattered from the Au target surface and the timing calibrator (ORTEC module 462), with the two independent results confirming each other to achieve a reliable time calibration.
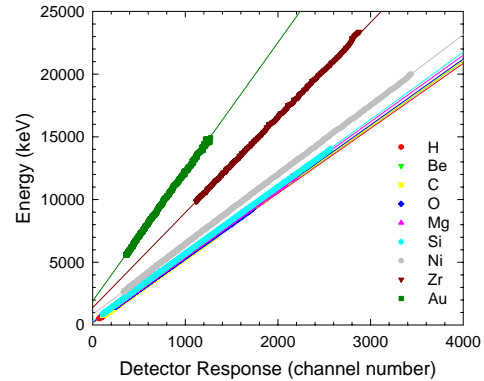
Fig. 2 True energy of various ions versus the pulse channel number from the Si detector.

The detector response (the measured pulse height) for ions with atomic number between 1 and 79 is shown in Fig. 2 versus particle energy. The results indicate that the pulse height-energy relation for each element can be described by a linear relationship (Eq. 1), where the mean slope (keV/channel) is the energy spanned by one channel and the mean offset (keV) is mainly the energy loss in the entrance window and dead layer of the detector. Although the data closely followed a straight line relation, small systematic deviations of the data were observed, even for light particles, which will be discussed in more detail.
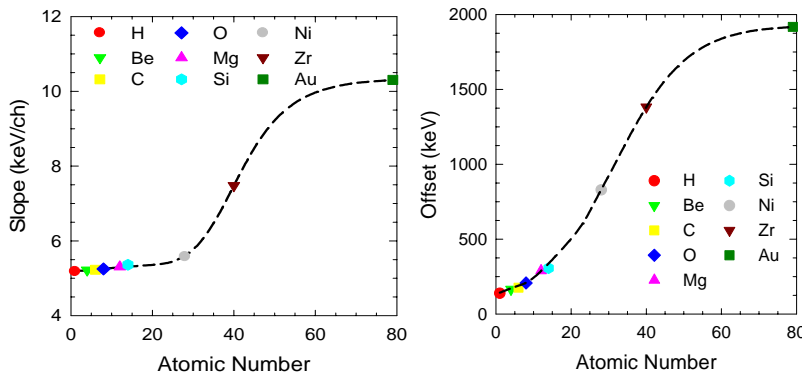
Fig. 3 Atomic number dependence of the mean slope and the mean intercept.
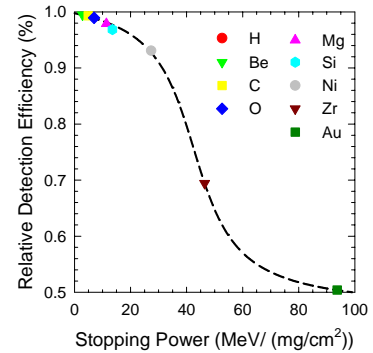
Fig. 4 Relative detection efficiency of e-h pair collection

The calibration parameters from Eq. 1 for a wide range of ions are shown in Fig. 3. A significant increase in the mean slope can be observed for heavy particles. The origin of this increase is unclear; however one might speculate that this is a consequence of non-linear effects and strong plasma recombination. It is important to note that the increase in the mean slope with atomic number is not a sufficient condition to determine if the effective electronic

energy deposition to excite an e-h pair varies because the slope also depends on the probability of e–h pair collection. The efficiency of e-h pair collection is markedly affected by the production, migration and recombination of e-h pairs in the dense plasma created along the ion track. The relative detection efficiency derived from this study is shown in Fig. 4 as a function of stopping power for various particles at energy of 500 keV per nucleon.
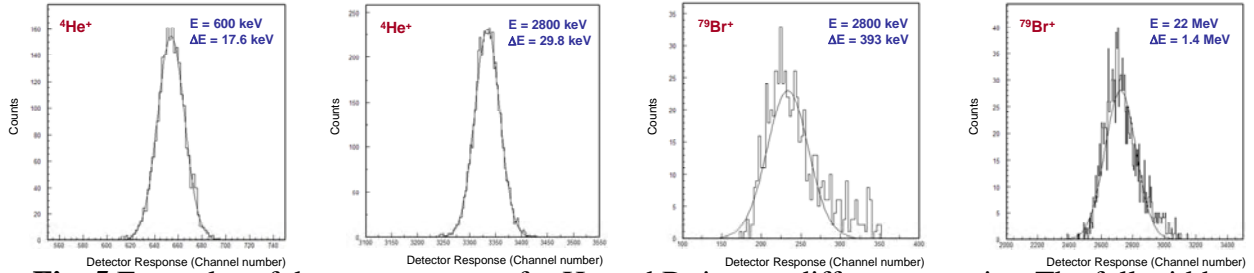
Fig. 5 Examples of detector response for He and Br ions at different energies. The full width at half maximum (FWHM) is illustrated in the corresponding plots.

The detector response for a given energy is shown in Fig. 5 using He and Br ions as examples. The peak broadening results from the intrinsic signal variance, together with the energy straggling in the carbon foil in the second timing detector and the detector contact/dead layers, as well as the uncertainties associated with the non-ionization part of the nuclear stopping. A new method of analysis of pulse height data is applied with corrections of the above mentioned uncertainties to obtain signal variance for silicon. The variation of the average energy for e-h pair creation is determined as a function of electronic stopping power.
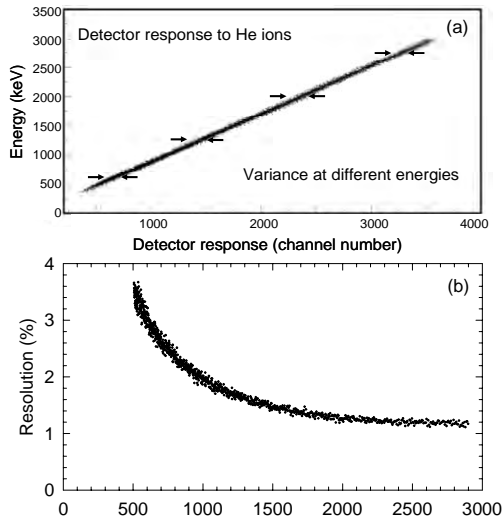
Fig. 6 (a) Detector response for He ions over a wide energy range, and (b) the measured energy resolution as a function of energy deposited in the detector.
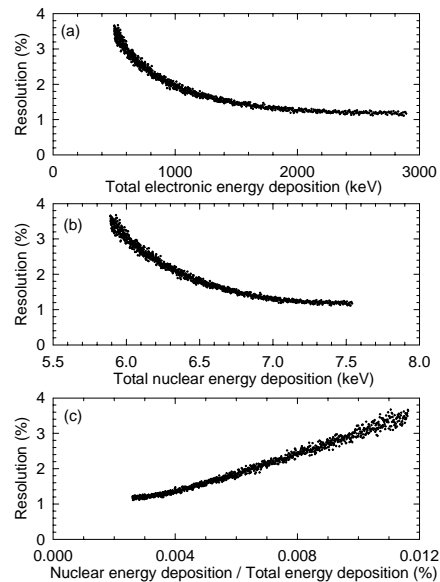
Fig. 7 Detector resolution as a function of (a) electronic energy deposition, (b) nuclear energy deposition, and (c) the ratio of energy that does not produce e-h pairs to total energy deposition

To demonstrate TOF-ion approach as a fast screening technique, 3.0 MeV He ions forward scattered from the Au target were used to test the detector response. The electronic modules were optimized for processing the signals. During the measurement, more than 6 million He ions were detected by both the Si detector and TOF telescope in a coincident mode in ~20 minutes. Fig. 6(a) shows the recorded detector response, for which the energy is determined by

the TOF telescope. The signal broadening results from the statistical fluctuations in the number of charge carriers, together with the energy straggling in the carbon foil in the second timing detector and the Si detector contact layer, the limited timing resolution, the uncertainties associated with the non-ionization part of the nuclear stopping, as well as the electronic noise. The measured energy resolution in the current study is defined as the full width at half maximum (FWHM) of the peak normalized to its energy, and the results indicate a decrease with increasing particle energy, as shown in Fig. 6(b). The saturation level at 1.2% is the detector resolution for He ions including all sources of variances.

The measured energy resolution for He ions is shown in Fig. 7 as a function of electronic [4] and nuclear energy deposition, as well as the ratio of non-detectitable to total ion energy. Similar behavior is observed from Figs. 6(b) and 7(a), since the majority of the e-h pairs is created from the electronic energy deposition. The broadening at lower energy ends, for both electronic and nuclear energy deposition, is attributed to statistical fluctuations due to relatively few charge carriers produced. Extrapolation of the results in Fig. 7(c) to zero should provide information about detector response when the radiation energy is deposited by electrons instead of ions.

For fast screening purposes, the candidates of radiation detector materials can be simply investigated using readily available energetic ions, such as He ions. The measured energy resolution observed in the candidate materials can be compared to the results from a standard detector, such as the Si detector in the current study.

Progress Report: Attempting to investigate the effects of confinement on Organophosphorus Hydrolase from P. diminuta by Molecular Dynamics simulation.

Diego Enry Barreto Gomes
Universidad Federal do Rio De Janeiro,
Rio De Janeiro. Brazil
and
Dr. Thereza Soares, C&ISD
Pacific Northwest National Laboratory
Richland, WA 99352

1. Introduction

Organophosphorous (OP) compounds are potent neurotoxic substances widely used as pesticides, insecticides and as chemical warfare nerve weapon. Because of the toxicity and general use of these neurotoxic compounds, several efforts focus on development methods to detect and detoxify these hazardous substances. Many analytical methods have been proposed[1] to detect OP compounds but they lack of portability and fast response, have high cost and require of people capacitation. A promising alternative to an efficient, highly sensitive and fast way of detection of OP compounds are the enzymatic biosensors based on Organophosphorous Hydrolase (OPH; EC 3.1.8.1) a dimeric, binuclear metalloenzyme isolated from the soil bacterium *Pseudomonas diminuta* which is capable to selectively catalyze a hydrolytic reaction in the P-O, P-S, P-CN, and P-F bonds present a large variety of OP compounds[2]. OPH biosensors have a potential use in Military, Industrial and Environmental applications as detection and even detoxification of contaminated samples. OPH-based biosensors take advantage of OPH responding to OP compounds as an enzyme substrate system, allowing a single-step direct method to measure enzyme activity[3]. By the end of the reaction the enzyme is reactivated and the biosensor can be reused for continuous monitoring or detoxification of OP compounds in the surrounding environment.

It has been show that confinement of OPH in a 2% HOOC Functionalized Mesoporous Silica (HOOC-FMS) provided both high affinity for the protein molecules and a favored microenvironment that resulted in exceptionally high immobilization frequency with enhanced stability and increased enzyme specific activity by 200\%[4] compared to OPH in solution, but the same effect in specific activity is not displayed with confinement in Unfunctionalized Mesoporous Silica. What happens to the enzyme in these confinement conditions to induce this outstanding increase in activity? How the nonspecific interactions between FMS molecules influence the vital reactions and events that define OPH activity?

In this report we investigate the effects produced by molecular confinement internal enzyme dynamics of OPH dimer in two simple models of confinement on the conformational dynamics of OPH dimmer from *Pseudomonas diminuta* and compare the results to OPH free in solution. We also would like to show how these effects may influence the interactions with soman as the substrate in order to produce a more efficient catalysis. We initiated this work based on the hypothesis that the adsorption of the enzyme to a circular array the oxygen atoms could mimic

the effects of confinement on the structure and stability of proteins and could thereby provide a suitable model system for the effects of confinement in a 2% HOOC-FMS.

2. Computational Methods

System setup: Four separate sets of MD simulations were undertaken, all using NWChem software[5], each running on 72 Itanium-2 Madison cores. The four studies differed in their starting configuration but shared a very similar simulation protocol. The OPH dimmer was obtained from the crystal structure 1HZY[6]. Partial atomic charges for Soman and carbamylated Lys-169 were determined to reproduce the molecular electrostatic potential by using the restrained electrostatic potential (RESP) procedure[7] applied to 6-31G* optimized B3LYP/DZVP structures, the bond and rotational parameters of a carboxylate were used for of Lys-169 and the bond, angle and rotational parameters involving central phosphorous in Soman were adapted from parameters involving the central phosphate group of nucleic acid. All other force field parameters were obtained from amber99 ff[8].

Based on pKa calculation with propKa[9] we assigned the proper protonation states to amino acid residues. Since propKa does not consider the contribution of charges from heteroatoms such as Zinc atoms, the assignment of the charges was dubious for HIS254. The four starting configurations were prepared as follows:

OPH-free and OPH-fix: These systems were simulated without any ligand and with HIS254 protonated only in chain B as proposed by propKa calculation. As an approach to represent confinement, *OPH-fix* had all surface LysNε atoms fixed to simulate the effect of confinement due to electrostatic interaction of these charged.

s-OPH-free and s-OPH-fms: These systems were simulated with Soman ligand docked to the active site, in a non-covalent bound. s-OPH-fms was adsorbed to an array of atoms as described below.

Representation of s-OPH adsorbed to FMS: To represent the functionalized mesoporous silica (FMS) as described by Lei et al[4] we used NANOPORE, our home made program, to design a 17nm diameter, 13nm length, quarter circle array of 1.0nm separated oxygen atoms with enough room to fit the OPH dimmer as shown in Figure 1. To properly orient the OPH dimmer (OPHd) on the surface of FMS we used APBS[10] to calculate the electrostatic surface OPHd and we used PyMol[11] to orient OPHd to best fit the charge complementarily.
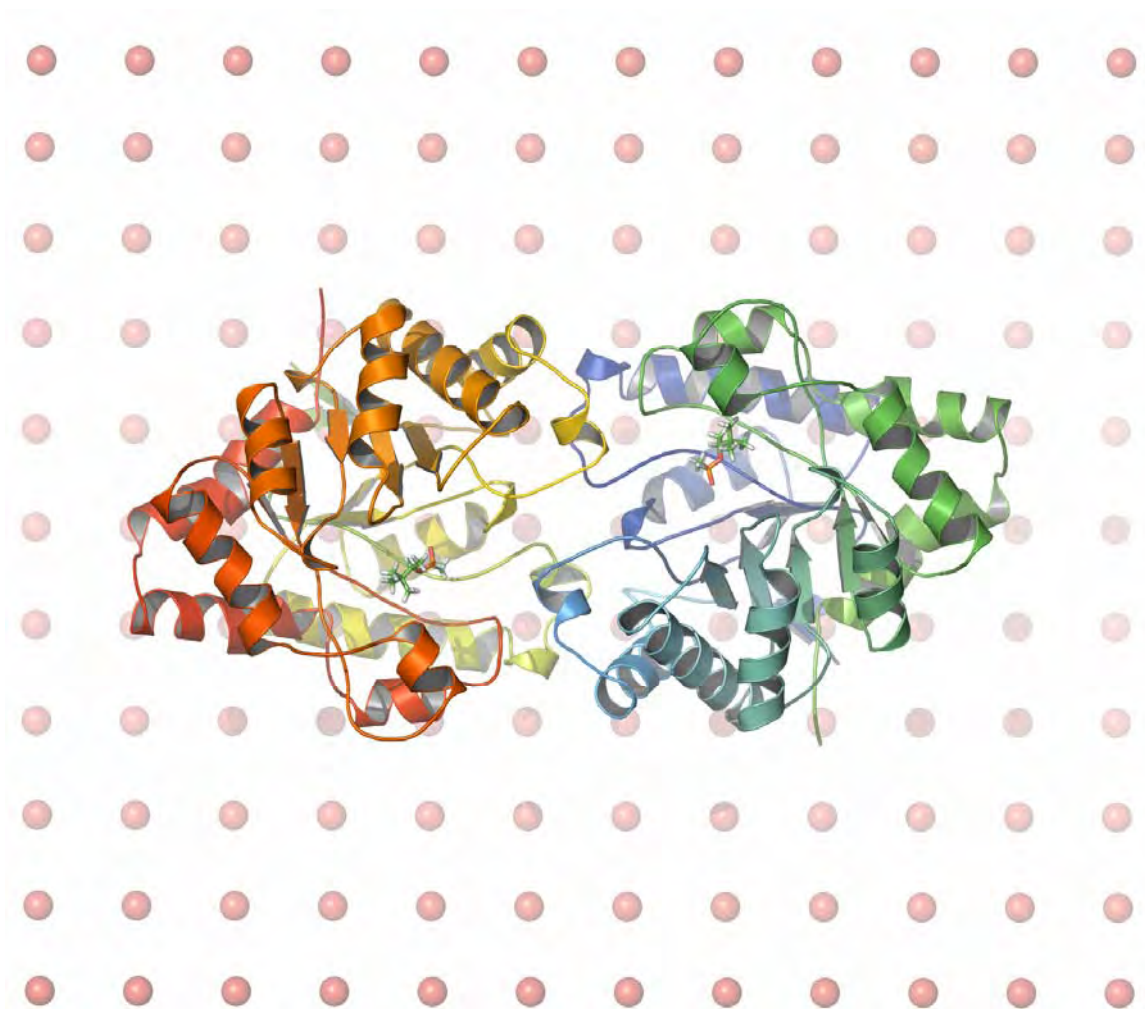
Figure 1 The Functionalized Mesoporous Silica represented as a 17nm diameter, 13nm length, quarter circle array of 1.0nm separated oxygen atoms (red spheres) with the OPH dimmer (ribbons) adsorbed**.**

PMF calculations: To estimate how the free energy of the interaction of OPH with Soman changes as a function of binding we applied the Potential Mean Force calculations with force constant ranging from 100kj/mol to 800kj/mol, equilibrating for 50k-100k steps and sampling for 50k-100k steps, with $\lambda = 0.01$nm.

Simulation setup: The molecules simulated were solvated with SPCE[12] water model in a 13x13x14nm box and counter ions were added to neutralize the charges. Non bonded interactions were considered to a cutoff of 1.0nm, updating the neighbor pair list every 10 steps, with time-step set to 2fs. The electrostatic interactions were calculated with the Particle Mesh Ewald method[13], and the SHAKE algorithm[14] was used to constrain all bond lengths involving hydrogens. The systems were thermodynamically coupled to a 298K bath and pressure coupling at 1 bar. An initial energy minimization was carried out followed by a 150 ps warm up simulation to equilibrate the systems before a production run of 5ns. The s-OPH-fms system was allowed to perform the minimization and warm up steps before adding the counter ions to the FMS grid and then repeat these two steps.

3. Results and Discussion

pKa calculations: The protonation state of residues was determined according to the method implemented in propKa for pH 7.0. Figure 2 shows the histidines of the active site of OPH. Although propKa is a very fast and accurate method it was not able take into account the Zinc atoms and assigned of HIS 254 as protonate, in conflict with the positively charged environment. Considering this limitation of propKa we decided to simulate each of the two OPH dimmer chains with a different protonation for HIS 254: non protonated for chain A (HIE) and protonated (HIP) for chain B.
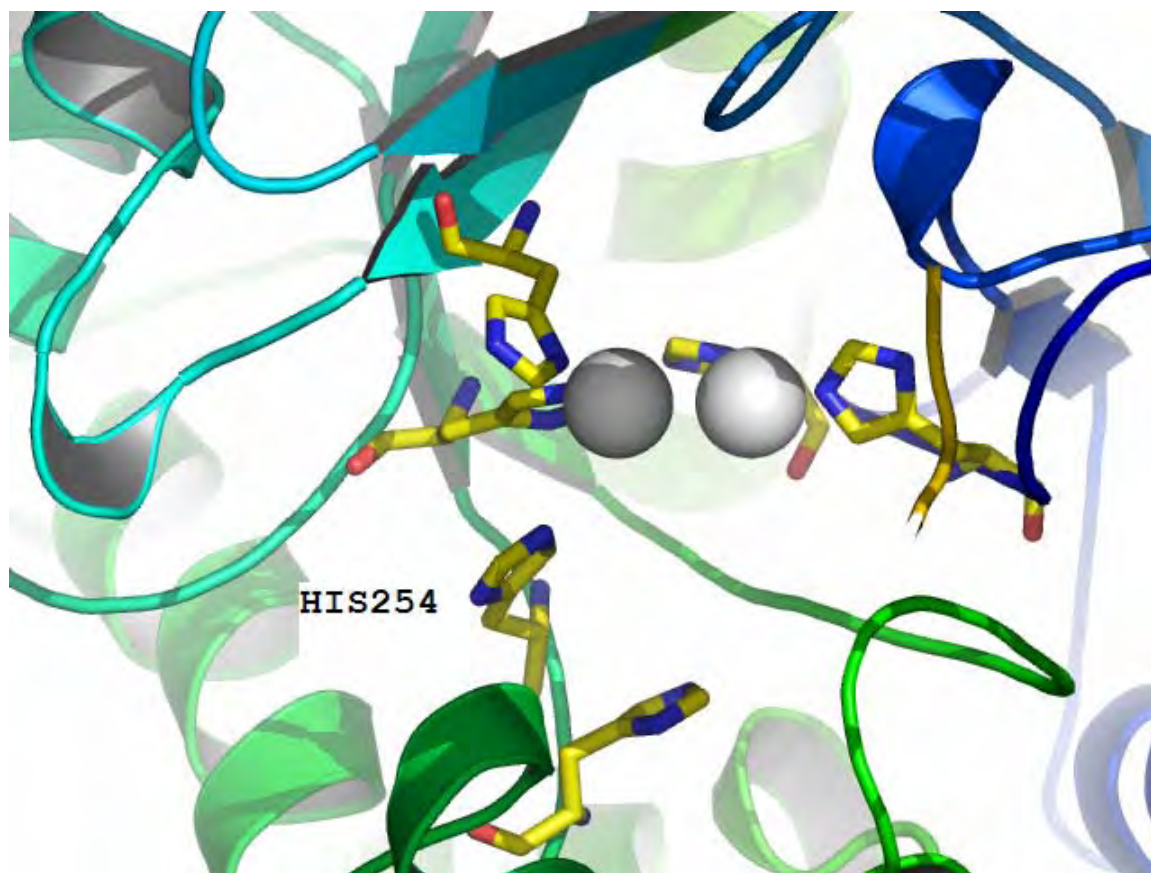
Figure 2 The histidines (sticks) of the active site of OPH (ribbons) and de Zinc atoms (gray spheres).

3.1 MD simulations of OPH with or without LYS restraints.

Trajectory stability: As a measure of structural stability we calculated the root-mean-square deviations (RMSD) for all backbone atoms in the OPH original file compared to each snapshot of the trajectory (Figure 3). We can see that the trajectory is stable after 2.0nsec. Energy and temperature remains steady over the course of the simulation (data not shown).
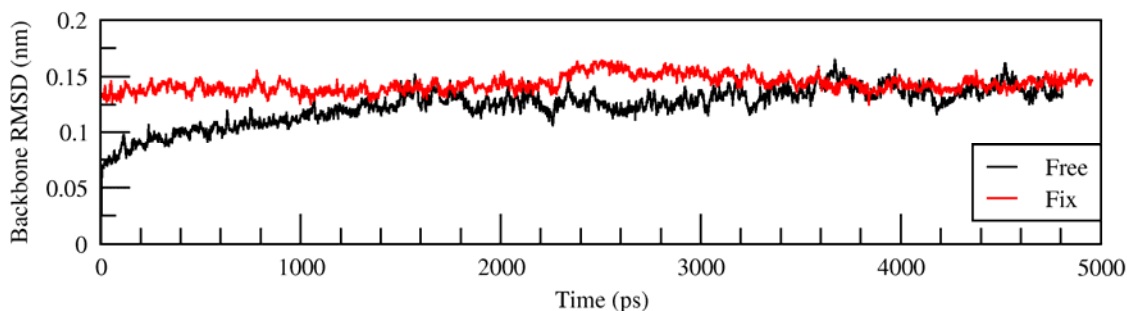
Figure 3 The Root Mean Squared Deviation to the first frame of molecular dynamics simulation for the backbone atoms for OPH-free (black) and OPH-fix (red).

Protein movements: To investigate if the effects of confinement on internal enzyme dynamics we performed the root-mean-square-fluctuation (RMSF) (Figure 4A and 4B)
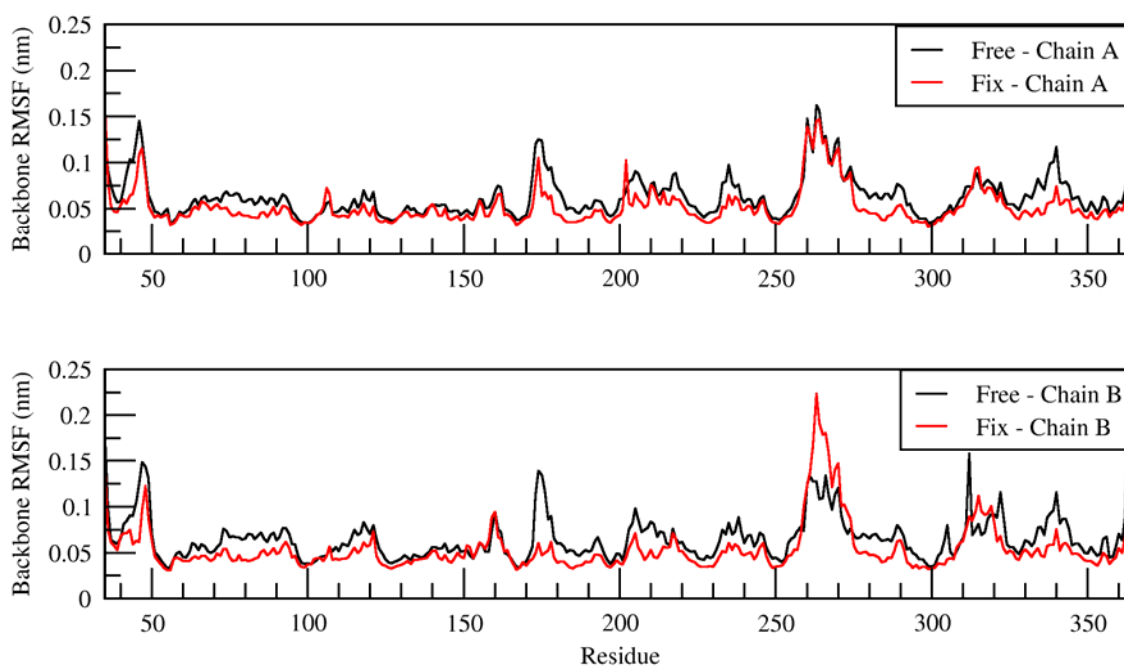
Figure 4 The Root Mean Squared Fluctuation to the mean structure calculated between 2000ps and 5000ps of molecular dynamics simulation for the backbone atoms for OPH-free (black) and OPH-fix (red) divided by chain A (top) and B (bottom).

and analyzed the covariance matrix to extract the essential dynamics (ED) (Figure 5) of OPH free and OPH _x. On both analyses we could observe some small discrepancies among the two systems and two specific hot spots on the RMSF and Eigenvector values located between protein residues 172-178, and residues 261-267 essentially on chain B.
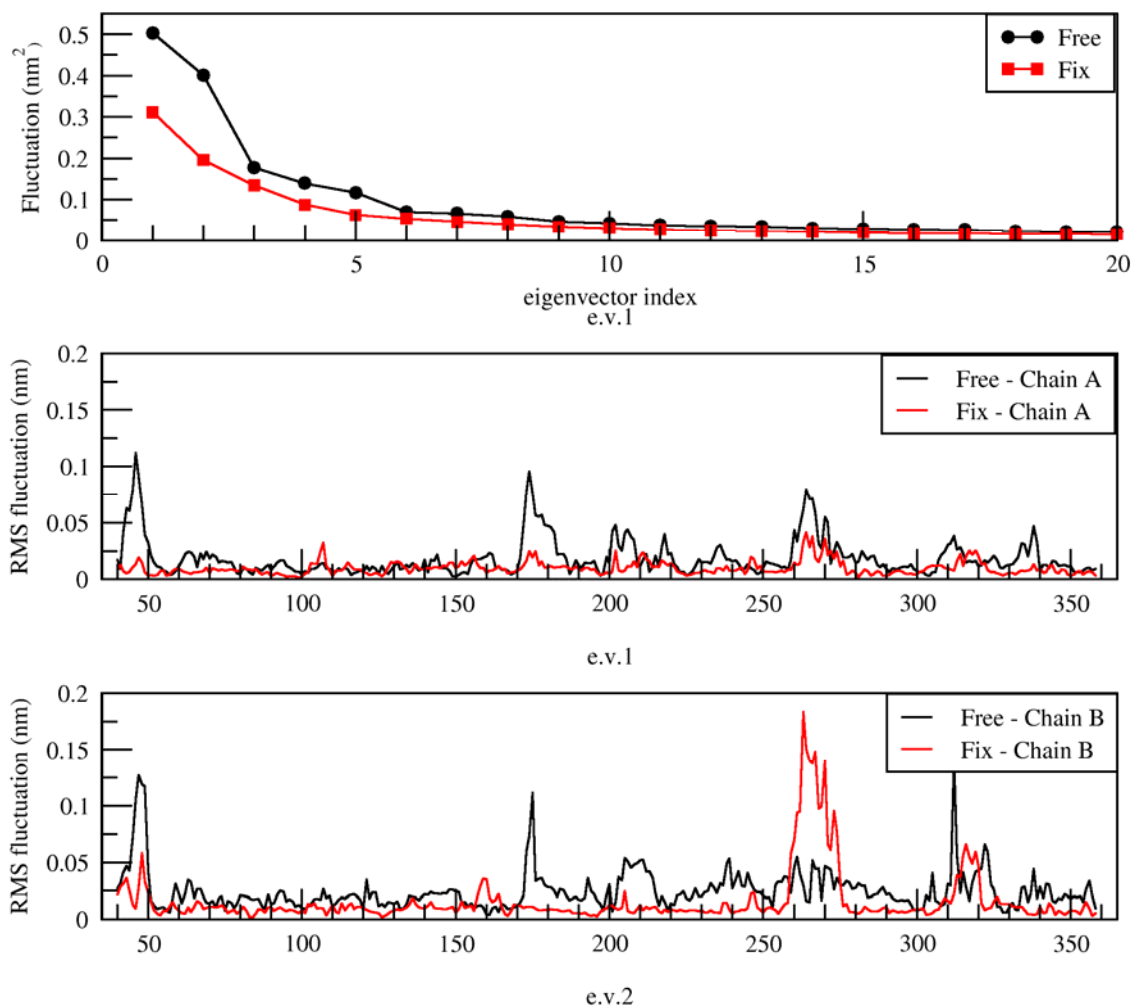
Figure 5 Eigenvalues for the first 20 eigenvectors (top). RMF fluctuation for the first eigenvector OPH-free (black) and OPH-fix (red) divided by chain A (middle) and B (bottom)OPH-free (black) and OPH-fix (red) divided by chain A (top) and B (bottom) \subsection{Free energy tests}

Figure 6A shows the 172-178 region, for these residues OPH-_x is stabilized compared to OPH-free but the movement of these residues is more visible on chain B. The restraint forced by fixing the Nz atom of the lysine near these residues is the most probable reason for producing this small stabilization on the fluctuation (RMSF) and the reduction on the RMS fluctuation of the first eigenvector (e.v.1). Figure 6B shows the 261-267 region where the opposite effect is observed also for chain B. For chain A, a small stabilization can be observe but for chain B, instead of reducing the residues fluctuation compared to OPH-free, this particular portion of OPH-_x shows a more flexible behavior with the first eigenvector clearly showing an extended movement directed outside the active site. This awkward behavior of 261-267 residues in chain B, but not in chain A, may be caused by the different charge distribution as a result of protonated HIS254 which also causes constant clashes of it's N" hydrogen during the initial steps of molecular dynamics and probably transmits this stress to surrounding atoms.
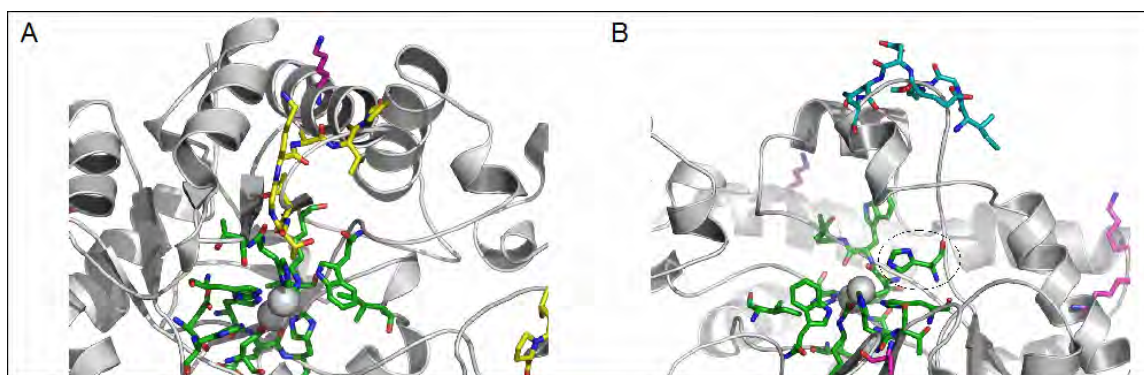
Figure 6 Hot spots on the RMSF and Eigenvector values. Residues of the active site are in green sticks, lysine residues in purple stick and protein in gray ribbons. Residues 172-178 are showed in yellow in figure 6A and residues 261-267 in blue in figure 6B. A and B are rotated by 180 degrees.

3.2 Free energy tests

We have run previous tests in order to estimate the free energy of binding of OPH with the organophophate nerve agent Soman. We performed a screening of different sets parameters for the Potential Mean Force calculations. The force constants were 100,200,400 and 800kJ/mol, equilibrations steps 50k and 100k steps and sampling rates were 50k and 100k steps. Figure 7 shows the different sampling windows of the PMF calculation with force 800kJ/mol, equilibration 50k steps with sampling set to 100k steps, even with this high force we were not able to transport the organophosphate out of the active site, indicating that Soman is tightly bounded to OPH, actually Soman is buried in the active site and embraced by the loops around the active site as showed in Figure 8.
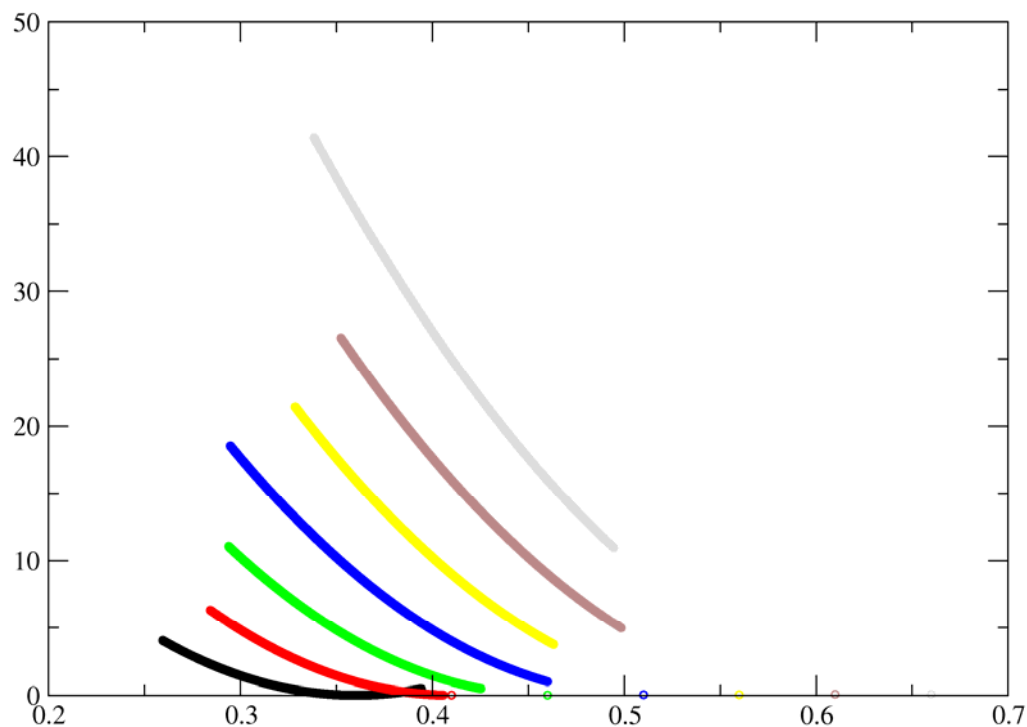
Figure 7 Sampling windows for the PMF calculation with force 800kJ/mol, equilibration 50k steps with sampling set to 100k steps. Force in Y axis, distance between the centers of geometry Active site residues and Soman in X axis.
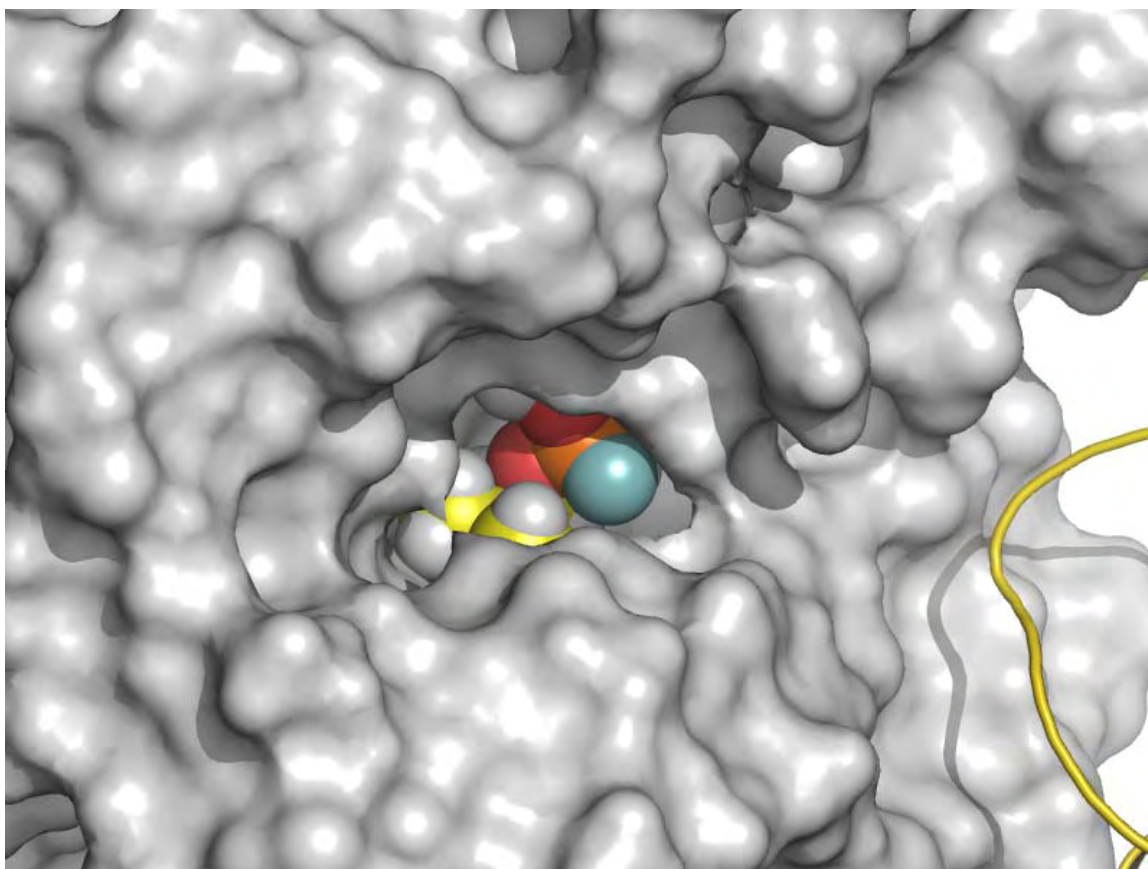
Figure 8 Soman buried in the active site and embraced by the protein loops.

3.3 MD simulations of OPH with nanopore.

An alternative model was proposed to represent the FMS was it's explicit representation as an array of charged Oxygen atoms, as showed in figure 1. According to the electrostatic potential surface, calculated with APBS as showed in Figure 9 the opposite side to the active site is more positively charged at pH 7.0. Using this as lead we adsorbed OPH to FMS and started the simulations. The simulations are still running and we expect this to be a more representative model for the confinement effects, which include the previous unconsidered charge effect attributed to HOOC functionalized silica.
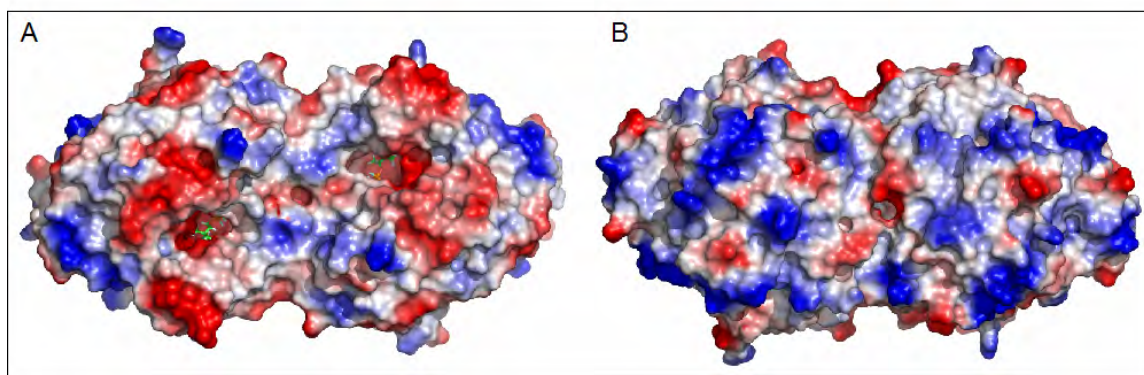
Figure 9 Electrostatic potential surface, calculated with APBS, blue is positive, red is negative, white neutral. The opposite side to the active site 9B is more positively charged than the active site side 9A of the protein at pH 7.0.

4 Concluding remarks

Due to its central importance, there is intense interest in understanding how confinement modulates protein kinetic activity. Several studies have show that proteins are stabilized upon encapsulation in silica gel 15. Eggers and Valentine16 reported that molecular confinement influences protein structure and enhances thermal protein stability, which is probably because decrease of protein flexibility due to reduced mobility by the confined water molecules interacting with the exposed atoms of the macromolecule.

In our simulations with lysines fixed by their Nz atoms, we identified two hotspots in protein movement but only representative in chain B. The stabilization residues 172-178 in the OPH-fixed simulation may influence enzyme-substrate interaction by keeping the proper reaction coordination for a longer period. In contrast the opposite side of the active site, residues 261-267, showed increased movement possibly as a direct effect of the protonation state of HIS254. Besides these two regions there is no considerable difference between internal enzyme dynamics of the two simulations that should explain the increased activity and stability of OPH in confined environment leading us to question if fixing the lysine Nz, as a way to represent the binding of OPH the Functionalized Mesoporous Silica, would be enough to represent the confined environment of the silica gel.

We are continuing the project now correcting HIS254 protonation state and also simulating the HOOC Functionalized Mesoporous Silica represented explicitly as an array of Oxygen atoms and expecting this to be as more appropriate way to describe the effects due confinement in silica gel.

5 References

1)

    (a) Mendoza, C. E. Thin-layer chromatography. In Pesticide Analysis; Dumas, K. G., Ed.; MarcelDekker: New York; 1981, pp 1-44. (b) Das, K. G.; Kulkarni, P. S. Gas-liquid chromatography. In Pesticide Analysis; Dumas, K. G., Ed.; Marcel Dekker: New York, 1981. (c) Hanks, A. R.; Colvin, B. M. High-performance liquid chromatography. In Pesticide Analysis; (d) Dumas, K. G., Ed.; Marcel Dekker: New York, 1981; pp 99-174. (e) Barcelo, D.; Lawrence, J. F. Residue analysis of organophosphorus pesticides. In Emerging Strategies for Pesticide Analysis; (f) Charins, T., Sherma, J., Eds.; CRC Press: Boca Raton, FL, 1992; pp 127-150.Palchetti, I.; Cagnini, A.; Del Carlo, M.; Coppi, C.; Mascini, M.; Turner, A. P. F. Anal. Chim. Acta 1997, 337, 315-321

2)

    (a) Russell, R.; Pishko, M.; Simonian, A. S.; Wild, J. R. Anal. Chem. 1999, 71, 4909-4912. (b) Raushel FM. Bacterial detoxification of organophosphate nerve agents. Curr Opin Microbiol. 2002 Jun ; 5(3): 288-95

3)

    (a) Singh AK, Flounders AW, Volponi JV, Ashley CS, Wally K, Schoeniger JS. Development of sensors for direct detection of organophosphates. Part I: Immobilization, characterization and stabilization of acetylcholinesterase and organophosphate hydrolase on silica supports. Biosens Bioelectron. 1999 Dec ; 14(8-9): 703-13 (b) Lei Y, Mulchandani P, Wang J, Chen W, Mulchandani A. Highly sensitive and selective amperometric microbial biosensor for direct determination of p-nitrophenyl-substituted organophosphate nerve agents. Environ Sci Technol. 2005 Nov 15; 39(22): 8853-7

(c) Mulchandani A, Chen W, Mulchandani P, Wang J, Rogers KR. Biosensors for direct determination of organophosphate pesticides. Biosens Bioelectron. 2001 Jun ; 16(4-5): 225-30 (d) Mulchandani P, Mulchandani A, Kaneva I, Chen W. Biosensor for direct determination of organophosphate nerve agents. 1. Potentiometric enzyme electrode. Biosens Bioelectron. 1999 Jan 1; 14(1): 77-85

4) Lei C, Shin Y, Liu J, Ackerman EJ. Entrapping enzyme in a functionalized nanoporous support J Am Chem Soc. 2002 Sep 25; 124(38): 11242-3

5) Kendall, R.A.; Aprà, E.; Bernholdt, D.E.; Bylaska, E.J.; Dupuis, M.; Fann, G.I.; Harrison, R.J.; Ju, J.; Nichols, J.A.; Nieplocha, J.; Straatsma, T.P.; Windus, T.L.; Wong, A.T. "High Performance Computational Chemistry: an Overview of NWChem a Distributed Parallel Application", Computer Phys. Comm., 2000, 128, 260-283

6) Benning, M.M., Shim, H., Raushel, F.M., Holden, H.M. High resolution X-ray structures of different metal-substituted forms of phosphotriesterase from Pseudomonas diminuta. Biochemistry v40 pp.2712- 2722, 2001

7) Christopher I. Bayly, Piotr Cieplak, Wendy D. Cornell and Peter A. Kollman, A Well-Behaved Electrostatic Potential Based Method Using Charge Restraints for Deriving Atomic Charges: The RESP Model. J. Phys. Chem. 97 (1993) 10269-10280.

8) J. Wang, P. Cieplak, and P.A. Kollman. How well does a restrained electrostatic potential (resp) model perform in calculating conformational energies of organic and biological molecules. J. Comp. Chem., 21:1049-1074, 2000.

9) Hui Li, Andrew D. Robertson, and Jan H. Jensen "Very Fast Empirical Prediction and Interpretation of Protein pKa Values" Proteins, 2005, 61, 704-721.

10) Baker NA, Sept D, Joseph S, Holst MJ, McCammon JA. Electrostatics of nanosystems: application to microtubules and the ribosome. Proc. Natl. Acad. Sci. USA 98, 10037-10041 2001

11) DeLano, W.L. The PyMOL Molecular Graphics System (2002) DeLano Scientific, San Carlos, CA, USA. http://www.pymol.org.

12) Berendsen HJC, Grigera JR, Straatsma TP, The missing Term in Effective Pair Potentials, Journal of Physical Chemistry 91 (1987) 6169-6271.

13) Darden T, Perera L, Li L and Pedersen L. (1999) "New tricks for modelers from the crystallography toolkit: the particle mesh Ewald algorithm and its use in nucleic acid simulations", Structure 7, R55-R60.

14) Ryckaert, J.P., Ciccotti, G. and Berendsen, H.J.C. (1977) J. Comp. Chem., 23, 327-341.

15) A.C. Pierre, (2004) The sol-gel encapsulation of enzymes. Biocatalysis and Biotransformation, 22, (3) 145-170.

16) Eggers DK, Valentine JS. Molecular confinement influences protein structure and enhances thermal protein stability. Protein Sci. 2001 Feb; 10(2): 250-61

CHARACTERIZATION OF AEROSOL SAMPLES COLLECTED DURING THE MILAGRO-2006 STUDY IN THE MEXICO CITY METROPOLITAN AREA

Kirsten Johnson and Dr. Mario Molina
Massachusetts Institute of Technology
Cambridge, MA
and
Rodrigo Gonzalez and Prof. Luisa Molina
Autonomous Metropolitan University
Mexico City, Mexico
and
Dr. Alexander Laskin and Dr. Yury Desyaterik
Pacific Northwest National Laboratory
Richland, WA

INTRODUCTION

Air pollution problems of mega-cities differ greatly and are influenced by a number of factors including topography, demography, meteorology, as well as the level and rate of industrialization and socio-economic development. The Mexico City Metropolitan Area (MCMA) is a rapidly growing urban area with a population of more than 18 million that suffers high pollutant emissions from a variety of area and mobile sources. It lies in an elevated basin which sits at near-tropical latitude and is surrounded by mountains on three sides. The complex terrain and meteorology, and their effects on the city's considerable air pollution problem have been the subject of many studies (e.g. Molina and Molina, 2002; de Foy et al., 2005; Fast and Zhong, 1998). A thorough understanding of particular matter ≤ 2.5 µm in diameter ($PM_{2.5}$) is extremely important for quantification of aerosol climate effects, particulate emissions inventories, and human health effects.

The MILAGRO (Megacity Initiative: Local and Global Research Observations) campaign was carried out during March 2006, partially to build upon results from the MCMA-2003 Field Campaign during April 2003. A major objective of MILAGRO was to characterize and quantify pollutant emissions within the city and its environs to better understand the composition, transport, and reactivity of its atmospheric constituents.

Research during the PNNL Summer Research Institute involved characterization of the chemical and physical properties of aerosol samples collected during MILAGRO from various city and suburban locations.

EXPERIMENTAL

Particles were collected nearly continuously from multiple sites in order to investigate spatial and temporal variability of the particles' chemical and physical properties. Samples were collected at "T0" (Instituto Méxicano de Petróleo, IMP) in an industrial area within the city, as well as "T1" (Universidad Autónoma de Tecamac) and "T2" (Rancho la Biznaga) located

~25 km and ~50 km northeast of T0, respectively. These sites were chosen to study generation of pollution inside the city and subsequent transport towards the city boundaries.

For single particle studies, samples were collected with the Time-Resolved Aerosol Collector (TRAC) (Laskin et al., 2003) at a time resolution of 15 minutes within size range 0.3 – 2.0µm particle diameter. Samples were also collected with 8 (0.18 – 18µm) and 10-stage (0.056 – 18µm) Micro-Orifice Uniform Deposit Impactors (MOUDI) with collection times of 2-3 hours. MOUDI samples from T0 were provided by permission of Dr. R. Mamani-Paco and Dr. T. Castro, UNAM. Cu-supported microscopy grids with thin carbon and lacy carbon films were used as sample substrates for both the TRAC and the MOUDI devices. The primary analysis techniques used were Computer-Controlled Scanning Electron Microscopy with X-ray analysis (CCSEM/EDX), manual SEM/EDX, and Transmission Electron Microscopy with X-ray analysis (TEM/EDS). The majority of SEM images were recorded in secondary electron (SE) mode with back-scattering (BSE) and transmitted electron (TED) imaging used for greater contrast in specific cases. Particles were analyzed for elemental composition, size, shape, morphology, and mixing state.

Bulk aerosol samples were also collected at T0, T1 and T2 sites for quantitative information on the chemical composition of $PM_{2.5}$. Samples were collected onto Teflon strips by means of a 3-stage DRUM impactor with the following cut-off sizes: Stage A (1.15 – 2.5µm), Stage B (0.34 – 1.15µm) and Stage C (0.07 – 0.34µm). Analyses for concentrations of elements Z > Na, hydrogen, and total mass were done in collaboration with Dr. V. Shutthanandan, PNNL, using Proton-Induced X-ray Emission (PIXE), Proton Elastic Scattering Analysis (PESA) and Scanning Transmission Ion Microscopy (STIM), respectively (Shutthanandan et al., 2002). The time resolution of the analyzed samples was 6 hr.

RESEARCH OBJECTIVES

Because more than 2000 samples were collected with thousands of particles per sample, a highly focused approach to single particle analysis was necessary. Preliminary information from the campaign including complimentary aerosol analyses and meteorological data was used to target the following areas:

- ♦ Evidence of aerosol processing (chemical reaction or physical mixing) from T0 to T1 sites through composition and morphological analysis
- ♦ The phenomenon of emissions of heavy metals and soot from overnight industrial activities at T0
- ♦ Internal structure and mixing characteristics of sulfur-containing particles
- ♦ Hygroscopic properties of mixed urban aerosol and susceptibility to wet-removal by washout/rainout
- ♦ Identification of major particulate emissions sources via PIXE/PESA/STIM and multivariate analysis

Investigations of aerosol processing from T0 to T1 was done primarily with MOUDI samples collected on 27 March 2006 in the following size categories: Stage 5 (1.0 – 1.8µm), Stage 6 (0.56 – 1.0µm), Stage 7 (0.32 – 0.56µm), and Stage 8 (0.18 – 0.32µm). CCSEM/EDX elemental composition for TRAC and MOUDI samples is expressed by ratio of element weight

percent to carbon (S/C, O/C, N/C) in order to account for the thin substrate of the collection grids (Laskin et al., 2002).

RESULTS

A series of four MOUDI samples – two each from T0 and T1 – collected on 27 March 2006 were chosen for detailed morphological and compositional study (Table 1). Initial efforts were focused on samples A and B to study differences on a temporal scale. Companion data (c/o Dr. J. Wang, LBNL) from a cloud condensation nuclei (CCN) counter located at T0 suggested that sample B particles were more hydrophilic than those of sample A. While particles in sample A were collected during a maximum in total particle count (measured by a Scanning Mobility Particle Sizer, SMPS) likely related to morning rush-hour traffic, sample B particles were collected during a peak in number of active CCN occurring several hours later. Possible explanations for the offset include chemical reaction (e.g. OH or O_3 oxidation) or physical processing (e.g. mixing with soluble inorganic salts) of the same type of particles, or emission of different types of particles altogether. SEM/EDX analysis confirmed both chemical and physical differences between the two. Whereas sample A (6 – 9am) contained a large number of irregular soot particles, sample B (11am – 2pm) showed marked differences in particle size and shape and a liquid-like appearance. CCSEM/EDX analysis showed that major elements for both were C, O, S, Si, K and Na. However, sample B was found to have lower S/C and O/C ratios, which was unexpected from the above hypotheses regarding chemical and physical processing which might lead to higher oxygen and sulfur content. Comparisons of samples A and B with C and D in relation to transport from T0 to T1 are in progress.

Table 1: Summary of MOUDI samples analyzed by CCSEM/EDX and SEM/EDX.

Sample	Location	Collection time
A	T0	6:00am – 9:00am
B	T0	11:00am – 2:00pm
C	T1	10:00am – 12:00pm
D	T1	1:00pm – 3:00pm
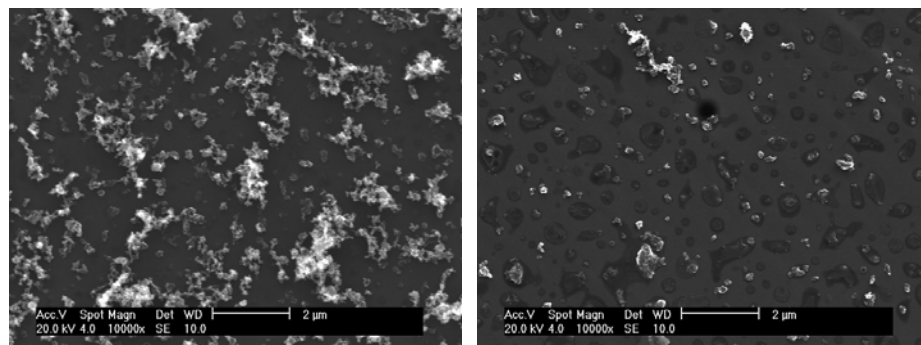
Figure 1. SEM images of MOUDI samples A (left) and B (right) from Stage 8 (0.18 – 0.32 µm).

Table 2. CCSEM/EDX statistics for MOUDI samples A and B.

	Sample A		Sample B	
	Average	Median	Average	Median
O/C	7.8e-2	4.7e-2	4.9e-2	3.6e-2
N/C	7.4e-3	0	9.0e-3	0
S/C	6.1e-3	3.7e-3	4.4e-3	0
Na/C	1.3e-2	5.6e-3	1.4e-3	0
Si/C	5.0e-3	4.2e-3	2.4e-3	0
K/C	9.0e-4	0	2.0e-4	0
O/S	11.5	8.5	8.0	6.2
Diameter (µm)	0.229	0.182	0.263	0.208
# Particles analyzed	3329		4084	

PIXE analysis during the MCMA-2003 campaign showed that overnight industrial emissions were important sources of metals that originated from northern sections of the city (Johnson et al., 2006). The location of the T0 site therefore provided a good opportunity for additional study on this phenomenon. Several early morning (~ 1am) samples were studied which corresponded with peak values in various metals including Zn and Pb measured by PIXE. Figures 2 and 3 show fine needle-like Zn particles mixed with soot from a sample collected on 23 March at T0. Zn and soot were commonly observed, as well as occasional small Pb particles distinguishable in BSE mode imaging.
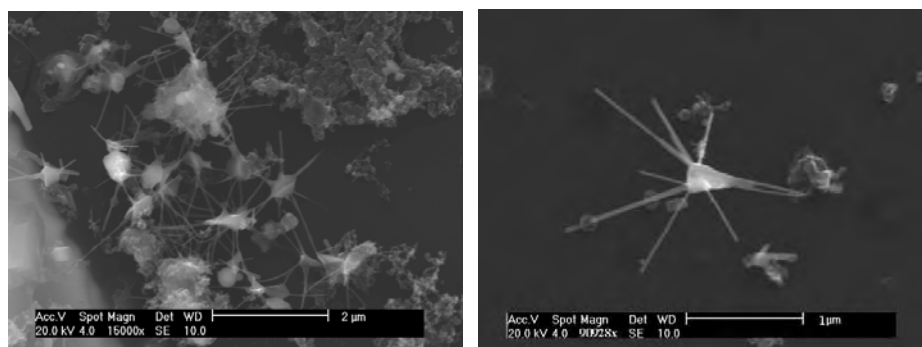
Figure 2: SEM images of samples collected on 23 March 1:30-1:45am (left) and 21 March 1:30-1:45am (right) at T0.
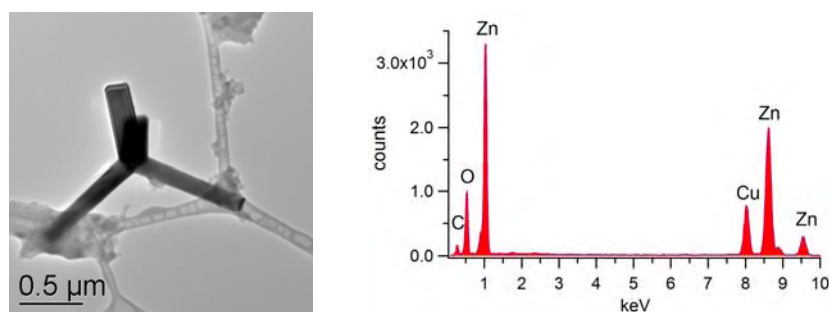
Figure 3: TEM image and X-ray spectrum of a Zn particle collected on 23 March (1:30-1:45am) at T0. Cu is an artifact of the substrate grid.

PIXE measurements at T0 indicate that the most abundant elements in non-volatile $PM_{2.5}$ were S, Zn, soil-related elements (Si, Al, Fe, Mg, Ca), K, Pb, and Cl. Soil elements track one another throughout the campaign (Fig. 4) as expected of a common emissions source. The concentration of Zn reaches peak values during early morning (~ 1am) hours (Fig. 5). Analysis of PESA/STIM data from T0 and PIXE/PESA/STIM from companion sites T1 and T2 is in progress, and multivariate analysis of these data is planned for identification of particulate emissions sources for comparison to MCMA-2003 (Johnson et al., 2006).
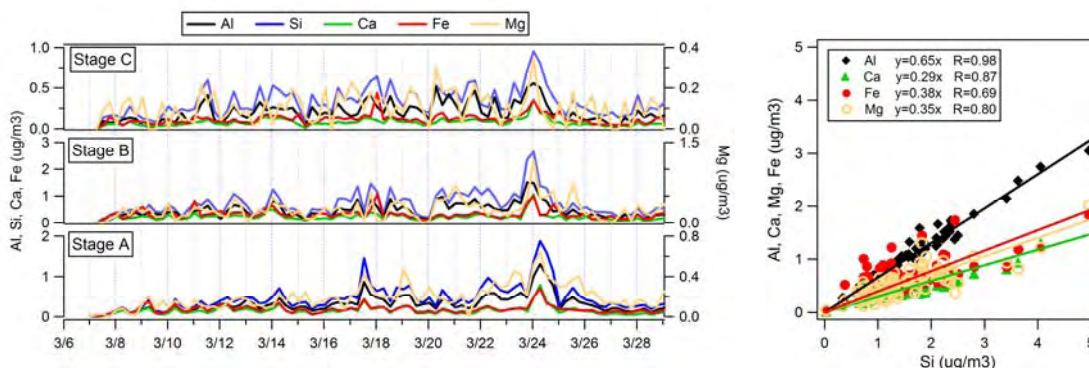
Figure 4. Time series of soil-related elements (Si, Al, Ca, Fe, Mg) at T0 from PIXE analysis in size categories Stage A (1.15-2.5µm), B (0.34-1.15µm) and C (0.07-0.34µm); correlation plot among these elements in $PM_{2.5}$ (sum of Stages A, B, C).
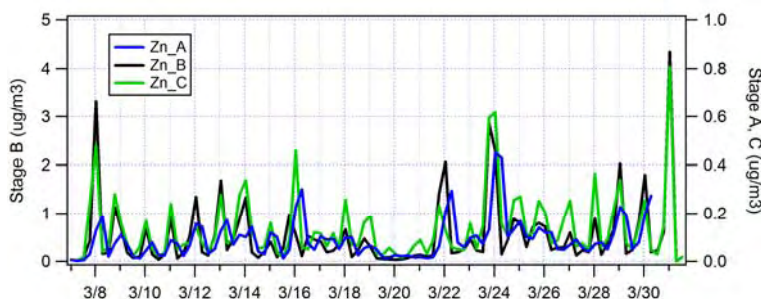
Figure 5. Time series of Zn at T0 by PIXE analysis in Stages A, B, C.

DISCUSSION

Preliminary analysis of aerosol samples collected during the MILAGRO campaign confirm previous results from MCMA-2003. Specifically we found that soot and sulfur were major components of MCMA aerosol, and TEM analysis of spherical sulfur-containing (likely sulfate) particles showed that they were often internally mixed with soot. This information is essential to understanding particulate mixing and reactivity in order to better quantify particles' lifetimes and their effects on the environment. In addition, different types of sulfur-containing particles were collected during MILAGRO and suggest that S may be present in different chemical forms. While one type of sulfur-containing particles were characterized by a spherical shape, electron beam sensitivity (to damage), and mixing with other elements (K, Cl, Sn) and soot particles, a second type had a liquid-like appearance, unaffected by the electron beam and were associated mostly with carbon only. Although SEM/EDX provides limited information on the chemical form of the elements present, analyses with Time-of-Flight Secondary Ion Mass Spectrometry (TOF-SIMS) at PNNL and with Scanning Transmission X-ray Microscopy (STXM) with Near Edge X-ray Absorption Fine Structure spectroscopy (NEXAFS) in collaboration with Dr. M. K. Gilles at Lawrence Berkeley National Laboratory (LBNL) are possible means of additional information. TOF-SIMS and STXM studies of MOUDI samples A – D are underway and may be helpful in better understanding compositional differences as a result of aerosol processing.

PIXE/PESA/STIM data is complimentary to single particle analyses and useful in quantifying $PM_{2.5}$ aerosol chemical composition. PIXE analysis from T0 samples confirms an abundance of S with average concentrations 0.066, 1.568, and 0.828 $\mu g/m^3$ for Stages A, B, and C, respectively. Zn was also present in fairly high concentration (averages 0.093, 0.541, 0.136 $\mu g/m^3$ for A, B, C) probably due to close proximity to industrial sources near T0. The strong correlation among elements related to soil/dust (Si, Al, Ca, Fe, Mg) parallels SEM/EDX analysis of individual soil/dust particles composed of the same elements.

CONCLUSIONS

Chemical and morphological analysis of aerosol samples collected during the 2006 MILAGRO campaign show that MCMA particles have a complex composition and are heavily mixed. Major types of particles include soot, dust and sulfur-containing particles, as well as metals associated with industry such as Zn and Pb. Comparisons of differences in morphology and composition of particles collected within hours of one another are useful to understanding how they react and become mixed. More information is needed on the chemical form of the composition elements and related meteorology during the collection period to understand these differences, however. Further studies are in progress.

REFERENCES

de Foy, B., Caetano, E., Magana, V., Zitácuaro, A., Cárdenas, B., Martínez, A. P., Retama, A., Ramos, R., Reyes, R., Sosa, G., Molina, L. T., and Molina, M. J.: Mexico City basin wind circulation during the MCMA-2003 field campaign, Atmos. Chem. Phys., 5, 2267-2288, 2005.

Fast, J. D., and Zhong, S.: Meteorological factors associated with inhomogeneous ozone concentrations within the Mexico City basin, J. Geophys. Res., 103, 18927-18946, 1998.

Johnson, K. S., Zuberi, B., Molina, L. T., Molina, M. J., Iedema, M. J., Cowin, J. P., Gaspar, D. J., Wang, C., and Laskin, A.: Processing of soot in an urban environment: Case study from the Mexico City Metropolitan Area, Atmos. Chem. Phys., 5, 3033-3043, 2005.

Johnson, K.S., B. de Foy, B. Zuberi, L.T. Molina, M.J. Molina, A. Laskin, Y. Xie, and V. Shutthanandan, "Aerosol composition and source apportionment in the Mexico City Metropolitan Area with PIXE/PESA/STIM and multivariate analysis", Atmos. Chem. Phys. Discuss., 6, 3997-4022, 2006.

Laskin, A., Iedema, M. J., and Cowin, J. P.: Time-resolved aerosol collector for CCSEM/EDX single-particle analysis, Aerosol Sci. Tech., 37, 246-260, 2003.

Laskin, A., Iedema, M. J., and Cowin, J. P.: Quantitative time-resolved monitoring of nitrate formation in sea salt particles using a CCSEM/EDX single particle analysis, Environ. Sci. Tech., 36, 4948-4955, 2002.

Molina, M. J., and Molina, L. T., ed.: Air Quality in the Mexico Megacity: An Integrated Assessment. Kluwer Academic, 2002.

Shutthanandan, V., Thevuthasan, S., Disselkamp, R., Stroud, A., Cavanagh, A., Adams, E. M., Baer, D. R., Barrie, L. A., Cliff, S. S., Jimenez-Cruz, M., and Cahill, T. A.: Development of PIXE, PESA and transmission ion microscopy capability to measure aerosols by size and time, Nucl. Instr. and Meth.. B, 189, 284-288, 2002.

On the Structural Stability of Ridig-Rod β-Barrel Pores

Matteo Guglielmi, and Ursula Röthlisberger
Ecole Polytechnique Federale de Lausanne (EPFL),
Laboratory of Computational Chemistry and Biochemistry,
Institute of Basic Sciences,
Lausanne 1015, Switzerland
and
Roberto D. Lins
Pacific Northwest National Laboratory,
Computational Biology and Bioinformatics,
Richland, WA 99352, USA

*Correspondence and requests should be addressed to RDL at the Pacific Northwest National Laboratory (e-mail: roberto.lins@pnl.gov) or UR at the Ecole Polytechnique Federale de Lausanne (e-mail: ursula.roethlisberger@epf.ch).

Introduction

Rigid-rod B-barrels pores are synthetically designed barrel-stave supramolecules developed to exploit the functional plasticity of their biological counterparts in biorganic chemistry [18]. They are constructed from elementary units made by *p*-octiphenyl staves connected to short peptide chains (usually 3-7 residues) [1] (Figure 1). The non structural-planarity of each unit, due to the presence of a single stave, directs cylindrical self-assembly β-barrel formation via hydrogen bond pattern between the peptide chains from neighboring units [1]. Being the product of a synthesis process, the functionality of the rigid-rod β-barrels pores can be tailored to specific task like molecular recognition, molecular translocation and molecular transformation simply by variation of their peptide chains [1-15]. Due to the alternating orientation of neighboring amino acid residues of peptides in β-sheet conformation, both inner and outer surface of rigid-rod β-barrels can be functionalized in a flexible, precise and straightforward manner. This characteristic offers potential application on a wide variety of fields, e.g., detector for medical diagnosis, drug delivery, gene therapy, food industry and environmental bioremediation [19]. Facile access to transmembrane, large, and stable synthetic pores with variable internal active sites is, however, a necessary prerequisite for their practical applications [17].

Several factors contribute to stability issue of rigid-rod β-barrels pores. They can be divided in two mutually exclusive categories: "intrinsic" pore parameters (*p*-octiphenyl length, peptide length and peptide sequence) and "environmental" factors (pH, ionic strength and membrane interaction). Previous experimental studies show that the changes in the pH are capable to tune the pore activity, i.e., activating/deactivating the macromolecular assembly by controlling the protonation levels of the internal dyads [2-15]. Such procedure aims to achieve a certain level of charge-charge repulsion in the inner barrel, which is considered to play an important role in terms of pore stability [6]. This effect has been named as internal change repulsion (ICR) model. The model states that intermediate ICR gives maximal pore activity, whereas insufficient and excessive ICR results in pore "implosion" and "explosion", respectively [6]. Additionally, the authors have also suggested the lateral pressure from the external membrane to play an essential role on barrel stability. Experimental observations led to the conclusion that the external membrane pressure (EMP) could trigger barrel implosion at low ICR while preventing barrel explosion at high ICR [16]. These findings have led to an update on the mechanism for rigid-rod β-barrel pores stability, the ICR-EMP model (Figure 2). While this is a sound model for such synthetic entities, biological pores can vary widely in their inner-pore net charge and dipole depending on the composition of the interacting molecule (ions, sugars, water, etc). On the other hand, proteins make use of a much more complex structural arrangement to interact with their medium (membranes), which might account for the same final balance. Therefore, if general, the ICR-EMP model would have an important impact in the understanding of the stability of biological pores.

In order to investigate the details and validity of these assumptions, a series of molecular dynamics simulations were carried out for two ICR-free β-barrel pores immersed into a biological membrane and in water. The pores are characterized by the peptide sequences GLNLNL and GLQLQL.

METHODOLOGY

Systems Setup

The GLNLNL and GLQLQL pores were modeled based on the experimental chemical data. The structures were studied immersed into a 148 phosphatidyl-ethonolanime lipid bilayer with two 18-carbon long aliphatic chains and free in water. A concentration molar of 0.1 M NaCl was added to reflect the experimental setup of similar pores previously studied. The

pore-lipid assembly was then solvated by SPC/E water molecules resulting in a system of 7.2 x 8.2 x 8.2 nm in size. In water, higher ionic strength (0.5 M) was also probed to completely abolish the possibility of any ICR (or ICR-like) effect.

Molecular Dynamics Simulations

All simulations were performed using the AMBER96 force field (Cornell et al., 1995) in conjunction with derived charges for the chemical groups not available in the force field (procedure described below) and implemented in the parallel version of the NWChem-4.7 program (Apra et al., 2005). The systems were equilibrated in a stepwise fashion. The systems were initially relaxed using up to 5000 steps of steepest descent energy minimization. It was followed by the system equilibration performed in successive 10-ps MD runs at 50, 100, 150, 200, 250, and 300 K, with velocity reassignments every 0.1 ps. The production runs were carried out in the isothermal-isobaric ensemble for 20 ns for the system immersed into the lipid membrane and 10 ns for the pores in water. The temperature was maintained at 300 K by weak coupling the solute and solvent separately to a heat bath (Berendsen et al., 1984) with a relaxation time of 0.1 ps. The pressure was kept at 1.025×10^5 Pascal using weak coupling to a pressure bath (Berendsen et al., 1984) via isotropic coordinate scaling with relaxation time of 0.1 ps. Long-range electrostatic interactions were handled using the smooth particle mesh Ewald (SPME) method (Essmann et al., 1995) A cutoff 1.0 nm was used for the short-range non-bonded interactions (van der Waals and real-space electrostatic contribution). The SHAKE (Ryckaert et al., 1977) algorithm was applied to constrain all bonds involving a hydrogen atom, and a 2-fs timestep was used to integrate the equations of motion based on the leapfrog algorithm (Hockney, 1970). Trajectory frames were recorded every 0.2ps for analysis.

Charge Model

Based on the optimized geometry of the *p*-octiphenyl groups, Hartree-Fock calculations at the 6-31G* level followed by a restrained electrostatic potential (RESP) fit (Bayly et al., 1995) were performed using the NWChem4.7 program (Apra et al., 2005) to compute the partial charges. Values of 0.005 a.u. for the harmonic and 0.001 a.u. for the hyperbolic restraints, respectively, were used in the RESP fittings. Charge derivation by means of RESP fitting preserves the dipole moment of a molecule to its quantum-mechanical value, and should therefore lead to a realistic description of intermolecular interactions with identical as well as distinct molecular species during the simulations. The charge-derivation procedure was

performed according to the AMBER96 force field philosophy (Cornell et al., 1995) in order to preserve force field compatibility. The final charge sets for the above-mentioned residues are shown in Figure 3. Since the *p*-octiphenyl staves present a weak molecular-wire character, a second set of charges was derived to take into account this effect and evaluate its influence on the evaluated quantities. Density functional theory at the B3-LYP/6-31G* level was used in this second charge set followed by a RESP fitting. A residual charge splitting at the *p*-octiphenyl staves termini producing the desired induced dipole. The resulting dipole along the stave was found to be ca. 4Db for charges derived without polarization, while the polarized charge set allowed a stave dipole of 7.5 Db. DFT B3-LYP/6-31G* was chosen over HF/6-31G* at this stage due to the apolar environment of the pores (membrane aliphatic chains). Additionally, comparison of point charges for an octiphenyl ring residue obtained with the two methods after a RESP fitting did not produce significant discrepancies, i.e., restricted to the second or third decimal points (data not shown). This is probably due to the apolar character of the studied chemical group.

RESULTS AND DISCUSSION

In order to evaluate the structural stability, we have monitored the inner pore dimensions (Figure 3), their corresponding conductances (Figure 4) and secondary structure stability (Figure 5) of the peptide chains as a function of the time series evolution. A higher ionic strength has also been probed for the pores free in aqueous solution. The systems have been given the following notation: 2ASN/2GLN (pores with non-polarized charge set immersed into the lipid membrane, 0.1M NaCl); 2ASN+/2GLN+ (pores with polarized charge set immersed into the lipid membrane, 0.1M NaCl); 2ASN+-/2GLN+- (pores with polarized charge set free in water, 0.1 NaCl); and, 2ASN++/2GLN++ (pores with polarized charge set free in water, 0.5M NaCl).

All the pores, except for 2ASN and 2ASN+ have collapsed into a "closed" conformation. Although the ICR effect seems to have an influence on pore stability, the presence of the membrane was able to hold these pores in their open state. It suggests that while ICR seems imperative for the stability of these systems in water, the presence of a lipid membrane can stabilize their open (biologically active) conformation depending on the peptide sequence chosen. The absence of the membrane has caused the pore dimensions and conductance of 2ASN/2ASN+ to diminish by almost half. Additionally, a decrease in stability

of the secondary structure content is observed in all membrane-free simulations compared to the ones when the membrane is present.

These results are contrasting with a hypothetical model drawn from experimental observations. In reference 16, the authors have avoided the closure of the structure of a pH-dependent pore, GLHLHL, at different pH values, by mutating the central leucine residue to an arginine, generating the sequence GLH**R**HL. This arginine, located outward the pore, would bind to functionalized external calixaarene ligands (Figure 2). These ligands of hydrophobic nature, (except for the functionalized group binding the arginine), were referred to act as "cushions" soothing the forces arising from external membrane pressure and the internal change repulsion. Our findings suggested that the presence of the membrane acts rather to hold the pore open, than applying an external closing pressure. Therefore, we hypothesize that their observations could be alternatively explained based on the fact on an increase of the total overall outer hydrophobic surface and consequently a maximization of the interaction with the lipid membrane.

CONCLUSIONS

We have studied the stability of ICR-free synthetic β-barrel pores via molecular simulations. We have investigated the influence of a double lipid membrane, and high ionic strength in the structural and functional stability of these systems. Our results indicate that the presence of the membrane not only stabilizes the open conformation of the pores, but also the secondary structure content; and, that the stability of a pore depends rather on its composition than on having an internal charge repulsion. The influence of an internal charge repulsion for these systems in water and immersed into a membrane will be assessed and shall soon be reported.

ACKNOWLEDGMENTS

References

1) S. Matile, Chem. Soc. Rev., 2001, *30*, 158-167.

2) N. Sorde' and S. Matile, J. Supramol. Chem., in press.

3) G. Das and S. Matile, Proc. Natl. Acad. Sci. U. S. A., 2002, *99*, 5183-5188.

4) G. Das, H. Onouchi, E. Yashima, N. Sakai and S. Matile, ChemBioChem, 2002, *3*, 1089-1096.

5) G. Das, P. Talukdar and S. Matile, Science, 2002, *298*, 1600-1602.

6) B. Baumeister, A. Som, G. Das, N. Sakai, F. Vilbois, D. Gerard, S. P. Shahi and S. Matile, Helv. Chim. Acta, 2002, *85*, 2740-2753.

7) B. Baumeister, N. Sakai and S. Matile, Org. Lett., 2001, *3*, 4229-4232.

8) A. Som, N. Sakai and S. Matile, Bioorg. Med. Chem., 2003, *11*, 1363-1369.

9) A. Som and S. Matile, Eur. J. Org. Chem., 2002, 3874-3883.

10) B. Baumeister and S. Matile, Macromolecules, 2002, *35*, 1549-1555.

11) G. Das, L. Ouali, M. Adrian, B. Baumeister, K. J. Wilkinson and S. Matile, Angew. Chem., Int. Ed., 2001, *40*, 4657-4661.

12) N. Sakai and S. Matile, J. Am. Chem. Soc., 2002, *124*, 1184-1185.

13) B. Baumeister, N. Sakai and S. Matile, Angew. Chem., Int. Ed., 2000, *39*, 1955-1958.

14) N. Sakai, B. Baumeister and S. Matile, ChemBioChem, 2000, *1*, 123-125.

15) N. Sakai, D.Houdebert and S. Matile, Chem. Eur. J., 2003, *9*, 223-232.

16) V. Gorteau, G. Bollot, J. Mareda, D. Pasini, D. Tran, A. N. Lazar, A. W. Coleman, N. Sakai and S. Matile, Bioorg. Med. Chem., 2005, *13*, 5171-5180.

17) S. Matile, The Chemical Record, 2001, **1**, 162-172.

18) N. Sorde', Ph.D. thesis entitled: "Rigid-Rod B-Barrel Pores as Enzyme Sensors", University of Geneve, 2004, #3575

19) N. Sakai, J. Mareda and S. Matile, Accounts of Chemical Research, **38**, 79-87

FIGURES
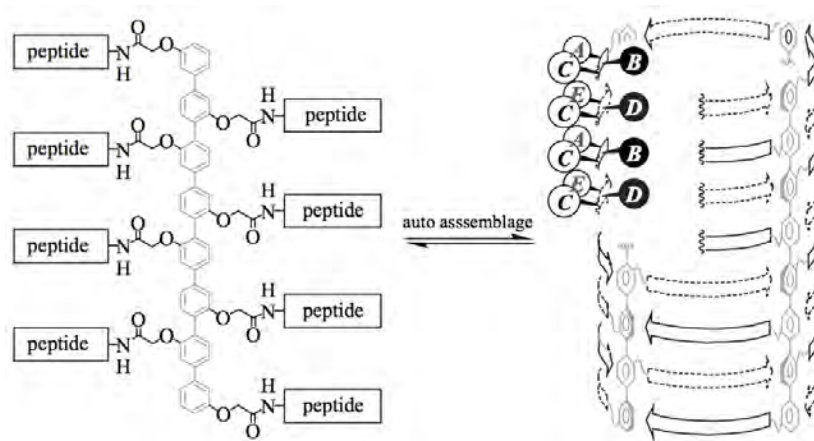
Figure 1. Schematic representation of the synthetic β-barrel pore unit (left) and assembly (right), as taken from reference 18.
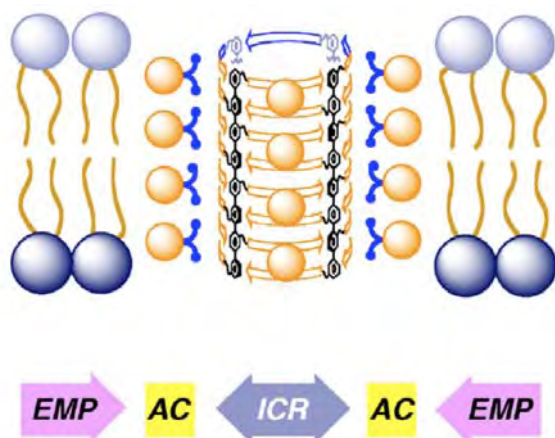
Figure 2. Schematic representation of the EMP-ICR model. The pore is shown with functionalized external calixaarene ligands that have been suggested to act as "cushions" between these two forces, as taken from reference 16.
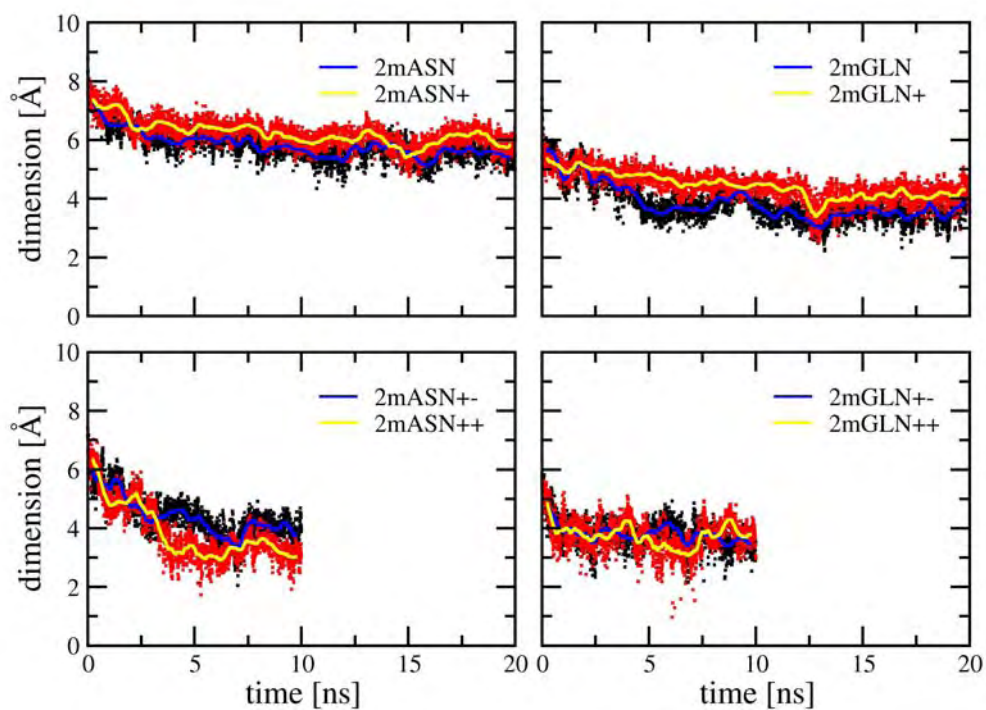
Figure 3. Inner pore dimensions as a function of time.
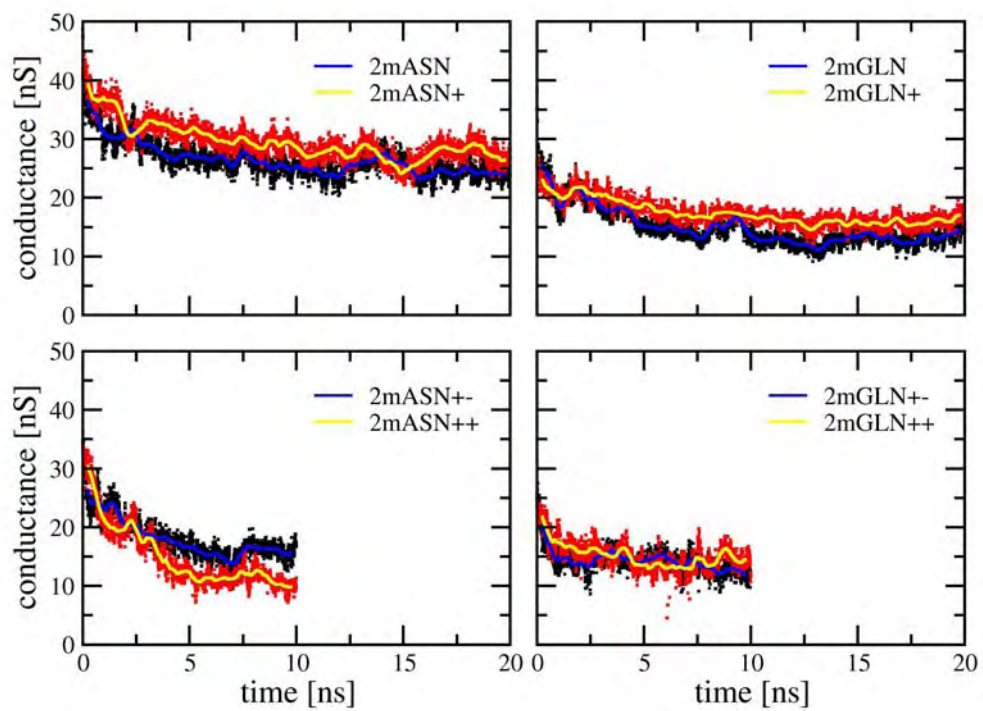
Figure 4. Pore conductance as a function of time.
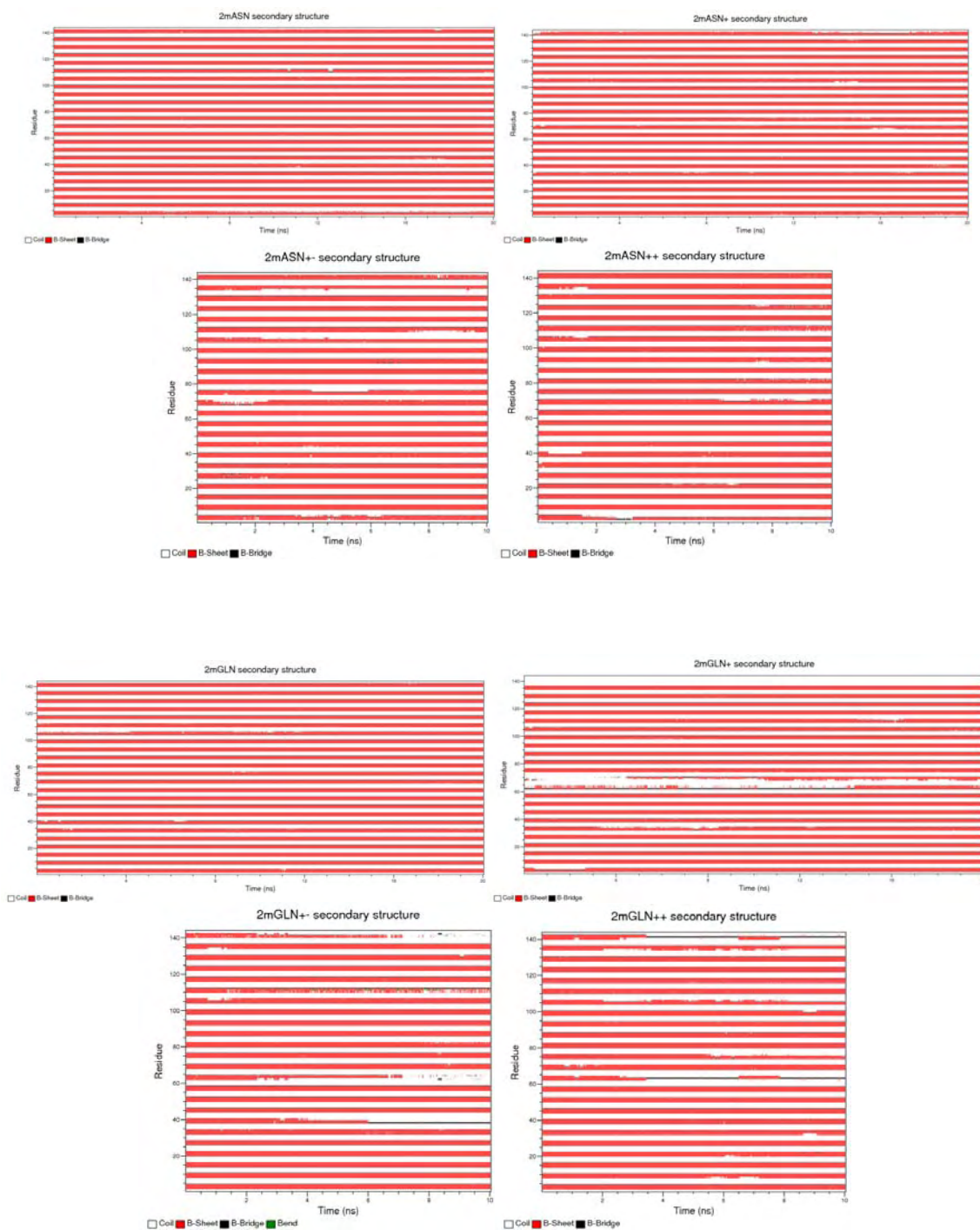
Figure 5. Secondary structure content as a function of time.

CHEMICAL SPECIATION OF SULFER IN MARINE AEROSOL PARTICLES

Rebecca J Hopkins and Mary K. Gilles
Chemical Sciences
Lawrence Berkeley National Laboratory,
Berkeley, CA
and
Alexander Laskin
Pacific Northwest National Laboratory
Richland, WA

1. Abstract

Chemical speciation and apportionment of sulfur containing compounds in individual marine particles is facilitated by a complementary combination of microanalysis techniques. Chemical speciation of sulfur has provided insight into the atmospheric chemistry of marine particles collected in a field study conducted at Point Reyes National Seashore, CA. The results indicate separate formation of methylsulfonic acid (MSA) in cloud droplets and ammonium sulfate in smaller particles. These observations are consistent with two different pathways in the multiphase oxidation chemistry of dimethyl sulfide (DMS) in the marine boundary layer as shown in the recent modeling study of *von Glasow and Crutzen*.[1]

2. Introduction

Dimethyl sulfide (DMS) is the most important gaseous precursor for sulfate aerosols over the oceans.[2] DMS is produced by phytoplankton and subsequently emitted to the atmosphere. Once in the marine boundary layer, it is oxidized *via* two main reaction pathways: addition of an O atom or abstraction of an H atom. The major DMS oxidation products fall into two classes: 1) those that form new particles and can act as new cloud condensation nuclei (CCN) such as H_2SO_4 and 2) those that condense onto existing particles increasing the particle diameter such as dimethylsulfoxide (CH_3SOCH_3 or DMSO), methanesulfinic acid ($CH_3S(O)OH$ or MSIA), methanesulfonic acid (CH_3SO_3H or MSA).[1] The partitioning between H_2SO_4 and other DMS oxidation products is important because increasing the number of particles and increasing particle size can impact climate related properties of aerosols and cloud droplets differently, *i.e.* scattering and absorption of sunlight (direct effect) as well as changing the microphysical structure, lifetime, and surface area of clouds (indirect effects).
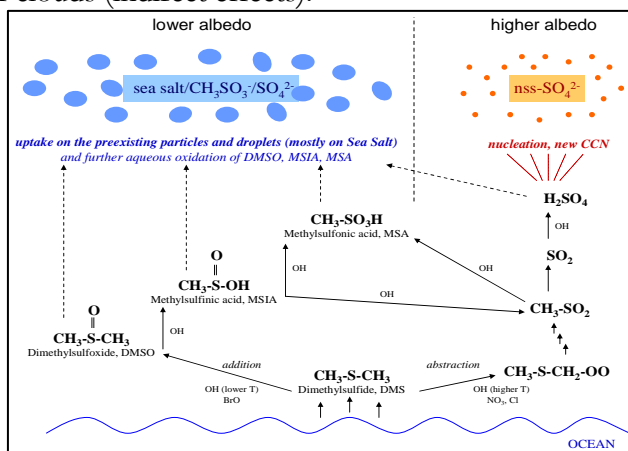
Figure 1 – Schematic diagram illustrating the different atmospheric oxidation pathways of DMS emitted from the ocean.

3. Results

Collaborative work conducted at Pacific Northwest National Laboratory (PNNL) and Lawrence Berkeley National Laboratory (LBNL) has shown the presence of both mixed $CH_3SO_3^-$/nss-SO_4^{2-}/ss-SO_4^{2-} and separate nss-SO_4^{2-} particles from atmospheric aerosols collected at Pt Reyes, CA. This confirms the existence of two oxidation pathways for DMS under cold, cloudy conditions. Scanning electron microscopy (SEM) images presented in Figure 2 illustrate the very different appearance of these particles. The mixed $CH_3SO_3^-$/nss-SO_4^{2-}/ss-SO_4^{2-} particles display a crystalline morphology while the nss-SO_4^{2-} are round in shape.

(a)   (b)
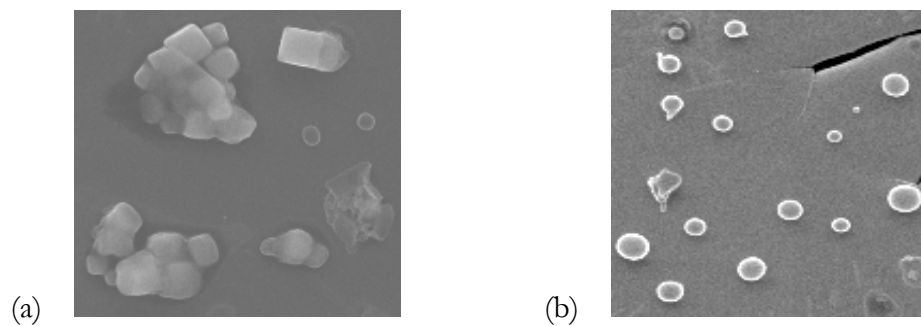
Figure 2 – SEM images of (a) crystalline mixed $CH_3SO_3^-$/nss-SO_4^{2-}/ss-SO_4^{2-} particles and (b) round nss-SO_4^{2-} particles.

Time-of-flight secondary ion mass spectrometry (TOF-SIMS) has been used to gain supplementary information in support of the observation of two particle types. TOF-SIMS ion maps show two types of externally mixed particles which can be attributed to Na^+/$CH_3SO_3^-$ (or $CH_3SO_3^-$/nss-SO_4^{2-}/ss-SO_4^{2-}) and NH_4^+/SO_4^{2-} (or nss-SO_4^{2-}) particles. However, while this data supports observations from SEM data, it should be noted that TOF-SIMS is a surface sensitive technique and therefore additional complimentary information has been sought by analysing these aerosol particles using scanning transmission X-ray microscopy (STXM) coupled with near edge X-ray absorption fine structure (NEXAFS) spectroscopy at LBNL.

(a)   (b)   (c)
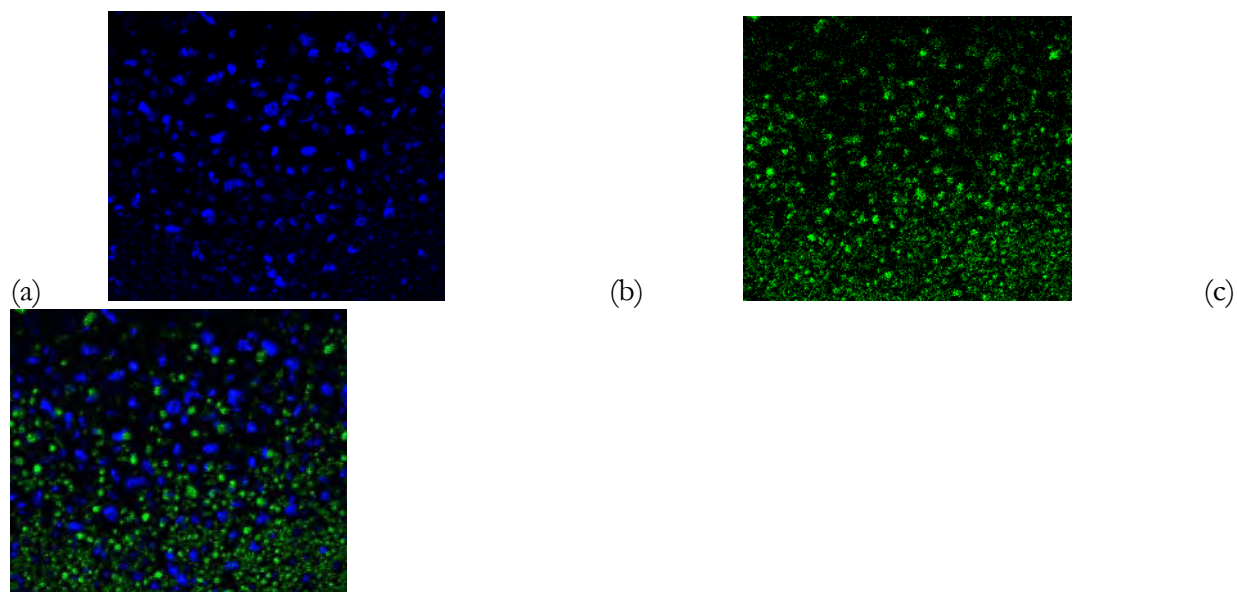
Figure 3 – TOF-SIMS ion maps of (a) Na^+/$CH_3SO_3^-$, (b) NH_4^+/SO_4^{2-} and (c) images (a) and (b) overlaid.

STXM/NEXAFS data has been used to calculate the partitioning of $CH_3SO_3^-$/nss+ss-SO_4^{2-} in individual aerosol particles,[3] but this result alone does not enable the branching ratio of the two oxidation pathways of DMS to be calculated. A combination of data collected using SEM/EDX at PNNL and STXM/NEXAFS at LBNL is needed to determine the $CH_3SO_3^-$/nss-SO_4^{2-} branching ratio. The $[S_{total}]/[Na]$ ratio has been measured for literally thousands of particles using SEM/EDX and when combined with the STXM/NEXAFS data which yields a mean $CH_3SO_3^-$/nss+ss-SO_4^{2-} ratio of 34/66 and the ss-SO_4^{2-}/Na ratio (0.06 for ss-SO_4^{2-}) previously reported in the literature,[4] it has been possible to calculate the $CH_3SO_3^-$/nss-SO_4^{2-} ratio and therefore the branching ratio of the two oxidation pathways of DMS (see equations 1 and 2).

$$\frac{[S]_{total}}{[Na]} = \frac{[SO_4^{2-}]_{ss}}{[Na]} + \frac{[SO_4^{2-}]_{nss}}{[Na]} + \frac{[CH_3SO_3^-]}{[Na]}$$

(1)

$$\frac{[S]_{total}}{[Na]} \times \frac{0.34}{0.66} = \frac{[CH_3SO_3^-]/[Na]}{[SO_4^{2-}]/[Na]} = \frac{\dfrac{[CH_3SO_3^-]}{Na}}{0.06 + \dfrac{[SO_4^{2-}]_{nss}}{[Na]}}$$

(2)

Figure 4 illustrates the combined SEM/EDX and STXM/NEXAFS data which plots the $CH_3SO_3^-$/nss-SO_4^{2-} ratio for five particle size ranges. It is evident that the branching ratio is size dependent, but an average value of 0.6 can be extracted. This branching ratio can now be used in atmospheric climate models to better understand the impact of sulfur chemistry on global climate change.
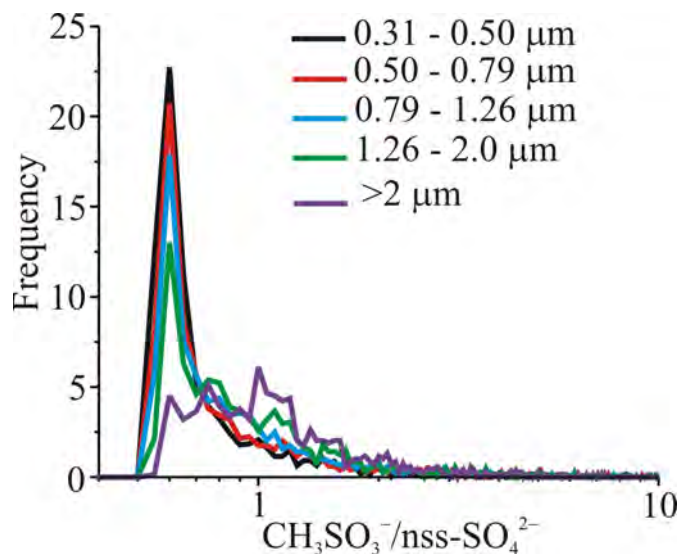
Figure 4 - Distribution of $CH_3SO_3^-$ to nss-SO_4^{2-} present in particles with diameter in the range $0.31 - 0.5$, $0.5 - 0.79$, $0.79 - 1.26$, $1.26 - 2$ and > 2 μm.

4. Conclusion

The branching ratio of two oxidation pathways of DMS which is emitted from the ocean into the atmosphere has been determined using the combined experimental data from three microanalysis techniques. SEM/EDX has been used to quantitatively assess the elemental composition of individual aerosol particles, TOF-SIMS has enables qualitative molecular speciation of sulfer containing compounds in individual particles and STXM/NEXAFS has facilitated quantitative assessment of $CH_3SO_3^-$ versus SO_4^{2-} within individual particles. The combination of these results has yielded an average branching ratio of 0.6 for this important atmospheric chemical reaction which can now be used to model the impact of this sulfur chemistry on global climate change.

5. References

1.   R. von Glasow, P. J. Crutzen,, *Atmos. Chem. Phys.*, 2004, **4**, 589.
2.   R. J. Charlson, J. E. Lovelock, M. O. Andreae, S. G. Warren, *Nature*, 1987, **326**, 655.
3.   R. J. Hopkins, A. V. Tivanski, Y. Desyaterik, A. Laskin, M. K. Gilles, *In preparation*.
4.   L. M. McInnes, D. S. Covert, P. K. Quinn, M. S. Germani, *J. Geophys. Res.*, 1994, **99**, 8257.

Mechanistic and Energetic Studies of Radical

Peptides by means of FT-ICR SID MS

Name: Ngor Wai (Corey) Lam and Ivan Keung Chu

Department of Chemistry,

The University of Hong Kong, Hong Kong

and

Dr. Julia Laskin

Pacific Northwest National Laboratory

Richland, WA

Collective efforts (Jean, Julia and Ivan K. Chu) from the 2005-ICPCPSRI have lead to successful execution of the proposed project and result significant contribution toward understanding of the gas phase chemistry of novel radical cationic peptides. With the previous demonstration of kinetic studies with molecular radical angiotensin, we will extend our investigation on anionic radical cationic angiotensin III using similar methodologies. Studies of odd-electron radical cationic $M^{\bullet+}$, $[M + H]^{\bullet 2+}$, and anionic $[M - 2H]^{\bullet-}$ peptides can help to bridge the gap between small cations and protonated peptide ions and facilitate a better understanding on the role of hydrogen atom that governs radical peptide fragmentation. Our intended studies will utilize time- and energy-resolved SID, combined with an RRKM-based modeling approach, to determine the energetics of dissociation of medium-size molecular radical anionic oligopeptides, such as angiotensin III(RVYIHPF) and its derivatives. Our recent success at forming a wide variety of radical anions of oligopeptides should greatly expand the scope of investigations of molecular radical cations of oligopeptides.[1] The ability to form peptide radical anions in the gas phase raises a question about their stability relative to those of the corresponding protonated species and smaller organic radical anions. Are the energetics of dissociation of these species similar to the dissociation energetics of smaller radical anions? Does conformational flexibility of these molecules have an effect on their gas phase stability? It is known that the bond dissociation energy for organic radical anions is in the range 2.5–6 eV,[2] while dissociation of protonated peptides requires only 0.8–2 eV.[3] This relative ease of dissociation of protonated peptides has been attributed to the presence of a proton that migrates along the backbone of the peptide and weakens the peptide bond in its

vicinity—the "mobile proton model".[4] Studies of $[M - 2H]^{\bullet-}$, $M^{\bullet+}$ and $[M + H]^{\bullet 2+}$ can help to bridge the gap between small organic anions and protonated peptide ions and facilitate an understanding of the factors that govern bond strengths in ionic systems. This $M^{\bullet+}$ and $[M + H]^{\bullet 2+}$ species have a large number of vibrational degrees of freedom, which results in a slow dissociation that is ideally suited for kinetic studies on the timescale of our FT-ICR SID MS. An ion of almost identical molecular weight—protonated angiotensin III(RVYIHPF)—has been studied extensively and validated using the proposed methodologies.

For the upcoming program in the Pacific Northwest National Laboratory's Summer Research Institute in Interfacial and Condensed Phase Chemical Physics, we will conduct experiments on molecular radical anionic oligopeptides using aforementioned method. The advantages provided by SID include very fast ion activation, which eliminates possible discrimination against higher-energy dissociation pathways, and efficient "amplification" of small changes in the dissociation parameters.[4] We will use this approach to address the question of stability of gas phase peptide radical anions. We will use a combination of experimental and computational approaches to conduct the first studies on the energetics of the dissociation of selected peptide radical anions and compare these results with the dissociation energetics of their corresponding cationic species. Collision energy-resolved studies provide important information on the appearance energies of different product ions and on the amount of energy required for dissociation of the precursor ions. Another dimension is added to SID experiments by conducting kinetic studies through varying the delay between the ion–surface collision and the analysis of the resulting products. Although studies of time- and energy-resolved spectra have been conducted so far for only a limited number of large ions, they have demonstrated a great potential for allowing the detailed elucidation of fragmentation energetics and mechanisms.[3]

References:

1. (a) Chu, I. K.; Rodriquez, C. F.; Lau, T. C.; Hopkinson, A. C.; Siu, K. W. M. *J. Phys. Chem. B* **2000**, *104*, 3393–3397. (b) Chu, I. K.; Rodriquez, C. F.; Lau, T. C.; Hopkinson, A. C.; Siu, K. W. M. *J. Am. Soc. Mass Spectrom.* **2001**, *12*, 1114–1119. (c) Bagheri-Majdi, E.; Ke, Y.; Orlova, G.; Hopkinson, A. C.; Siu, K. W. M. *J. Phys. Chem. B* **2004**, *108*, 11170–11181.(d) Chu, I. K.; Siu, S. O.; Lam, C. N. W.; Chan, J. C. Y.; Rodriquez, C. F. *Rapid Commun. Mass Spectrom.* **2004**, *18*, 1798–1802. (e) Chu, I. K.; Lam, C. N. W. Manuscript in preparation.

2. McLafferty, F. W.; Turecek, F. *Interpretation of Mass Spectra*, 4th Ed., University Science Books, 1993.

3. (a) Laskin, J. *Eur. J. Mass Spectrom*. **2004**, *10*, 259–267. (b) Schnier, P. D.; Price, W. D.; Jockush, R. A.; Williams, E. R. *J. Am. Chem. Soc.* **1996**, *118*, 7178–7189. (c) Schnier, P. D.; Price, W. D.; Strittmatter, E. F.; Williams, E. R. *J. Am. Soc. Mass Spectrom.* **1997**, *8*, 771–780.

4. (a) Laskin, J.; Denisov, E.; Futrell, J. H. *J. Am. Chem. Soc.*, **2000**, *122*, 9703–9714. (b) Laskin, J.; Denisov, E.; Futrell, J. H. *Int. J. Mass Spectrom.* **2002**, *219*, 189–201. (c) Laskin, J.; Bailey, T. H.; Futrell, J. H. *J. Am. Chem. Soc*. **2003**, *125*, 1625–1632. (d) Laskin, J.; Bailey, T. H.; Futrell, J. H. *Int. J. Mass Spectrom.* **2004**, *234*, 89–99.

Tandem Accelerator and Ion Beam Techniques

Vu H. Lam and Kevin Coffey

Advanced Materials Processing and Analysis Center

University of Central Florida

Orlando, Florida

and

Theva Thevuthasan

Pacific Northwest National Laboratory

Richland, Washington

I. Introduction

When I joined Interfacial and Nanoscale Science Facility (INSF) at Environmental Molecular Sciences Laboratory (EMSL) as a Summer Research Intern (SRI) student intern, my project was to learn the ion beam capabilities commonly utilized in the accelerator facility and help the users in the laboratory. Several projects were identified for me to work on in collaboration with various users and EMSL scientists including; (1) learning the components of the accelerator, beam lines and end stations, (2) mastering the simulation packages such as SIMNRA and GUPIX along with the experimental capabilities, in particular, Rutherford backscattering spectrometry (RBS), nuclear reaction analysis (NRA), and proton induced x-ray emission (PIXE), (3) participate and contribute to the experiments conducted by a user from Harvard university, and (4) contribute to the maintenance of the instrumentation in the accelerator facility. During my stay at EMSL, there was a breakdown of the analyzing magnet due to cooling lines break down and as a result the lab was shut down for three weeks for intensive repair of the magnet cooling system and the high energy beam line electronics. This activity provided a very good opportunity to troubleshoot some of the instrumentation and, as a result, I could learn and obtain hand on experience in fixing some instrumentation in the laboratory.

Overall, the visit to EMSL as a part of this program gave me an opportunity to learn new things. In addition, it provided valuable experience in running and maintaining some experimental systems which may not be widely available. This report summarizes the components and capabilities available in the accelerator facility. Finally, I sincerely appreciate the opportunity given to me to visit EMSL and work with the scientists at EMSL by the SRI administration.

II.   Ions Beam Materials Accelerator Laboratory (IBMAL)
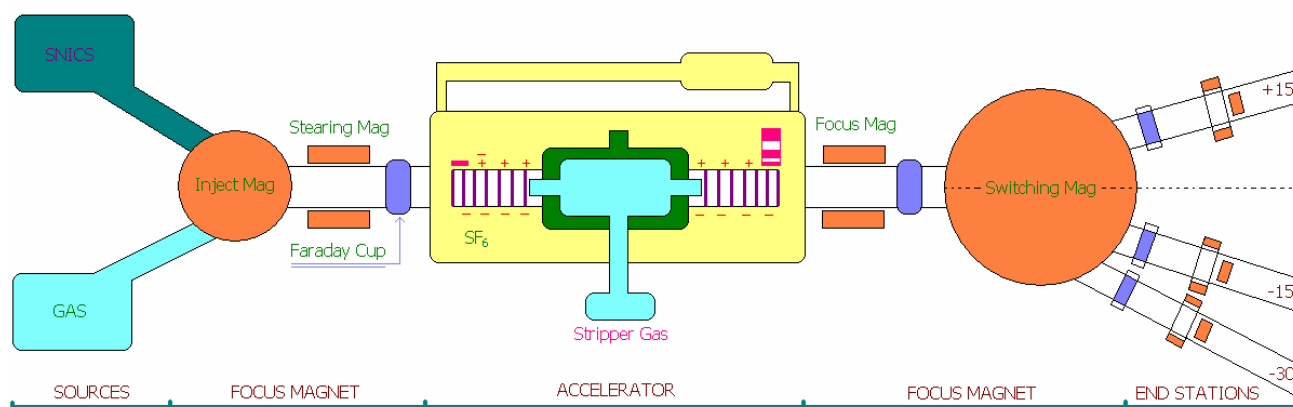
Fig 1: IBMAL

The accelerator lab can be break down to three main sections. The first section contains the sources of the ions beam. Second is the accelerator chamber and at last are the end stations. In general, the operation of the accelerator lab can be described as follow. First, negative ions will immerge from the source into the accelerator chamber. Right in the middle of the chamber consist of highly stored potential that was build up by using the Van de Graff method. From the beginning of the chamber to the middle region, the negative ions will attract by the positive potential and accelerate with the speed corresponding to the applied voltage. When the ions reach the middle regions, stripper gas will stripped off some of the electrons surrounding the particles and change the ions from negative to positive. The end region of the chamber will be grounded, in which creates a region that will attract the positive ions. From here, the positive ions that were created by the stripper gas will accelerate with the same potential as it first went from the beginning toward the middle of the tube. In general, the ions will accelerated twice as much of energy as the initial applied voltage. When the positive ions go out of the accelerator tank, it will then be focus down and steer to the end stations desired. There are three end

stations; positive 15 degree, negative 15 degree, and negative 30 degree. Each station performs different experiments such as PIXE, NRA, RBS, and ERDA (Elastic Recoil Detection Analysis).

Each section of the IBMAL will be analyze separately and discuss in greater detail about its functionality and operations. Like the name indicated, the source provides the ions to be accelerate. Within the source section, there will be two distinct kind of source. One is considered to be a solid source and the other is gas. The solid source is called SNICS (Source of Negative Ion by Cesium Sputtering) source.
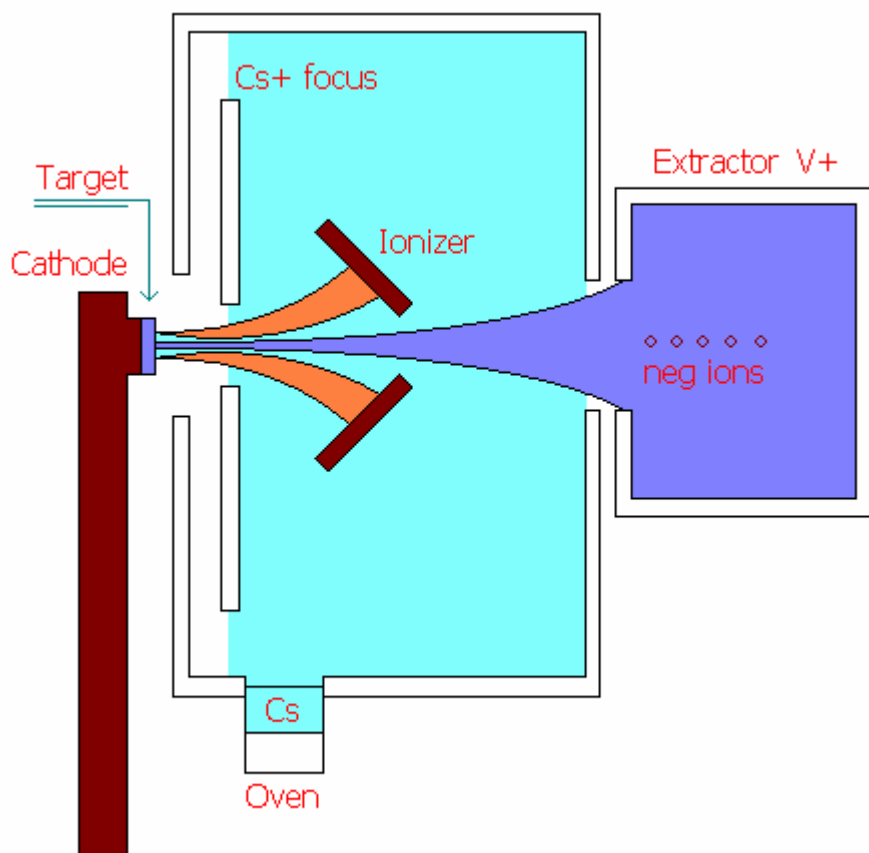
Fig 2: SNICS Source.

The target was hold by the cathode arm and was placed in the windows that can be access by the Cesium focus beam. The target can be any target that the user desired. The most common used target in the accelerator lab is gold (Au). The Cesium source was first placed in the oven chamber. The initial form of the Cesium source started as liquid. When the oven starts to heating up, the Cesium begins to vaporize. The temperature of the SNICS chamber increase

gradually from room temperature to 150º C. Cesium particles will then be ionized by the electric field created by the ionizer. Because the target was attached to the cathode, the positive Cesium ions will accelerate and focus on the target's surface. The Cesium ions started to sputter the target and kick out target particles. In this stage, surround the chamber will contain lots of target's electrons and holes pair created by the Cesium sputtering. The extractor has positive voltage applies at the end, therefore attract target electrons. In the end, the ions coming out of the SNICS source will be negative ions.
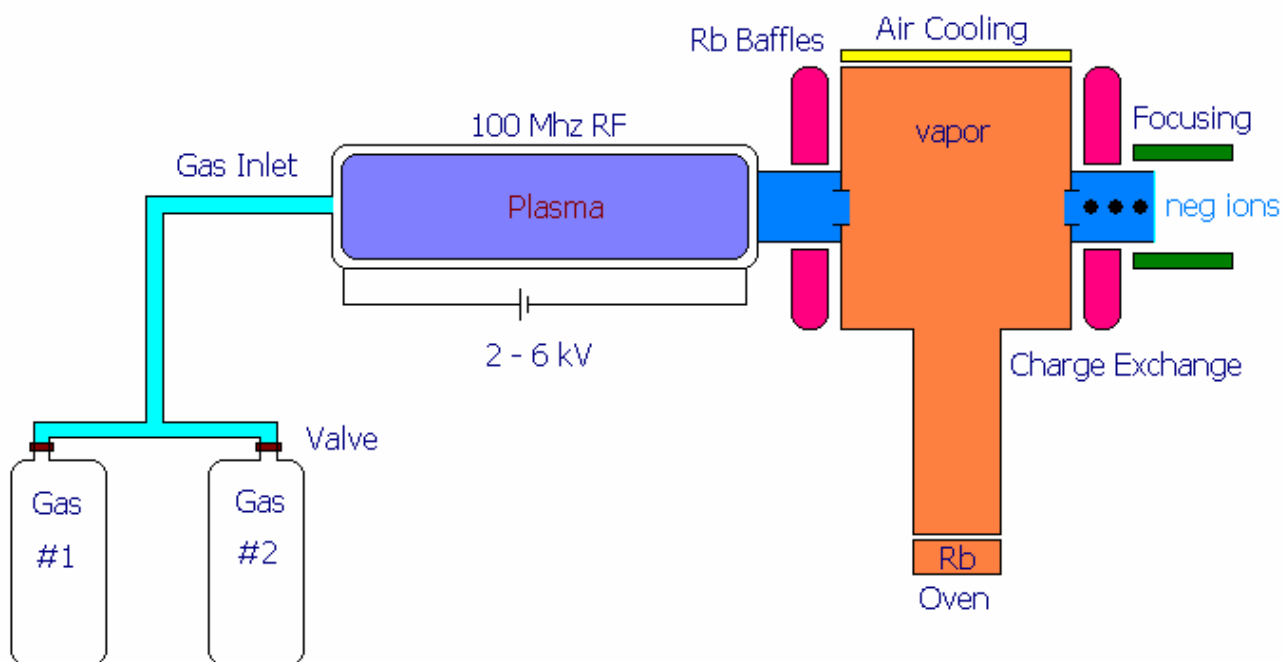
Fig 3: Gas Source.

Figure above illustrates the structure as well as the operations of the gas source. The gas source contains two separate gas tanks. One is Helium and the other is Hydrogen. The gas that most common used is Helium. The gas will enter the plasma chamber where they will be ionized. The plasma chamber has an applied potential of 6 kV. This potential has to increase slowly from 2 to 6 kV during the warm up sequence. The frequency that is use for this chamber is 100 MHz. The RF (Radio Frequency) power supply will ionized the He gas and created plasma. The Helium ions will then enter the charge exchange chamber. In this chamber, the Rubidium source was heat from the oven below from room temperature to 250º C. The Rubidium source starts as a liquid form then vaporize by the heat. This source will give away electrons and make the ions turning from positive to negative ions.

Next stage is the focus magnet. In this region when the ions were injected from the source, the magnet was used to focus the size of the beam. The Faraday cup is also used in the area to control the beam before it enters the accelerator chamber.
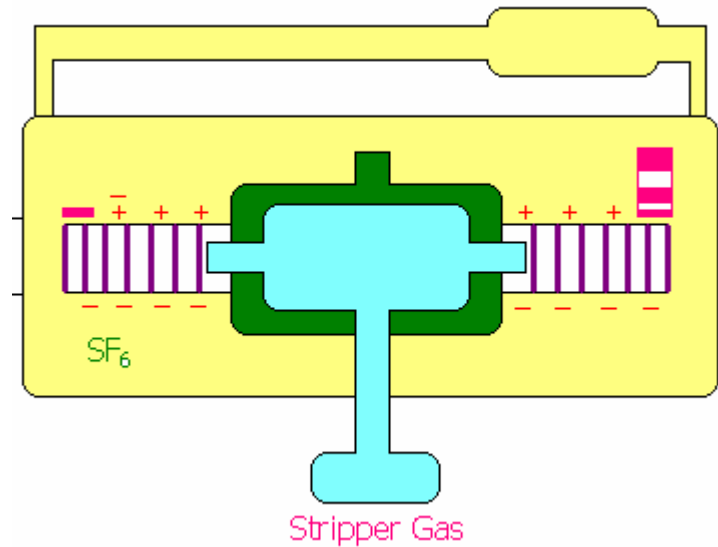
Fig 4: Accelerator Chamber.

There are many important components that inside the accelerator chamber. The first most important component is the applied potential. The energy of the ion beam can be defined in the equation below in which E is the ions energy, q is the charge of the ions and V is the terminal voltage.

$E = (q + 1) * V$

The terminal voltage (V) has a voltage range from 0.5 MeV to 3.0 MeV. By using the Van de Graff method, the potential can be build up from a 50 kV source.
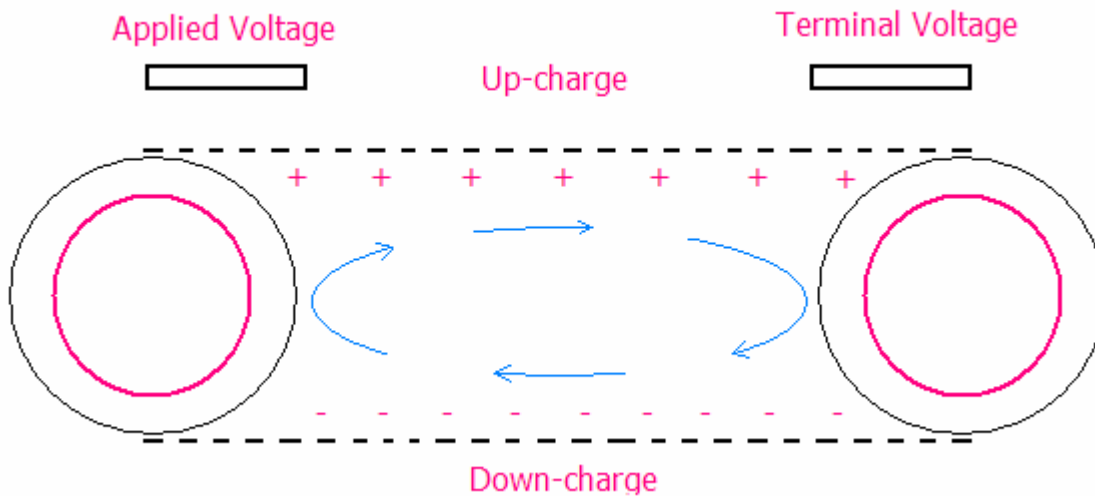
Fig 5: Van de Graff Method.

At the applied voltage region, negative charge will be applied in which attract the positive charge that will be localized on the surface of the chain. The voltage that applied at this region is about 50 kV. The chain will then carry the positive charge to the terminal voltage region where it was collect and store. This procedure keeps repeating until it reaches a desire potential. The charge of the ions (q) can be described as follow. When the negative ions enter the entrance of the accelerator chamber, it will accelerate toward the middle of the chamber where the terminal voltage applied. The middle region of the accelerator chamber will perform a special task called charge exchange. A gas tank is connect to the middle region of the chamber and contains either Nitrogen gas or Argon gas. These gases were used to strip off the electrons from the ions and converted it from negative ions to positive ions. During this interaction, the ions will obtain different charge such as +1, +2, +3, +4, +5, or +6. This is the number that is used to calculate the energy obtained. The end of the accelerator chamber is grounded; therefore attract the positive ions in which make it accelerate toward the end of the chamber.

Between the chain in the middle of the chamber and the surround tube, the entire hollow region was filled by an insulating gas (SF6) to insulate the high potential created in the accelerator chamber. This is a dangerous gas due to its nature to consume Oxygen. The upper pipe on tope of the main tube is used to filter out the moisture of the gas to keep it more insulated.

When the ions beam exit the accelerator chamber, it will then enter the focusing area. After focus the beam into smaller diameter, it was then steer it to a destination station by using the switching magnet. The angle of the outgoing beam was treated as a reference point and there are 3 end stations, one positive 15º, one negative 15º, and one negative 30º. Each branch consists of two basic instruments that use to aid the accuracy of the beam. One is the Steering Magnet and other is the Faraday Cup as figure 6 illustrate. Because the beam enter the branch is not guarantee to be right at the middle of the pipe, therefore the Steering Magnet was used to ensure that the beam is right on the middle and be able to arrive at the end station. The Faraday Cup is used to control the beam whether allow or not allow the beam to enter the vacuum chamber. One drawback is only one station can be access the beam once at a time.
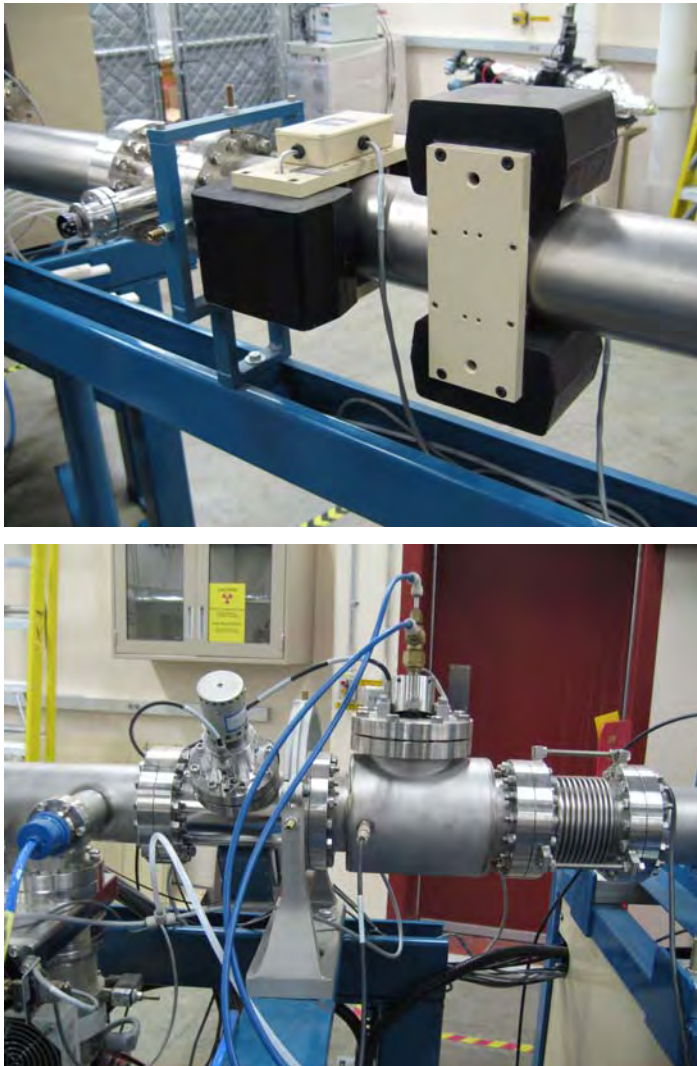
Fig 6: (a) Steering magnet, (b) Faraday cup.

III.   Applications.

Each station in the accelerator lab performs different experiments. The end stations with the branch of positive 15 degree can performs multiple experiments such as PIXE, PESA, STIM, RBS, and ERDA. Each experiment will be discussed briefly about its definition and its fundamental operation. The most common experiment that's using PIXE, PESA, and STIM is characterized aerosol samples. Aerosol samples are thin Teflon film with aerosol particles coating on its surface. The sample was collected in Mexico City to study about the pollution in the air. The samples are fairly thin so the beam can penetrate through. It is 2.5 μm thick with particle deposits on its surface. PIXE is an experiment that using the ions beams to create and collect X-ray from the sample. When the beam hit the core electron of the atoms and has enough energy to kick out that electron, the next highest energy electron will fall down and filling the gap. When this electron moves down, it will emit X-ray. The X-ray was then detected and display with the corresponding energy of the ion beams. PIXE can be use to detect elements in which range from Sodium to Uranium. PESA (Photon Elastic Scattering Analysis) in the other hand is used to measure the Hydrogen quantity in the sample. The ions beams that use in PESA is Hydrogen ion. When the Hydrogen ions hit the sample, it will collide with the Hydrogen atoms inside the sample and scatter away at an angle. A detector will be place at a desire angle and will collect the scattering Hydrogen ions. The graph yields from the measurement represent the amount of Hydrogen inside the sample. In this experiment, PESA is not an ideals method to measure higher element such as Carbon, Oxygen, and Fluorine due to their close range of mass. However, PIXE can be use in this case to detect a while range of elements.
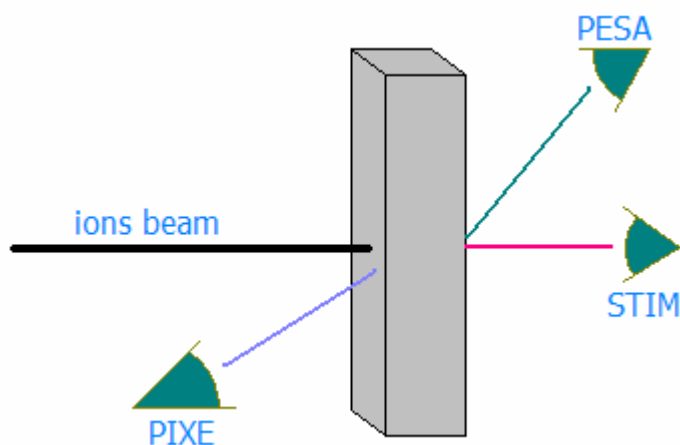
Fig 7: PIXE, TIM, and PESA.

STIM (Scanning Transmission Ion Microscopy) is used to calculate the total mass of the aerosol particle deposited. The Hydrogen beam penetrated the thin sample and exit to the other side. Initially, the Hydrogen beam is coming in with a known energy (Eo). When the Hydrogen beam exits the sample, it will lose some of it energy due to collision inside the sample. This energy (E1) is measured and used to calculate the total mass of the aerosol collected based on this equation.

$\Delta E = Eo - E1$

RBS (Rutherford Backscattering Spectrometry) can be described in a similar way. For this method, user can find the composition of the material as well as its elements. As illustrate in Figure 8a, the ions beam coming in to collide with the sample surface. The sample atoms consist of different elements. Each element has it own mass and it can be heavier or lighter comparing to the mass of the ion beam. When the ion beam hit the sample atoms, it will lose some of its energy when bounding backward. The initial energy (Eo) will always be greater than the back scattering energy (Em). For heavy atom, the ion will bound back with much greater distance as well as energy compare to the atoms with lighter mass. When the ions pass through the first layer, it will lose some energy (E'o) and collide with the second layer in the sample. Through this, sample thickness can be illustrated.
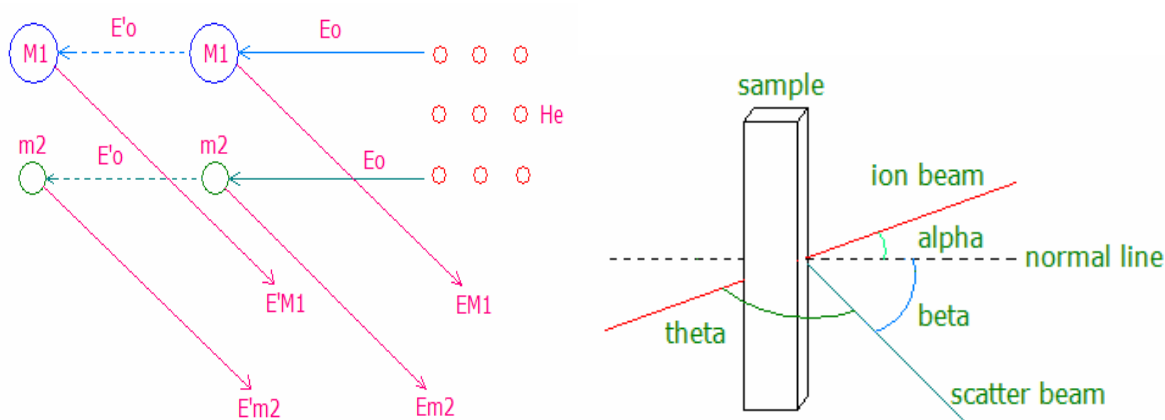
Fig 8: RBS (a) ions beam collision, (b) angles beam.

After achieve the graph of the RBS data, a simulation need to be performs to calculate the composition of the sample's elements. The simulation software called SIMNRA was used to analyze the data. In order to perform the simulation, certain information need to be provided

such as alpha (α) angle, beta (β) angle, and theta (θ) angle as Figure 8b. It also needs the initial guess of the elements and its composition. From there, user can change the parameter to simulate the graph so it can be identical to the experiment graph. After succeed the simulation, the software will provide the user the composition of the sample as well as the thickness. One drawback of RBS is it's not that sensitive to lighter elements.
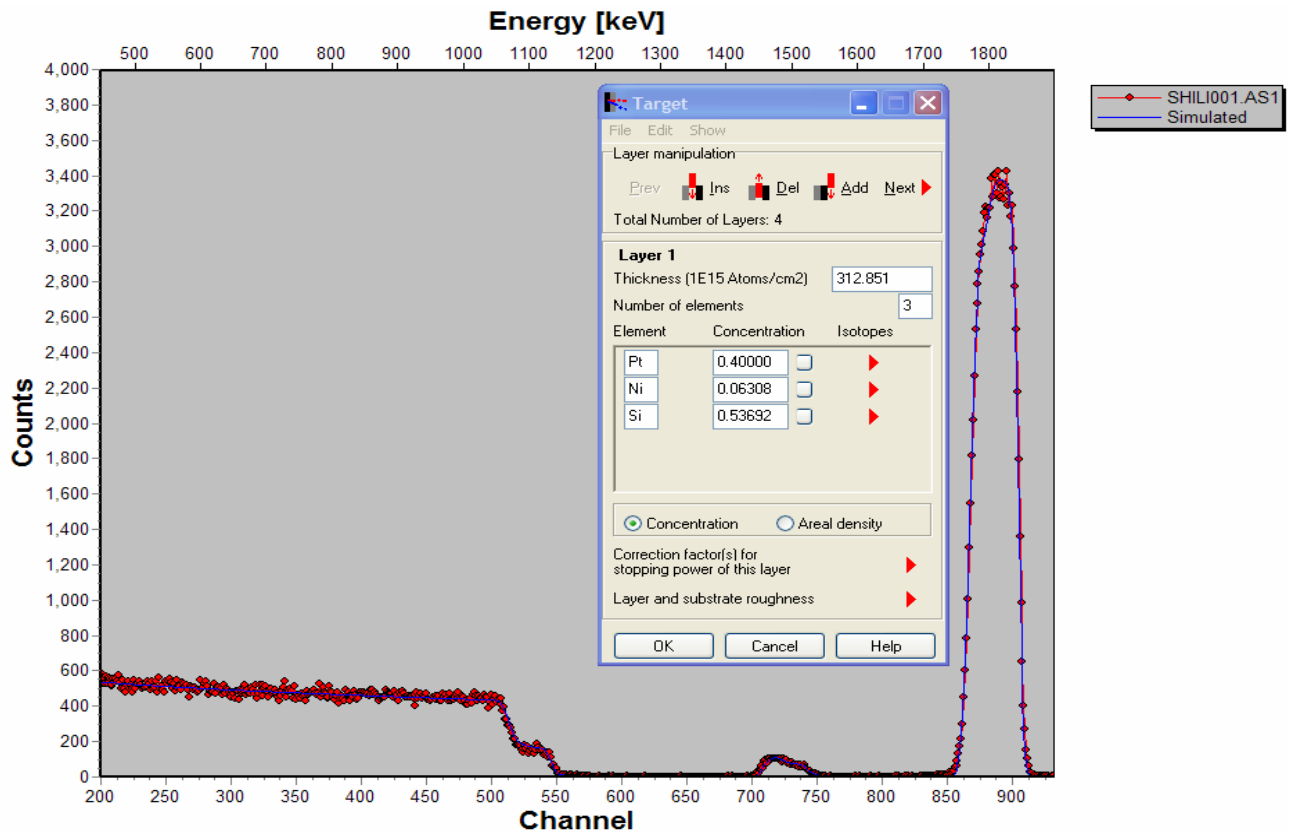
Fig 9: SIMNRA

ERDA (Elastic Recoil Detection Analysis) is mainly used to find material's surface sensitivity. It's also called Time-of-Flight ERDA. It's consists of few main components and first is the target. The target is defined by the user in which determine the ions that use for sensitivity testing. Second is the beam line. The ions beam for this experiment can be either Hydrogen or gold. Third is the detector station. There are two stations separate with a fix distance. Each station contains a carbon foil in which use for start and stop signal. At the end of the arm, another station is located to measure the energy of the beam line. There are two distinct tests that can be run by using the ERDA chamber. First is sensitivity sensor by using hydrogen ions beam line. The target that is used for this run is normally SiO2. Due to the lightness of

hydrogen, when the beam hit the target, it will bounce toward the detectors. The ions will first hit the first carbon foil and produce secondary ions on the surface of the foil. The carbon foil's thickness is just about few micron meters; therefore ions beam can be easily pass through and very sensitive for detection. When the carbon foil creates ions on its surface, the detector will collect those ions by the applied potential and produce a pulse of signal that will recorded as a starting point. The hydrogen beam continues to travel toward the second detector where it again produce secondary ions and recorded as the stopping point. After passing through the second detector, it will collide with the last detector that located at the end of the arm. From here, the detector obtains the energy of the ions. Velocity (V) of the ions beam can be obtains by a simple equation where D is the fixed distance of the two detectors and T is the time measured when passing through the carbon foil.

$$V = D / T$$

With the energy (E) obtain by the last detector, mass (M) can be calculated.

$$E = \frac{1}{2} M * V^2$$

Hydrogen ions beam is very limited when dealing with sensitivity of other materials. Therefore the second method is using the gold ions beams for sensitivity sensor of other materials. The target for this test can be any films that the user desired. However, the common target that was used in the lab is SiO_2. Unlike hydrogen beam line, the gold ions beam is much heavier in which can knock out the particles of the target. When the gold ions beam coming in, it collided with SiO_2 target and sputter Silicon and Oxygen particles toward the detectors instead of the gold ions themselves. The measurement of the Silicon and Oxygen is identical to the Hydrogen ions when passing through the detectors. However, one advantage of this method offer is to create a broader range of materials that can be test for their mass and energy.
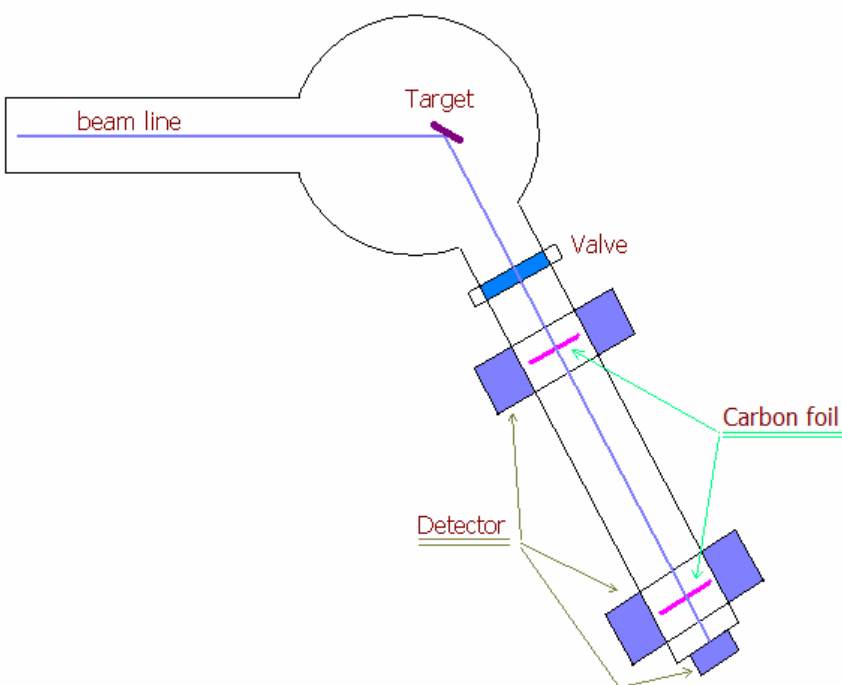
Fig 10: ERDA.

NRA (Nuclear Reaction Analysis) is an experiment that very similar to RBS. However, RBS is ideal for heavy elements and NRA is for light elements. When the ions beam collided with the sample, it will hit the nucleus and change its characteristic. During this interaction, the nucleus will emit gamma ray and particles. NRA also used to analyze crystal lattice structure and the damages of the interfaces between different materials. It's also known as channeling. In a crystal lattice structure, the atoms are formed in a specific orientation and created a hollow region between them. This hollow region is called a channel. When the ions beam hit the surface of the sample, it will collide with the first layer. If the crystal is perfectly perpendicular with the ions beam, only the first layer atoms will interact with the beam. The region when the beam hit the atoms will yield the scattering energy. However, when the beam hit the channel region, it will not collide with any atoms; therefore the scattering energy will be very small. By using this technique, scientist can determine the alignment between the channel and the ions beam.
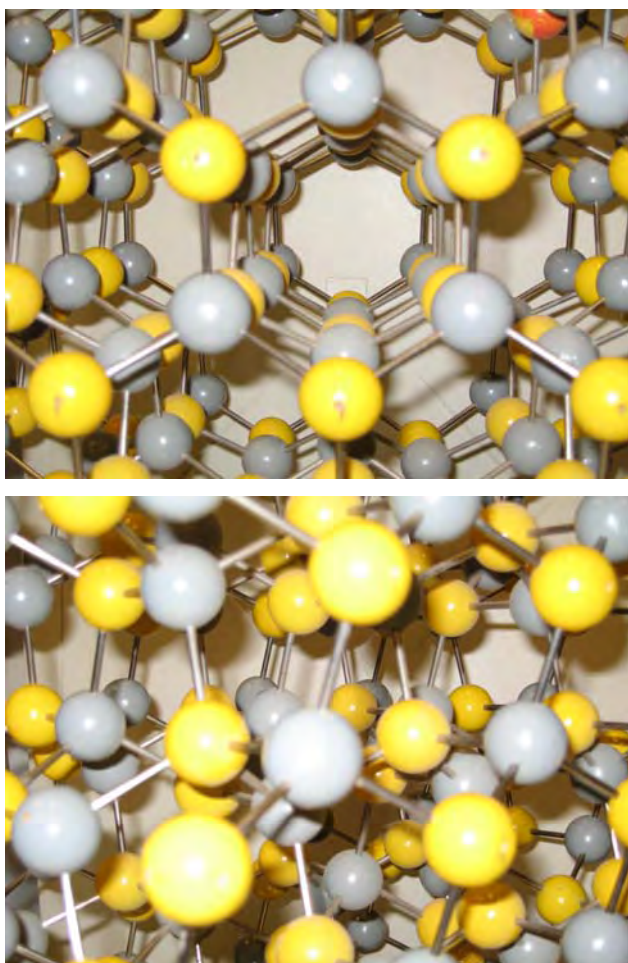
Fig 11: Crystal lattice structure. (a) Channel orientation, (b) Random orientation.

Before performing an alignment experiment in the crystal structure, a channel needs to be found. Finding a channel in the lattice requires multiple rotations of sample positions. Initially, place the sample as perpendicular to the beam as much as possible. The following step is to apply the ions beam to the sample. There are two main positions that need to be rotated. First position is along the X-axis. The sample will stay still at the middle region and only rotate at the end point along the X-axis. During this rotation, the ions beam will hit the surface of the sample and collect energy reading. A pattern needs to be recognized while recording the data. The energy will start high, then decreasing, and will increasing. This indicates that the middle region is the channel. To increase accuracy, second or a third run is recommended for the same axis. The second position is along the Y-axis. This procedure will repeat until a channel is found. After obtained the coordinate of the X and Y axis, repeat the run for one more time to make sure the crystal lattice is align with the beam. There are several advantages by using NRA. First advantage of the channeling method is used to determine the lattice alignment between two films, the substrate and the film. When the channel is found, the beam will go

through the channel and pass through each layers of the film. If the lattice structure of the substrate and the film are aligned, the scattering will yield very low and uniform energy. If not, the experiment proves that the film and the substrate crystals lattice structure are not aligned. Second advantage of this method is to see the defect of the interface layer. Even though the film and the substrate has their crystal lattice structure aligned, however the interface between them may distorted. This method provides a deeper understanding at the interface level between two surfaces. The third advantage is to test the uniformity of the film surface compare to the rest of the crystal lattice structure. The film itself and the substrate lattice structure maybe aligned; however, the surface can be distorted. The figure 12b indicates, the beam will go through some region that the lattice align and collide with some region that the surface is distorted. With this method, scientist can learn about film quality on the surface level.

Fig 12: NRA (a) interface distorted, (b) surface distorted

IV.   Acknowledgments.

Thermal and Non-thermal Reactions at the Water/TiO$_2$(110) Interface

Christopher Lane and Thomas Orlando
Department of Chemistry & Biochemistry
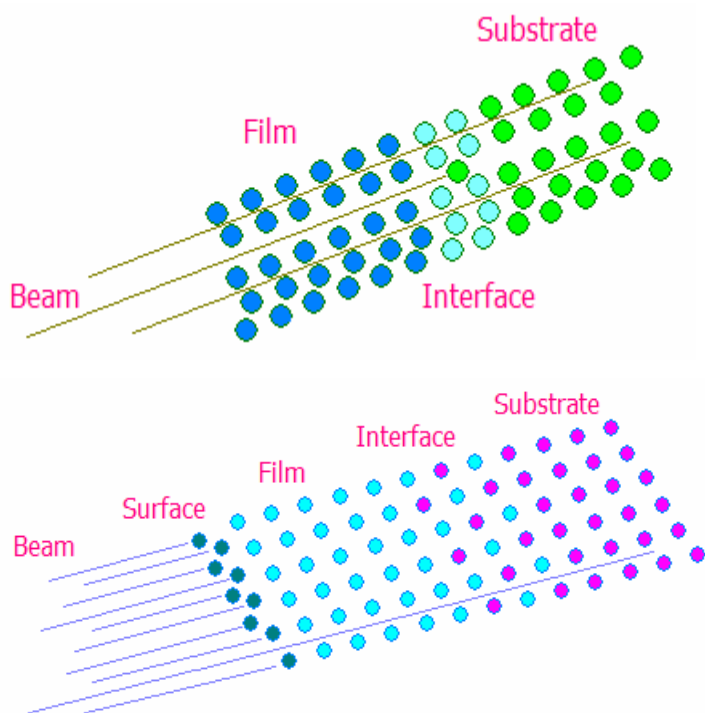Georgia Institute of Technology,
School of Chemistry and Biochemistry
Atlanta, GA
and
Dr. Greg Kimmel
Pacific Northwest National Laboratory
Richland, WA

Titanium dioxide is an environmentally abundant material that has become a lucrative industrial commodity for its uses and applications such as white pigments in paints and cosmetics, heterogenous catalyst, corrosion-protective coating, optical coating, and electric devices such as varistors. [1] Besides its applicability, TiO$_2$(110) is the most studied model transition metal oxide making it a standard surface to understand thermal and non-thermal reaction dynamics of water dissociation. Hydrogen production from a non-organic source is one route for manufacturing a fuel that is completely greenhouse gas emission free. Fujita et al. has demonstrated hydrogen production via the photocatalytic dissociation of water on the TiO$_2$ surface. [2]

To understand the complete reaction landscape of the following reaction:

$$2H_2O(a) \rightarrow 2H_2(g) + O_2(g)$$
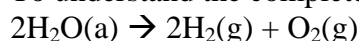
where (a) is an adsorbed water species and (g) represents gas, we planned to study the direct interactions and non-thermal energy dissipation of water as well as hydrogen and oxygen on the TiO$_2$ surface. Our experimental apparatus consists of a low-energy electron gun, a closed-cycle helium cryostat, a molecular beamline for adsorbate deposition, an Auger electron spectrometer, and a quadrupole mass spectrometer (QMS) with an integrating cup. Typical base pressures for the system were 1×10^{-10} Torr. The 1 cm diameter TiO$_2$(110) crystal was mounted in a resistively heated molybdenum base plate. K-type thermocouples attached to the TiO$_2$ single crystal and to the molybdenum were used to monitor heating and cooling cycles in the range of 27 – 1050 K. The amorphous solid water (ASW) ice films were deposited with the molecular beam ($\sim 2 \times 10^{14}$ molecules/cm^{2}s) at normal incidence to the TiO$_2$(110) surface at 100 K. The molecular beam produced a film centered on the substrate having a diameter smaller than that of the substrate. The first monolayer (ML) coverage of water was defined as the desorption yield from the Ti^{+4} rows in the TPD spectra. During ESD experiments, the electron beam was oriented 35° to the sample normal where the films were irradiated with variable energy 100 eV incident electrons. The water films were uniformly irradiated by repeatedly scanning the electron beam in a grid pattern over an area slightly larger than the film. A typical instantaneous current density per scan is $\sim 2 \times 10^{15}$ electrons/cm^2 s, and beam spot size is ~ 1.5 mm.

Prior to experiments, the TiO$_2$ was annealed in vacuum. This process introduces intrinsic defects or oxygen vacancies into bulk crystal thus increasing the conductivity and greatly reducing charging effects during electron irradiation experiments. Before each experiment, the TiO$_2$(110) surface was cleaned by Ne ion sputtering for 3 min at 300 K then

annealed for 10 min at 950 K. From the integral of the high temperature recombinative TPD peak of H_2O, the surface has approximately 5% oxygen vacancies. [3,4]

As depicted in Fig. 1, the (110) surface is composed of corrugated rows of O^{-2} and Ti^{+4} in the [001] direction. Two types of oxygens exist on this surface, the threefold coordinated oxygen that resembles the bulk oxygen, and the twofold coordinated bridge bonding oxygen (BBO). When a BBO is thermally removed, an oxygen vacancy is created which is denoted by the white dashed circle in Fig. 1. Two electrons remain in this vacancy leaving two reduced Ti^{+3} ions. These defect sites drive much of the chemistry on this surface and are the subject of much debate in the literature. [1]
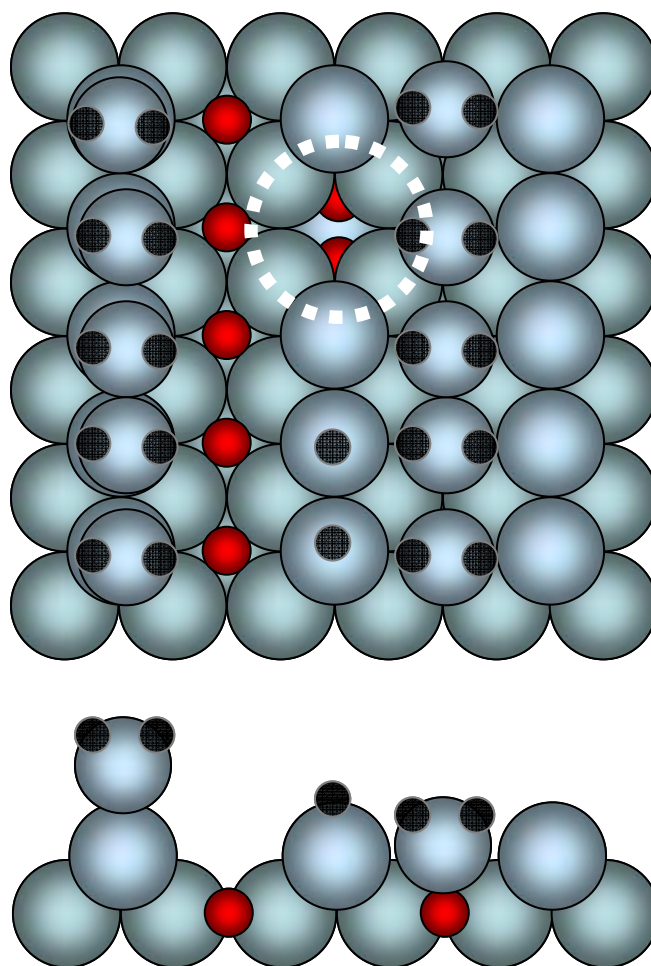
Figure 1. Ball model of the TiO_2(110) surface with adsorbed H_2O. Red balls represent titanium; Blue balls, oxygen; black balls, hydrogen. Water can adsorb on the bridge bonding oxygens (BBOs) and on the Ti^{+4} sites. An oxygen vacancy site is shown encircled by the white dashed line. When H_2O reacts with an oxygen vacancy, two hydroxyls are produced side by side which is also depicted. [5]

We implemented temperature programmed desorption (TPD) and electron stimulated desorption (ESD) measurements to gain an understanding of how water interacts with the TiO_2(110) surface. Briefly, the TPD spectrum of water from the TiO_2 (110) surface is composed of four peaks near 170 K, 200 K, 300 K, and 500 K which have been attributed to the multilayer, water adsorbed on the bridge bonding oxygen, water in the Ti^{+4} rows, and water

from the recombination of surface hydroxyls, respectively. [3] In our figures and discussion, 1 ML (monolayer) coverage of H_2O refers to only the Ti^{+4} site saturation adsorption of H_2O (5.2 x 10^{14} molecules/cm^2).

A summary of the observations and results for our first publication in preparation is given below. Our explanations for these results are still speculative. Other experiments not presented here are also in preparation for publication.

Production of Oxygen Adatom Species Via Electron Irradiation of H_2O on $TiO_2(110)$
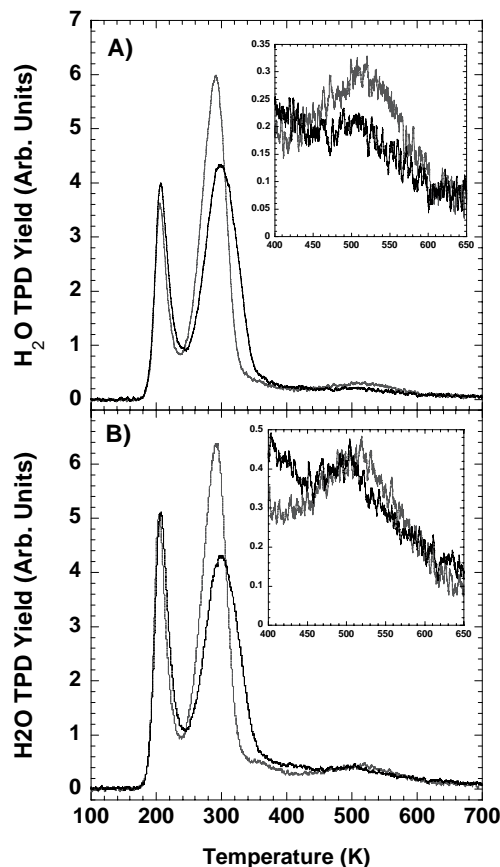
Figure 2. TPDs of 1.2 ML coverage of H_2O taken A) before (gray) and after (black) 700 Torr*s predose of O_2 at 90 K and B) before (gray) and after (black) N=500 rasters of 100eV electrons of 1.2. The insets are enlargements of 500 K recombinative H_2O TPD peak.

The H_2O TPD spectra in both A) and B) frames of Fig. 2 depict the thermal desorption of 1.2 ML coverage of H_2O. In A), we reproduced an experiment done by Henderson et al. [6] where a new surface state of H_2O was observed after predosing the surface with molecular oxygen. The gray TPD H_2O spectrum in A) was taken from an annealed (110) surface having ~5% vacancies, while the black TPD H_2O spectrum was taken from a surface predosed with 700 Torr*s of O_2. The new H_2O surface state seen as a broadening and shift to higher temperature of the water desorbing from the Ti^{+4} rows appears in the O_2 predosed H_2O TPD. Henderson et al. attributed this to molecular oxygen reacting with the oxygen vacancy sites, thereby depositing an oxygen into the vacancy and an oxygen in the Ti^{+4} row. The oxygen adatom in the row further reacts with the adsorbed water producing either two hydroxyls

directly or a precursor that leads to two hydroxyl groups in the Ti^{+4} row. [6] This mechanism explains the shift in the water TPD from the Ti^{+4} rows and the oxidation of the vacancy sites seen as a decrease in the high temperature recombinative peak show in the inset of A).

We have observed a similar water TPD state by simply irradiating the water film with 100 eV electrons which is depicted in B). The shift in the water TPD peak produced by electrons is experimentally similar to that produced by molecular oxygen. They are both dependent on the initial oxygen vacancy concentration and have similar annealing temperatures to remove the oxygen adatoms that affects the water TPD (data not shown). For our irradiation experiment, the shift in the water TPD is maximized when water saturates the Ti^{+4} row adsorption sites. Since our results are similar to Henderson's, we seem to be producing oxygen adatoms or a precursor leading to oxygen adatoms via electron irradiation.

Although water reacts with an oxygen vacancy site, the Ti^{+3} ions are not fully oxidized, and an electron remains delocalized beneath the hydroxyl groups. [7,8] This configuration is still a surface defect having an electron trap state approximately 1 eV below the conduction band edge. [9,10] When electron-hole pairs are created during irradiation whether from an excitation from the valence band to the conduction band in TiO_2 or the $1b_1$ level of water to the conduction band of TiO_2, this hydroxyl defect configuration or electron trap site is conducive to electron-hole recombination. This explains the initial oxygen vacancy concentration dependence of the water TPD shift due to irradiation. When the electron and hole recombine, energy is distributed locally inducing dissociation and desorption of the neighboring water in the Ti^{+4} rows. An oxygen adatom or precursor to an oxygen adatom is a resultant from the dissociated water.

In conclusion we have reproduced similar results with irradiation of a water film on TiO_2 (110) that Henderson et al. have observed with molecular oxygen predosing prior to dosing water on the TiO_2 (110). Instead of non-thermally dissociating water to produce an oxygen adatom species on all the surface sites, we found that this event is dependent on the initial oxygen vacancy concentration, and occurs specifically at these sites. We agree with the literature that these sites are electron traps even after they react with water, and a source of chemical reactions due to their increased probability of electron-hole recombination.

References

[1]   U. Diebold, Surf. Sci. Rep. 48 (2003) 53.
[2]   A. Fujishima and K. Honda, Nature 238 (1972) 37.
[3]   M.B. Hugenschmidt, L. Gamble, and C.T. Campbell, Surf. Sci. 302 (1994) 329.
[4]   M. A. Henderson, Surf. Sci. 355 (1996) 151.
[5]   S. Wendt, J. Matthiesen, R. Schaub, E.K. Vestergaard, E. Laegsgaard, F. Besenbacher, and B. Hammer, Phys. Rev. Lett. 96 (2006) 066107/1.
[6]   M. A. Henderson, W.S. Epling, C.L. Perkins, C.H.F. Peden, and U. Diebold, J. Phys. Chem. B 103 (1999) 5328.
[7]   C.D. Valentin and G. Pacchioni, (submitted) (2006).
[8]   J. Zhao, B. Li, K.D. Jordan, J. Yang, and H. Petek, Phys. Rev. B 73 (2006) 195309.
[9]   M. A. Henderson, W.S. Epling, C.H.F. Peden, and C.L. Perkins, J. Phys. Chem. B 107 (2003) 534.
[10]   A.K. See and R.A. Bartynski, J. Vac. Sci. Technol., A 10 (1992) 2591.

First-Principles Calculations of $La_{(1-x)}Sr_{(x)} Co_{(y)} Fe_{(1-y)} O_3$ (LSCF) Solids and Surfaces

Chan-Woo Lee, Susan B. Sinnott, and Eric D. Wachsman
Department of Materials Science and Engineering
University of Florida
Gainesville, Florida 32611-6400
and
Ram Devanathan
Pacific Northwest National Laboratory
Richland, WA

1. Introduction

   As materials for electrolytes become more conductive and/or are manufactured as thin films, electrode polarization and heterogeneous kinetics at the electrode surface dominate its overall performance. In order to improve our understanding of heterogeneous electrocatalytic phenomena at the surface of ion conducting ceramics, it is essential to investigate the role of defects and charge transfer at these surfaces. The goal of the present work is to understand heterogeneous electrocatalytic phenomena at the surface of LSFC. As LSFC is single-phase mixed conductor [1-4], it conducts using both ionic and electronic conduction mechanisms. Thus, LSFC has a two phase boundary (2PB) plane where the electrolyte and cathode are contacted [4], as illustrated in Fig. 1a. In contrast, ordinary electronic conducting SOFC cathodes have a three-phase boundary (3PB) circumference where the cathode, electrolyte and gas meet [4], as shown in Fig. 1b.
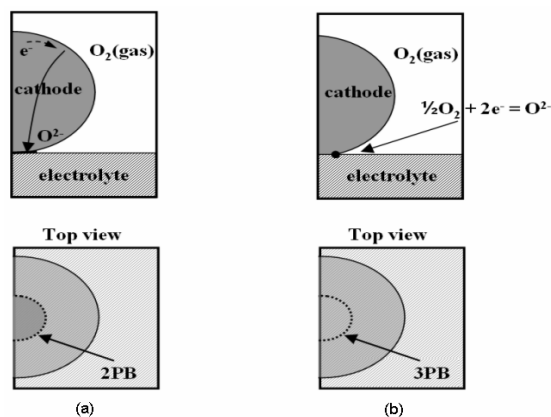

Fig.1 Schematic representation of (a) a two-phase boundary (2PB) plane and (b) a three-phase boundary (3PB) circumference. After figures 2 and 3 in Ref. 4.

This 2PB increases the efficiency of ionic conduction of LSFC. In particular, it is expected that oxygen molecules readily dissociate to O^{2-} over a significant portion of the LSFC cathode surface. The oxygen ion then moves into the lattice and diffuses into the electrolyte by passing the 2PB area, as shown in Fig.1a. Thus, understanding the dissociation of O_2 at the surface and the transport of O^{2-} through bulk LSFC, and documenting how these processes change depending on composition and surface structure is important. As a first step of the project, we start with the $LaFeO_3$, system which is the basis material for LSCF. The system was optimized using the density functional theory (DFT) with consideration of magnetism. After that, the energetics of LaO, FeO_2 and FeO terminations of (001) plane were compared. As expected, LaO termination with fewer dangling bonds was relatively stable.

2. Computational details

The total energies of bulk and surface systems of $LaFeO_3$ were calculated with the generalized gradient approximation (GGA) with the Perdew-Burke-Ernzerhof (PBE) functional [5] to DFT. Projected-augmented wave (PAW) [6,7] potentials which are implemented in the Vienna *ab-initio* simulation package (VASP) were used to describe each element in the system. A cutoff energy of 600 eV and $4\times4\times4$ *K*-points within Monkhorst-Pack scheme [8] were chosen for a bulk unit cell system containing 4 La, 4 Fe, and 12 O atoms. For La, Fe, and O bulk systems, *K*-points of $18\times18\times18$, $16\times16\times16$, and $8\times8\times8$ were chosen. In optimizing bulk and surface systems, magnetism was taken into account to have accurate total energies and geometries. Surface calculations of ceramic oxides usually need enough layers to describe the effect of long range reaction of ionic bonding. However, here, 5 layers were chosen for test calculations for different surface configurations. For surface calculations, a vacuum slab thickness of 10 Å was chosen to describe a pseudo-vacuum condition and cutoff energy=600 eV and *K*-points=$4\times4\times1$ were used. All parameters including K-points, cutoff energy, and vacuum slab thickness were determined after extensive convergence tests.

3. Results and discussion

Table 1 shows calculated lattice constants and magnetic moment for $LaFeO_3$ with paramagnetic and ferromagnetic conditions with the setting of cutoff energy=600eV and *K*-point=$4\times4\times4$. Here, lattice constants calculated with the consideration of ferromagnetism showed better accuracy than those with non-magnetic calculations. Also, G-type antiferromagnetism was perfectly described [9]. Cell shape and volume changes in ferromagnetic calculations were due to magneto volume effect of Fe atoms and this effect was also observed in structure optimization of Fe bulk system.

Table 1 Lattice constants and magnetic moment of DFT calculations of LaFeO$_3$ bulk system compared with experimental data

	Ferromagntic	**Paramagnetic**	**Exp. [10]**
a (Å)	5.6856027 (**2.0755%**)	5.378 (**-3.4470%**)	5.570
b (Å)	7.8598143 (**-0.0151%**)	7.565 (**-3.7654%**)	7.861
c (Å)	5.5672217 (**0.2020%**)	5.433 (**-2.2138%**)	5.60
Moment (μ$_B$)	3.769 (**-18.07%**)	.	4.6

With this bulk unit-cell, among possible low miller index planes, {010}, {110}, {111}, {011} and {101} [11], surface systems were developed by (010) plane with LaO, FeO, and FeO$_2$ terminations.
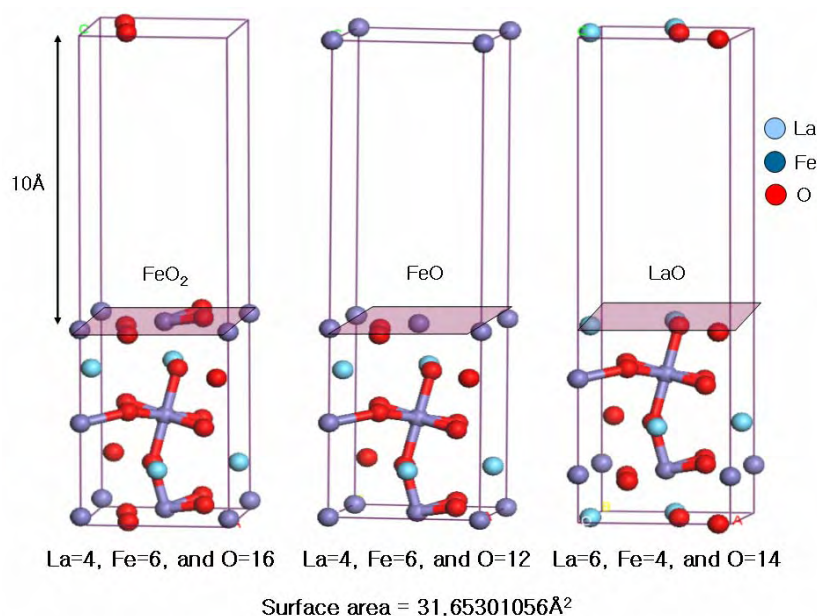
Fig. 2 Schematic description of LaO, FeO$_2$, and FeO terminations of LaFeO$_3$ (010) plane

As all surface systems in LaFeO$_3$ are non-stochiometric, we can not compare bulk total energy and surface free energy directly. Hence, by using equation 1 formulated by Hagen *et al.*[12], we can compare relative stability of different configurations shown in Fig. 2.

$$\sigma = \frac{1}{A_s}(G_s - \sum_i \mu_i N_i) \text{ Eq.1}$$

Here, G$_s$ represents the total free energy of the supercell, A$_s$ is surface area of the supercell, index *i* denotes the elements within the supercell: La, Fe, and O. μ_i denotes chemical potential of *i*th element and N_i is the number of atoms of each element within the supercell.

Table 2 Calculated surface free energies of LaO, FeO, and FeO_2 terminations of $LaFeO_3$ (010) plane

	LaO	FeO	FeO$_2$
Surface free energy $(eV/Å^2)$	-3.9207	-2.7501	-3.2150

It is evident that the LaO termination is the most stable and FeO termination shows the highest instability. This can be explained by the possibility of having dangling bonds. For LaO_2 termination, we have only one dangling bond. However, (010) plane terminated by FeO has three dangling bonds.

3. Results and discussion

Using DFT, $LaFeO_3$ system was optimized by considering magnetic properties. Structural properties were predicted more accurately by this consideration and antiferromagnetism of $LaFeO_3$ system was perfectly described. With this optimized system, surface free energies were calculated for (010) planes with different terminations: LaO, FeO, and FeO_2. LaO terminated (010) plane has the lowest surface free energy which means the highest stability. This can be explained based on the number of dangling bonds.

References

1. J. Mizusaki, T. Sasamoto, W.R. Cannon, H.K. Bowen, J. Am. Ceram. Soc. 66 (1983) 247
2. J.E. ten Elshof, H.J.M. Bouwmeester, H. Verveij, Solid State Ion. 81 (1995) 97
3. J.E. ten Elshof, H.J.M. Bouwmeester, H. Verveij, Solid State Ion. 89 (1996) 81
4. S. B. Adler, Chem. Rev. 104 (2004) 4791
5. J. P. Perdew, K. Burke, and M. Ernzerhof, Phys. Rev. Lett. 77 (1996) 3865
6. G. Kresse and J. Furthmuller, Comp. Mater. Sci. 6 (1996) 15
7. G. Kresse and J. Furthmuller, Phys. Rev. B 54 (1996) 11169
8. H.J. Monkhorst, J.D. Pack, Phys. Rev. B 13 (1976) 5188
9. K. Ueda, H. Tabata, T. Kawai, Phys. Rev. Lett. 60 (1999) 561
10. I. Wærnhus, P.E. Vullum, R. Holmestad, T. Grande, K. Wiik, Solid State Ionics 176 (2005) 2783
11. M. Alfredsson, J.P. Brodholt, D.P. Dobson, A.R. Oganov, C.R.A. Catlow, S.C. Parker, G.D. Price, Phys. Chem. Minerals 31 (2005) 671
12. M. Hagen, M. W. Finnis, Philosophical Magazine A 77 (1998) 447

Summary of research in the field of PVDF Polymers and Nanocomposites

Jiangyu Li
University of Washington
and
Leo Fifield
Pacific Northwest National Laboratory

Jiangyu Li visited PNNL twice in June and July, hosted by Leo Fifield. Each time he stayed one week there.

During Li's visit, Fifield and Li had extensive discussion on potential research collaboration in active polymers. The discussion has led to a joint white paper on PVDF polymers, submitted to DOE BES Materials Science program, which was invited to submit a full proposal. The joint proposal, entitled "Fundamental Studies on Phase Transition Characteristics and Electromechanical Behavior of Disordered Poly(vinylidene fluoride) Polymers Using Multi-scale Modeling and In-situ Characterization," was submitted to DOE BES in September.

In addition, research collaboration on conductive nanocomposites has been discussed, and a joint program involving Boeing, University of Washington, Tsinghua University, and Battel/PNNL is likely to be launched.

During Li's visit, preliminary studies on PVDF polymers have also been carried out. PVDF films have been spin coated, and IR spectrum has been measured.

A Photoelectron Spectroscopy and *ab initio* Computational Study of Boron Oxide Anions BO⁻ and BO₂⁻

Si-Dian Li
Department of Chemistry
Xinzhou Teachers' University
Shanxi, China
and
Hua-Jin Zhai, Lei-Ming Wang, and Lai-Sheng Wang
Pacific Northwest National Laboratory
Richland, WA

ABSTRACT   Combining photoelectron spectroscopy and *ab initio* calculations, we have revisited the $^2\sum^+$ ground-state of BO neutral, determined the excitation energy from the ground –state $^2\sum^+$ BO to the first excited state of $^2\prod$ BO to be 2.96 eV, and obtained the electron affinity of BO_2 at 4.49 eV in this work. The first and second excited states of BO_2 molecule are found to lie 2.23 eV and 3.01 eV above the ground-state. Our results indicate that density functional approach provides satisfactory predictions for the bond parameters, vibrational frequencies, and the vertical one-electron detachment energies of both boron monoxide and boron dioxide.

We performed a systematic combined PES and DFT investigation on boron oxides B_xO_y (x=1-10 and y=1-3) during the three months in Summer Research Institute. A brief summary on the smallest species of BO⁻ and BO₂⁻ will be reported here.

Both boron monoxide BO and boron dioxide BO_2 belong to the most important boron oxide clusters in gas phases. As the smallest boron oxide species, BO neutral and BO⁻ anion have attracted much attention in both experiments and theory.[1-8] BO_2 forms a typical linear Renner-Teller molecule [9-11] with the bond length of $r_{B=O}$=1.2653 Å and an estimated EA value of 4.288 eV from equilibrium data. However, there has been no PES spectra reported for BO_2^- anion to date.

Experimental and computational procedures

PES measurements. Cluster syntheses and PES measurements are carried out on a magnetic-bottle-type PES apparatus equipped with a laser vaporization supersonic cluster source which has been detailed elsewhere. BO⁻ and BO₂⁻ monoanions were produced by laser vaporization of high purity ^{10}B target in the atmosphere of helium carrier gas seeded with 0.01 or 0.5% of $^{16}O_2$, mass-selected with a time-of-flight mass spectrometer, and finally photo-detached at the laser energies of 355nm (3.493 eV), 266 nm(4.661 eV), 193 nm(6.424 eV), or 157 nm(7.898 eV), depending on the intensities of the mass spectra and PES signals. The PES spectra of BO⁻ and BO₂⁻ at different detachment energies are presented in Fig.1 and Fig.2, respectively.

Density functional theory computations. DFT structural optimizations and frequency analyses were performed using the hybrid B3LYP procedure with the augmented Dunning's all-electron basis (aug-cc-pVTZ) implemented in Gaussian 03. Excited-state energies of the

neutrals were calculated with time-dependent DFT (TDDFT) method at the ground-state structures of the anions. Both BO_2 and BO_2^- strongly favor $D_{\infty h}$ linear structures over other bent geometries, similar to the well-known CO_2^+ and CO_2. Table 1 compares the measured and calculated one-electron vertical detachment energies of the two anions. Coupled cluster calculations (CCSD(T)) were performed to calculate the adiabatic detachment energies (ADEs) and vertical detachment energies (VDEs) of these small clusters at DFT structures. The valence orbital pictures of both closed-shell BO^- and BO_2^- are shown in Fig.3 to facilitate spectrum assignments.

Franck-Condon factor simulations. The vibrational progressions of the well-resolved X $^2\sum^+$ BO band in Fig.1 (a) and A $^2\prod$ BO band in Fig.1 (c) have been modeled employing the Franck-Condon fitting procedure. The simulated results are compared with measured PES spectra in Fig. 4.

Features of the PES spectra

The X $^2\sum^+$ BO band in Fig. 1(a), which originates from the electron transition from $^1\sum^+$ BO^- to $^2\sum^+$ BO, gives the one-electron detachment energies of ADE=2.505 eV and VDE=2.505 eV for $^{10}BO^-$. This defines an EA value of 2.505eV for ^{10}BO neutral, a value in nice agreement with the reported value of EA=2.508$\pm$0.008 eV for ^{11}BO. X band also clearly features with vibrational characteristics, with one hot band at 2.296 eV and two vibrational peaks at 2.745 eV and 2.986 eV, respectively,

| **Fig.1** Photoelectron spectra of BO^- at (a) 355 nm (3.493 eV), (b) 266 nm (4.661eV), and (c)193 nm (6.424eV). | **Fig.2** Photoelectron spectra of BO_2^- at (a) 193 nm (6.424 eV) and (b) 157 nm (7.898 eV). |
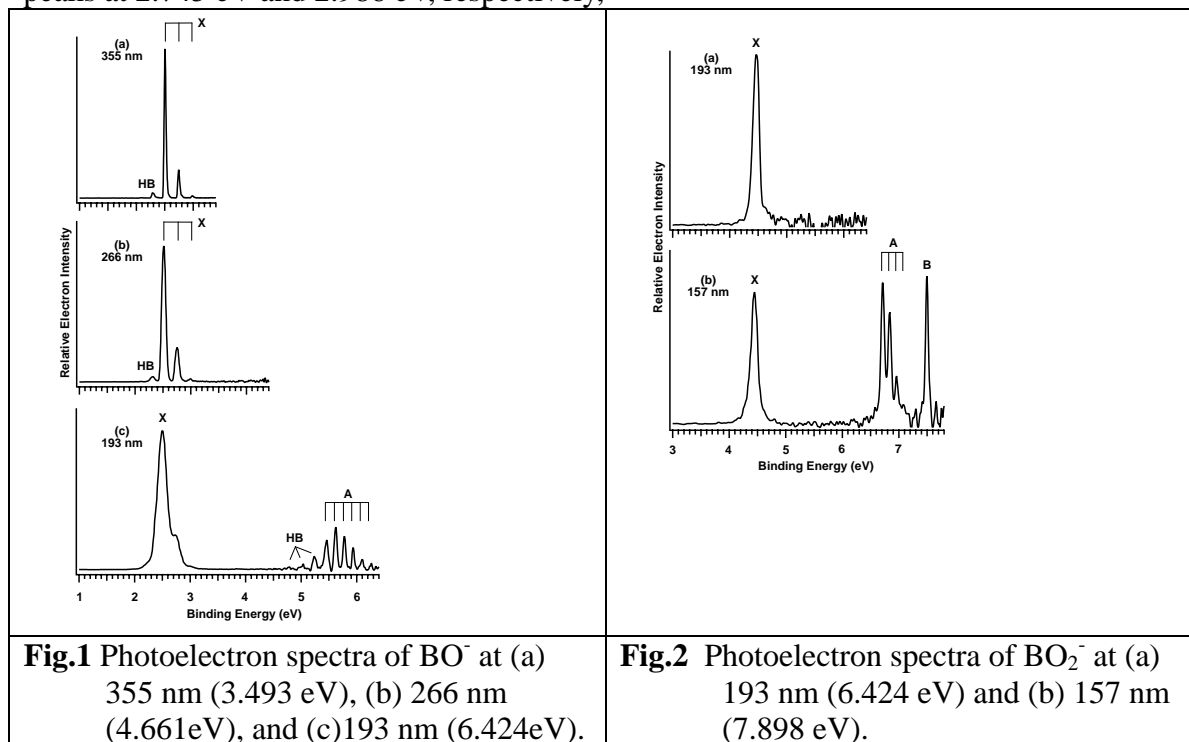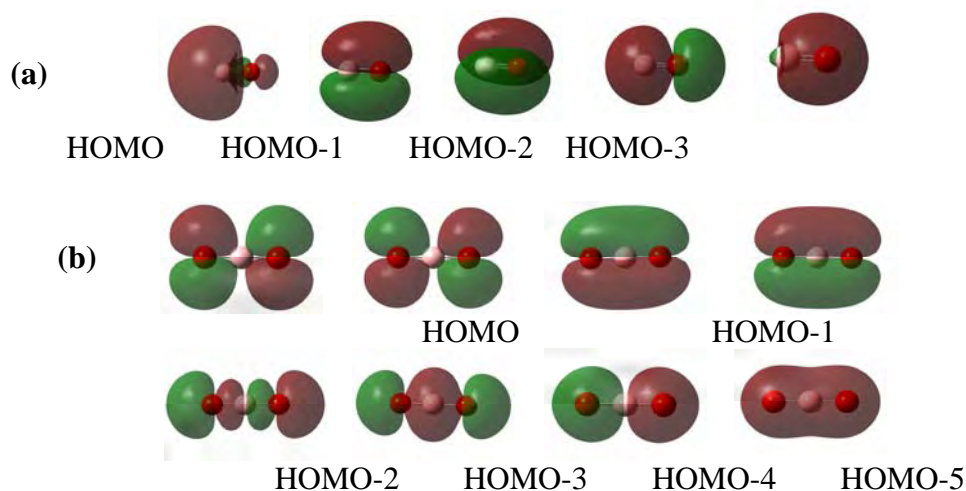
Fig. 3 Molecular pictures of BO$^-$ (a) and BO$_2^-$ (b) at B3LYP level.

Fig.4 Franck-Condon factor simulations of (a) the X $^2\Sigma^+$ band and (b) the A $^2\Pi$ band of BO$^-$.
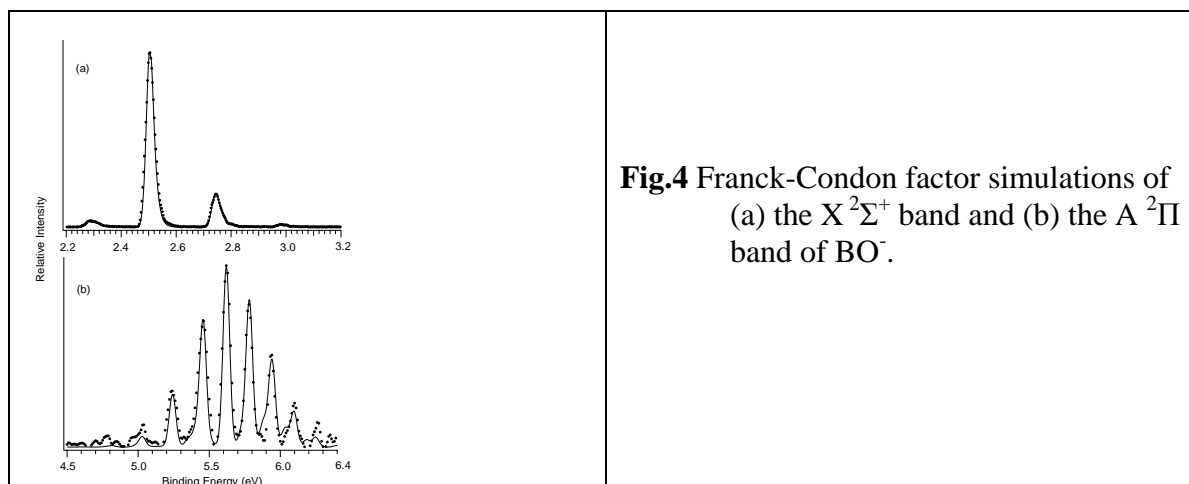
indicating a vibrational frequency of ~1927 cm^{-1} for the ground-state of $^2\Sigma^+$ ^{10}BO neutral and a vibrational frequency of ~1735 cm^{-1} for the ground-state of $^1\Sigma^+$ ^{10}BO$^-$ anion.

More interestingly, the second band A $^2\Pi$ BO, which corresponds to a electron transition from $^1\Sigma^+$ BO$^-$ to A $^2\Pi$ BO, exhibits a well-resolved vibrational progression with eight peaks (see Fig.1(c)), with two hot bands at 5.02 eV and 5.24 eV, ADE=5.46 eV, VDE=5.62 eV, and four vibrational peaks at 5.78 eV, 5.94 eV, 6.10 eV, and 6.26 eV, respectively. This vibrational progression leads to a vibrational frequency of ~1340 cm^{-1} for the first excited state of $^2\Pi$ ^{10}BO neutral and a vibrartional frequency of ~1735 cm^{-1} for the ground-state of $^1\Sigma^+$ ^{10}BO$^-$ anion.

BO$_2^-$ anion possesses a single feature in its X $^2\Pi_g$ BO$_2$ band with ADE=VDE=4.49 eV, indicating an EA value of 4.49 eV for BO$_2$. At higher detachment energy of 157 nm, both its A $^2\Pi_u$ BO$_2$ at 6.72 eV and B $^2\Sigma_u^+$ BO$_2$ at 7.50 eV bands appeared to have high PES intensities (see Fig.2 (b)).

Table 1 Experimental and calculated vertical detachment energies (eV) of BO$^-$ and BO$_2^-$ anions

PES Features	VDE (Exp.)	Molecular Orbital	Final State	VDE (TD-B3LYP)	VDE (CCSD(T))
BO$^-$					
X A	2.505 5.62	HOMO($1\sigma^+$) HOMO-1($1\pi_u$)	$^2\Sigma^+$ $^2\Pi$	2.627 5.900	2.497
BO$_2^-$					
X A B	4.49 6.72 7.50	HOMO($1\pi_g$) HOMO-1($1\pi_u$) HOMO-2($1\sigma_u$)	$^2\Pi_g$ $^2\Pi_u$ $^2\Sigma u^+$	4.321 6.724 7.419	4.466

Theoretical assignments

At B3LYP level, the ground-states of ^{10}BO and ^{10}BO$^-$ have the bond lengths of 1.203 Å and 1.234 Å and bond energies of 8.41 eV and 9.32 eV, respectively. These values are all in nice agreement with the previously reported values. Their vibrational frequencies turned out to be 1913 cm^{-1} and 1739 cm^{-1}, well in line with the measured values of 1927 cm^{-1} and 1735 cm^{-1} obtained in our PES spectra, respectively. For BO$^-$, the calculated DFT ADE=2.588 eV and VDE=2.627 eV. Nice agreement was achieved at CCSD(T) level, with ADE=2.484 eV and VDE=2.497 eV. These CCSD(T) values almost exactly reproduce the experimental ADE and VDE, with a derivation smaller than 0.01 eV.

The valence electronic configuration of $^1\Sigma^+$BO$^-$ ground-state is $(3\sigma^+)^2(2\sigma^+)^2(1\pi)^4(1\sigma^+)^2$. Detaching one electron from the HOMO $(1\sigma^+)$ of the anion produces the X $^2\Sigma^+$ BO band corresponding to the electron configuration of $(3\sigma^+)^2(2\sigma^+)^2(1\pi)^4(1\sigma^+)^1$. The HOMO $(1\sigma^+)$ of BO neutral with one unpaired electron is basically an anti-bonding orbital mainly concentrated on B side with the main contribution from B $2p_x$. The anti-bonding nature of the HOMO is evidenced by both the increased bond lengths from neutral to the anion discussed above and the reduced Wiberg bond orders from WBI$_{B=O}$=1.79 in BO to WBI$_{B=O}$=1.57 in BO$^-$. Removing one electron from the degenerate HOMO-1 (1π) of the anion (which has the main contribution from O $2p_y$ and O $2p_z$) generates the second band A $^2\Pi$ BO in Fig.1 (c), which corresponds to the first excited state of the neutral $(3\sigma^+)^2(2\sigma^+)^2(1\pi)^3(1\sigma^+)^2$.

At DFT level, linear BO$_2$ and BO$_2^-$ possess the B=O bond lengths of 1.262 Å and 1.264 Å and the corresponding bond orders of 1.58 and 1.60, respectively, with ADE=VDE=4.321 eV for BO$_2^-$. At CCSD(T) level, ADE=4.465 eV, VDE=4.466 eV for BO$_2^-$, both in excellent agreement with the experimental value of 4.49 eV. As a Renner-Teller molecule, the two degenerate bending vibrational modes of the X $^2\Pi_g$ ^{10}BO$_2$ ground-state loose their degeneracy: they possess two different vibrational frequencies at 417 cm^{-1} and 504 cm^{-1}, respectively. The calculated O=B=O symmetric stretching modes turned out to have the frequencies of 1088 cm^{-1} and 1096 cm^{-1} for $^2\Pi_g$ ^{10}BO$_2$ ground-state and $^1\Sigma_g^+$ ^{10}BO$_2^-$ ground-state, respectively. These vibrational modes were not observed in our measured PES spectra. But our DFT $^2\Pi_g$ ^{10}BO$_2$ vibrational mode at 1088 cm^{-1} nicely fits the measured value of v_1=1071 cm^{-1} for $^2\Pi_g$ ^{11}BO$_2$.

The closed-shell ground-state of $^1\Sigma_g^+$ BO$_2^-$ possesses the electron configuration of

$(2\delta_g)^2(2\delta_u)^2(1\delta_g)^2(1\delta_u)^2(1\pi_u)^4(1\pi_g)^4$. Detaching one electron from HOMO($1\pi_g$), HOMO-1($1\pi_u$), or HOMO-2($1\delta_u$) produces the ground-state of X $^2\Pi_g$ BO$_2$, the first excited state of A $^2\Pi_u$ BO$_2$, or the second excited state of B $^2\Sigma_u^+$ BO$_2$, respectively. DFT approach produced the vertical detachment energies of $^2\Pi_g$ BO$_2$ at 4.321 eV, $^2\Pi_u$ BO$_2$ at 6.724 eV, and $^2\Sigma_u^+$ BO$_2$ at 7.419 eV, all well in agreement with the corresponding measured VDE values of 4.49 eV, 6.72 eV, and 7.50 eV, respectively.

Franck-Condon simulation nicely reproduces both the X $^2\Sigma^+$ BO and A $^2\Pi$ BO vibrational progressions (see Fig.5 for details). The simulated B=O bond length of the first excited state $^2\Pi$ turned out to be 1.340 Å, a value 0.013 Å shorter than the previously reported value of 1.353 Å.[1] The high vibrational temperature above 1650 K indicates that BO$^-$ anions were not effectively cooled down in helium carrier gas under the our experimental conditions.

Acknowledgments

References

1. K. P. Huber and G. Herzberg, *Constants of Diatomic Molecules*, Van Nostrand Reinhold, New York, 1979. pp. 102.
2. R. S. Mulliken, Phys. Rev. **25**, 259(1925).
3. J. Almlof, A. V. Nemukhin, and A. Heiberg, Int. J. Quant. Chem. **XX**, 655(1981).
4. F. Melen, I. Dubois, and H. Bredohl, J. Phys. B **18**, 2423 (1985).
5. P. Botschwina, Chem. Phys. **28**, 231(1978).
6. A. V. Nemukhim, J. Almlof, and A. Heiberg, Chem. Phys. **57**, 197(1981).
7. M. Tanimoto, J. Chem. Phys. **84**, 1210(1986).
8. D. E. Jensen, J . Chem. Phys. **52**, 3305(1970).
9. D. K. Russsell, M. Kroll, and R. A. Beaudet, J. Chem. Phys. **66**, 1999(1977).
10. K. Kawaguchi, E. Hirota, and C. Yamada, Mole. Phys. **44**, 509(1981).
11. T. R. Burkholder and L. Andrews, J. Chem. Phys. **95**, 8697(1991).

Characterization of Microstructure and Composition of Magnetostrictive Nanobars as Bio-sensor Platform

Suiqiong Li and Zhongyang Cheng
Materials Engineering
Auburn University
Auburn, AL
and
Dr. Chongmin Wang
Pacific Northwest National Laboratory
Richland, WA

ABSTRACT

The magnetostrictive nanobar and its array were recently induced as a high performance biosensor platform. In this research, the magnetostrictive Fe-B nanobars, which were synthesized using a template-based electrochemical deposition, were systematic characterized. The composition and microstructure, which are directly related to the performance of the nanobars, of the Fe-B nanobar were determined using scanning electron microscopy (SEM), transmission electron microscopy (TEM), x-ray photonelectron spectroscopy (XPS) as well as Auger electron spectroscopy (AES). Morphologically, nanobars are featured by very flat top and smooth cylindrical surface, which are critical factors for obtaining high performance as sensor platform. Structurally, XRD and electron diffraction reveal that the Fe-B nanobar is amorphous. AES analysis indicates that the nanobar shows no significant compositional variation along the length direction. HRTEM reveals that the nanobars were covered by an oxidization layer of a typical thickness of ~ 10 nm. It is believed that this oxidation layer is related to the passivation of nanobars in air. High temperature annealing and subsequent structural and compositional analysis indicate that the Fe-B nanobars possess a good thermal stability.

INTRODUCTION

We recently induced magnetostrictive particles (MSPs), such as strips and bars, as a new type of acoustic wave (AW) devices as a sensor platform.[1] A extremely high sensitivity and a high Q value make the MSP much better sensor platform than the current platforms, such as microcantilevers. More importantly, the MSP technology provides a methodology to bring the target species to the sensor, which is a challenge for current technologies. All these make the MSP a great candidate for developing high performance biosensors.

The theoretical simulation and experimentally characterization indicated that, given the material parameters of the MSPs constant, the mass sensitivity of MSPs exponentially increases with the decrease of their size.[1] To obtain extremely high mass sensitivity, such as the capability of detecting a single or several cells (~ pg), the MSPs in size from nanometer to micrometer are required. In this research, amorphous Fe-B alloy was selected as the magnetostrictive material to fabricate nano-sized MSPs. The magnetostrictive nanobars and nanobar arrays, in diameter ranging from 50 to 200 nm, were fabricated by electrochemically depositing amorphous Fe-B alloy into ion track-etched polymer membranes. Their

morphology, microstructure, and composition were systematically studied by SEM, HRTEM and Auger electron spectroscopy.

RESULTS AND DISCUSSIONS

The morphology of the nanobars was observed using scanning electron microscopy (LEO 982 SEM), which is shown as figure 1. The SEM images showed that straight Fe-B nanobars of 50nm-200nm in diameter and 2-5 µm in length were fabricated in high density by the template-based synthesis. The nanobars in uniform length can be fabricated on a substrate (Figure 1. (a) and (c)) so that a sensor array can be fabricated; as well as can be released from the substrate to get individual nanobar (Figure1. (b)). The SEM images revealed that the nanobars have very flat end (Figure 1. (d)). The flat end of the nanobars is very favorable for obtaining high Q value when the nanobars are operated as a resonator. The SEM images indicated that there was no morphologic difference between the nanobars with different diameter/length and formed under different current density. Since the polymer template is relatively soft, the pore size is not strictly defined, which cause the diameter of deposited nanobars slightly increased along the pore axis.
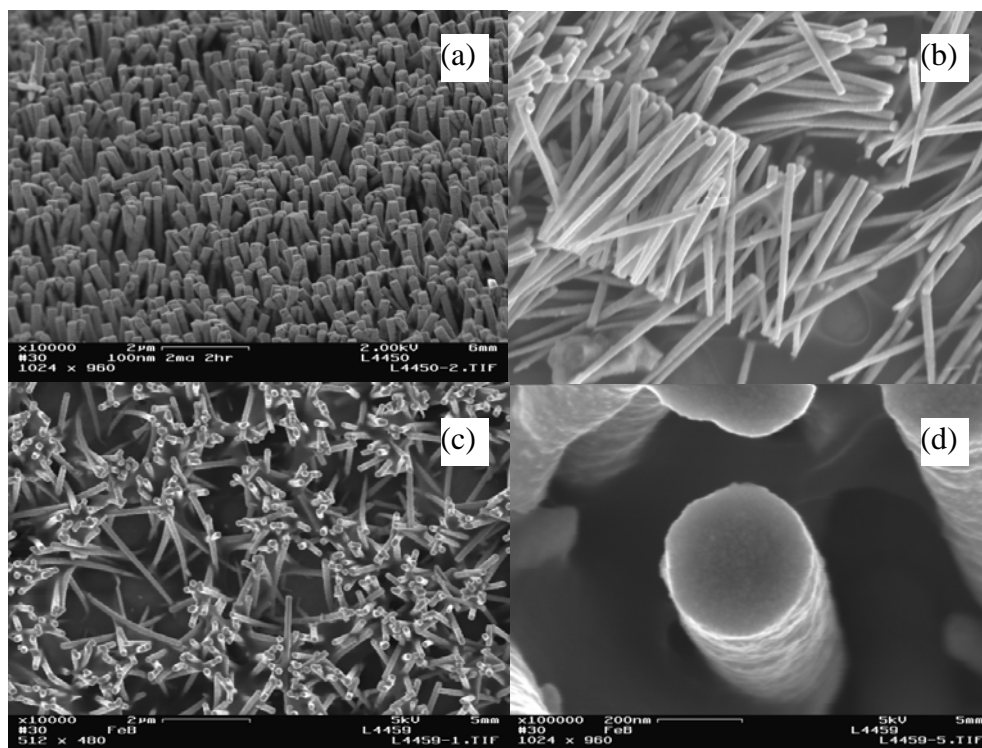
Figure 1. SEM image for (a) Fe-B nanobar array in diameter of 200nm, (b) & (c) Fe-B nanobars in diameter of 50nm, and (d) top surface of the Fe-B nanobar in diameter of 100nm.

High-resolution transmission electron microscopy (JEOL 2010 HRTEM) was employed to characterize more details of the morphology and microstructure of the Fe-B nanobars. The Fe-B nanobars were placed on the Cu TEM grid coated with lacy carbon for the observation. Figure 2 showed the TEM image and the electron diffraction pattern of the Fe-B nanobar in diameter of 50nm. The electron diffraction pattern revealed that the microstructure of the

nanobars is amorphous, which is as desired. The individual nanobar was characterized with the electron diffraction focused on the selected areas along the nanobar; the results confirmed that the Fe-B nanobar has uniform amorphous microstructure along the whole nanobar.

Figure 2. TEM image (a) and electron diffraction pattern (b) of the nanobars in diameter of 50nm

The details of the composition of the Fe-B nanobars were studied by Auger electron spectroscopy (Model 680 AES). Nanobars released from substrate were placed on a Cu TEM grid coated with lacy carbon. To study the composition of the nanobar along the length direction as well as along the diameter direction, 10 spots along the individual nanobar length were sel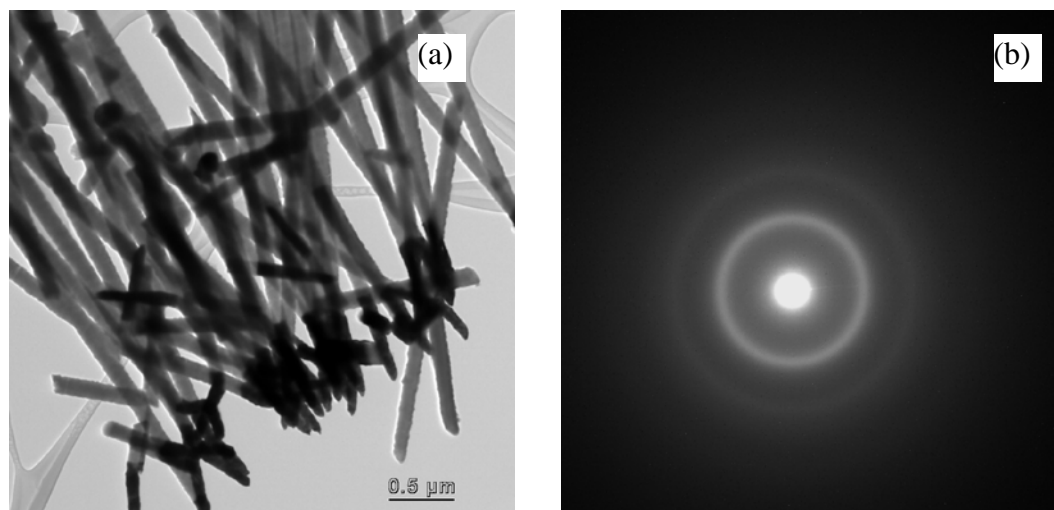ected. The composition of each spot was analyzed by AES with the e-beam focused onto the spot with diameter of 20nm. After analysis along the length direction, certain amount material along the nanobar diameter direction was sputtered off by Ar ion-beam sputtering. The composition analysis was carried out repeatedly as the nanobar was sputtered off 5nm, 10nm, 20nm, 30nm and 40nm. The analysis results showed that there are contamination and oxidation observed on the surface of the deposited nanobar. However, this layer is very thin, only about 10 nm. After sputtered off 10nm, the contamination can not be observed anymore and only very small amount of the Oxygen can be detected. Except the contamination layer, the Fe and B composition along the nanobar diameter is uniform. The analysis results also revealed the uniform composition distribution along the nanobar length direction. The variation in the Fe and B composition along the nanobar length direction was less than 4%. The analysis demonstrated that the whole nanobar exhibits uniform composition distribution with about 10nm oxidation layer covered on the surface, which is believed that this oxidation layer is related to the passivation of nanobars in air. There is some amount of C was detected. It should not come from the nanobars. Even though the e-beam was focused on the nanowire, since the nanowire is thin, the background still contributed signals. Most of C detected should come from the lacy carbon. The AES analysis of the nanobars deposited under different current showed same uniform composition contribution.

The thermal stability of the Fe-B nanobars was studied by annealing the nanobars in the N_2 environment. The nanobars were annealing at 200, 300, and 400 ^oC for 1 hour. The morphology and microstructure of the nanobars annealed at different temperature were characterized by HRTEM. The electron diffraction patterns showed that the nanobars still kept

amorphous microstructure after annealed at 200 ^{o}C and 300 ^{o}C. It was found that BCC iron crystal formed after annealed at 400 ^{o}C. The Fe-B nanobars exhibit good thermal stability.

CONCLUSIONS

Magnetostrictive nanobars and nanobar arrays with uniform length and smooth morphology in diameter of 50 ~ 200 nm were synthesized by depositing amorphous Fe-B alloy into ion-track etched membranes. The SEM characterization of the nanobars demonstrated that the nanobars are featured by very flat end and smooth cylindrical surface. The template synthesized Fe-B nanobars exhibited uniform composition, amorphous microstructure and good thermal stability. They have great potential to be high performance AW sensor platform.

ACKNOWLEDGMENTS

REFERENCE

1. Suiqiong Li, Lisa Orona, Liling Fu, Z.-Y. Cheng, "Electrosynthesis of Magnetostrictive Nanosensor Array", Mater. Res. Soc. Symp. Proc. 900**E**, (2005), *Nanoparticles and Nanostructures in Sensors and Catalysis*, edited by Chuan-Jian Zhong, Nicholas A. Kotov, Wayne Daniell, Francis P. Zamborini, 0900-O08-04

Assembly of an Ion Trap Mass Spectrometer for LD-CI Experimentation

Julie A. Lloyd and Murray V. Johnston
Department of Chemistry & Biochemistry
University of Delaware
Newark, DE 19716
and
M. L. Alexander
Environmental Molecular Sciences Laboratory
Pacific Northwest National Laboratories
Richland, WA 99352

Although laser desorption and chemical ionization have both been commonly used in the field of mass spectrometry, the hyphenated LD-CI technique has not been studied as widely.[1-6] A renewed interest in this technique has taken place in the field of aerosol mass spectrometry where laser desorption is well established. The new aspect of chemical ionization provides a soft ionization technique to help characterize polar, polyfunctional oxygenated organics and high molecular mass species found in aerosols. Therefore, the main objectives of this research are to 1) assemble an ion trap mass analyzer, 2) become trained on the use and operation of the ion trap and complementary components, and 3) conduct basic testing of the ion trap analyzer using different ionization techniques with a test compound.

An ion trap mass analyzer was assembled for laser desorption (LD) of analyte molecules followed by electron and chemical ionization (EI/CI) (Figure 1). The ion trap mass analyzer was controlled by existing electronics and software.[7] The software was further developed in-house specifically for laser studies, but also for more efficient data analysis. Figure 2 shows a schematic of the laser set-up. LD-EI/CI experiments used a Continuum Nd:YAG laser at a wavelength of 10.6 μm with a maximum energy output of ~ 6 mJ per pulse (5 ns width). No focusing optics were used. The laser beam measured approximately 3 mm in diameter and hit the sample probe at a 90 degree angle. Sample probes were machined in-house and varied in material used (i.e. stainless steel, aluminum, ceramic sleeved, etc.), type of surface (flat/grooved), and diameter of the probe. Perylene, a robust, nonvolatile PAH, was selected as a test compound to optimize the system parameters. A 2 mg/mL solution of perylene was prepared in benzene. The solution was applied to the sample probe in small aliquots and was allowed to dry before insertion in the vacuum chamber. For CI, acetonitrile was leaked into the vacuum chamber as the chemical ionization reagent. Experiments were conducted to optimize the ionization time, laser trigger delay, and laser energy. Buffer gas pressures, the concentration of perylene, CI agent, and the probe position were held constant.

Prelimilary results showed a combination of laser desorption and thermal desorption. A prolonged firing of the laser showed an increase in the analyte signal for both aluminum and stainless steel materials; however, the increase was more apparent using the aluminum probe. Several ionization processes other than electron ionization were also occurring within the system. With a high laser energy (>3 mJ), the analyte underwent laser desorption ionization (LDI), thermal desorption laser ionization as well as electron ionization. The EI mass spectrum showed the most intense peaks at 252 m/z ($M^{\bullet+}$) and 250 m/z ($M^{\bullet+} - 2H$) (Figure 3). Very few fragment ions at 224 m/z and 126 m/z were detected mainly due to the robust structure of perylene. Other lower mass peaks were observed and were attributed to the probe material and hydrocarbons from the turbomolecular pump oil. For CI experiments, a 3 mJ laser energy was

used to eliminate other ionization processes as described above. The CI mass spectrum showed the most intense peak at 253 m/z relating to MH$^+$. Perylene fragment peaks were not present. Also, fewer background ions in the lower mass range were detected making the spectrum "cleaner".

Overall, the objectives of this research project were met; however, continued work is necessary to optimize the system. Increased mass range and sensitivity, continued software development, improved calibration methods, and noise elimination from electronics are all major factors that are required for improving the system.
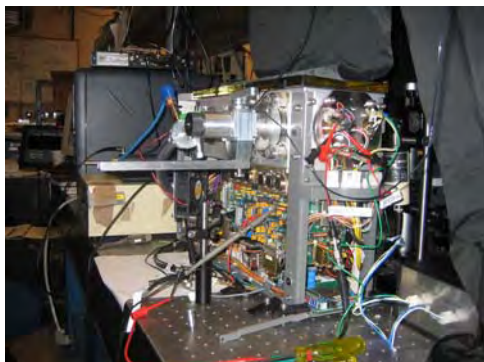
Figure 1. A snapshot of the assembled ion trap mass analyzer.
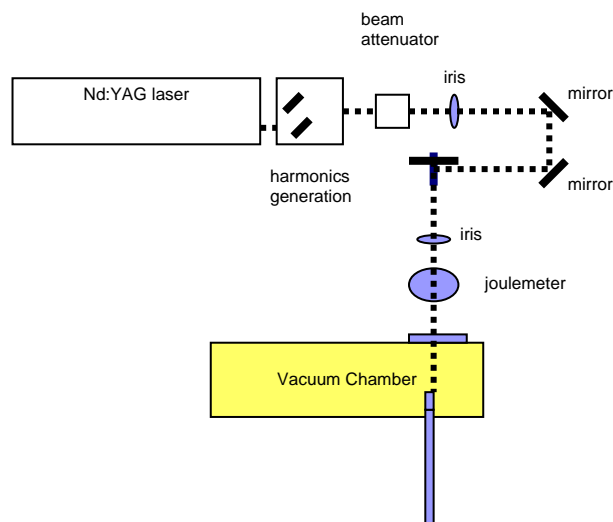
Figure 2. Schematic of the Nd:YAG laser set-up for laser desorption from the sample probe.
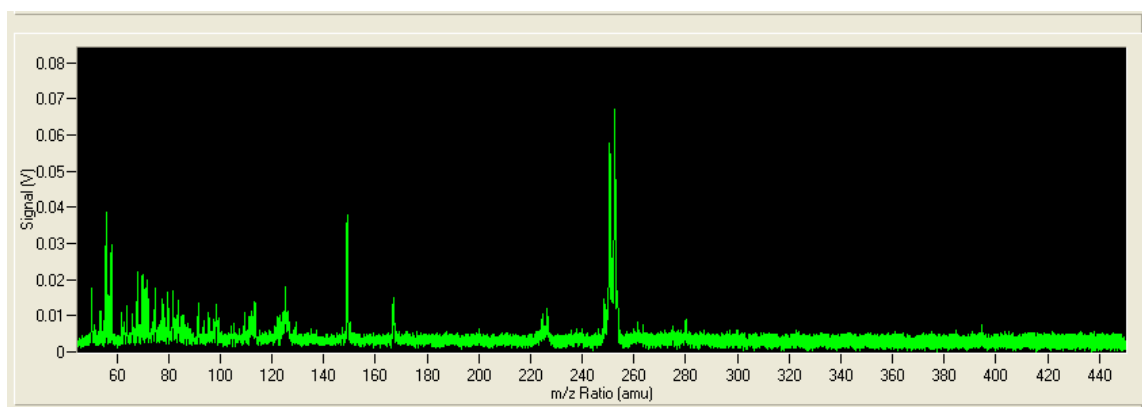
Figure 3. LD-EI mass spectrum of perylene on a stainless steel probe using ~4.5 mJ laser energy.
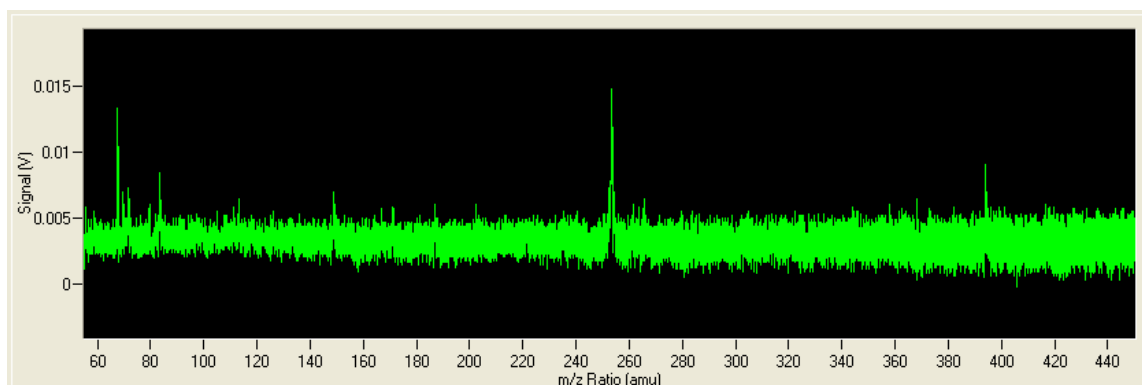
Figure 4. LD-CI mass spectrum of perylene on a stainless steel probe using ~3 mJ laser energy.

Literature Cited

(1)   Cotter, R. J. *Anal. Chem.* **1980**, *52*, 1767-1770.
(2)   Heller, D. N.; Lys, I.; Cotter, R. J. *Anal. Chem.* **1989**, *61*, 1083-1086.
(3)   Yost, R. A.; Wilder, B. J. *Anal. Chem.* **1983**, *55*, 2002-2005.
(4)   Tronendle, F. J.; Reddick, C. D.; Yost, R. A. *J Am Soc Mass Spectrom* **1999**, *10*, 1315-1321.
(5)   Speir, J. P.; Gorman, G. S.; Cornett, D. S.; Amster, I. J. *Anal. Chem.* **1991**, *63*, 65-69.
(6)   Wood, T. D.; Marshall, A. G. *J Am Soc Mass Spectrom* **1991**, *2*, 299-304.
(7)   Hopkins, D. F.; Alexander, M. L.; Swanson, K. R.; Buschbach, M. A. *Scientific Computing and Instrumentation* **2004**, 18-20.

Investigation into the Effect of Milling Ammonia Borane with Magnesium Hydride

Rebecca Lowton and Peter Edwards

Inorganic Chemistry

University of Oxford, Worcester College,

Oxford, England

and

Thomas Autrey,

Pacific Northwest National Laboratory

Richland, WA

Introduction

One of the most pressing problems currently facing mankind is the search for alternative fuel sources. Taking into account the nature of the current political climate, the rate of global warming[1] and diminishing fossil fuel reserves, it is clear that this is a problem which requires a rapid solution.

Amongst the many contenders as a replacement fuel are ethanol, liquid petroleum gas and methyl tertiary butyl ether. However, it is hydrogen that is widely believed to be the most promising future energy carrier in the transportation sector. Having a gravimetric energy density three times that of petroleum, the use of hydrogen in conjunction with fuel cell technology results in efficiencies of between 40 and 65% (compared to gasoline in internal combustion engines which has an efficiency of only 10 – 15%)[2]. Hydrogen is also non-toxic, safe to breath, dissipates freely (meaning that an uncontained hydrogen leak would amount to nothing more than a waste of valuable fuel) and has an explosion limit ¼ that of octane[3].

There are two major barriers to the wide – scale implementation of hydrogen as a fuel.

i) Production

Molecular hydrogen (H_2) does not occur in large amounts naturally and therefore must be produced from another source. In order for hydrogen to be used as an energy carrier in the long term, it is necessary to find a way of producing large quantities of the gas from renewable energy sources (wind, wave, solar etc).

Several possibilities are currently under investigation. Some of the most promising include the nuclear powered electrolysis of water using polymer electrolyte membrane (PEM) electrolysers, the photoelectrolysis of water, and the gasification of biomass[4],[5]. Unfortunately, given the very low yields of H_2 produced compared with processes using non-renewable sources (outlined below), these methods are currently far too expensive for large scale production, and so these procedures are still very much at the development stages.

At this time, the cheapest way of generating H_2 is by gasification of coal over a metal catalyst[6], or by steam reformation of natural gas[7]. Both of these methods derive their H_2 from non-renewable hydrocarbon-based sources and therefore suffer from many of the problems associated with the direct use of fossil fuels. These methods could, however, be used in the short term to assist in the transition to a hydrogen economy whilst methods using renewable sources are under further development. Not only is the efficiency of fossil fuels increased when used in this manner, but these methods also have the added advantage of localising the emissions of CO_2 and other greenhouse gases.

ii) Storage

One of the most serious problems preventing the implementation of hydrogen technology is the lack of a suitable hydrogen storage medium. Whilst Hydrogen has an excellent energy storage capacity per unit mass, its storage capacity per unit volume is very poor indeed. For instance, the hydrogen required to travel the same distance as that travelled on the average full tank of petrol would occupy $49m^3$ at room temperature and pressure[8]. The challenge facing researchers is to find a way of storing this large volume of gas in a vessel that will fit easily into the smallest car.

Research into hydrogen storage materials for the transportation sector has several main focal points. These include compressed gas storage, cryogenic storage and chemical storage.

Compression of hydrogen in light weight, high strength cylinders such as those designed by Quantum Fuel Systems Technologies[9] may seem like the simplest option for storage given that they have high gravimetric storage densities and are safe up to 800 bar pressure. However, there are many disadvantages associated with this method, the most notable of which is the large energy penalty on compression. The pressurization of the gas from standard pressure to 800 bar uses approximately 18% of the latent energy stored within the hydrogen every time the cylinder is charged[10] resulting in very low overall energy efficiency.

Cryogenic storage of hydrogen is possible only at very low temperatures as hydrogen has it's critical point at 33.2K. Approximately 1/3 of the latent heat energy stored within the hydrogen is required for cooling the gas to this temperature and even then, due to the exothermic conversion of ortho – to para – H_2, boil off at a rate of ~5% per day is unavoidable. These problems combine to make this method of storage very expensive and inefficient.

The third and most extensive area of research is into chemical storage of hydrogen in metallic and complex hydrides and it is this area on which the remainder of this report will focus.

The criteria deemed necessary by the US Department of Energy for a suitable hydrogen storage material are listed below[11]. It is important to realize that these benchmarks are the values set for 2015 and are meant to be guidelines only.

- High storage capacity: minimum 6.5 wt % abundance of hydrogen and at least 65g L^{-1} of hydrogen available from the material.
- A decomposition temperature, $T_{dec} = 60 – 90$ °C, corresponding to the optimum working temperature of PEM fuel cells.
- Reversibility of thermal absorption / desorption cycle: low temperature of hydrogen desorption and low pressure of hydrogen absorption (a plateau pressure of the order of a few bars at room temperature), or ease of non – thermal transformation between substrates and products of decomposition.
- Low cost.
- Low toxicity of non – explosive and possibly inert (to water and oxygen) storage medium.

The performance requirements of the materials will ultimately be determined by the market and are expected to increase over time.

Since it is necessary for a hydrogen storage material to have a high gravimetric storage capacity, the choice of elements on which to base such materials is very much limited to those elements with low atomic mass, at the beginning of the periodic table. Unfortunately, the vast majority of hydrides based on these light elements are ionic or covalent in nature and thus often have very high decomposition temperatures and can not simply be recharged by the application of H_2 gas.

Much research focus has been given to ammonia borane (NH_3BH_3, AB) during the last few years as a potential hydrogen storage material. First prepared by Shore and Parry in 1956[12], its decomposition was investigated in 1978 by Hu *et al*[13] and its potential as a hydrogen storage material first suggested by Baitalow *et al.*[14] Thermal decomposition takes place in the range 77 – 137°C and complete decomposition occurs at 112°C releasing 1 mol of hydrogen per mole of complex.

This temperature is higher than the optimum working temperature of fuel cells (as water evaporation strongly decreases PEM conductivity at higher temperatures) and hence, this material would be a very promising hydrogen storage material if it's decomposition temperature could be lowered. This report will focus on attempts to lower this decomposition temperature by milling AB with magnesium hydride (MgH_2).

Experimental Details

Ammonia borane (Aviabor, 99%) was mechanically milled with MgH_2 (Alfa Aeser, 98%) in proportions of 1:1 and 2:1 by Dr Chun Lu using a mechanical mill. The reactants were weighed out in a glovebox and placed into a container with several tungsten carbide balls and was then mounted onto a shaker mill. The mixture was milled for 2 minutes and then allowed to stand for 10 minutes in order to dissipate the generated heat. This process was repeated 8 times amounting to a total milling time of 16 minutes.

Calorimetric data was collected using a Setraram C80 calorimeter using a heating rate of 1 K min^{-1}. Volumetric data was collected using standard volumetric apparatus as shown in figures 1a and 1b. For the lower temperature experiment, the 1:1 mixture was heated to 80°C and this

temperature was maintained until H_2 release stopped. The temperature was then raised to 100°C and maintained until H_2 release ceased. Corrections were made for the expansion of the gas in the apparatus.
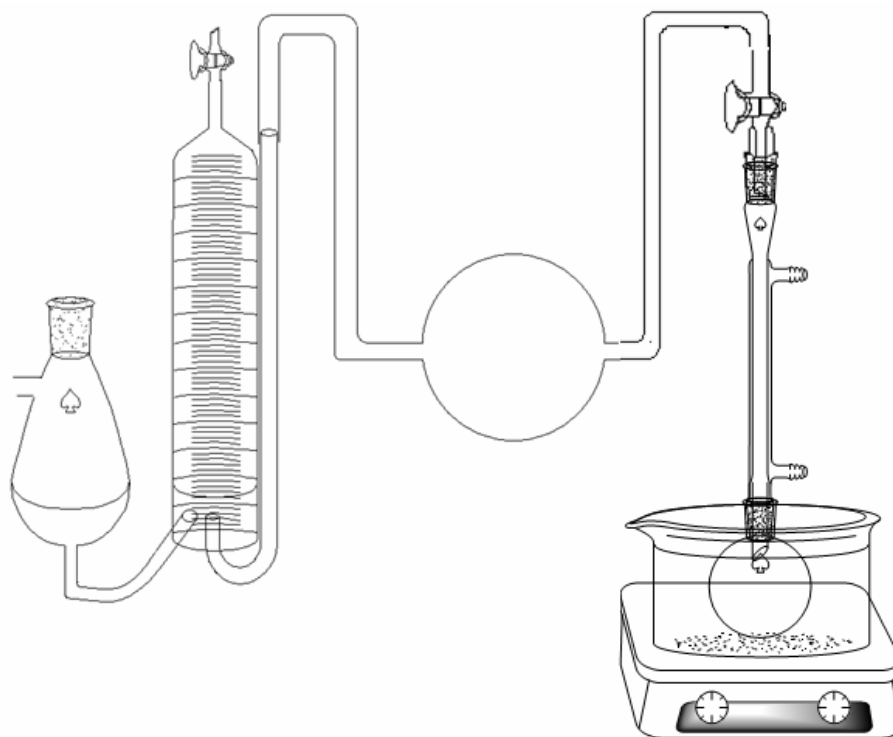
Figure 1a: Volumetric apparatus used for temperatures up to 100 °C
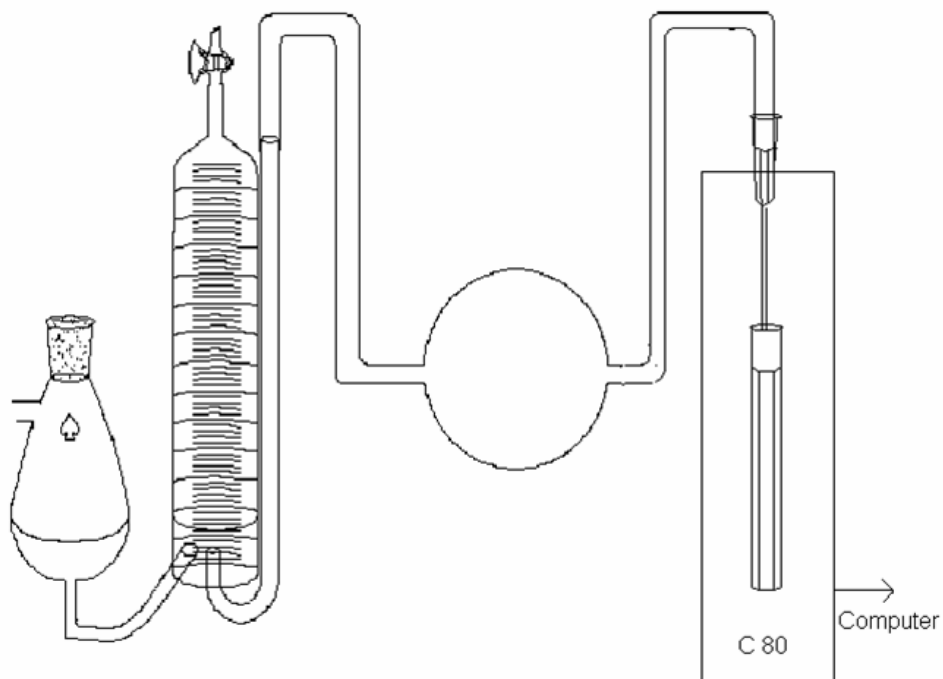
Figure 1b: Volumetric apparatus used for temperatures up to 200°C

Results

Pure Ammonia Borane

Solid state ^{11}B NMR of AB shows a peak at – 32ppm.
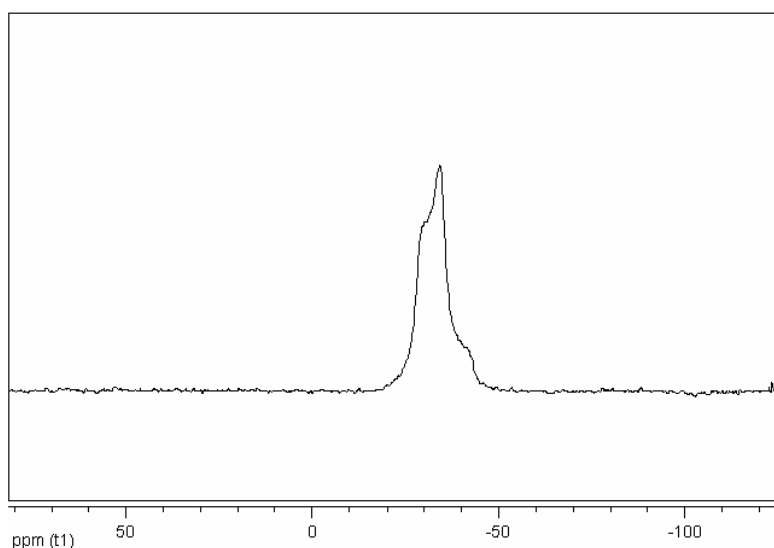
Figure 2: ^{11}B solid state NMR of AB

Calorimetric data for AB collected on the C80 shows two exothermic effects during the heating of the compound to 250 °C, the first beginning at 110 °C, peaking at 113 °C, and the second beginning at 137 °C and peaking at 151°C.
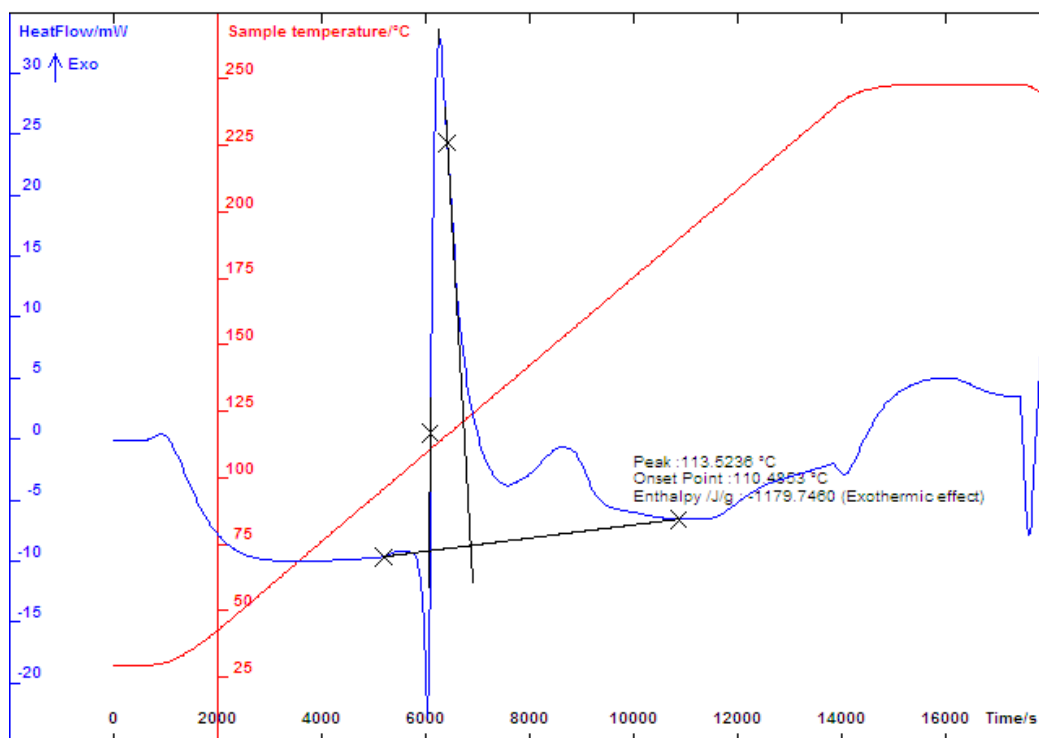
Figure 3: ^{11}B solid state NMR of AB

1:1 AB + MgH$_2$

^{11}B solid state NMR of the product of the 1:1 milling reaction showed a shift in the AB peak from -32 ppm to -29 ppm and the development of a new second peak at – 40ppm, showing the formation of a new material during the milling reaction.

ppm (t1)
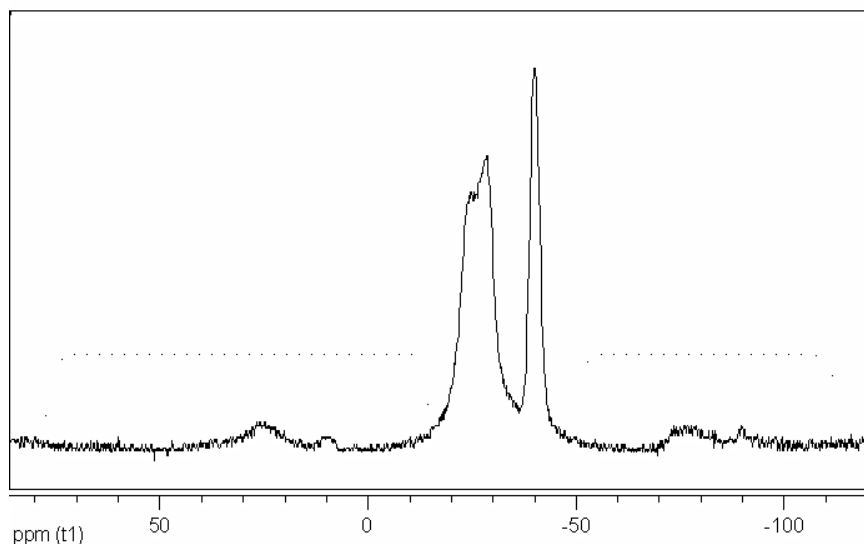
Figure 4: ^{11}B solid state NMR of 1:1 AB + MgH$_2$

The chemical shift of the peak corresponds well with Mg(BH$_4$)$_2$, however, unlike Mg(BH$_4$)$_2$, the material is not soluble in THF. Hence, the material is postulated to contain a borohydride unit of some description; however, further analysis will be needed to confirm this.

Heating the product formed to 250°C on the C80 gave the following data:
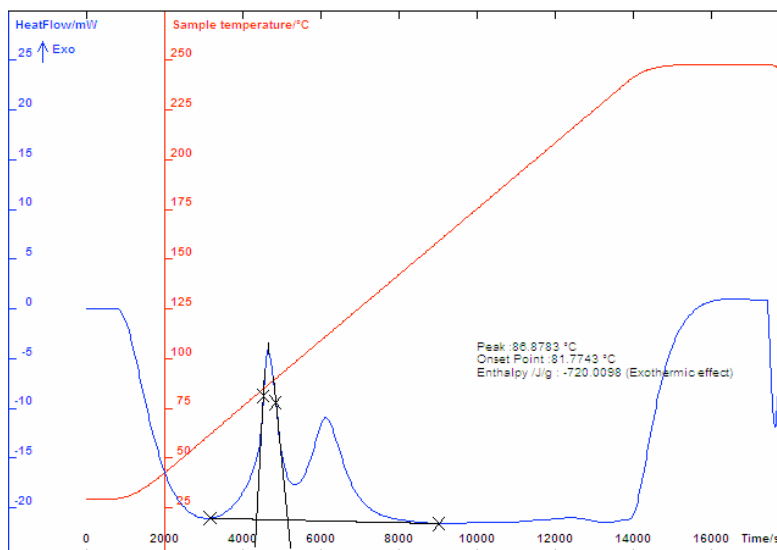
Figure 5: C80 plot of 1:1 AB + MgH$_2$ heated to 250 °C

The temperature at which the first exothermic effect begins in the product of the 1:1 reaction is lower than that of pure AB. The first effect begins at 82°C and peaks at 87°C (compare to AB, peaking at 113°C). There is considerable overlap between the first and second effects and therefore the point at which the 2nd effect commences is unknown, however, it peaks at 111°C. The total enthalpy of the change is calculated to be – 720 Jg[-1].

The ^{11}B solid state NMR of the product before and after desorption is shown below:
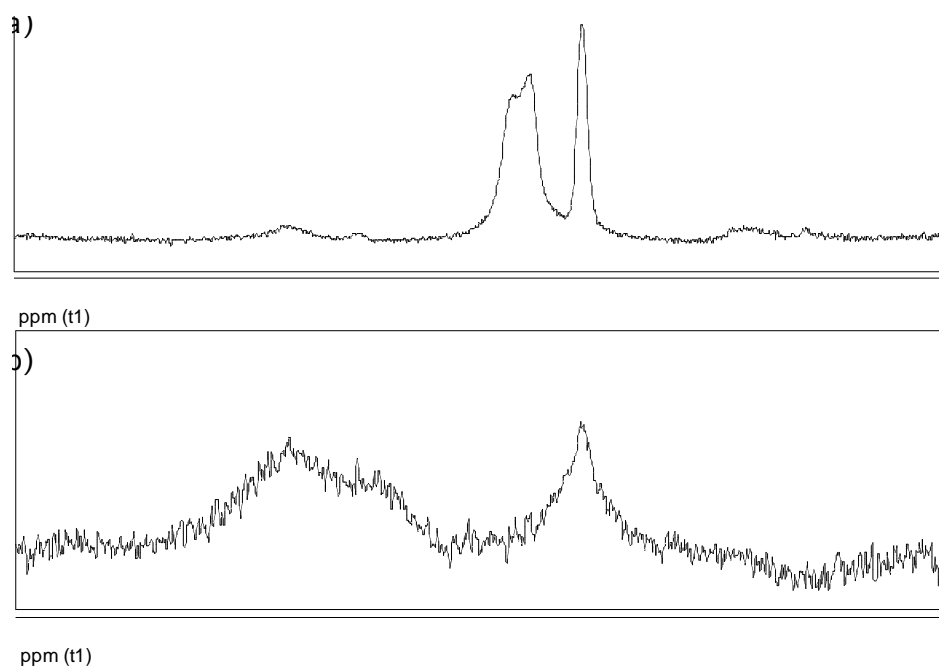
Figure 6: ^{11}B solid state NMR of 1:1 AB + MgH$_2$ a) before and b) after desorption to 250°C

It is clear that heating to 250°C results in decomposition of AB only, as the peak for the new material appears broadened, but essentially still in tact.

Volumetric studies give more detailed information regarding the release of hydrogen.

Experiments show that up to 3 wt% H_2 is desorbed below 80°C, 5.4 wt% below 100°C, and 8.4 wt% below 200°C:
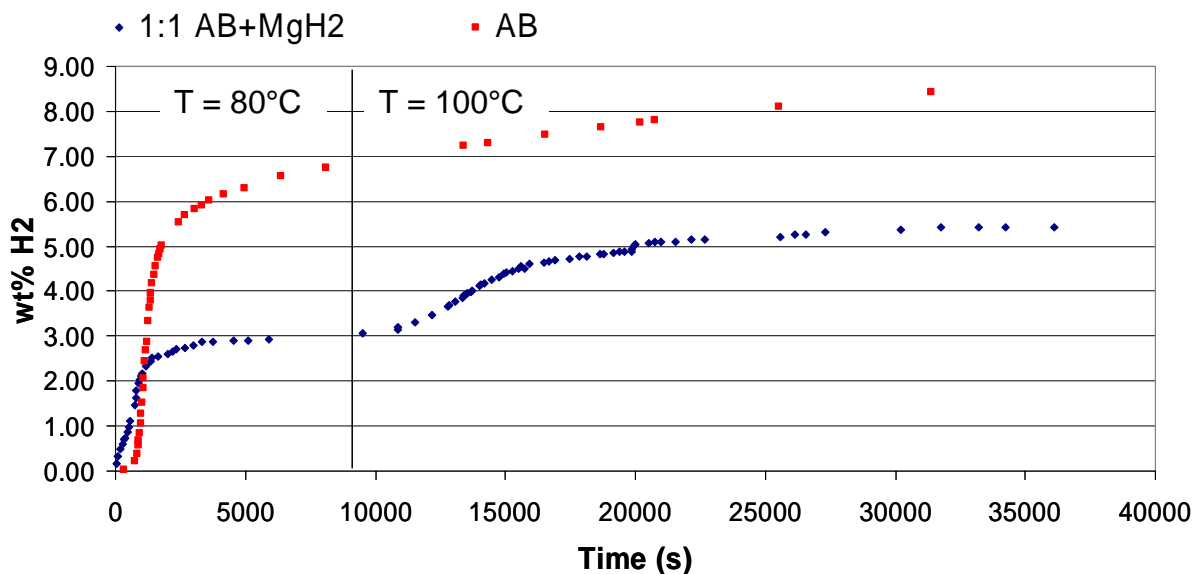
Figure 7a: Wt% H_2 desorbed at 80 °C and 100 °C from AB and 1:1 AB + MgH$_2$

5.4 wt% corresponds to 1.5 equivalents of H_2 desorbed below 100°C. Given that the rate of desorption[15] at 100°C is approximately ¼ of that at 80°C (rates of 0.011 wt% min^{-1} and 0.041 wt% min^{-1} respectively), it appears that the type of H_2 released at the each of the temperatures may be from two different desorption processes. It could be that the 2nd desorption step corresponds to the beginning of the second exothermal effect in the calorimetric data, and that if the temperature had been raised to 111°C, the decomposition would have continued, releasing the full two equivalents. Heating to 200°C yields 8.4 wt% H_2 (2.2 H_2 equivalents).
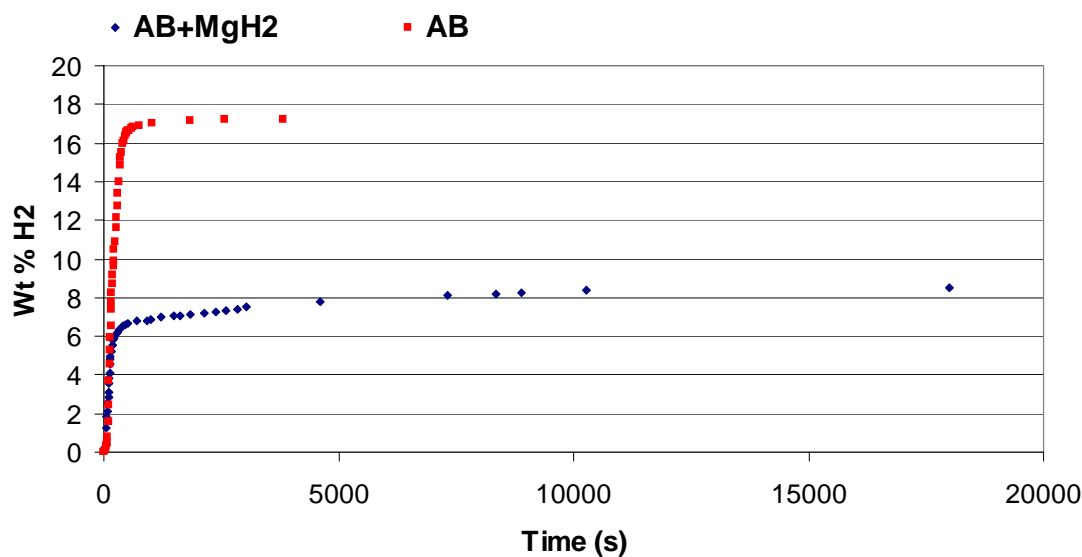
Figure 7b: Wt% H_2 desorbed at 200 °C from AB and 1:1 AB + MgH$_2$

The ^{11}B NMR spectrum of the products of decomposition of AB and 1:1 AB + MgH$_2$ to 100°C and 200°C shown in figures 7 and 8, respectively. In both sets of spectra, the peak at – 40ppm in the decomposition product of the 1:1 mixture is still very much present, implying that all of the H$_2$ formed comes from the AB still present in the material after the milling reaction. This conclusion is supported by the fact that the amount of hydrogen liberated during the decomposition reaction of AB is approximately twice that released from the 1:1 AB + MgH$_2$.
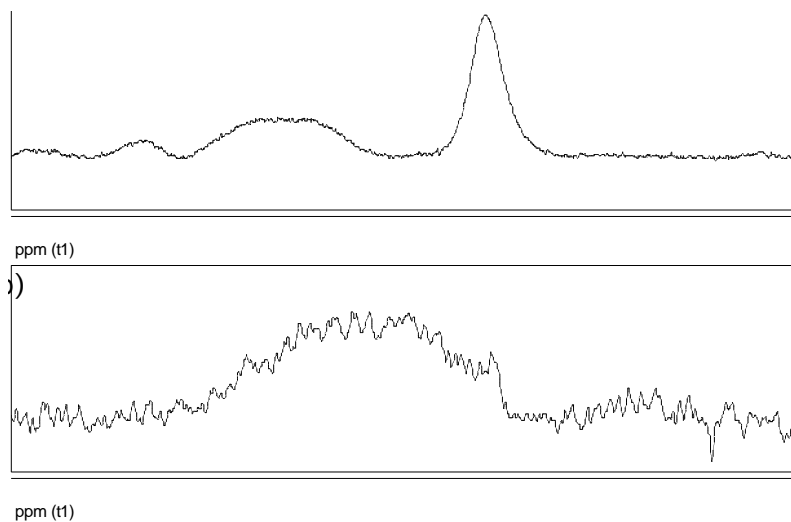
Figure 8: ^{11}B NMR of products of thermal decomposition of a) 1:1 AB + MgH$_2$ and b) AB at 100 °C
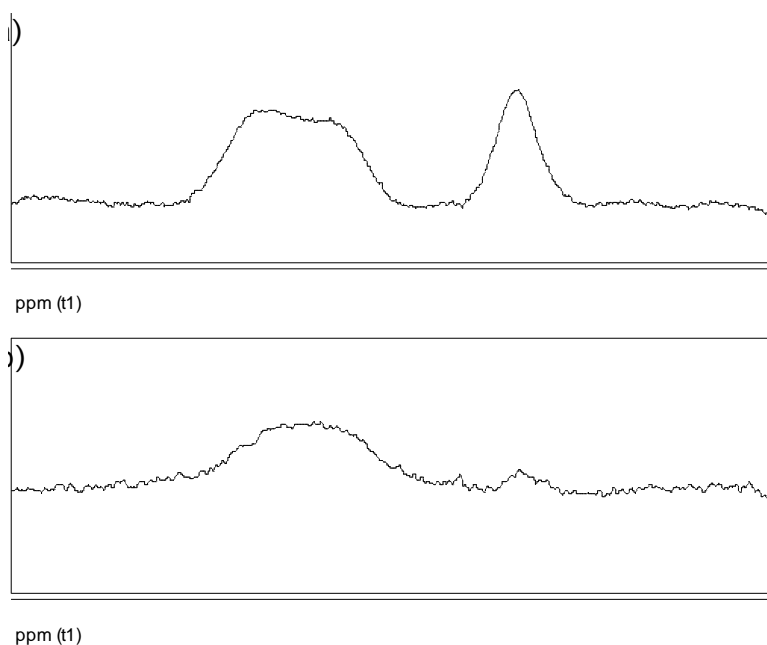
Heating the 1:1 mixture at a rate of 1K min^{-1} up to the end of the 2nd exothermal effect (168°C) gave the following results, showing a total H_2 desorption of approximately 7 wt%. Desorption clearly occurs in a 2 step process with each of the steps corresponding to an exothermal effect.
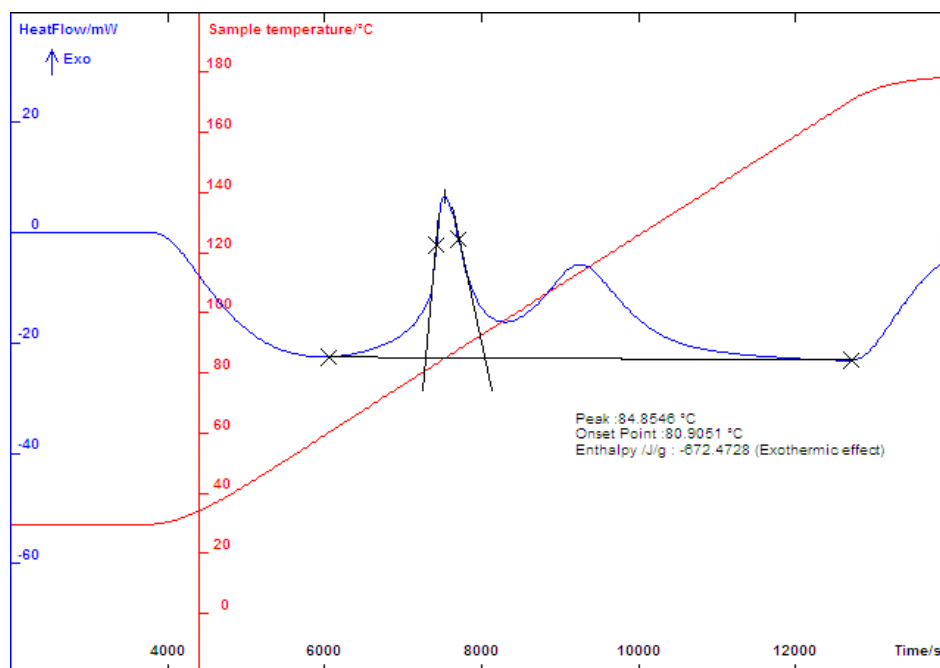
Figure 10: C80 Plot of 1:1 AB + MgH$_2$ quenched after the 2nd exothermal effect
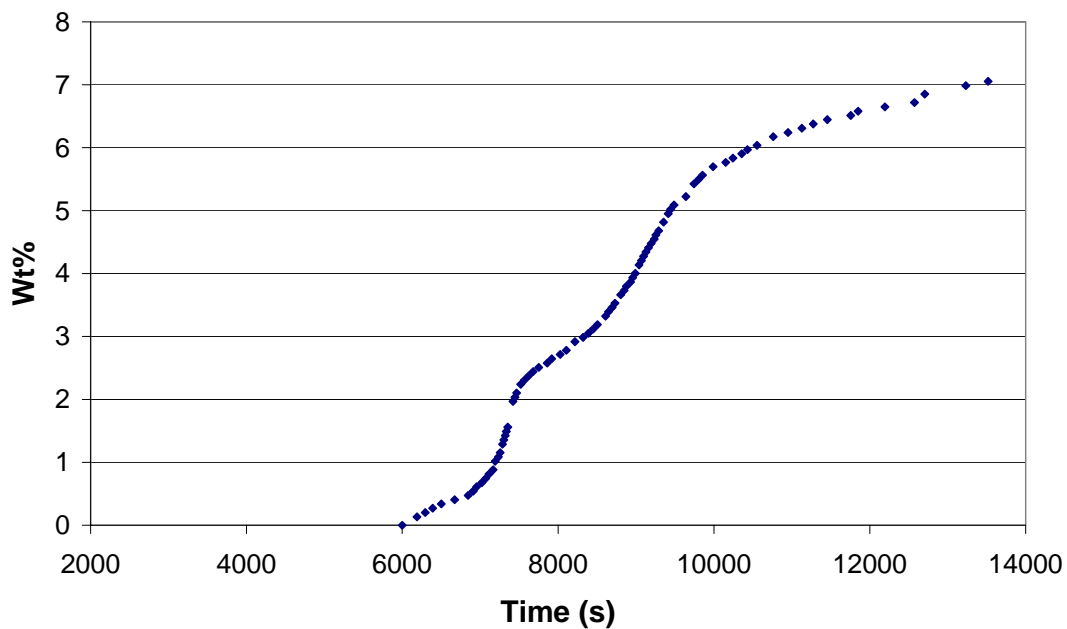
Figure 11: Wt% H$_2$ desorbed from 1:1 A + MaH$_2$ up to the end of the 2nd exothermic effect

2:1 AB + MgH$_2$

The ^{11}B solid state NMR spectrum shows only one peak corresponding to AB, and hence, the product formed in the 1:1 reaction of AB with MgH$_2$ does not form in the 2:1 reaction.
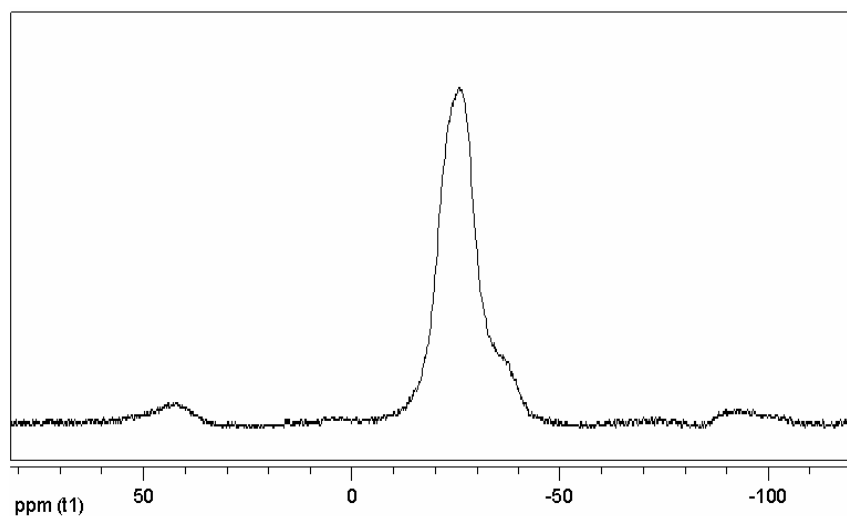
Figure 12: ^{11}B NMR of product of 2:1 AB + MgH$_2$

The calorimetric data collected on the C80 during heating to 250°C gives very similar results to that of AB heated to 250°C. The onset point of the exothermal effect is at 109°C (cf AB at 110°C) and the effect peaks at 113°C (AB also at 113°C).
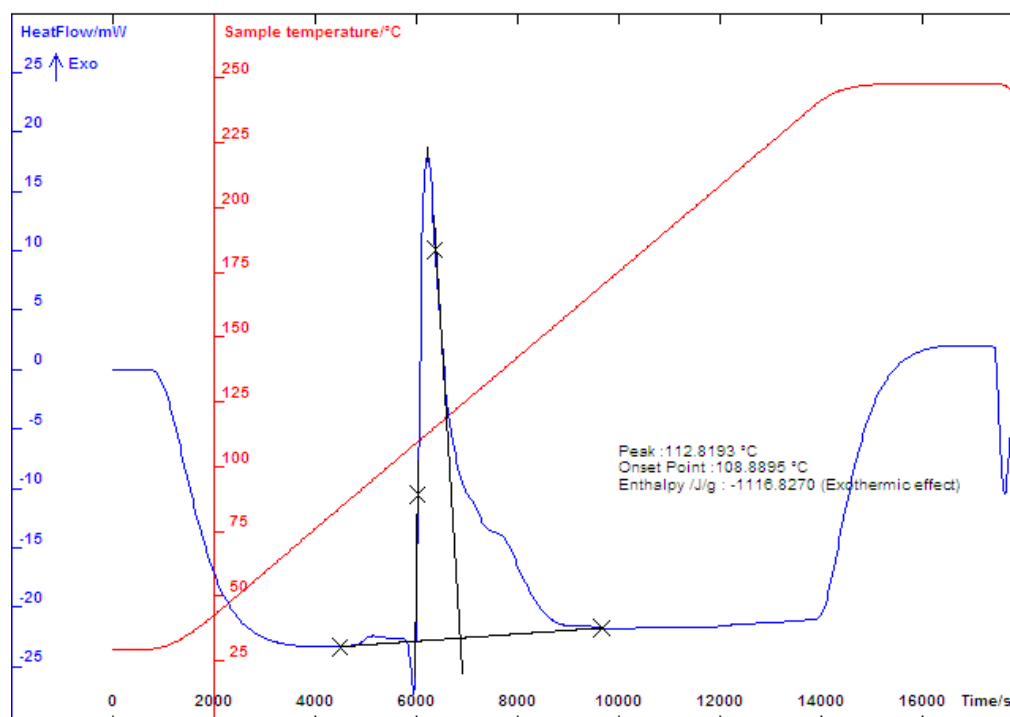
Figure 13: C80 Plot of 2:1 AB + MgH$_2$

Conclusions

The mechanical milling of a one to one mixture of ammonia borane and magnesium hydride produces a new material which has the effect of lowering the decomposition temperature of the remaining ammonia borane from 113°C to 84°C. The H_2 storage capacity of the 1:1 mixture below 250°C is reduced by approximately 50% compared to that of pure ammonia borane. The 2:1 reaction of ammonia borane with magnesium hydride does not produce the new material and the product behaves in a similar way to pure ammonia borane.

Acknowledgments

References

1. Choi, O., Fisher A., *Climate Change,* **2003**; 58: 147

2. http://www.rmi.org/sitepages/pid540.php, 05/06/06

3. www.msdssearch.com

4. See www.bellona.no/en/energy/hydrogen

5. www-formal.stanford.edu/jmcprogress/hydrogen.html

6. Timpe, R.C., Kulas, R.W., Hauserman, W.B., Sharma, R.K., Olson, E.S., Willson, W.G., *Int. J. Hydrogen Energy,* **1997**; 22: 487-492

7. Lipman, T.E., DeLucchi, M.A., *Int. J. Vehicle Design,* **1997;** 17: 562

8. PV = nRT

9. I. R. Harris, D. Book, P. A. Anderson, P.P. Edwards, *Fuel Cell Rev.,* **2004** June/July: 17

10. L. Zhou, *Renewable Sustainable Energy Rev.,* **2005**; 9: 395

11. W. Grochala , P.P. Edwards*, Chem. Rev*., **2004**; 104: 1283

12. Shore S.G., Parry W., *J. Am Chem. Soc*., **1956**; 78: 503

13. Hu M. G., Greanangel R. A., Wendlandt W. W., *Thermochim Acta*.

14. Baitalow F. Baumann J., Wolf G., Jaenicke-Rößler K., Leitner G., *Thermochim Acta,* **2002;** 391: 159

15. The desorption rates were calculated as the ratio between the amount desorbed and the time taken to go from 20 to 80% of capacity measured at each temperature.

Molecular Modeling of the N-acyl homoserine lactone hydrolase from *Bacillus thuringiensis*.

Wagner A. Lucena
Insect Molecular Biology Laboratory,
EMBRAPA Algodão, Campina Grande, PB 58107-720, Brazil
and
Roberto Lins
Pacific Northwest National Laboratory
Richland, WA
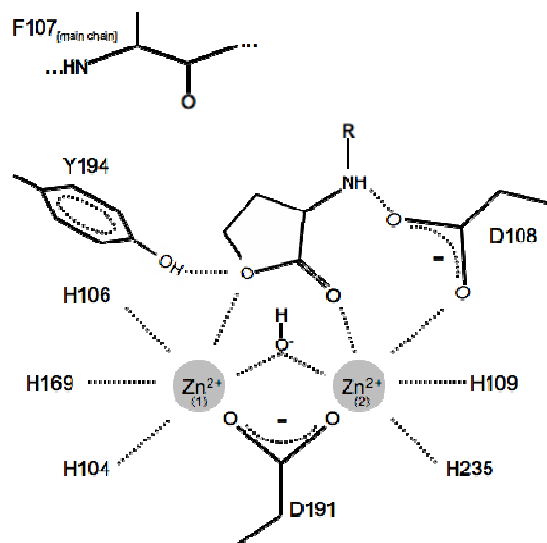
Influence of the N-acyl group on the binding of homoserine lactones to the quorum-quenching N-acyl homoserine lactone hydrolase from *Bacillus thuringiensis*.

Wagner Lucena[2] Tjerk P. Straatsma[1] and Roberto D. Lins[1,*]

[1]Computational Biology and Bioinformatics, Pacific Northwest National Laboratory, Richland, WA 99352, USA

[2]Insect Molecular Biology Laboratory, EMBRAPA Algodão, Campina Grande, PB 58107-720, Brazil

[*]To whom the correspondence should be addressed. Phone: +1-509-375-2755; Fax: +1-509-372-4720; E-mail: roberto.lins@pnl.gov.

INTRODUCTION

Quorum Sensing (QS) may be defined as the ability that some bacterial strains have to coordinate collective behavior using a regulatory mechanism that is dependent of expression of a group of genes and a signal transduction pathway. This phenomenon was first reported for the luminescent marine bacterium *Vibrio fischeri* (Naelson, 1970). Bacteria use QS mechanism to regulate a range of biological functions such as biofilm formation, bioluminescence, antibiotic production and virulence factor expression (Camilli, 2006). Since alterations on the QS can interfere in acute infections, devising ways to modulate QS can be a useful tool to coordinate the bacteria behavior via control of the population density, e.g., transgenic plants resistant to root diseases (Fray, 1999), biofilm formation in *Pseudomonas aeruginosa* (Davis, 1998; Dong, 2002), regulation of Ti plasmid in *Agrobacterium tumenfasciens* (Zhang, 1991; Hao and Burr, 2006).

The general pattern is dependent of a production of small diffusible molecules namely autoinducers (AI) synthesized in low concentrations. When the signaling molecule concentration reach a threshold, it binds to a receptor and initiate a cascade signal that ends with the activation of a set of genes that are involved with a specific phenotype. While a peptide-based signal is typically used by Gram-positive bacteria (Spoering and Gilmore, 2006), N-acyl homoserine lactones (AHLs) serve as the signal autoinducer molecules in Gram-negative type bacteria (Rasmussen, 2006). The homoserine lactones (HSLs) are synthesized by the family of LuxI homologue proteins, using acyl-carrier proteins as the major N-acyl chain donor and S-adenosyl methionine to provide with the homoserine lactone moiety (Parsek et al., 1999 in Rasmussen, 2006). With exception of LuxLM from *V. harveyi* (Bassler et al., 1993), all HSL synthases are LuxI homologs and they usually produce HSLs with different N-acyl chains, which also cause different catalytic activity levels. Those enzymes are expressed in low cell densities and promote an accumulation of HSLs up to a certain level when binding to LuxR (DNA-binding proteins) occurs. They form a multimeric complex (TF-transcriptional factor) that recognize the Lux box DNA sequence and induce the expression of gene coordinated by *lux* operon, which includes LuxI (Val and Cronan, Jr. 1998).

A second group of enzymes, the N-acyl homoserine lactone hydrolases, (lactonases), is responsible for the cleavage of the autoinducer homoserine ring (Dong et al., 2000), and therefore is known as a quorum-quenching (QQ) enzyme. The inactivation and/or absence of the QS messenger molecules can downshift the population density and inhibit biofilm formation. Recently, a 250-residue long N-acyl homoserine lactone hydrolase (AiiA) was isolated from *Bacillus thuringiensis* (BTK), a Gram-positive entomopathogenic soil bacterium (Dong et al., 2000). This enzyme family is spread with high similarity among isolates and strain of *B. thuringiensis, B. cereus* and *B. mycoides* but not in *B. sphaericus* and *B. fusiformis* (Dong et al., 2002). The BTK-AiiA enzyme presents a highly-conserved zinc-binding domain (^{104}HXHXDH^{109}≈ H^{169}) similar to the metallo-β-lactamase superfamily (Dong et al., 2002; Lee et al., 2002; Kim et al., 2005), and its metal-binding site is identical to the human glyoxalase II. The activity has been shown to be zinc-dependent through the use zinc chelators to decrease and reconstitute its catalysis (Thomas et al., 2005). BTK-AiiA is known to hydrolyze N-acyl-(S)-homoserine lactone substrates whith acyl chains varying from 4-12 carbons long, revealing an acyl chain length preference with a maximum activity for C10-AHL. The overall hydrophobicity of the substrate is given by a balance between the hydrophilic homoserine lactone ring and the hydrophobic chain side. This amphipathy of the N-acyl-HSL allows them to navigate the phospholipid bilayer of the cell as well as the aqueous intracellular and extracellular environments (Fuqua et al., 2001). The overall structure of BTK-AiiA reveals a αβ/βα sandwich fold. The N-terminal repeat (1-152) is formed by seven β-sheets, three α-helices and six shorts 3_{10} helices. The C-terminal (153-250) contains five β-sheet strands and three α-helices. Two loops are importantly evolved with the acyl-chain binding: H18-K29 and V58-I73. The crevice formed by the residues L16, V35, M53, P54, A57, L73, P75, M77, F107 and M138 acts as a pocket to the side-chain. Finally, the catalytic site is formed by H104, H106, D108, H109, H169, D191, Y194 and H235 (Liu et al., 2005; Kim et al., 2005). Although the enzyme is active against a range of N-acyl-HSL substrates it does not cleaves HSL itself. It has led to the suggestion that the amide linkage may be essential for proper substrate binding (Kim et al., 2005). Despite those data, analysis of the reaction products after incubation of racemic C6-HSL with AHL confirms that this enzyme hydrolyzes the lactone and not the amide bond of the substrate (Thomas et al., 2005).

One proposed catalytic mechanism is based on a nucleophilic attack by a water/hydroxide, bridging the two zinc ions, on the substrate's carbonyl carbon. The carbonyl bond would become more susceptible to the nucleophilic attack due to an enhanced

polarization caused by the interactions with the zinc ions with the lactone ring and the carbonyl oxygens of the HSL. Both D108 and Y194 have been proposed to play a strong role in the catalysis (Liu et al., 2005; Kim et al., 2005). HSL binding to lactonases could possibly occur in two main distinctive configurations regarding the interaction of the lactone ring and carbonyl oxygen atom to the two zinc ions (Figure 1). Additionally, the positioning of the oxygens of the lactone ring can lean towards D108 or Y194 (*si* and *re* face, respectively) could lead to further insights into the catalytic mechanism. Y194 could either serve as a hydrogen-bonding partner stabilizing the tetrahedral adduct (Liu et al., 2005) or a general acid to protonate the leaving group (Liu et al., 2005; Kim et al., 2005). Alternatively, D108 has been proposed to act as a proton shuttle if the substrate binding takes place as in mode-2 and *si* face (Liu et al, 2005). Aiming to elucidate this problem Kim and co-workers reported the crystal structure of BTK-AiiA complexed with a L-HSL molecule (Kim et al., 2005). In this study, the enzyme did not show any significant conformational change upon HSL binding (0.13 Å root-mean-square deviations for the protein C_α atoms). HSL binding to the enzyme active site presented 0.75 occupancy with an average B-factor of 34.9 $Å^2$. The HSL carbonyl group was found to bind the Zn2 (see Figure 1) located in close proximity of the side chain of D108, while the ring oxygen is sandwiched between Zn-1 (see Figure 1) and the hydroxyl group of Y194 (mode-1 in Figure 1). The lactone nitrogen atom lies within at 3.3 Å from D108-Oδ2, hence suggesting the presence of a hydrogen-bond between these two groups. The authors naturally assume that the binding of the HSL molecule is representative of the substrate binding, however other possibilities for substrate binding orientation have been reasoned based on the crystal structure of BTK-AiiA complexed with glycerol (Liu et al., 2005).

Kinetic and substrate specificity measurements have showed that AiiA displays no or little residual activity to non-acyl lactones (Wang et al., 2004; Kim et al., 2005). Based on the fact that the presence of N-acyl chain is *sine qua non* to the catalysis, N-formyl-L-homoserine lactone (NFH) was proposed to serve as the lactonase simplest substrate (Kim et al., 2005). The backbone chain amide groups of F107 and D108 have been suggested to possibly orient the acyl carbonyl helping the AHLs fitting into the active site pocket, while I73 and M138 have been proposed to take part in the N-acyl chain binding (Kim et al., 2005). Those interactions between the substrate's N-acyl group and the enzyme would explain why HSL itself cannot be hydrolyzed.

In order to verify the influence of the N-acyl group in the binding of the lactone ring to the lactonases, molecular dynamics simulations of the BTK-AiiA have been carried out for the enzyme free in solution, complexed with HSL and NFH (Figure 2). Our results show that the lactone ring can only bind to BTK-AiiA in mode-1 and that the conformational variability of the lactone ring in the protein active is diminished upon attachment of a N-formyl group to the ligand.

METHODOLOGY
Molecular Systems

The crystal structure of the homoserine lactone hydrolase (HSL) with Protein Data Bank (PDB) entry code 2A7M solved at 1.6 Å resolution, (Liu et al., 2005) was used as a starting point for all simulations. Three systems were considered: i) AiiA: explicit-solvated protein with one hydroxyl and two zinc ions in the active site; ii) AiiA-HSL: AiiA complexed with a homoserine-lactone molecule (HSL); and iii) AiiA-NFH: AiiA complexed with N-formyl-homoserine lactone (NFH). Initial positions for HSL and NFH molecules were modeled by positioning their carbonyl and ring oxygen atoms in respect to the enzyme active site as described in the crystal structure of the AiiA complexed with HSL (Kim et al., 2005) (mode-1 in Figure 1). Although the latter, a 1.7 Å resolution AiiA with PDB entry code 2BR6 have been

resolved with the atomic positions for the homoserine lactone into the enzyme active site, the atomic positional coordinates of the protein residues 61-72 have not been determined. Therefore, HSL and NFH were modeled onto the coordinates for the PDB ID entry 2A7M (Liu et al., 2005) instead.

In all cases, simulations were performed under periodic boundary conditions based on a cubic box of initial edge lengths 7.8 nm. The systems were solvated by filling the box with extended simple-point-charge (SPC/E) water molecules (Berendsen et al., 1987) imposing a minimum distance of 0.28 nm between water molecules and any solute atom, and preserving the coordinates of the 180 crystallographic water molecule oxygen atoms. The distances between the Zn^{2+} ions and their corresponding coordinating histidine nitrogen atoms were treated as a bonded-term with an equilibrium distance of 0.20 nm and 4.184×10^4 kJ/mol force constant. Histidines 104, 109, 169, 235 were protonated on their δ-nitrogen atom. All the other histidines displayed the proton at their ε-nitrogen atom. A total of 7 water molecules with the highest electrostatic potential at the oxygen site, and a minimum distance of 0.8 nm from any protein atom, were successively replaced by 6 Ca^{2+} and 1 Na^+ ions in order to neutralize the systems. This procedure resulted in the following systems: i) AiiA: 1 protein molecule (3,948 atoms), 2 Zn^{2+} ions, 1 hydroxyl anion (OH^-), 7 counter ions, and 14,512 water molecules (47,495 atoms); ii) AiiA-HSL: 1 protein molecule (3,948 atoms), 1 homoserine lactone molecule (HSL), 2 Zn^{2+} ions, 1 OH^-, 7 counter ions, and 14,509 water molecules (47,500 atoms); and iii) AiiA-NFH: 1 protein molecule (3,948 atoms), 1 N-formyl homoserine lactone (NFH), 2 Zn^{2+} ions, 1 OH^-, 7 counter ions, and 14,460 water molecules (47,358 atoms).

Molecular Dynamics Simulations

All simulations were performed using the AMBER96 force field (Cornell et al., 1995) in conjunction with newly-derived charges for the HSL and NFH molecules (procedure described below) and implemented in the parallel version of the NWChem-4.7 program (Apra et al., 2005). The systems were equilibrated in a stepwise fashion. First, the solvent and the substrates (when present) were relaxed using up to 5000 steps of steepest descent energy minimization, keeping the protein and ions fixed. This was followed by an additional 500 steps of minimization without solute constraints. System equilibration was continued by performing successive 10 ps of MD runs at 50, 100, 150, 200, 250, and 300 K, with velocity reassignments every 0.4 ps. Following the equilibration time, production MD runs were carried out in the isothermal-isobaric ensemble for 4.0 ns. The temperature was maintained at 300 K by weak coupling the solute and solvent separately to a heat bath (Berendsen et al., 1984) with a relaxation time of 0.1 ps. The pressure was kept at 1.025×10^5 Pascal using weak coupling to a pressure bath (Berendsen et al., 1984) via isotropic coordinate scaling with relaxation time of 0.1 ps. Long-range electrostatic interactions were handled using the smooth particle mesh Ewald (SPME) method (Essmann et al., 1995) A cutoff 1.0 nm was used for the short-range non-bonded interactions (van der Waals and real-space electrostatic contribution). The SHAKE (Ryckaert et al., 1977) algorithm was applied to constrain all bonds involving a hydrogen atom, and a 2-fs timestep was used to integrate the equations of motion based on the leapfrog algorithm (Hockney, 1970). Trajectory frames were recorded every 0.2 ps for analysis.

Charge Model

The present simulations were carried out using the AMBER96 force field (Cornell et al., 1995) to describe the hydroxyl ion and the HSL and NFH substrate molecules, except for the charges, which were not readily available and hence needed to be derived. Based on the optimized geometry of the hydroxyl anion and the HSL and NFH substrates, Hartree-Fock calculations at the 6-31G* level followed by a restrained electrostatic potential (RESP) fit

(Bayly et al., 1995) were performed using the NWChem4.7 program (Apra et al., 2005) to compute the partial charges. Values of 0.005 a.u. for the harmonic and 0.001 a.u. for the hyperbolic restraints, respectively, were used in the RESP fittings. Charge derivation by means of RESP fitting preserves the dipole moment of a molecule to its quantum-mechanical value, and should therefore lead to a realistic description of intermolecular interactions with identical as well as distinct molecular species during the simulations. The charge-derivation procedure was performed according to the AMBER96 force field philosophy (Cornell et al., 1995) in order to preserve force field compatibility. The final charge sets for the above-mentioned ion/molecules are shown in Table I.

RESULTS AND DISCUSSION
Protein Flexibility

The root-mean-squared deviations (RMSD) of all protein atoms were calculated over 2 and 4 ns trajectories taking as a reference frame the crystallographic structure PDB ID 2A7M. The time evolution of the RMSD with respect to the 3D structure provides a measurement of the convergence of the dynamical properties of the protein. The RMSD ranges from 0.025 to 0.225 nm (Figure 3). All four studied systems presented RMSDs higher than the BTK-AiiA lactonase without substrates, suggesting that the homoserine lactone ring increases the displacement of BTK-AiiA lactonase. N-formyl homoserine lactone (mode 1) promotes a slightly higher RMSD even when was compared at 2 and 4 ns trajectories.

The root-mean-square atomic positional fluctuations (RMSF) of NFH and HSL (mode1) and HSL free systems showed wide deviations from the B-factor 3D crystallographic obtained, when the most flexible protein portions were observed (Figure-4). There are six flexible loops formed by the residues 22-28 (loop 1), 53-78 (loop 2), 125-138 (α3 and loop 3), 175-186 (loop 4) 190-209 (loop 5) and 220-233 (loop 6). The loops 1 and 2 showed marked increase of RMSF; 0.7 and 0.8, respectively. These loops are responsible to fit the N-acyl substrate chain into the hydrophobic channel (Kim et al., 2005; date no shown).

Previous experimental data showed 0.75 occupancy and an average B-factor of 34.9 Å^2 for HSL. Our calculated B-factors from the 4 ns MD trajectory (equilibration excluded) for HSL and NFH were ca. 46 Å^2 and ca. 23 Å^2, respectively, suggesting that the NFH is more stable into the BTK-AiiA lactonase catalytic site.

HSL and NFH binding modes

Wang et al., 2004, using biochemical assays, presented specificity and kinetics data for BTK-AiiA lactonase testing several substrates. The lactonase showed low activity for the HSL. Others workers hypothesize that HSL is not a substrate indeed, but an inhibitor (Kim et al., 2005; Liu et al., 2005) and the N-acyl chain is necessary to the lactonase catalysis, although the enzyme cleaves at the carbon carbonyl of lactone ring.

We did measurements of the distances from zinc ions to the leaving group and carbonyl oxygens of the lactone ring (Figure 5).

The carbonyl oxygen distances of the HSLs to the nearby zinc are constant at ca. 0.2 nm in all simulated systems. The leaving group oxygen of the HSL (modes 1 and 2) also presented similar zinc distances, ranging from ca. 0.25 nm to ca. 0.6 nm through both trajectories. These results suggest that the HSL ring do not interact with the metal site. Comparing HSL and NFH trajectories, we observed that the HSL ring, both modes 1 and 2, showed tree configurations at the catalytic site, changing the position of the lactone ring plane related to the zinc site (data no shown). NFH-mode 2 rotates its leaving group backwards to the metal site, presenting a zinc distance around 0.45 nm at the 2ns simulation. Only NFH-mode-1 remains near to the zinc site with a leaving group oxygen distance of ca. 0.325 nm, therefore

binding the enzyme in a stable manner. These zinc ion/oxygen interactions are important to attach the lactone ring at the lactonase catalytic site.

All these results confirmed the presence of an N-acyl chain is necessary to stabilize the substrate in the catalysis site, and probably contribute to the nucleophilic attack by interactions with the zinc atoms.

Important residues in the binding of lactones

The residues F107, I73, M138, F64, M53, D108 and Y194 have been point out as important to the binding and catalysis reaction. The behavior of these and other residues nearby the active site and the binding molecule have been monitored throughout the trajectories. The analyses for the residues of identified significant importance for HSL and NFH binding are presented below.

The analysis of the distance variation between C3 (carbonyl carbon of the lactone ring), N4 (HSL and NFH), O5 (carbonyl group of N-acyl chain) and C6 (methyl group) of the N-formyl chain and those residues showed some interesting aspects of AHL binding mode.

Kim et al. 2005 and Liu at al. 2005 postulated that the catalysis is mediated by D108 and Y194 residues, the HSL can present two substrate-binding orientations (modes 1 and 2) and that the carbonyl carbon of the lactone ring can place either its *si* or *re* face towards the zinc ions.

To point light over these questions, we measured the distances between the carbonyl carbon of the lactone ring (HSL and NFH mode 1) and the OD1 of the D108 and the OH of the Y194 (Figure 6).

The C3-HSL/OH-Y194 distance variation suggested that this residue do not interact with the lactone ring. In spite the fact that the C3-HSL/OD1-D108 distance varied around ca. 0.3 nm over almost the entire simulation, this supposed interaction is not enough to stabilize the HSL at the activity site and do not contribute to the discrepant configurations found to HSL inside of the catalytic site.

The OD1-D108 and OH-Y194 distances to C3-NFH obtained from the trajectories were ca. 0.35 nm and ca. 0.3 nm, respectively. However, the C3-NFH/OD1-D108 distance ranged less than the Y194 measurements, suggesting that the N-formyl interact with D108 in a stable manner, therefore present a *si* face, with the leaving group and carbonyl oxygen of the AHL ring oriented towards the D 108 residue.

The N4/D 108 distances showed different profiles, when the HSL and NFH were compared, trough the 4 ns trajectories (Figure-7). HSL distances varied from ca. 0.27 nm to ca. 0.67 nm and after 2.5 ns of simulation ranged widely, suggesting that D 108 do not interact with the N4. However, the N-formyl-HSL remains attached at the catalytic site by the interaction with D108, which distance continue constant around ca. 0.4 nm.

The distances between the carbonyl oxygen of the N-acyl chain of NFH (modes 1 and 2) and the amide group of F107 were ca. 0.65 nm and 0.4 nm, respectively. F107 amide group showed no apparent influence on the binding configuration of the ligand (Figure 8). The NFH-mode 2 distance was lower, but probably due to the spatial positioning of the initial configuration submitted to the MD and not because these residue interacts strongly with the NFH.

Although carbonyl group of the N-formyl chain in mode-1 seems remained fully solvated and does not interact with any residue of the protein throughout the entire trajectory, the methyl group of the NFH in mode-1 was observed to interact within a 0.5 nm radius with I73, F64 and F107, flanking residues of the hydrophobic channel (data not shown).

Finally, to identify the most occurring substrate-binding configurations, we calculated the clusters for HSL and NFH (mode 1) (Figure 9). HSL presented seven clusters with two

corresponding to 52.3% and 44.8% of total and NFH presented 12 clusters, with 92.9% concentrated at the two higher (69.3% and 23.6%, respectively). The frequency and position of these two major clusters of both systems suggest that N-formyl binds to the catalytic site in a preferential manner. The analysis of the binding modes reveals that this preferential positioning is potentially more susceptible to the BTK-AiiA lactonase cleavage.

CONCLUSION

The biological functions regulated by AHLs are considerable scientific, economic, and medical importance (Dong et al., 2000). The disestablishment of such AHL-mediated QS systems has thus been targeted as a promising approach for a novel control technique of virulence gene expression in bacterial infections (Kim et al., 2005). Understanding the molecular basis of the phenomenon, i.e., the catalytic mechanism, is therefore of crucial importance. In the present report we have used molecular dynamics simulations to characterize the binding of homoserine lactones to the BTK-AiiA active site. The absence of the N-acyl group in these molecules leads to an increased flexibility in the active site and to a non catalytic-competent binding mode. On the other hand, the substrate is held into a better-defined binding mode via a hydrogen bond between the D108 and its N-acyl group and hydrophobic interactions between its methyl group and the side chains of I73, F64 and F107. The placement of the NFH lactone ring lies towards Y194, suggesting this residue as the potential catalytic residue. However, given the intrinsic limitations of the classical approach, further implications on the issue cannot be made at this time.

In summary, we have shown that the presence of the N-acyl group is essential for an efficient catalysis of the homoserine lactone molecules by BTK-AiiA; characterize the binding mode for the substrate; and, identified the key-player residues for substrate binding. The importance of long N-acyl chains in the substrate binding will be further inferred and shall soon be reported. These findings aid the understanding of the first step into the molecular basis of the quorum-quenching regulation in *B. thuringiensis* and shed light into the devising the control of bacterial biofilm formation.

REFERENCES

Bassler BL, Wright M, Showalter RE, Silverman MR. Intercellular signalling in Vibrio harveyi: sequence and function of genes regulating expression of luminescence. Mol Microbiol. 1993. Aug; 9(4):773-86.

Camilli, A. and Bassler, B. 2006. Bacterial small-molecule signaling pathways. Science. 2006 Feb 24; 311(5764):1113-6.

Davies, D. G., M. R. Parsek, J. P. Pearson, B. H. Iglewski, J. W. Costerton, and E. P. Greenberg. The involvement of cell-to-cell signals in the development of a bacterial biofilm. Science. 1998. 280:295-298.

Dong YH, Gusti AR, Zhang Q, Xu JL, Zhang LH. Identification of quorum-quenching N-acyl homoserine lactonases from Bacillus species. Appl Environ Microbiol. 2002 Apr; 68(4):1754-9.

Dong, Y.-H., J.-L. Xu, X.-C. Li, and L.-H. Zhang. AiiA, a novel enzyme inactivates acyl homoserine-lactone quorum-sensing signal and attenuates the virulence of Erwinia carotovora. Proc. Natl. Acad. Sci. 2000. USA 97:3526-3531.

Fray, R. G.; Throup, J. P.; Daykin, M.; Wallace, A.; Williams, P.; Stewart, G.S.A.B. and Grierson, D. Plants genetically modified to produce N-acylhomoserine lactones communicate with bacteria. Nat Biotechnol. 1999 Oct; 17(10):1017-20.

Fuqua, C.; Parsek, M. R. Greenberg, P. Regulation of Gene Expression by Cell-to-cell Communication: Acyl-Homoserine Lactone Quorum Sensing.1991. Annual Review of Genetics. Vol. 35: 439-468.

Hao, G. and Burr, T. J. Regulation of Long-Chain N-Acyl-Homoserine Lactones in Agrobacterium vitis. J Bacteriol. 2006, Mar. p. 2173–2183.

Kim MH, Choi WC, Kang HO, Lee JS, Kang BS, Kim KJ, Derewenda ZS, Oh TK, Lee CH, Lee JK. The molecular structure and catalytic mechanism of a quorum-quenching N-acyl-L-homoserine lactone hydrolase. Proc Natl Acad Sci U S A. 2005 Dec 6;102(49):17606-11.

Lee, S.J.; Park, S-Y.; Lee, J-J.; Yum, D. Y., Koo, B.-T. and Lee, J.-K. Genes Encoding the N-Acyl Homoserine Lactone-Degrading Enzyme Are Widespread in Many Subspecies of Bacillus thuringiensis Applied and Environmental Microbiology. August 2002, p. 3919-3924, Vol. 68, No. 8.

Liu, D.; Lepore, B. W.; Petsko, G. A.; Thomas,P. W.; Stone, E. M.; Fast, W. and Ringe, D. Three-dimensional structure of the quorum-quenching N-acyl homoserine lactone hydrolase from Bacillus thuringiensis. Proc Natl Acad Sci U S A. 2005 Aug 16; 102. (33):11882-7.

Nealson, K.H.; Platt, T.; Hastings, J.W. Cellular control of the synthesis and activity of the bacterial luminescent system. J Bacteriol. 1970 Oct; 104(1):313-22.

Parsek, M.R.; Val D.L.; Hanzelka, B.L.; Cronan, J.E.; and Greenberg, E.P. Acyl homoserine-lactone quorum-sensing signal generation. Proc. Natl. Acad. Sci. USA 96. 1999: 4360–4365.

Rasmussen TB, Givskov M. Quorum sensing inhibitors: a bargain of effects. Microbiology. 2006 152:895-904.

Spoering, A. L. and Gilmore, M. S. Quorum sensing and DNA release in bacterial biofilms. Current Opinion in Microbiology. 2006. Volume 9, Issue 2 , April 2006, Pages 133-137.

Thomas PW, Stone EM, Costello AL, Tierney DL, Fast W. The quorum-quenching lactonase from Bacillus thuringiensis is a metalloprotein. Biochemistry. 2005 May 24; 44(20):7559-69.

Val D.L. and Cronan, J.E. Jr. In vivo evidence that S-adenosylmethionine and fatty acid synthesis intermediates are the substrates for the LuxI family of autoinducer synthases. J Bacteriol.1998. May;180(10):2644-51.

Zhang, L.-H., Murphy P. J., Kerr, A. and Tate, M. E.. Agrobacterium conjugation and gene regulation by N-acyl-L-homoserine lactones. Nature. 1993.362:446-447.

Berendsen HJC, Grigera JR, Straatsma TP. The missing term in effective pair potential. J Phys Chem 1987; 91: 6269-6271.

Cornell WD, Cieplak P, Bayly CI, Gould IR, Merz KM, Ferguson DM, Spellmeyer DC, Fox T, Caldwell JW, Kollman PA. A 2nd generation force-field for the simulation of proteins, nucleic-acids and organic-molecules. J Am Chem Soc 1995; 117: 5179-5197.

Berendsen HJC, Postma JPM, van Gunsteren WF, DiNola A, Haak JR. Molecular dynamics coupling to an external bath. J Chem Phys 1984; 81: 3684-3690.

Esmann U, Perera L, Berkowitz ML, Darden T, Lee H, Pedersen LG. A smooth particle mesh Ewald method. J Chem Phys 1995; 103: 8577-8593.

Ryckaert JF, Ciccotti G, Berendsen HJC. Numerical-integration of Cartesian equations of motion of a system with constraints - molecular-dynamics of n-alkanes. J Comp Phys 1977; 23: 327-341.

Hockney RW. The potential calculation and some applications. Methods Comput Phys 1970; 9: 136-211.

Apra E., Windus TL, Straatsma TP, Bylaska EJ, de Jong W, Kowalski K, Hirata S, Valiev M, Hackler MT, Zhao Y, Harrison RJ, Dupuis M, Smith DMA, Nieplocha J, Tipparaju V, Krishnan M, Auer AA, Brown E, Cisneros G, Fann GI, Fruchtl H, Garza J, Hirao K, Kendall R, Nichols JA, Tsemekhman K, Wolinski K, Anchell J, Bernholdt D, Borowski P, Clark T, Clerc D, Dachsel H, Deegan M, Dyall K, Elwood D, Glendening E, Gutowski M, Hess A, Jaffe J, Johnson B, Ju J, Kobayashi R, Kutteh R, Lin Z, Littlefield R, Long X, Meng B, Nakajima T, Niu S, Pollack L, Rosing M, Sandrone G, Stave M, Taylor H, Thomas G, van Lenthe J, Wong A, and Zhang Z, "NWChem, A Computational Chemistry Package for Parallel Computers, Version 4.7" (2005), Pacific Northwest National Laboratory, Richland, Washington 99352-0999, USA.

Kim MH, Choi WC, Kang HO, Lee JS, Kang BS, Kim KJ, Derewenda ZS, Oh TK, Lee CH, LEE JK. The molecular structure and catalytic mechanism of a quorum-quenching N-acyl-L-homoserine lactone hydrolase. Proc. Natl. Acad. Sci. 2005; 102 17606-17611.

Liu D, Lepore BW, Petsko GA, Thomas PW, Stone EM, Fast W, Ringe D. Three-dimensional structure of the quorum-quenching N-acyl homoserine lactone hydrolase from Bacillus thuringiensis. Proc. Natl. Acad. Sci. 2005; 1023:11882-11887.

Wang L-H, Weng L-X, Dong Y-H, and Zhang LH (2004) Specificity and Enzyme Kinetics of the Quorum-quenching N-Acyl Homoserine Lactone Lactonase (AHL-lactonase). J. Biol. Chem. 279: 13645–13651.

FIGURES
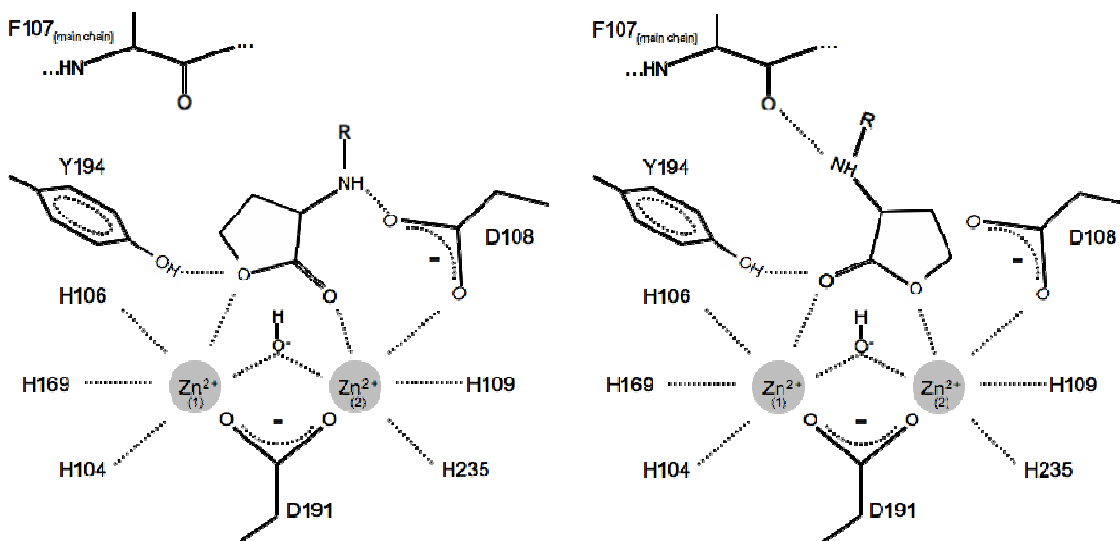
Figure 1. Hypothetical HSL binding modes. Mode 1 shown at left and 2 at right. (*si* and *re* faces involve a rotation orthogonal to the lactone ring in respect to D108 and Y194 residues; their representations are not shown here).
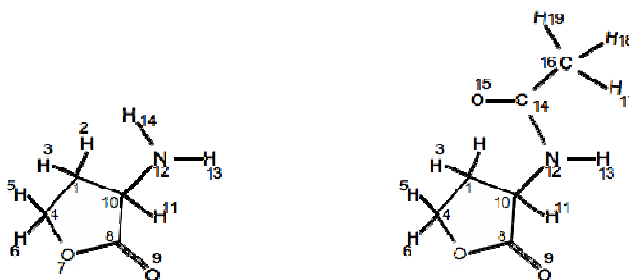
Figure 2. HSL (left) and NFH (right) molecules. (Atom numbers are for index purposes only).

TABLES

Table I. Atomic point charges for HSL and NFH. (Atoms are indexed according Figure 2).

Index	HSL atoms (e)	NFH atoms (e)
C1	-0.199	-0.199
H2	+0.062	+0.062
H3	+0.062	+0.062
C4	+0.240	+0.240
H5	+0.014	+0.014
H6	+0.014	+0.014
O7	-0.447	-0.447
C8	+0.716	+0.716
O9	-0.605	-0.605
C10	+0.395	+0.395
H11	+0.024	+0.024
N12	-0.815	-0.815
H13	+0.360	+0.360
H14$_{(HSL)}$/C14$_{(NFH)}$	+0.360	+0.778
O15		-0.599
C16		-0.075
H17		+0.025
H18		+0.025
H19		+0.025
Net Charge	**0.000**	**0.000**
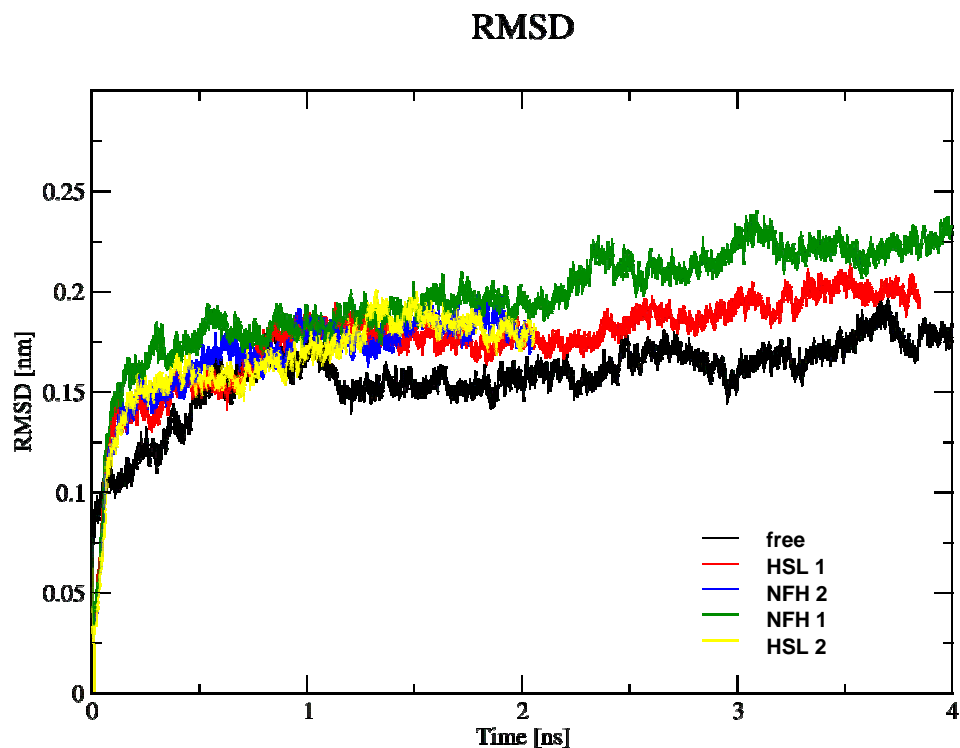
RMSD

Figure-3: Root-mean-square atomic positional deviations (RMSD) from the AiiA-BTK crystallographic structure.

RMSF
Homoserine Lactone Hydrolase
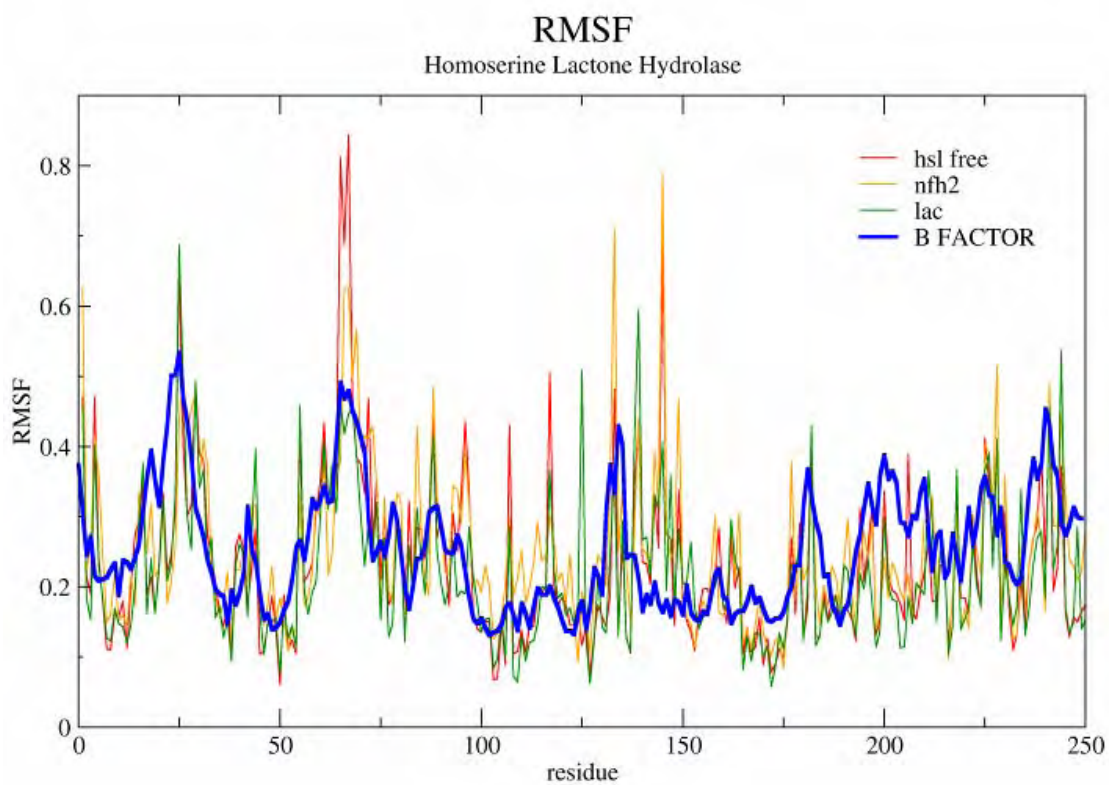
Figure-4: Root-mean-square atomic positional fluctuations (RMSF)
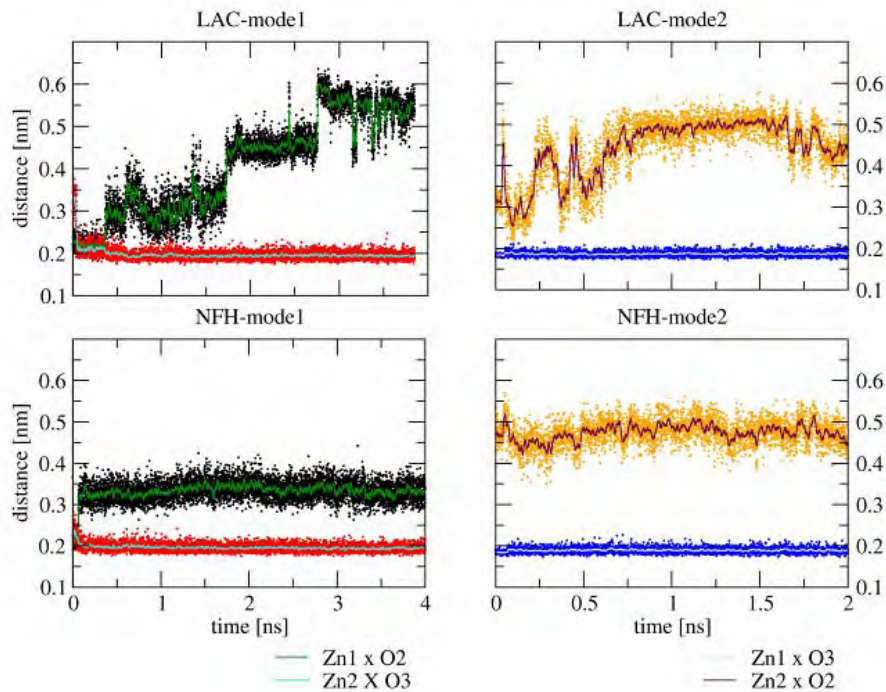
Figure-5: Distance variation between HSL oxygens and zinc atoms.
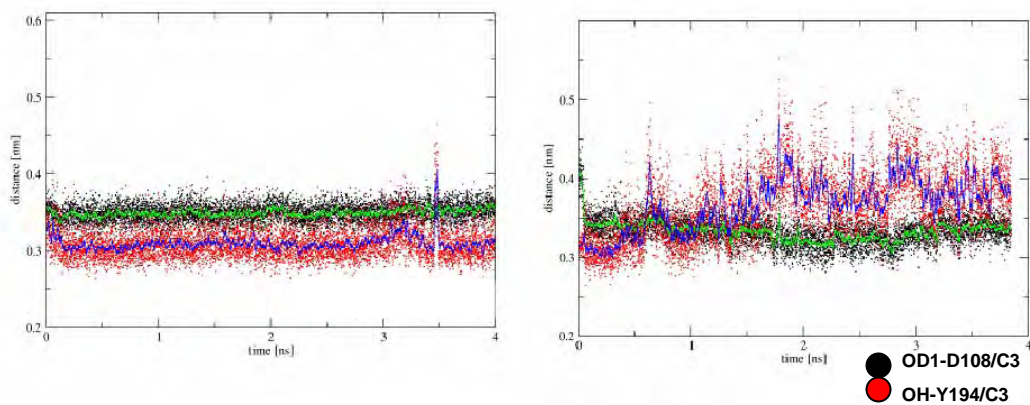
Figure- 6: Distance variation between the C3 of HSLs (mode 1) and two residues pointed out as responsible for the catalysis, OD1 of D108 and OH of Y194, respectively. A- N-formyl-homoserine lactone. B- Homoserine lactone
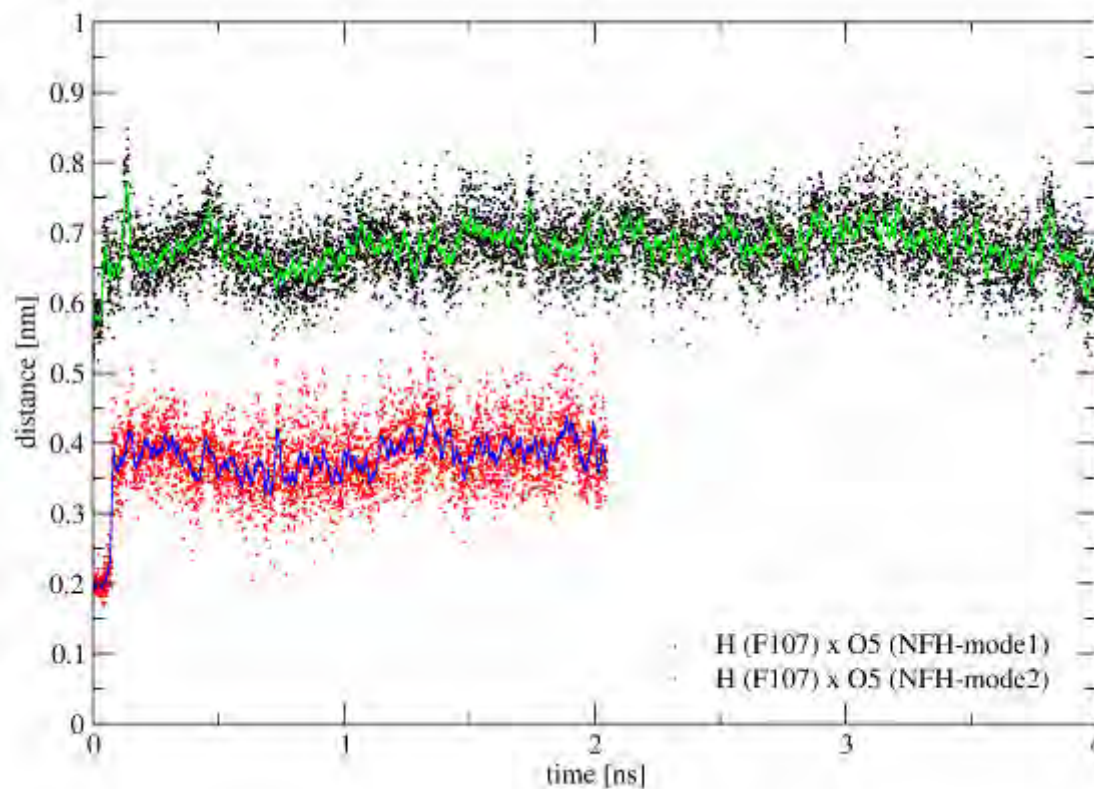
Figure-7: Distance variation between OD1 of the aspartic acid 108 and N4 of the HSLs mode-1.
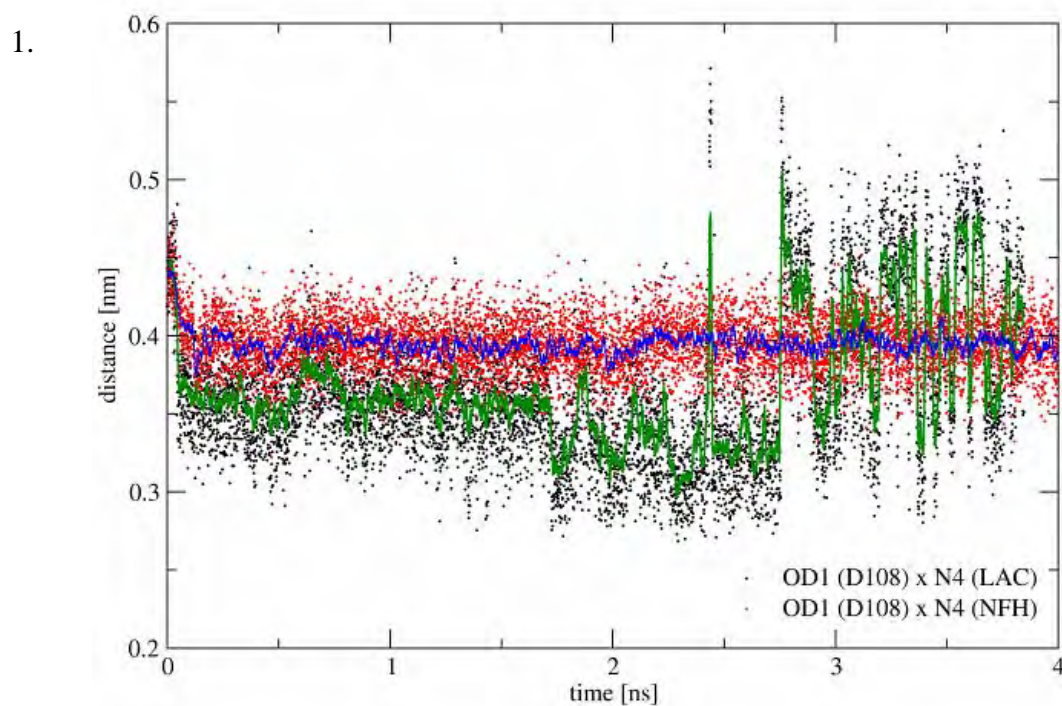
Figure-8: Distance variation between O5 (N-acyl chain) of N-formyl homoserine lactone and F107 main chain amide group.
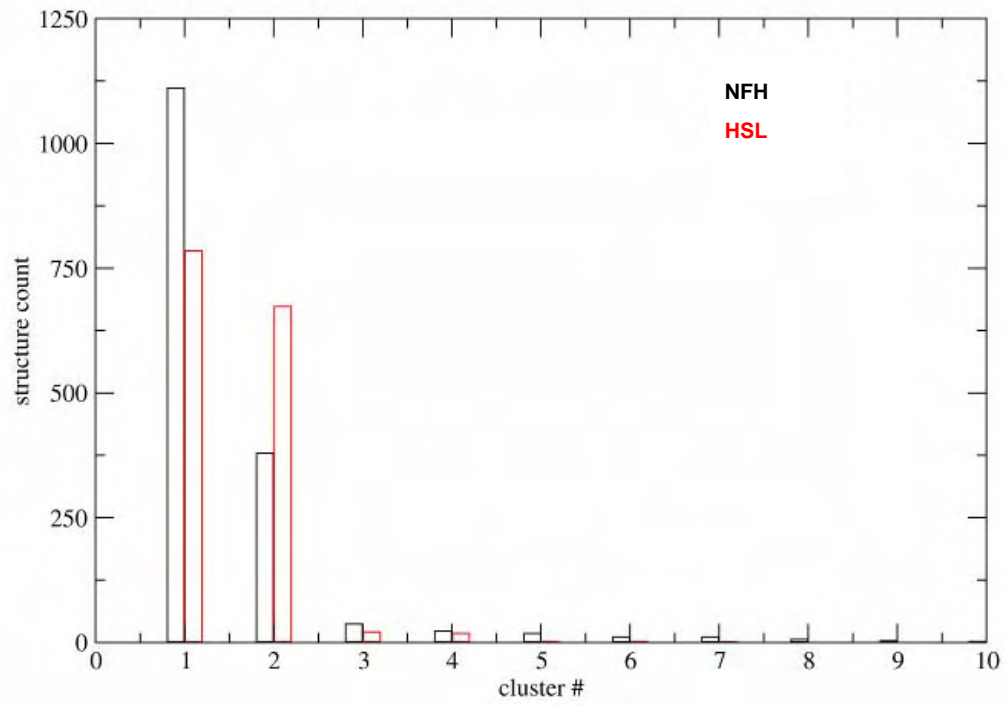
Figure-9: LAC and NFH most occurring configurations

Characterization of
Polyaniline-Gold Nanocomposites

Amir Saheb
Mira Josowicz, Jiri Janata
Georgia Institute of Technology, School of Chemistry and Biochemistry
Atlanta, Georgia 30332

and

Donald Baer
Pacific Northwest National Laboratory
Richland, WA 99354

amir.saheb@chemistry.gatech.edu Tel : 404.894.0589
mira.josowicz@chemistry.gatech.edu, jiri.janata@chemistry.gatech.edu

Introduction

The objective of this study was to explore the possibility of growing gold clusters containing low number of atoms, using the ability of PANI to switch from the conductive to insulating form and to use the ability of imine nitrogens to form strong chloroaurate complexes. Under normal electrochemical conditions as described in our paper the imine sites act as catalytic nucleation centers for forming the gold clusters containing large number of Au atoms[1].

$$(-N=) + AuCl_4^- \longrightarrow [(-N=)AuCl_4]^-$$

$$[(-N=)AuCl_4]^- + 3e^- \longrightarrow [(-N=)Au^o]Cl^- + 3Cl^-$$
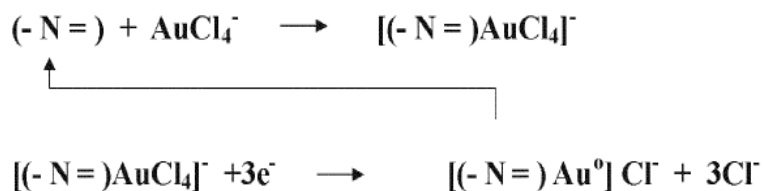
We applied novel synthetic conditions that should lead to the formation of low-atomic Au dispersion in PANI. We then conducted analysis that would help us to characterize the size, of the monodispersed Au atoms in the composite material.

Experimental

Three types of differently synthesized Au-PANI nano-composite materials were prepared using the following processes:

A.   Fully electrochemical process.

A thin PANI film was deposited electrochemically on Pt-foil from solution containing 0.1 M aniline and 2 M HBF_4. After the synthesis a cyclic voltammogram (CV) of the PANI film was recorded in 2 M HBF_4. Then potential of 1 V vs. the Ag/AgCl reference electrode in 0.1 M KCl solution was applied to the Pt-PANI electrode. As the potential was held at 1V a 1mM solution of $KAuCl_4$ in 0.1 M HCl was added to the PANI to form $AuCl_4$/PANI complex. After that the cell was washed again with 0.1 M KCl for 12 minutes to remove excess $AuCl_4^-$ and as the final step, a potential of 0.4 V was applied for 15 second to form Au(0). Samples with n=1, 2, 3, 4, 5 and 8 repetitions of the above procedure were prepared, each containing Au_n clusters. For comparison also PANI thin films on Pt-foils were prepared where the same treatment was done, but without $KAuCl_4$ salt.

B.   Electrochemical-chemical process.

Thin PANI films were electropolymerized using cyclic voltammetry (25 cycles) on Pt foils as described above and the background CV was obtained in 1M HCl. After that the chemical oxidation-reduction treatments of the PANI films were carried out chemically, using Ce(IV) and hydrazine, respectively. This process led to the formation of PANI-Au atomic clusters. After the preparation the PANI-Au materials were characterized by recording cyclic voltammograms (CV) in 1 M HCl solution. With the help of CVs the oxidation potential, E_{ox}, of Au to $AuCl_4^-$ and the reduction potentials, E_{red}, of $AuCl_4^-$ to Au as well as the charge under the oxidation, Au $_{ox}$ and reduction peaks, Au $_{red}$ were determined. The results are summarized in Table 1.
The solution used in chemical oxidation reaction were:
-        0.025 M $Ce(SO_4)_2$ in 1 M HCl
-        $1 \cdot 10^{-5}$ M $KAuCl_4$ in 1M HCl
-        0.1 M Hydrazine dichloride

The first step consisted of a 20 sec treatment with 0.025 M $Ce(SO_4)_2$ in 1 M HCl. This oxidized the PANI film from the emeraldine salt to the pernigraniline salt. Then the film was submerged in a 10^{-5} M $KAuCl_4$ in 1M HCl for 30 secs after which it was treated with a fresh solution of 0.025 M $Ce(SO_4)_2$ in 1 M HCl for 5 minutes washing out the unreacted gold. In addition, 5 mins of rinsing with deionized water was performed before the final 20 sec treatment with 0.1 M hydrazine dichloride to reduce Au^{3+} into metallic

Au^0. This would complete one cycle in the gold cluster growth at the imine site, further cycles would add one gold atom at a time.

C.   Chemical process.

PANI-base of 5000 kD obtained from Aldrich was used as a starting material. After treatment with 10 M NH_4OH, filtering and cleaning with methanol the material was converted to PANI salt using 1 M HCl. After filtration the PANI was treated with the same chemical-oxidation solutions that were used in the above process (B). The samples were collected from the filtering funnel after the consecutive treatments n =1, 2 3, 5, 7 and 10, washed with 1 M HCl and dried in desiccator overnight. It is expected that these materials will contain $PANI/Au_n$ composites.

XPS measurements were then performed using a Physical Electronics Quantum 2000 Scanning ESCA Microprobe. This system uses a focused monochromatic Al Kα x-rays (1486.7 eV) source and a spherical section analyzer. The instrument has a 16 element multichannel detector. The X-ray beam used was a 100 W, 100 μm diameter beam that was rastered over a 1.4 mm by 0.2 mm rectangle on the sample. The X-ray beam is incident normal to the sample and the photoelectron detector was at 45° off-normal. Wide scan data was collected using a pass energy of 117.4 eV. For the Ag $3d_{5/2}$ line, these conditions produce FWHM of better than 1.6 eV. Narrow scan or high energy resolution data is collected using a pass energy of 46.95. For the Ag $3d_{5/2}$ line, these conditions produced FWHM of better than 0.98 eV. The binding energy (BE) scale is calibrated using the Cu $2p_{3/2}$ feature at 932.62 ± 0.05 eV and Au 4f at 83.96 ± 0.05 eV for known standards.

Several other elemental analysis techniques were utilized including HRTEM, TOF-SIMS, Laser ablation-MS, and ICP-MS. However, due to the trace amounts and small size (angstrom level) of the gold clusters these proved ineffective in detecting the atomic clusters. In addition, PIXE (proton induced x-ray emission) is currently being conducted on the PANI-Au powder samples at EMSL as an alternative to XPS.

Results

Both wide and narrow scan XPS, Figure 1 and 2, was performed on the PANI-Au film samples. However, only the narrow scan spectra was analyzed for quantitative atomic concentrations of Au, N, C, O, and Cl.

XPS analysis of the electrochemically prepared (Procedure A) PANI-Au samples showed a correlation between the number of gold treatments and the atomic concentration of Au in the sample with respect to N, Figure 3. The consistency of the films were also probed by measuring the N:C atomic ratio as plotted in Figures 4 and 7.
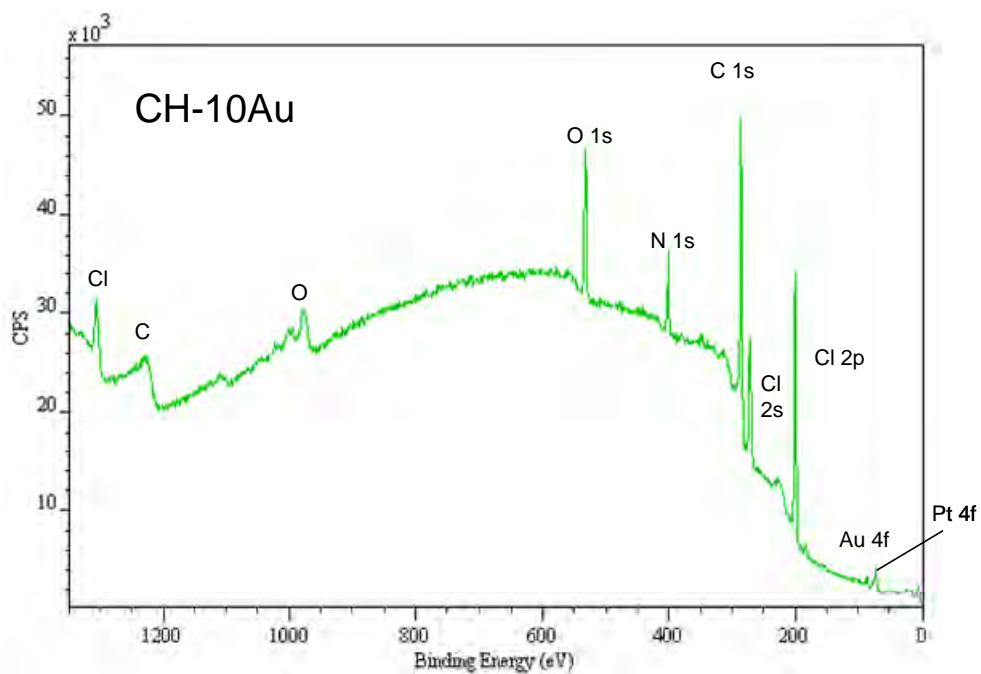
Figure 1. Wide scan XPS of PANI-Au films prepared chemically with 10 consecutive treatments of $AuCl_4^-$.
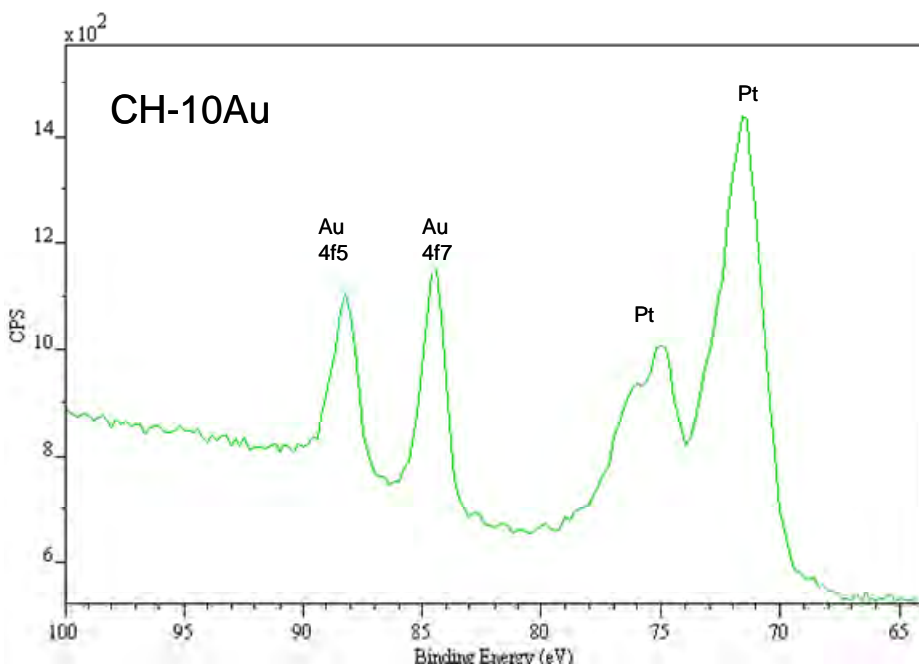
Figure 2. Narrow scan XPS of PANI-Au films prepared chemically with 10 consecutive treatments of $AuCl_4^-$.
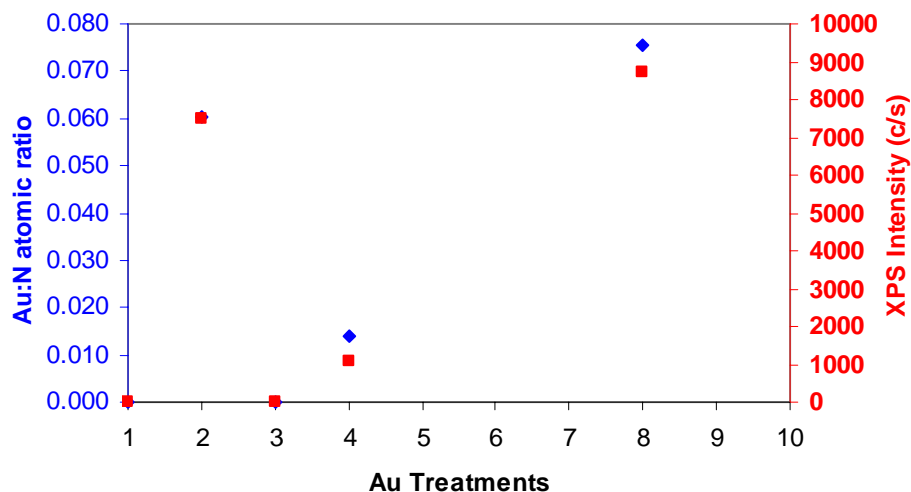
Figure 3. Changes of Au 4f7:N 1s atomic ratio with the number of Au treatments for the electrochemically prepared PANI-Au films (Procedure A).
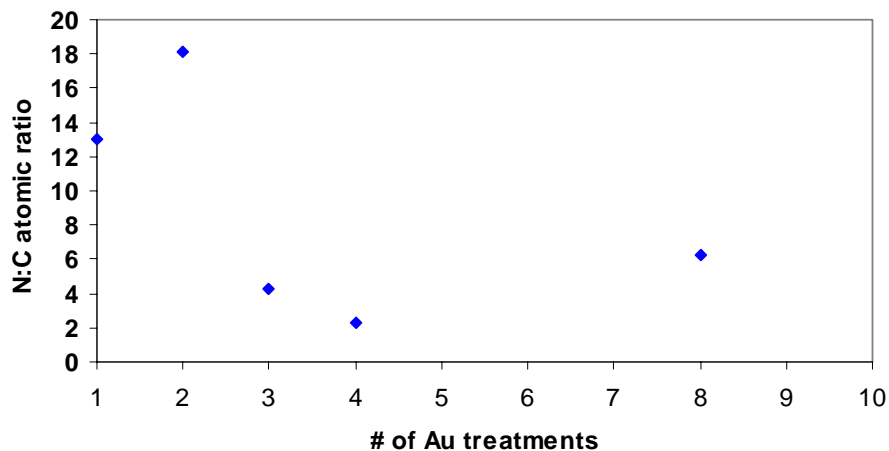
Figure 4. Dependence of N:C atomic ratio on $AuCl_4^-$ treatments of electrochemically prepared PANI-Au films (Procedure A).

With the exception of treatment #2, each consecutive treatment resulted in an increase in the $Au_{4f7/2}$ peak. In addition, the binding energy decreased with more Au treatments as seen in Figure 5. All the binding energies are referenced to the N 1s peak.
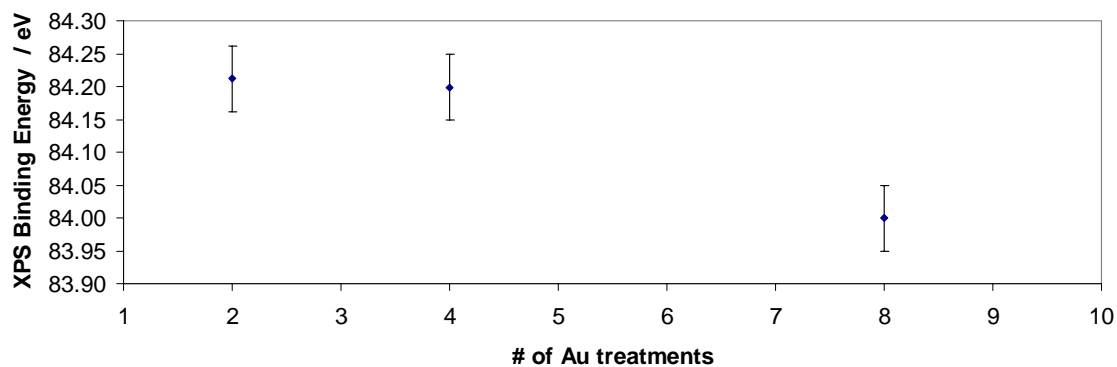
Figure 5. BE of the electrochemically prepared films as a function of Au treatements.

The chemically prepared PANI-Au films (Procedure B) also exhibited the same behavior, Figure 6 and 8. It however, should greater consistency with regards to the N:C atomic ratio, Figure 7.
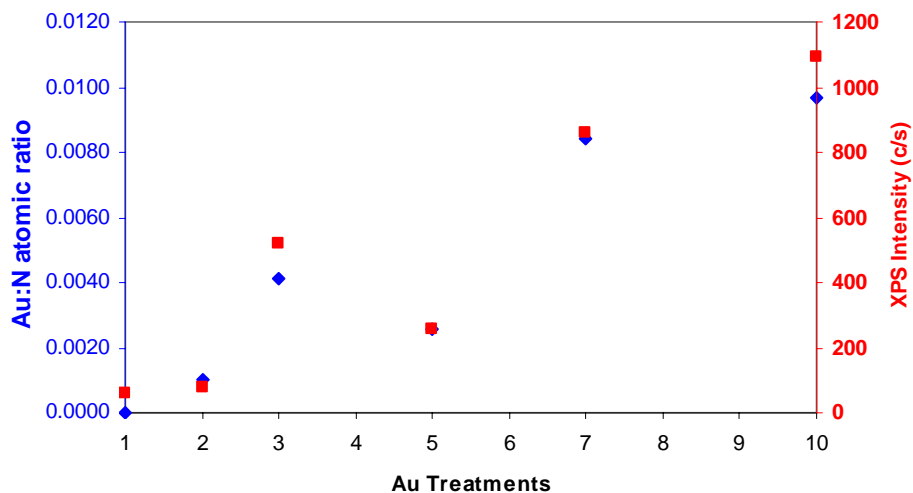
Figure 6. Changes of Au 4f7:N 1s atomic ratio with the number of Au treatments for the chemically prepared PANI-Au films (Procedure B).
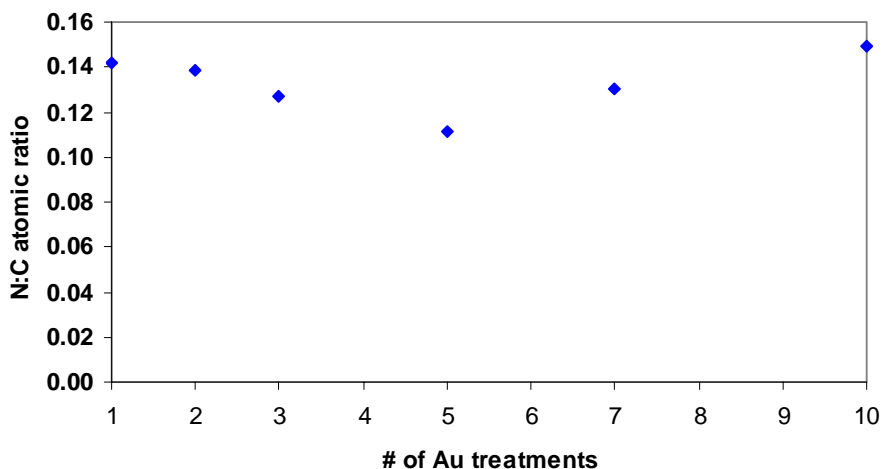
Figure 7. Dependence of the N:C atomic ratio on $AuCl_4^-$ treatments of the chemically prepared PANI-Au films (Procedure B).
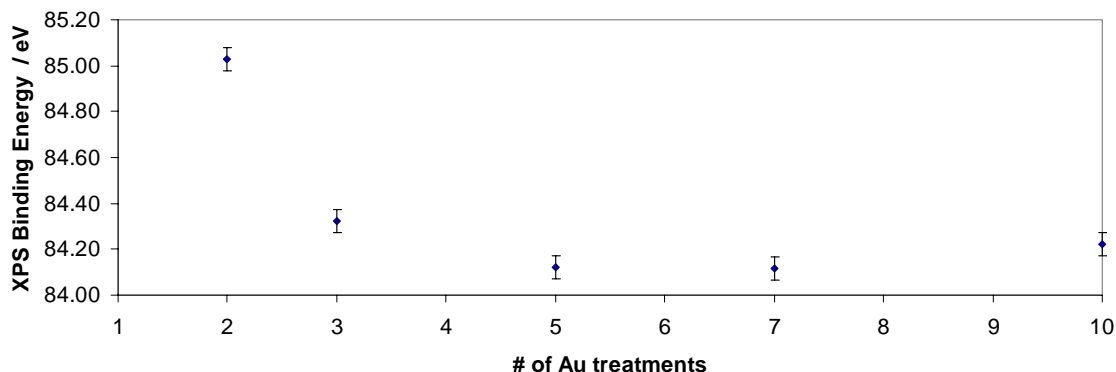
Figure 8. BE of the chemically prepared films as a function of Au treatements.

XPS analysis of the powder samples (Procedure C) showed no detectable gold. However, this may simply be a result of the sample itself which is in particulate form, thus having bulk properties as compared to the films. XPS is also not an appropriate technique for bulk analysis as it does not have the penetration depth required for larger particles.

Discussion

Particles on the order of the de Broglie wavelength have size and shape dependent properties. In addition, the high surface to volume ratio of nanoparticles in the composite results in a large number of binding sites available for chemical sensing or catalysis[2]. This combination of conducting polymers with metallic nanoparticles yields materials with new properties.

Analysis of both the electrochemically and chemically prepared PANI-Au films on Pt-foil show a relationship between the shift in binding energy of Au in PANI and the number of Au treatments received. The shape of the binding energy curve is seen to

follow the Coulomb interaction correction to the radius dependent ionization potential. The concept
of the effect of the contact potential is extended to show its contribution to the measured binding energy differences of the gold particle $Au_{4f7/2}$ doublet as the particle size decreases.

References

1   J. A. Smith, M. Josowicz, M. Engelhard, D.R. Baer J. Janata, *Phys. Chem. Chem. Phys.*, 2005, **7**, 3619.

2   J. A. Smith, M. Josowicz and J. Janata, *J. Electrochem. Soc.*, 2003, **150**, E384.

Acknowledgments

Report on Interfacial and Condensed Phase Chemical Physics Summer Research Institute at PNNL Richland, WA, Sept 1-30, 2006

Photochemistry of Liquid Waterand Radiation Induced Solvation

Andrzej L. Sobolewski
Institute of Physics
Polish Academy of Sciences
Warsaw, Poland
and
Sotiris Xantheas
Pacific Northwest National Laboratory
Richland, WA

The photochemistry of liquid water and radiation induced solvation is a topic of considerable interest. The radiation-induced decomposition of water or electron detachment phenomenon plays an important role, for example, in nuclear reactor technology and in the radiation damage of living matter. However, the mechanisms of photoinduced ionization and dissociation of liquid water as well as photosolvation phenomena are, despite extensive experimental investigation, still poorly understood.

In a series of our recent papers a new paradigm of excited-state proton-transfer (PT) related reactivity (photoacidity) was proposed [1]. While PT in the electronic ground state is a charge-separation process (ion-pair formation), formation of a radical pair is the primary step in excited-state PT reactions. Other than ground-state PT, excited-state PT is not driven and stabilized by long-range polarization effects, but rather by nonadiabatic (curve-crossing) dynamics. As a consequence, cluster-size effects are less relevant in excited-state hydrogen-transfer reactions than in ground-state PT processes. The primary mechanisms of excited-state hydrogen-transfer reactivity can thus be unraveled by spectroscopic and theoretical investigations of clusters.

One of the important issues of water photolysis is catalysation of the reaction by the UV/VIS absorbing chromophores. Aqueous clusters of metal cations have been the subject of considerable interest in this respect since they represent a first approximation to the phenomenon of aqueous solvation. In the following we discuss the preliminary results of

ab initio study on the photophysics of the $Al^{3+}(H_2O)_6$ cluster where the Al^{3+} ion is coordinated with the first solvation shell of water.

The optimal MP2/aug-cc-pVDZ geometry of the $Al^{3+}(H_2O)_6$ cluster has the T_h symmetry [2] (c.f. Fig. 1) with the Al-O bondlength of 1.936Å. Water molecules are coordinated to the Al^{3+} ion in the sp^2 hybrydization which means a significant charge transfer to the central ion. The lowest excited singlet states of the system calculated at the ground state geometry with the aid of the CC2/aug-cc-pVDZ method (Table 1) result from the HOMO(t_g)$\rightarrow$ LUMO(a_g) and HOMO-1(t_u)$\rightarrow$ LUMO(a_g) excitations. These excitations can be assigned as internal excitations of water (Fig. 1). Energy of these transitions is higher by about 3 eV as compared to excitations of bare clusters of water [3] which once again indicate of a significant degree of ionization of water coordinated to the Al^{3+} ion.

Table 1. Vertical energy gap (ΔE) and oscillator strength (*f*) of the $Al^{3+}(H_2O)_6$ cluster calculated at the ground-state equilibrium geometry with the CC2/aug-cc-pVDZ method.

State	ΔE/eV	f
^1T_g	10.37	0.0
^1T_u	10.38	0.426
^1A_u	12.53	0.0
^1A_g	12.83	0.0
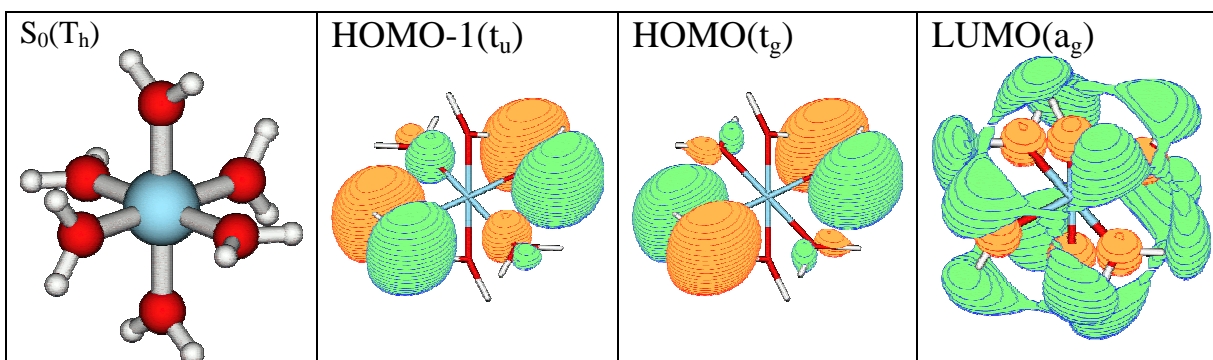
Fig. 1. The ground-state equilibrium geometry of the $Al^{3+}(H_2O)_6$ cluster determined at the MP2/aug-cc-pVDZ level and the frontier molecular orbitals involved in the lowest optical excitations of the system. Only one component of the triply degenerated orbitals is shown.

Since the lowest excited singlet states of the system are degenerated they subject to the Jahn-Teller effect which breaks the T_h symmetry of the system upon optical excitation. Although, the resulting effects of the symmetry breaking need a more systematic study, in Fig. 2 we show preliminary results for a particular pathway of the excited-state geometry optimization at the CC2/aug(O)-cc-pVDZ level of theory presuming the $T_h \rightarrow C_{2v}$ symmetry breaking pattern.
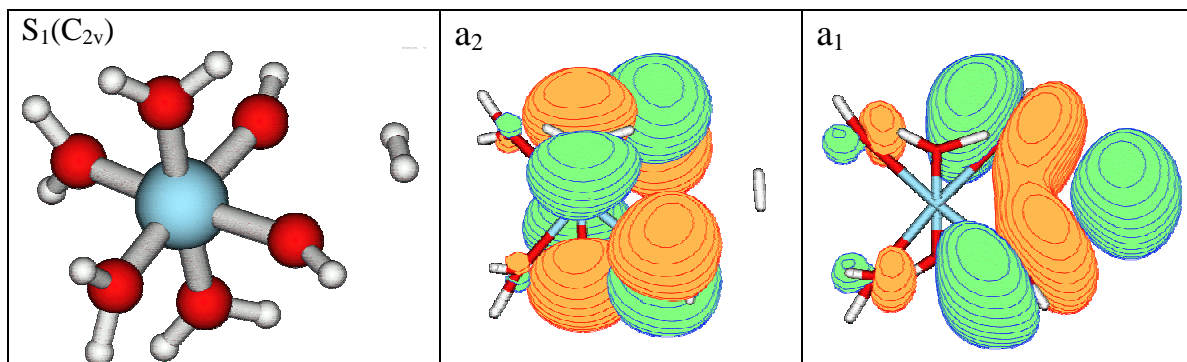
Fig. 2. The resulting structure of the CC2/aug(O)-cc-pVDZ optimization of the first excited singlet state of the $Al^{3+}(H_2O)_6$ cluster upon the $T_h \rightarrow C_{2v}$ symmetry breaking and the singly occupied molecular orbitals in the $^1A_2$ state.

The interesting aspect of the theoretical results shown in Fig. 2 is that the $T_h \rightarrow C_{2v}$ symmetry breaking of the $Al^{3+}(H_2O)_6$ cluster does not result in dissociation of water molecules, but in formation of molecular hydrogen, instead. This effect can be explained in terms of nodal structure of the LUMO orbital (Figs. 1 and 2) which has a character of the Rydberg orbital of water with the nodes at the OH bonds.

The structure shown in Fig. 2 does not correspond to the equilibrium geometry. This is the last structure for which the CC2 iteration has converged in the course of optimization. At the next predicted geometry the ground state crosses the S_1 state and this precludes investigation of the system at the CC2 level. The strong non-adiabatic effects expected at the S_1–S_0 (conical) intersection drive the system to the ground state. Thus further study of the reaction is confined to the ground state.

Preliminary results discussed above shown an important calatytic effect of the metal ion in the photolytic splitting of water. Further study should concentrate on elucidation of the physical mechanism which is beyond of the effect and on the search for other metallic or organic chromophores which can drive excitation energy of the cluster into the UV/VIS range.

1. W. Domcke and A. L. Sobolewski, Science, **302** (2003) 1693
2. E. Wasserman, J. R. Rustad, S. S. Xantheas, J. Chem. Phys. **106** (1997) 9769
3. J. N. Harvey, J. O. Jung, R. B. Gerber, *J. Chem. Phys.* **109**, 8747 (1998); Y. Miller, E. Fredj, J. N. Harvey, R. B. Gerber, *J. Phys. Chem. A* **108**, 4405 (2004).

Molecular dynamics of aqueous interfaces:

The surface propensity and thermodynamic properties of aqueous anions

Jennie L. Thomas, Barbara J. Finlayson Pitts, and Douglas J. Tobias
Department of Chemistry,
University of California, Irvine
Irvine, CA
and
Liem X. Dang
Pacific Northwest National Laboratory
Richland, WA

Unique interface chemistry at the surface of sea-salt particles, comprised primarily of aqueous sodium chloride, has been postulated as an important source of photochemically active chlorine in the troposphere.[1,2] Molecular chlorine then goes on to absorb sunlight and form atomic chlorine, a known oxidant of organics and an initiator of ozone formation in urban areas.[3] A variety of oxides of nitrogen react with sea-salt particles, leading to replacement of chloride by nitrate ions as particles age.[4-8]

There are a number of factors that could impact Cl_2 production from aerosols comprised of a mixture of nitrate and chloride. If chloride and nitrate are equally available at the interface, then molecular chlorine production could drop as aerosols age. Alternatively, if nitrate resides in the bulk and pushes chloride to the interface, Cl_2 production would stay more constant even as the chloride concentration in the aerosol decreases. Aerosol chamber experiments to characterize the amount of Cl_2 produced from mixed $NaCl/NaNO_3$ aerosols are currently underway at University of California, Irvine.[9] In coordination with these experimental studies, this work will focus on investigating aqueous $NaNO_3$ as well as mixtures of $NaNO_3$ and $NaCl$ using classical molecular dynamics (MD) simulations.

MD simulations were used to investigate the behavior of aqueous $NaNO_3$ in interfacial environments. A slab system[10,11] was constructed containing

condensed phase water and ions with a region of vacuum (representing the vapor phase) along the elongated z-axis. The surface potential aqueous $NaNO_3$ and neat water slabs was calculated using the method described by Wick and Dang in 2006.[12] The difference in the potential drop across the interface, from the condensed phase to the gas phase, between neat water and 1.5 and 6.8M $NaNO_3$ solutions was compared to experimental data summarized by Randles in 1977.[13]
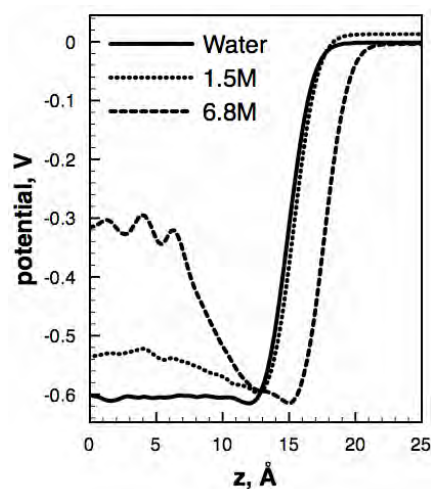
Figure 1. Calculated surface potential for 1.5M and 6.8M $NaNO_3$ compared to the surface potential water, calculations were completed using 2ns of simulation data. The difference in the potential for $NaNO_3$ solution and neat water is compared to experimental data.

Figure 1 shows potential as a function of z coordinate in the slab for water, 1.5M, and 6.8M $NaNO_3$. Subtracting the water potential in the center of the slab from the $NaNO_3$ potential gives values that can be compared with measured data, which is always given as a difference from neat water. For an overview of the experimental techniques used in measuring surface potentials the reader is referred to Randles 1977 article.[13] Experimental data is available for 1.5M $NaNO_3$, with a measured surface potential of 0.25V.[13] The difference from water should increase with increasing concentration, which is reproduced by calculations.

A profile of the concentration of ions and water verses position in the slab was constructed for both pure $NaNO_3$ and mixed $NaNO_3$/NaCl in water. The goal is to characterize the interface of pure sodium nitrate solutions and mixed sodium

nitrate/sodium chloride solutions, a model for aged sea-salt aerosols. Figure 2 shows density profiles for pure NaNO$_3$ and mixed NaNO$_3$/NaCl solutions.
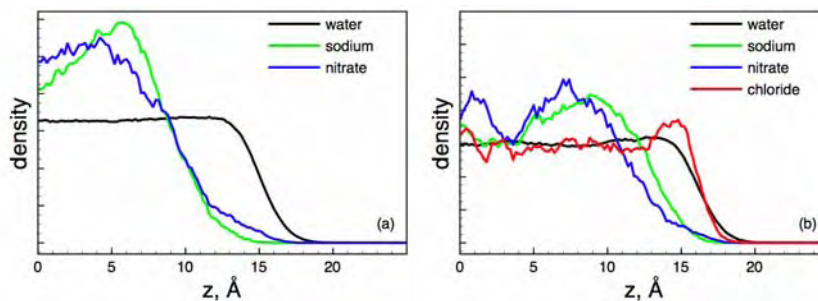
Figure 2. Density profiles for pure 1.5M NaNO$_3$ in water (a) and mixed 2M NaNO$_3$ with 2M NaCl in water (b).

Clearly, nitrate resides below the air/water interface of both solutions. In the mixed system, chloride is available at the interface and may be important for reactions that occur on the surface of aged particles in the atmosphere.

An initial investigation of the behavior of one iodide ion in a water slab was completed at three temperatures.   Recent studies show that constructing potential mean force curves (PMF) at three temperatures suggests interfacial ion solvation can be investigated using spatially resolved free energy, entropy, and enthalpy curves.[14,15] This method was combined with Dang's work[16] on ion binding at the liquid vapor interface, to investigate the behavior of iodide at the air/water interface. PMF curves were calculated at three temperatures using 1ns of simulation data per PMF point. Figure 3 shows calculated PMF curves for iodide crossing the air/water interface at three temperatures.
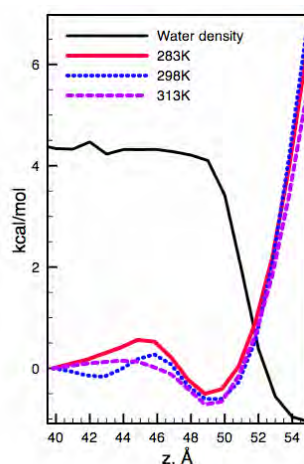
Figure 3. Calculated PMF curves for iodide crossing the air/water interface.

However, it was discovered the behavior of these as a function of temperature was not appropriate for the proposed analysis. Alternative methods to calculate the entropic and enthalpic contributions to ion solvation are under investigation.

(1)   Knipping, E. M.; Dabdub, D. *J. Geophys. Res.* **2002**, *107*.
(2)   Knipping, E. M.; Lakin, M. J.; Foster, K. L.; Jungwirth, P.; Tobias, D. J.; Gerber, R. B.; Dabdub, D.; Finlayson-Pitts, B. J. *Science* **2000**, *288*, 301.
(3)   Finlayson-Pitts, B. J. *Chem. Rev.* **2003**, *103*, 4801.
(4)   Dall'Osto, M.; Beddows, D. C. S.; Kinnersley, R. P.; Harrison, R. M.; Donovan, R. J.; Heal, M. R. *J. Geophys. Res.* **2004**, *109*.
(5)   Laskin, A.; Iedema, M. J.; Cowin, J. P. *Environ. Sci. Technol.* **2002**, *36*, 4948.
(6)   Ro, C. U.; Oh, K. Y.; Kim, H.; Kim, Y. P.; Lee, C. B.; Kim, K. H.; Kang, C. H.; Osan, J.; De Hoog, J.; Worobiec, A.; Van Grieken, R. *Environ. Sci. Technol.* **2001**, *35*, 4487.
(7)   Kerminen, V. M.; Teinila, K.; Hillamo, R.; Pakkanen, T. *J. Aerosol Sci.* **1998**, *29*, 929.
(8)   Posfai, M.; Anderson, J. R.; Buseck, P. R.; Sievering, H. *J. Geophys. Res.* **1995**, *100*, 23063.
(9)   Moskun, A.; Wingen, L.; Finlayson-Pitts, B. J., Personal communication.
(10)   Benjamin, I. *Journal of Chemical Physics* **1991**, *95*, 3698.
(11)   Wilson, M. A.; Pohorille, A. *Journal of Chemical Physics* **1991**, *95*, 6005.
(12)   Wick, C. D.; Dang, L. X.; Jungwirth, P. *Journal of Chemical Physics* **2006**, *125*.
(13)   Randles, J. E. B. *Phys. Chem. Liq.* **1977**, *7*, 107.
(14)   MacCallum, J. L.; Tieleman, D. P. *Journal of the American Chemical Society* **2006**, *128*, 125.
(15)   van der Vegt, N. F. A.; Lee, M. E.; Trzesniak, D.; van Gunsteren, W. F. *Journal of Physical Chemistry B* **2006**, *110*, 12852.
(16)   Dang, L. X. *Journal of Physical Chemistry B* **2002**, *106*, 10388.

The Investigation on:
Ⅰ. The Solvation of CN(H₂O)ₙ⁻ and N(CN)₂(H₂O)ₙ⁻
Ⅱ. The Configuration of MOOC(CH₂)ₙCOO- (M=Na, K)
Ⅲ. Some Oxygen-rich Vanadate Anion Species by Combination of Photoelectron Spectrometry and Electron-spray

Guanjun Wang and Mingfei Zhou
Department of Chemistry
Fudan University
Fudan, PRC
and
Dr. Lai-sheng Wang, Dr. Xuebin Wang, Dr. Hin-Koon Hoo
Pacific Northwest National Laboratory
Richland, WA

The combination of electron-spray with photo-electron spectrometry (PES) is a fruitful tool in the investigation on the solvation of anion and the multi-charge anion since it was introduced by Prof. Wang. A lot of novel phenomena was discovered such as the negative electron detachment energy in some multi-charge anion; the transition from linear to cyclic configuration by the interaction of water molecule in some aliphatic dicarboxylate dianion; and the hydrogen bond between O⁻ and aliphatic C-H was discovered in $CH_3(CH_2)_nCOO^-$ (n>5) molecule by low-temperature PES firstly.

Ⅰ. The investigation on the solvation of N(CN)₂(H₂O)ₙ⁻ and CN(H₂O)ₙ⁻

The solvation effect of some anion have been investigated by PES in this group, such as SO_4^{2-}, NO_3^-, N_3^-, $^-OOC(CH_2)_nCOO^-$. In the case of SO_4^{2-} and $^-OOCCOO^-$, the bare anion isn't stable in gas phase while the salvation affection of H_2O molecule contributes to the stabilization of hydrate anion.

We have investigated the hydrated CN^- and $N(CN)_2^-$ by PES. The PES spectra were shown in Figure 1.1 and 1.2 respectively.

In the case of $N(CN)_2^-(H_2O)_n$, the number of water molecule can is up to n=12 when the mass spectra signal of anion keep detectable. The spectra pattern is very similar for these all hydrated anions except that the peak get broaden with the increase of H_2O molecules. The electron detachment energy of bare $N(CN)_2^-$ anion is 4.12eV. While the electron detachment energy increase to 4.52eV and 4.91eV respectively when first two H_2O molecules were attached to anion. The shift is very similar, which mean that the first H_2O molecule were trapped to the anion in the same way. The next two H_2O molecules give 0.25 and 0.26 electron detachment energy shift respectively which mean these two guys were trapped to anion in a different way from the first two. Then all other H_2O molecules bring smaller shift about 0.1eV, so these H_2O molecules should be capture as the second solvent shell by hydrogen bond with the first four ones.

N(CN)$_2^-$(H$_2$O)$_n$

n=0

(a)

4.12

n=1

(b)

4.52

n=2

(c)

4.91

n=3

(d)

5.16

n=4

(e)

5.42

n=5

(f)

5.55

n=6

(g)

5.65

n=7

(h)

5.8

n=8

(i)

5.9

n=9

(j)

6.0

n=10

(k)

6.1

n=11

(l)

6.2

2   3   4   5   6

BE/ev
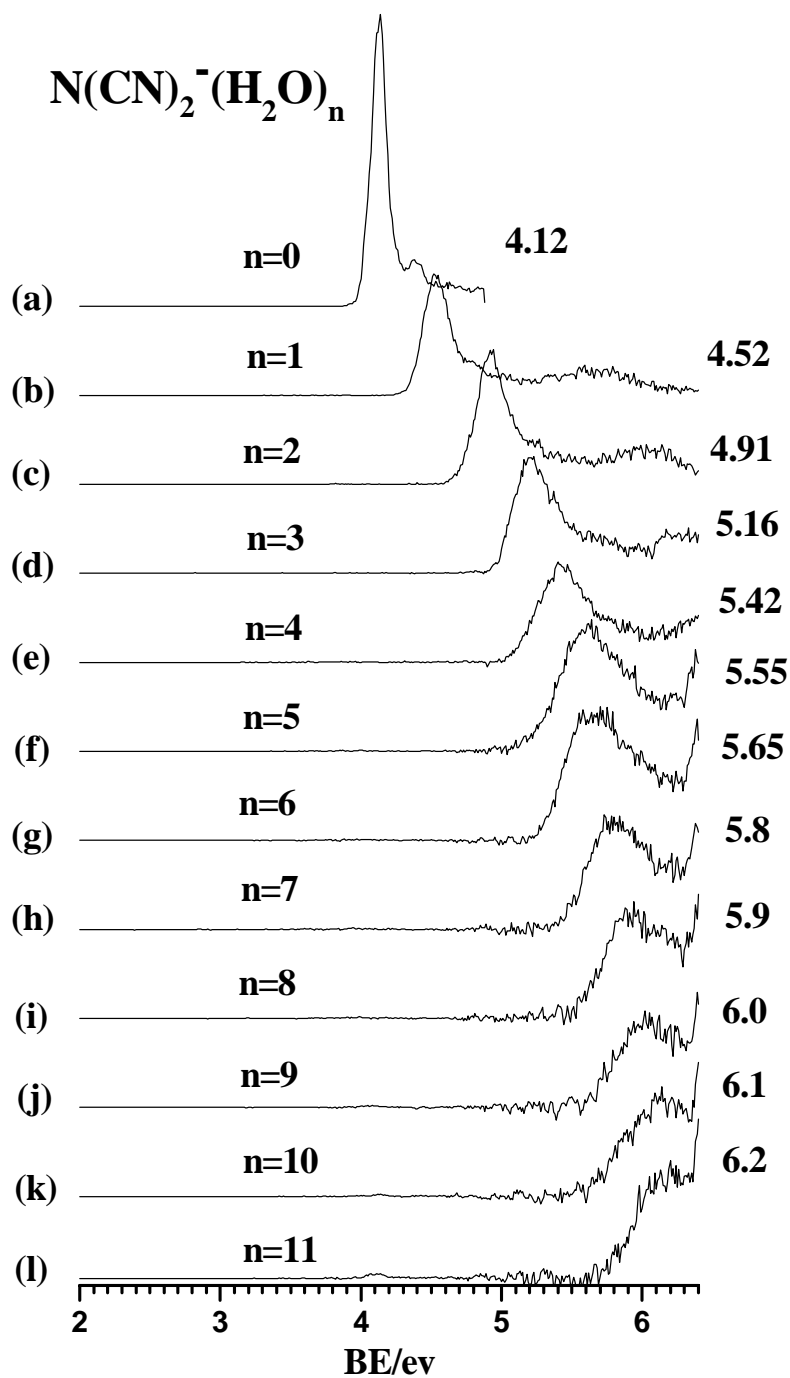
Figure 1.1 Photoelectron spectra of N(CN)$_2^-$(H$_2$O)$_n$ (n=0-11)measured at 193 nm (6.424 eV). The value list on right is the VDE/eV.

In the case of $CN(H_2O)_n^-$, we can't get the signal of bare CN- anion in the mass spectra because the mass limitation of Quadrapole Ion-Guide. But the electron detachment energy of CN- has been measured in this group by the laser-ablation on the CuCN target, and the VDE is 3.85eV. While the electron detachment energy increased to 4.35, 5.10 and 5.50 respectively when three H_2O molecules were captured. We found that the second H_2O molecule give larger electron detachment energy shift than first one. Then we assume that the second H_2O was attached to the other end of CN- from the first one, so we guess that two H_2O molecules maybe stabilized the anion synergeticlly. While the signal of $CN(H_2O)_n^-$ (n>3) in mass spectra is too weak to detect.
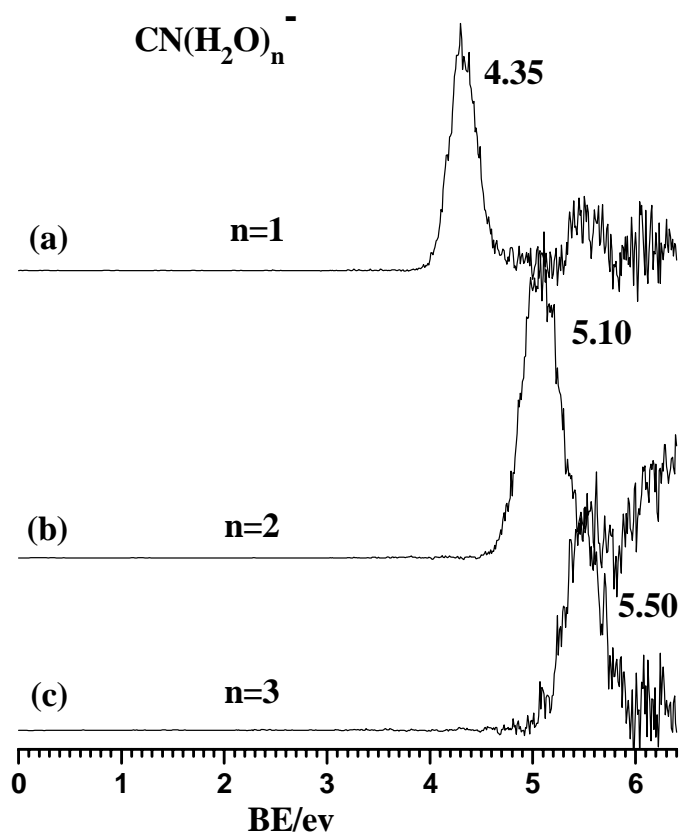
Figure 1.2 Photoelectron spectra of $CN^-(H_2O)_n$ (n=1-3)measured at 193 nm (6.424 eV). The value list on right is the VDE/eV.

Ⅱ. The transition of configuration in alkali dicarboxylate mono-anion $MOOC(CH_2)_nCOO^-$ (n=1-6, M=K and Na) molecule: from linear to cyclic

The PES spectra of aliphatic $MOOC(CH_2)_nCOO^-$ (n=1-6) were shown in figure 2.1 (M=K) and figure 2.2 (M=Na) respectively. All the peaks is relatively broad in both case and the ADE increase with the length of $(CH_2)_n$, Which is different from the $HOOC(CH_2)_nCOO^-$ and $CH_3(CH_2)_nCOO^-$ that have been investigated in this group previously. The values were list in Table 2.1 for comparison. The ADE of $HOOC(CH_2)_nCOO^-$ is about higher 1.0eV than $H_3C(CH_2)_nCOO^-$, because the former molecule is cyclic and is stabilized by the strong intra-molecule hydrogen bond. While it is found that the ADE of $MOOCCH_2COO^-$ (M=Na and K) is approximate to the $H_3CCH_2COO^-$ in this experiment, which mean that the $MOOCCH_2COO^-$ should be linear. And the molecule shape tend to cyclic with the increase of $(CH_2)_n$ length because the ADE increase.

Table 2.1 The VDE of $CH_3(CH_2)_nCOO^-$, $HOOC(CH_2)_nCOO^-$, $NaOOC(CH_2)_nCOO^-$ and $KOOC(CH_2)_nCOO^-$ n=1-6

n	$CH_3(CH_2)_n$ COO^-	$HOOC(CH_2)_n$ COO^-	$NaOOC(CH_2)_n$ COO^-	$KOOC(CH_2)_n$ COO^-
1	3.4	4.65	3.65	3.55
2	3.4	4.64	4.00	3.80
3	3.4	4.58	4.10	4.20
4	3.4	4.46	4.15	4.30
5	3.4	4.41	4.20	4.40
6	3.4	4.54	4.25	4.50

It is notable that the ADE of $KOOCCH_2COO^-$ increase more fast than the $NaOOCCH_2COO^-$ with the length of $(CH_2)_n$, because the radii of K^+ is larger than the Na^+, which mean that the $(-O^- K^+ O-)$ fraction in cyclic molecule have more ability to adapt the ring tension.
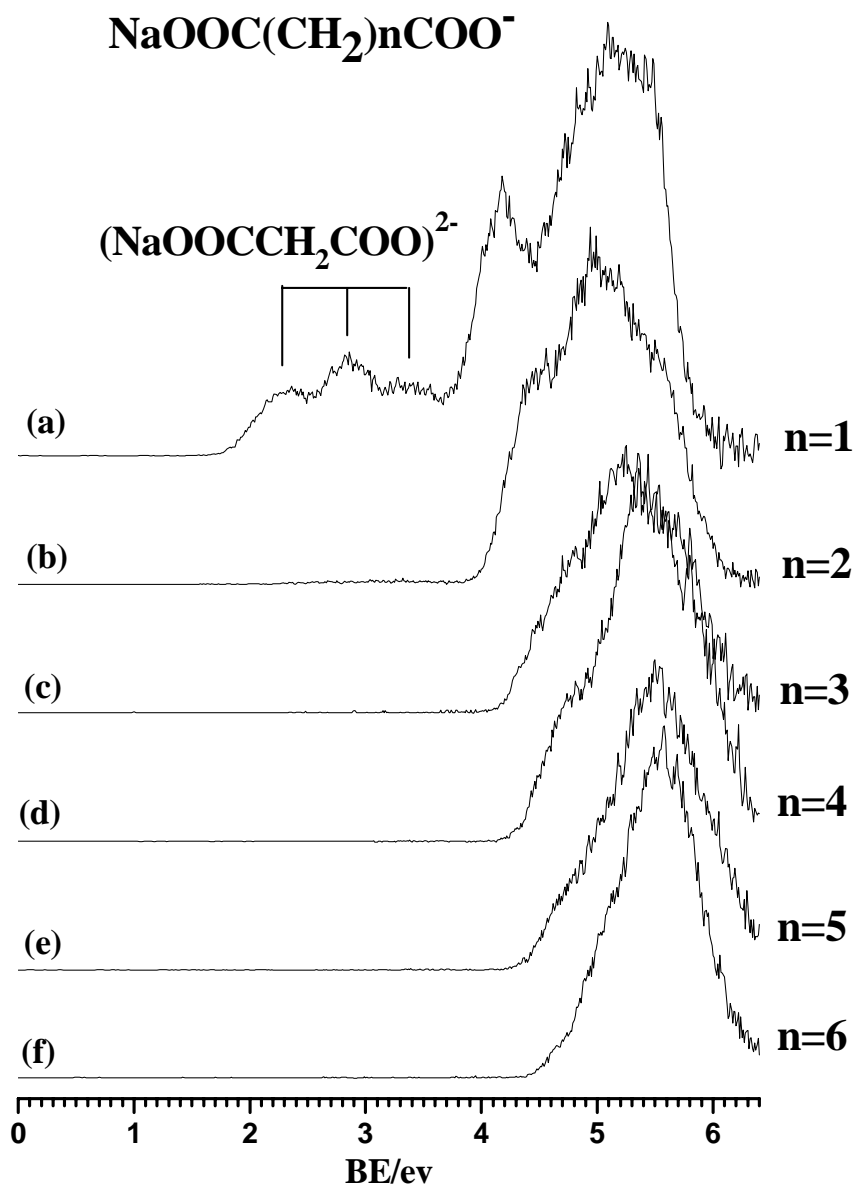
Figure 2.1 Photoelectron spectra of $NaOOC(CH_2)_nCOO^-$ (n=1-6) measured at 193 nm (6.424 eV). The value list on right is the VDE/eV.

It is also notable that the peak of dimmer dianion $(NaOOCCH_2COO)_2^{2-}$ is always very strong in the PES spectra of $NaOOCCH_2COO^-$ although we have optimized the condition, we think the reason is that the Na^+ is stronger Lewis acid and can be coordinated by the $–O^-$ than K^+, so the dianion is more preferable.
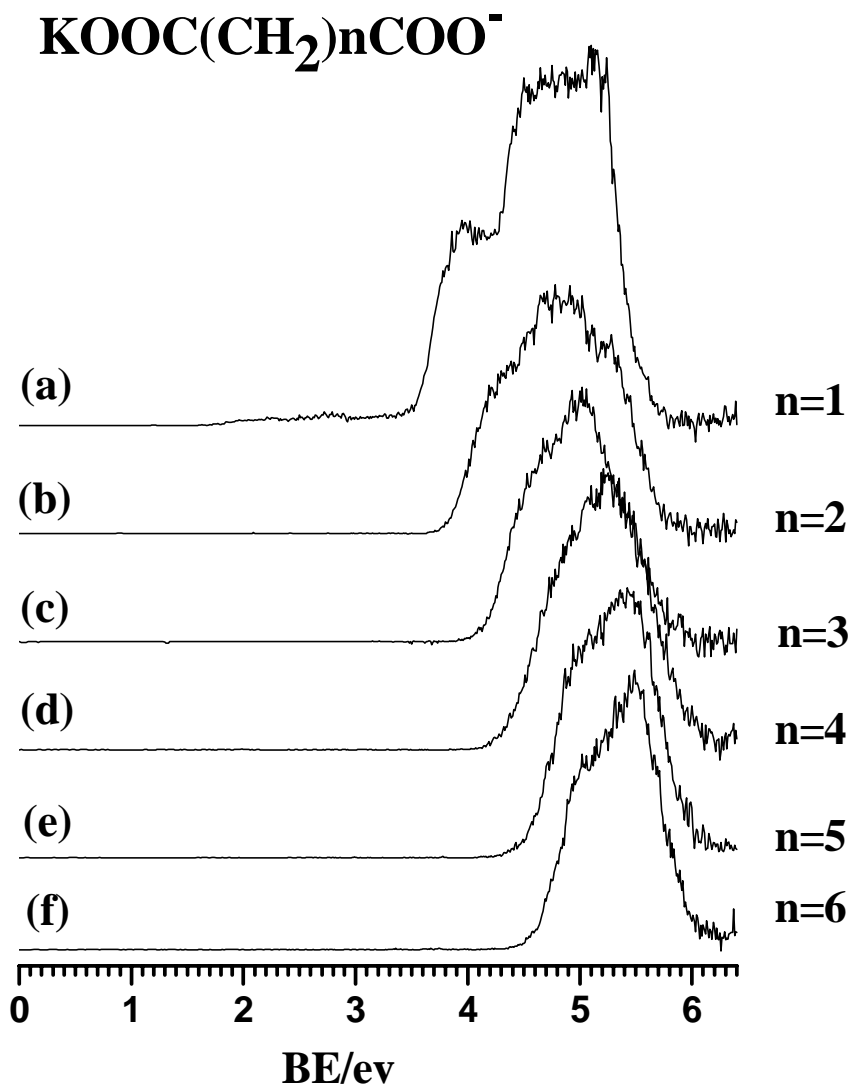
Figure 2.2 Photoelectron spectra of $KOOC(CH_2)_nCOO^-$ (n=1-6) measured at 193 nm (6.424 eV). The value list on right is the VDE/eV.

Ⅲ. Some oxygen-rich vanadate anion species prepared by the electro-spray of NaV$_2$O$_6$/H$_2$O$_2$/H$_2$O/CH$_3$CN solution.

We have done the electro-spray experiment with the solution of NaV$_2$O$_6$/H$_2$O$_2$/H$_2$O/CH$_3$CN. Some new oxygen-rich anions were found and identified, which will be discussed in detail.

Only the VO$_x^-$ (x=1-4) can be prepared by the laser-ablation on the vanadium target, while we found that VO$_5^-$, VO$_6^-$ and V$_2$O$_{10}^{2-}$ can also be prepared by electro-spray of solution.

The figure 3.1 show the PES spectra of VO$_5^-$ and VO$_6^-$, the pattern is similar to the VO$_4^-$, because there is no electron in *d*-orbital of vanadium, all photo-electron are from the *p*-orbital of oxygen, and the ADE of VO$_5^-$ is lower than the VO$_4^-$ and VO$_6^-$, we think that the poorer delocalization of the extra electron ascribed to the odd oxygen atom in VO$_5^-$ anion.
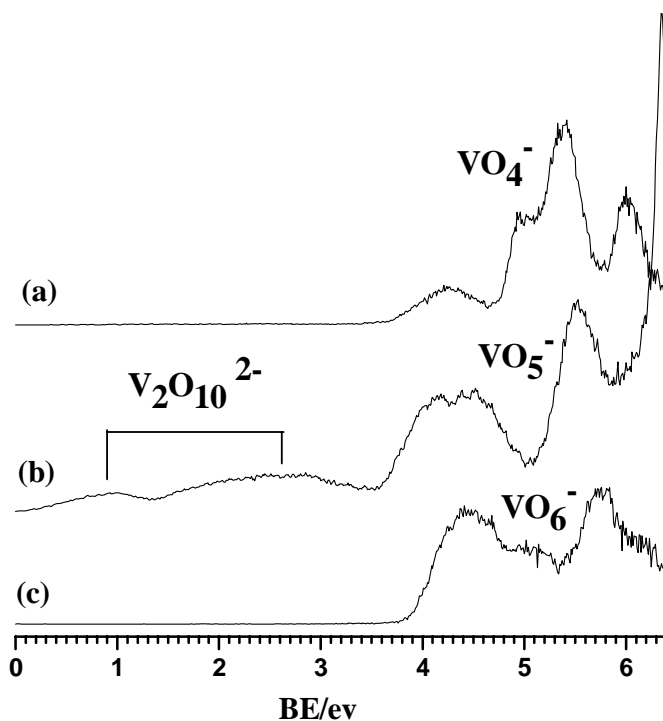
Figure 3.1 Photoelectron spectra of VO$_x$ (x=4-6) measured at 193 nm (6.424 eV). The value list on right is the VDE/eV.

As shown in Figure 3.2, the dianion $V_2O_{10}^{2-}$ can be prepared by adjusting the condition of electron-spray. The absence of some peak in the PES spectra with 266 nm and 193 nm laser is ascribed to the coulomb barrier which is the character of multiple-charge anion, which confirms the asignatin of these peaks to dianion $V_2O_{10}^{2-}$, which was shown in figure 3.3.
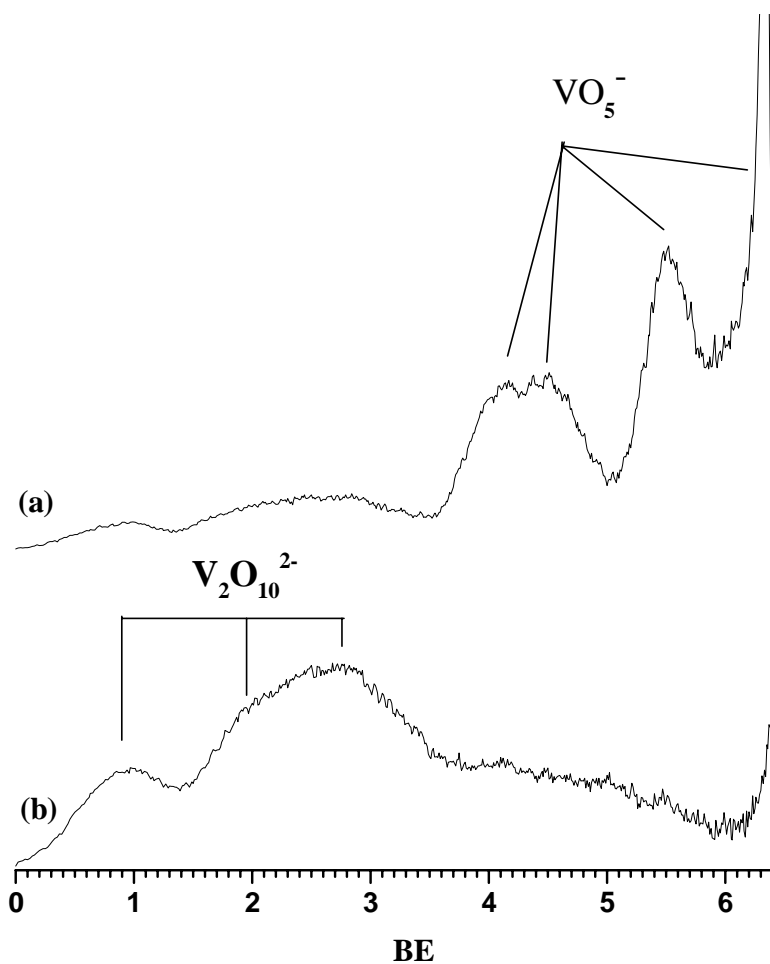
Figure 3.2 Photoelectron spectra of (a) VO^{5-}, (b) $V_2O_{10}^{2-}$ measured at 193 nm (6.424 eV).
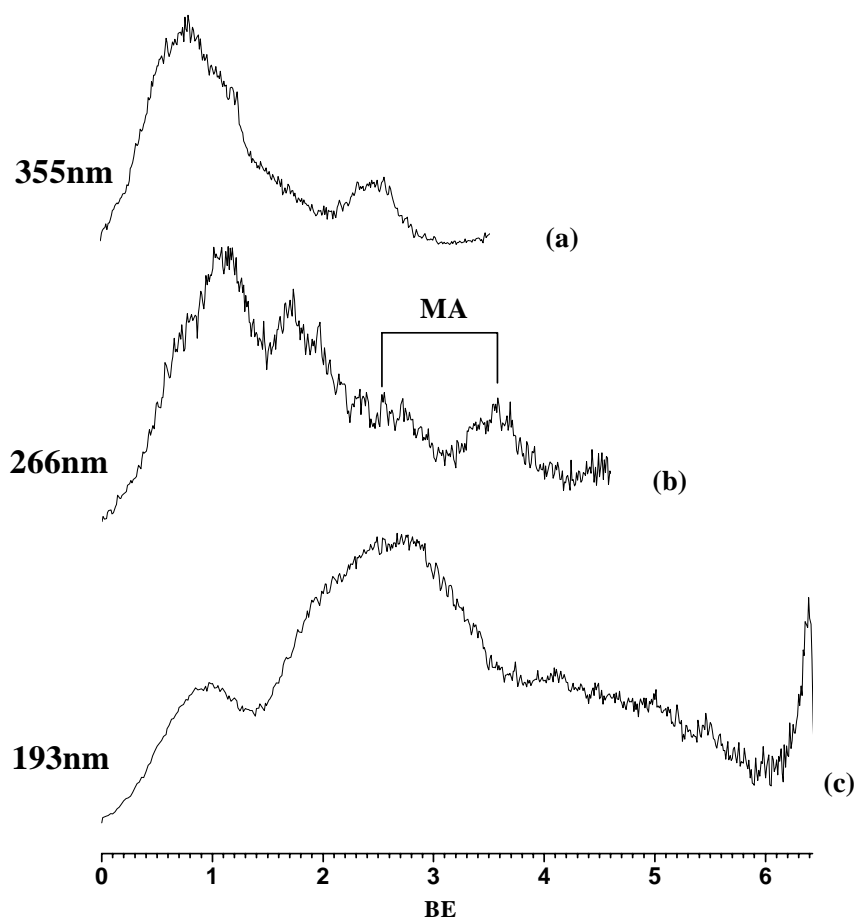
Figure 3.3 Photoelectron spectra of $V_2O_{10}^{2-}$ measured at different laser wavelength (a)355 nm (3.5eV), (b)266 nm (4.662eV), (c)193 nm (6.424 eV).

It is very interesting that we have observed the $V_2O_{10}^{2-}(H_2O_2)$, the solvated $V_2O_{10}^{2-}$ by H_2O_2. The PES spectra was shown in Figure 3.4. It was showed that the pattern of two spectra is very similar except that the shift. The ADE of $V_2O_{10}^{2-}$ is very low and approximate to 0.1eV, while the ADE $V_2O_{10}^{2-}(H_2O_2)$ increase to 0.9eV, the shift is large than the attribution by one H_2O molecule in the salvation of anion. So we suggest that the two O-H of H_2O_2 were attached to the $V_2O_{10}^{2-}$ spontaneously.
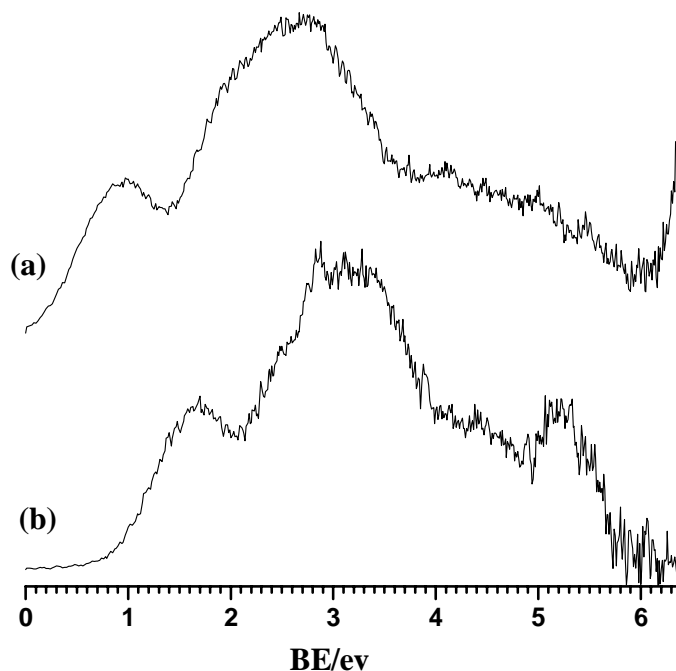
Figure 3.4 Photoelectron spectra of (a) $V_2O_{10}^{2-}$, (b) $V_2O_{10}^{2-}(H_2O_2)$ measured at 193 nm (6.424 eV).

References:

(1) Wang, X. B.; Yang, X.; Nicholas, J. B.; Wang, L. S. *Science* **2001**, *294,* 1332

(2) Wang, X. B.; Woo, H. K.; Kiran, B.; Wang, L. S. *Angew. Chem. Int. Ed.* **2005**, *44, 4968*

(3) Wang, X. B.; Woo, H. K.; Kiran, B.; Wang, L. S. Lau, K. C. *J. Phys. Chem. A* **2006**, *110,* 7801

(4) Wang, X. B.; Yang, X.; Nicholas, J. B.; Wang, L. S. *J. Chem. Phys.* **2003**, *119,* 3611

(5) Wu, H. B.; Wang, L. S. *J. Chem. Phys.* **1998**, *108,* 5310

Appendix: The Survey and Responses

Interfacial and Condensed Phase Chemical Physics Summer Research Institute (ICPCPSRI): follow-up Questionnaire

Dear Colleague;

From my perspective, the third year of PNNL's ICPCPSRI went well. However, your perspectives are much more important and will largely determine the fate of this program. Therefore, I encourage each of you to take a few minutes to answer some questions and to append any additional comments, suggestions, etc., to your reply. I would appreciate reply by 21 September, even if it is incomplete. If at a later time, you wish to add anything, please do so.

Directions
Not every question applies to everyone, and it is not necessary to answer everything that does apply. The more complete your answers, the more useful they are. I may wish to use your comments in follow-on documentation, please indicate whether you wish for me to attribute the comments to your or would prefer to remain anonymous.

•May I quote you with attribution?

Section I. Contact Information

Please provide me with current contact information
Name
Address
City, ST Zipcode,
E-mail:

Are you willing to be contacted for further follow-up questions?

Section II: Measures of success (or not)
PNNL mentors and faculty advisors
1. Was this summer's activity part of an on-going collaboration?

2. How likely is this summer's experience to contribute to future collaboration outside the auspices of the summer program?

3. Did the work contribute to your research or project aims? How?

All
4. How likely is this work to appear in publication(s), presentation(s)? (If you are planning to publish or present, please provide some detail—where, when, etc.— approximately)

5. Was the visit supported by the NSF?

6. (*Grad students only*) How likely is this work to contribute to your Ph.D. Thesis?

7. Were any new avenues of research opened?

8. Did your work here produce any intellectual property (IP) or is it likely to lead to IP development? (If yes, please give some description without disclosing the IP itself)

9. Would you recommend others to apply to or participate in this program?
Please add any additional comments you wish on the intellectual, technical or scientific success or shortcomings of the program.

Section III. The experience
All
1. What aspects of the program did you feel were particularly good?

2. What can we do to improve the program?

3. (*Participants who visited PNNL*) What difficulties did you encounter coming here or during your stay?

Section IV. Comments
Please take a moment to add any additional comments, opinions or anecdotes about the program, your visit, the research, etc.

Thank you,
Stephan E. Barlow
Director
ICPCPSRI
(509) 376-9051
se.barlow@pnl.gov

Survey Responses

The following responses to the survey were elicited from our participants. Certain questions gave very little information and so are not included here. For example, two or three people indicated that the summer's work might lead to intellectual property, however nothing specific was reported, so those answers are omitted here. One visitor asked to remain anonymous and another reported some difficulties so that we judged it best to grant anonymity. In some case obvious spelling or grammatical errors have been corrected as well. The designation N/A here means "No Answer."

Faculty or Supervisor	II.1. Was this summer's activity part of an on-going collaboration?
William Arnold	Yes. It provided Chan Lan Chun with additional experience and skills that will enhance our ongoing research project on mineral particle reactivity
Zhongyang Cheng	Yes. Dr. Wang has been collaborating with us on the characterization of nano-scale magnetostrictive materials. The activity in this summer program is a part of that collaboration.
G. Barney Ellison	Yes. We are working with Dr. S. E. Barlow and Dr. A. Selenium
Si-Dian Li*	Yes
Jiri (Art) Janata	Yes

Faculty or Supervisor	II.2. How likely is this summer's experience to contribute to future collaboration outside the auspices of the summer program?
William Arnold	Somewhat likely
Zhongyang Cheng	The summer's experience is great for our collaboration. This experience helps us to look for future collaboration.
G. Barney Ellison	It is certain that we will continue to collaborate with EMSL and Drs. Barlow and Zelenyuk
Si-Dian Li*	It will help deepen further collaborations
Jiri (Art) Janata	We are hoping that the results obtained during the SRI will be included in a joint publication and will also form a basis of joint proposal to DOE

Faculty or Supervisor	II.3. Did the work contribute to your research or project aims? How?
William Arnold	Yes. It provided Chan Lan Chun with additional experience and skills that will enhance our ongoing research project on mineral particle reactivity.
Zhongyang Cheng	Yes. The results obtained are highly needed for further development of nano-biosensor. The results provide a solid background and guideline for our investigation of nano-scale magnetostrictive materials as sensor platforms

G. Barney Ellison	Yes, this summer's work contributed to our interests in organic aerosols. Luis and I learned a great deal about the ability of aerosols to take up water.
Si-Dian Li*	Yes. The results achieved during the program will form a new foundation for future collaboration.
Jiri (Art) Janata	It provided experimental verification of our hypothesis that metal/polyaniline composites can be built from the "bottom-up", by atom-by-atom deposition.

Faculty or Supervisor	II.4. How likely is this work to appear in publication(s), presentation(s)? (If you are planning to publish or present, please provide some detail—where, when, etc.—approximately)
William Arnold	Unsure
Zhongyang Cheng	We will have articles published in Journals. We are preparing two right now
G. Barney Ellison	Luis and Dr. Zelenyuk have one paper in press in Anal. Chem. and they have submitted abstracts for the Dec. meeting of the Am. Geophys. Union. When our aerosol mass spectrometer is fabricated and operational, we will submit a paper to J. Phys. Chem.
Si-Dian Li*	The first paper of our work is nearly finished and will be submitted to the Journal of Chemical Physics.
Jiri (Art) Janata	As soon as we receive and analyze the final data we would like to start writing a manuscript. Hopefully, the work will be of high quality that would allow us to go to some top-tier journal.
	II.7. Were any new avenues of research opened?
William Arnold	No
Zhongyang Cheng	Yes
G. Barney Ellison	N/A
Si-Dian Li*	Our work may open a new area of boronyl chemistry
Jiri (Art) Janata	Yes

Faculty or Supervisor	II.9. Would you recommend others to apply to or participate in this program?
William Arnold	Yes
Zhongyang Cheng	Yes
G. Barney Ellison	This is an excellent experience and I recommend it to everyone.
Si-Dian Li*	Without hesitation
Jiri (Art) Janata	Yes. I may recommend my students to apply the program next year.

Faculty or Supervisor	III.1. What aspects of the program did you feel were particularly good?
William Arnold	The level of support and collaborative opportunities offered.
Zhongyang Cheng	The opportunity to graduate students to conduct experiments and work with others.
G. Barney Ellison	N/A
Si-Dian Li*	Training on first class instrumentation; interaction with world experts;
Jiri (Art) Janata	Very good and useful

Faculty or Supervisor	III.2. What can we do to improve the program?
William Arnold	More widely advertise
Zhongyang Cheng	N/A
G. Barney Ellison	N/A
Si-Dian Li*	Cut back on the red tape
Jiri (Art) Janata	To further open the laboratory.

Faculty or Supervisor	III.3. What difficulties did you encounter coming here or during your stay?
William Arnold	N/A
Zhongyang Cheng	N/A
G. Barney Ellison	N/A
Si-Dian Li*	Airfare to Richland is outrageously expensive; one of the co-PI's (Mira Josowicz, former PNNL employee!!!!) encountered major bureaucratic problems with arranging her visit, which had to be cancelled.
Jiri (Art) Janata	Visiting other laboratories and going shopping were the biggest difficulties

Faculty or Supervisor	IV General comments
William Arnold	N/A
Zhongyang Cheng	N/A
G. Barney Ellison	N/A
Si-Dian Li*	I used to be Associate Director of the group in which my student, Amir Saheb, received his training and performed the experiments. It has been particularly gratifying to see EMSL functioning as a true user facility, precisely as it was initially set up.
Jiri (Art) Janata	I hope PNNL can further increase the scale of the program to have more international students.
	* Prof. Li was a visiting faculty participant

PNNL Host	II.1. Was this summer's activity part of an on-going collaboration?
Tom Autrey	No, it was to start a new one
Don Baer	I had two students. Both are parts of on going efforts. One is formal and involves the Minnesota group active on one of my research projects. One is long standing, but has no funding.
Liem Dang	Yes
Ram Devanathan	Yes
Leo Fifield	It was the beginning of what promises to be an ongoing collaboration.
Vanda Glezakou	I would say it was not, since this was my first time as a host.
Julia Laskin	This project provided an opportunity to follow up on our last summer pilot study, resolve some open questions and expand the range of systems to get a more general perspective on the gas-phase chemistry of odd-electron peptide ions.
Roberto Lins	I had two students. One was part of an on-going collaboration, the second one not.
Thereza Soares	No, although the ongoing work will result in a collaboration after the summer student returns to his University
Chongmin Wang	Yes
Sotiris Xantheas	No, but it was aimed at establishing a future collaboration
Alla Zelenyuk	Yes

PNNL Host	II.2. How likely is this summer's experience to contribute to future collaboration outside the auspices of the summer program?
Tom Autrey	very likely
Don Baer	Collaborations and interactions will continue
Liem Dang	It is a good experience for students to be at the national lab
Ram Devanathan	Quite likely
Leo Fifield	It has already led to submission of a joint proposal for outside funding (BES).
Vanda Glezakou	The visitor decided she wanted to get more experience in molecular simulations, so she worked more closely with my colleague Liem Dang. Still, this interaction can potentially lead to further collaboration of Liem and me with Professor Jordan's group
Julia Laskin	There is no doubt that these collaborations will continue in the future.
Roberto Lins	100%
Thereza Soares	I believe the summer student will continue the project as his thesis work. I will also extend the research in collaboration with Dr. Chenghong Lei here at PNNL
Chongmin Wang	The collaboration will continue
Sotiris Xantheas	Very likely
Alla Zelenyuk	Very likely

PNNL Host	II.3. Did the work contribute to your research or project aims? How?
Tom Autrey	not existing programs but helped to develop understand for future programs
Don Baer	The Chan Lan Chun activities move our research forward and will likely help define future work by the whole project team. The research by Amir is still taking place and results are unknown.
Liem Dang	It is contributed somewhat to my research, but I let the student choose the projects to work on so that she can feel more familiar with the subjects
Ram Devanathan	Not really. The SRI work was only slightly related to my research
Leo Fifield	The visitor and I have complimentary expertise and the combination strengthens our individual efforts
Vanda Glezakou	It has not been assessed yet.
Julia Laskin	Yes. This area of research has been incorporated into my BES program. The novel findings from this summer research will have a significant impact on my program
Roberto Lins	Yes. The student who came as part of an existing collaboration have generated, processed and analyzed data producing enough material for a scientific article, which will be soon written. The second student has learned the basic methodology will continue the work. He has also asked me about the possibility of being his Ph.D. co-supervisor
Thereza Soares	It may contribute to possible grant proposal
Chongmin Wang	Yes, this contributes our research interests in nano materials
Sotiris Xantheas	Yes. During the visit the faculty member interacted with several PNNL staff members who are working in the general area of excited electronic states of aqueous clusters both in the experimental and theoretical fields.
Alla Zelenyuk	Yes

PNNL Host	II.4. How likely is this work to appear in publication(s), presentation(s)? (If you are planning to publish or present, please provide some detail—where, when, etc.—approximately)
Tom Autrey	the work will be published next year
Don Baer	Work will likely appear, location not yet certain.
Liem Dang	My summer student finished some calculations while she was here, but I am not sure that will lead to publication.
Ram Devanathan	Not likely right now. This work is in the initial stages
Leo Fifield	The work from this year will not be included in a presentation--not enough progress yet.
Vanda Glezakou	Possibly
Julia Laskin	The results will be presented at the 22nd Asilomar Conference on Mass Spectrometry, Pacific Grove, California, October 20 - 24, 2006; 4th International UPPSALA Conference on ECD/ETD Mass Spectrometry, Hong-Kong, China, December 12-15, 2006; Gordon Research Conference on Gaseous Ions: Structures, Energetics & Reactions, Ventura, CA, Feb 25-Mar 2, 2007. Several papers summarizing our results are in preparation
Roberto Lins	One or two scientific publications should appear in a biophysics/biochemistry peer-review indexed journal mid/late 2007
Thereza Soares	I estimate that the work should lead to a scientific manuscript. I expect it to be submitted for publication sometime in the summer 2007. We don not know as of yet where we will send it for publication, but I will gladly inform the SRI once the manuscript is out.
Chongmin Wang	A joint publication is under drafting
Sotiris Xantheas	Very likely
Alla Zelenyuk	Very likely. An abstract was submitted to the Fall 2006 AGU meeting (San Francisco, CA December 2006

PNNL Host	II.7. Were any new avenues of research opened?
Tom Autrey	Yes
Don Baer	Started doped nano particle efforts with Chan Lan
Liem Dang	N/A
Ram Devanathan	Yes. We used ab initio calculations to study oxide surfaces
Leo Fifield	In situ methods, not previously considered, were conceived of and developed
Vanda Glezakou	Possibly, interns of more collaborations, getting to know the work of other scientists, and making our work known to them.
Julia Laskin	Yes. Gas-phase chemistry of peptide radical anions is a completely new unexplored area of research. Our study provides a first very fundamental insight on the energetics and dynamics of unimolecular fragmentation for these systems
Roberto Lins	Yes. The research project started by one of the students addressed an important fundamental problem in the understanding of bacterial biofilm formation and may provide material for future grant applications.
Thereza Soares	Possibly, but it is difficult to say just yet
Chongmin Wang	Not yet,
Sotiris Xantheas	N/A
Alla Zelenyuk	Yes

PNNL Host	II.9. Would you recommend others to apply to or participate in this program?
Tom Autrey	yes this is a very good program
Don Baer	I am to the stage where I am not useful as a mentor because I am not accessible. In all cases I need to line up others to do the hands on effort. This does not always work equally well.
Liem Dang	N/A
Ram Devanathan	Yes
Leo Fifield	Yes
Vanda Glezakou	Absolutely
Julia Laskin	Yes
Roberto Lins	Definitely yes
Thereza Soares	Yes, I would certainly recommend either colleagues or students to participate in the program. However, one should be aware that this is a "free-time" activity since there are no work packages for it. In other words, one must be really motivated about mentorship to supervise a student in his/her free time
Chongmin Wang	yes
Sotiris Xantheas	N/A
Alla Zelenyuk	Yes

PNNL Host	III.1. What aspects of the program did you feel were particularly good?
Tom Autrey	N/A
Don Baer	N/A
Liem Dang	N/A
Ram Devanathan	I enjoyed mentoring the student.
Leo Fifield	The ability to meet face-to-face and work in the lab together
Vanda Glezakou	Discussions with the visitor, scientific and other, share experiences and cultural information, help the visitor solve specific problems
Julia Laskin	The program provided support to cover expenses that allowed participants to spend a descent amount of time at PNNL
Roberto Lins	Organization and welcoming of the participants; flexibility and understanding of the organizers to fit the needs of different attendees. In particular, I would like to thank Ms. Nikki Avery for the efficient, knowledgeable and friendly coordination of the project.
Thereza Soares	I have appreciated the opportunity of mentoring a student which is not readily available in the National Laboratories due to the non-academic character of these Institutions. However, the nicest aspect of the program is the freedom to choose a research project that is not necessarily related to the mentor ongoing research.
Chongmin Wang	Diversified research experience for students
Sotiris Xantheas	The access of the visitors to several research areas and the interaction with PNNL staff. The opportunity to attend meetings, seminars etc and be exposed to several aspects of scientific research
Alla Zelenyuk	N/A

PNNL Host	III.2. What can we do to improve the program?
Tom Autrey	N/A
Don Baer	N/A
Liem Dang	N/A
Ram Devanathan	It is fine the way it is
Leo Fifield	N/A
Vanda Glezakou	N/A
Julia Laskin	The program provided support to cover expenses that allowed participants to spend a descent amount of time at PNNL
Roberto Lins	i) I think a short seminar series might help to stimulate discussion and social interaction among the participants. The seminars, scattered throughout the period so to fit everybody's schedule, could be short (15 min) and would not have to involve results - the student project plan would suffice. That would also inform the other participants about the different projects being carried out at PNNL by their colleagues; ii) Transportation aid. Some of the participants (most of them I would think) were housed at the PNNL housing facility. While the facility is an excellent resource, transportation between the campus and the town is not quite convenient. Having the bus to come up to the campus once or twice a day or at least the possibility of a shuttle service once or twice a week to the town (on a fixed-schedule basis) would help the participants to organize themselves to go shopping for groceries.
Thereza Soares	It is hard to say since I believe the program has a nice and flexible format. However, I would suggest that every student should give a talk about the work done before leaving. Certainly it involves more work, but I think it will give a sense of accountability to the students. Of course, I would gladly help with the organization of such a thing if needed.
Chongmin Wang	seems to be run seamless
Sotiris Xantheas	I felt that the program was running very smoothly thanks to the SRI director and his staff. The environment was very friendly and supportive. I cannot think of any further improvements to an already successful program
Alla Zelenyuk	To accommodate more participants

PNNL Host	III.3. What difficulties did you encounter coming here or during your stay?
Tom Autrey	N/A
Don Baer	N/A
Liem Dang	N/A
Ram Devanathan	N/A
Leo Fifield	N/A
Vanda Glezakou	I think it is a very valuable part of the PNNL environment. Everybody involved did an excellent job to integrate the visitors here and provided a lot of help to the hosts in dealing with the necessary paperwork
Julia Laskin	N/A
R. Lins	N/A
T. Soares	N/A
C, Wang	N/A
Sotiris Xantheas	N/A
Alla Zelenyuk	N/A
PNNL Host	IV General comments
Tom Autrey	N/A
Don Baer	N/A
Liem Dang	N/A
Ram Devanathan	N/A
Leo Fifield	N/A
Vanda Glezakou	N/A
Julia Laskin	Steve's barbeques were great!
Roberto Lins	I believe the program provides us with a good opportunity to establish and/or to continue collaborative research with Academia.
Thereza Soares	I will leave this to the students ….
Chongmin Wang	Steve and his team are running a wonderful program and this provides an eye opening opportunity for graduate student
Sotiris Xantheas	I think this is a highly valuable program both for the visitors and PNNL staff. It is run quite efficiently and effectively and I hope that it will be continued in the future for the mutual benefit of both visitors and hosts
Alla Zelenyuk	N/A

Visitor	II.1. Was this summer's activity part of an on-going collaboration?
Jeremy Cain	Yes
Luis A. Cuadra-Rodriguez	Yes
Jun Cui	Yes
Diego Gomes	N/A
Rodrigo González Abraham	Yes
Matteo Guglielmi	N/A
Rebecca J Hopkins	Yes. This was part of an active collaboration between the groups of Alexander Laskin (PNNL) and Mary Gilles (LBNL)
Ngor Wai Lam	N/A
Chan-Woo Lee	Yes
Suiqiong Li	N/A
Rebecca Lowton	Yes
Amir Saheb	Yes
Guanjun Wang	N/A
(name on file)	Yes
(name on file)	N/A

Visitor	II.2. How likely is this summer's experience to contribute to future collaboration outside the auspices of the summer program?
Jeremy Cain	Not much. We planned on collaborating together regardless of what happened this summer. However, the results obtained this summer helped with our collaboration, as we worked well together.
Luis A. Cuadra-Rodriguez	N/A
Jun Cui	Very Likely
Diego Gomes	N/A
Rodrigo González Abraham	Very likely
Matteo Guglielmi	N/A
Rebecca J Hopkins	This opportunity is likely to reinforce the existing collaboration. A better appreciation of potential opportunities for research in the future has been gained through this experience
Ngor Wai Lam	N/A
Chan-Woo Lee	The experience at PNNL gave me a good idea about my research and strengthen my potential as a researcher
Suiqiong Li	N/A
Rebecca Lowton	Very Likely
Amir Saheb	Depending on the final results more characterization may follow.
Guanjun Wang	N/A
(name on file)	Very
(name on file)	N/A

Visitor	II.3. Did the work contribute to your research or project aims? How?
Jeremy Cain	Yes. The work we are collaborating on is essentially my doctoral project.
Luis A. Cuadra-Rodriguez	N/A
Jun Cui	Yes, the skills I learned in PNNL will be used for my current and future project.
Diego Gomes	N/A
Rodrigo González Abraham	Yes: Helping on the Chemical and Physical characterization of the suspended particles in the Mexico city atmosphere.
Matteo Guglielmi	N/A
Rebecca J Hopkins	Yes. Significant experimental progress was made towards the project aims. Samples collected during a scientific field mission were examined using experimental techniques available at PNNL. The results obtained from these experiments will determine the direction of experiments conducted at LBNL.
Ngor Wai Lam	N/A
Chan-Woo Lee	Yes. I learned my things about my research that I might miss if I didn't attend SRI
Suiqiong Li	N/A
Rebecca Lowton	Partially. I am expecting to continue with my project here as is, but also using analysis techniques developed at PNNL
Amir Saheb	Yes, samples prepared previously at my institution were characterized using the latest elemental analysis techniques.
Guanjun Wang	N/A
(name on file)	Yes. This research was a valuable follow-up on a previous collaboration for chemical analysis of aerosol samples from the Mexico City Metropolitan Area. We were able to build on previous results of physical and chemical characteristics of MCMA aerosol, as well as pursue several new research directions. EMSL at PNNL has excellent research facilities, and a unique capability to bring together results from different analytical techniques to better understand a given question.
(name on file)	N/A

Visitor	II.4. How likely is this work to appear in publication(s), presentation(s)? (If you are planning to publish or present, please provide some detail—where, when, etc.—approximately)
Jeremy Cain	Very likely to be published within a year
Luis A. Cuadra-Rodriguez	This is a continuation of ongoing collaboration with Dr. Alla Zelenyuk where we have publish a paper on Analytical Chemistry (available online). Also the work done during the summer is submitted to be presented at the AGU meeting on Dec. 2006
Jun Cui	The project is under progress. We are expecting some publications and presentations in the future. But now, we cannot predict the exact time.
Diego Gomes	Yes, as soon as we get the final results, analyze and discuss them, we would like to present this work at a conference for further discussion and then publish in a specialized journal.
Rodrigo González Abraham	Very likely, we do not have exactly dates yet.
Matteo Guglielmi	We are writing the paper and I'll present the results at the EPFL (Switzerland) by the end of this year
Rebecca J Hopkins	This work was recently presented at two conferences - ACS in San Francisco and AAAR in Minnesota.
Ngor Wai Lam	Part of the materials and results are presented in 54th ASMS in Seattle by Dr. Julia Laskin this year (28May2006 to 1June2006)
Chan-Woo Lee	Yes
Suiqiong Li	The work will be presented at 2006 MRS (Materials Research Society) Fall Meeting, which will be held at Boston this December. The proceeding will be published after the meeting. I am also preparing a journal paper based on the work I did at SRI. I plan to submit it to Journal of Nanoscience and Nanotechnology.
Rebecca Lowton	Unknown
Amir Saheb	It is likely to appear in a publication or presentation with relation to chemistry or materials science journals or conferences
Guanjun Wang	There are one or two potential publication on this work
(name on file)	Very likely to feature into a future publication on the MILAGRO-2006 study and/or conference presentation.
(name on file)	This summer's work is actually fairly unlikely to appear in a publication because the quality of the data is poor. Although the idea is/was novel, a shortage of time and the early stage of development of the instrumentation will not allow a quality publication to result

Visitor	II.6. How likely is this work to contribute to your PhD. Thesis?
Jeremy Cain	Absolutely. The work done this past summer will go into my doctoral thesis.
Luis A. Cuadra-Rodriguez	The contributed in all aspects of my research, from design to understanding the system. These are preliminary experiments that had help us understand better particle generation and analysis, which will help us design and build a new aerosol mass spectrometer to study aqueous organic aerosols
Jun Cui	The work will be part of my continuing project as a postdoc in the group. I also used the skills I learn in PNNL for my PhD. Proposal.
Diego Gomes	The work is not intended to be part of the Ph.D. Thesis but the same techniques and simulation approaches learned at PNNL will be applied to another biological system.
Rodrigo González Abraham	N/A
Matteo Guglielmi	This will be one of the 23 topics of My Ph.D. Thesis.
Rebecca J Hopkins	N/A
Ngor Wai Lam	N/A
Chan-Woo Lee	The work will improve creativity and productivity of my Ph.D. Thesis
Suiqiong Li	One of the chapters in my dissertation will be written based on the work I did at SRI.
Rebecca Lowton	Unknown
Amir Saheb	It will probably play a role in my thesis if we continue with the work and extend it beyond the preliminary results.
Guanjun Wang	This work is very helpful to my Ph. D
(name on file)	Several aspects of the SRI summer research will contribute to my thesis, although it primarily focuses on our previous collaboration from 2003
(name on file)	This work will most likely be a small chapter of my Ph.D. thesis. I feel that I gained more experience and general knowledge rather than physical data and conclusions to contribute to my thesis

Visitor	II.7. Were any new avenues of research opened?
Jeremy Cain	Quite possibly. In talking to researchers at the lab, I can get a feel for what kind of new work could possibly be done
Luis A. Cuadra-Rodriguez	One other possibility opened where we could have two types of particle generation that leads to different schemes for analysis. This is going to be incorporated in the design
Jun Cui	N/A
Diego Gomes	N/A
Rodrigo González Abraham	Yes
Matteo Guglielmi	This work will contribute to the understanding of the stability of pores immersed into biological membranes.
Rebecca J Hopkins	Yes. A possible further collaboration between LBNL and PNNL was identified.
Ngor Wai Lam	Yes
Chan-Woo Lee	I found that surface/interface science (experiments) are very interesting
Suiqiong Li	This research introduced a novel magnetostrictive acoustic wave sensor platform, which have great potential to be the high performance biosensor for future biological analysis.
Rebecca Lowton	Yes
Amir Saheb	Depends on final analysis of the results
Guanjun Wang	Yes
(name on file)	Yes, specifically we are investigating the subject of aerosol processing and transport through samples collected from various field sites in and surrounding the MCMA urban area.
(name on file)	No

Visitor	II.9. Would you recommend others to apply to or participate in this program?
Jeremy Cain	Yes. The facilities at PNNL are very nice and give a researcher the ability to conduct excellent research. It is a great experience because it shows the student what he/she will most likely be doing in the years to come
Luis A. Cuadra-Rodriguez	I think the program is great. Is an excellent opportunity to meet established scientists in the field and other fields and students from all over the country as well. The facilities and help from everyone in program were outstanding making research develop smoothly.
Jun Cui	Yes
Diego Gomes	Absolutely. It was a great opportunity to work with top quality researchers and abundance of computational resources, together with a very well organized institution it's a quite good place work and produce high quality science.
Rodrigo González Abraham	Yes
Matteo Guglielmi	Absolutely.
Rebecca J Hopkins	Yes. I would recommend that others participate in this program. I think that exposure to the wide range of research being conducted at PNNL is very beneficial.
Ngor Wai Lam	Yes, I strongly recommend my colleagues to apply the program in the coming year
Chan-Woo Lee	Yes
Suiqiong Li	Yes
Rebecca Lowton	Yes
Amir Saheb	Yes
Guanjun Wang	Yes
(name on file)	Absolutely.
(name on file)	Yes and no. I would say yes because the program itself is very well organized and provides graduate students with an excellent opportunity to work in a lab outside of their university, to have access to state-of-the-art facilities, and to network with scientists who are well known in their respective fields. The reason that I would say no relates to the relationship with the mentors in the program. A student absolutely must be in contact with the mentor before arriving at PNNL. There did seem to be components built into the application process to ensure contact with the mentor; however in reality, the program did not make this a requirement. With only 10 short weeks to conduct research within the walls of PNNL, the student and mentor need to set realistic project goals, and the student must be better prepared on background aspects of the project in order to be more productive during his/her stay.

Visitor	III.1. What aspects of the program did you feel were particularly good?
Jeremy Cain	The program made the travel arrangements necessary. Also, I think it is excellent that they cover a rental car costs for those who wish to travel on the weekend.
Luis A. Cuadra-Rodriguez	Facilities and organization
Jun Cui	I had a great chance to learn the research environment in PNNL, and knew more undergoing research in my field. I also learned the research skills for studying liquids with molecular dynamics.
Diego Gomes	N/A
Rodrigo González Abraham	The access to the Facilities at any time and the provided support for develop research.
Matteo Guglielmi	The possibility to have scientific exchange at PNNL and its facilities.
Rebecca J Hopkins	I thought that the program was very well organized. The staff at PNNL did an excellent job of making it possible to get the most out of the experience.
Ngor Wai Lam	i) Visit the laboratory and facilities in EMSL. ii) The advance instruments in PNNL open the new area in my research field and development.
Chan-Woo Lee	Great opportunity of interacting with other researchers at PNNL/Great mentoring system
Suiqiong Li	This program gave me the opportunity to have the hand-on experience with the advantage facilities. Another great part is that I was able to directly discuss my project with my mentor and other experts in my research area (nanomaterials), and got advice from them. This accelerated the progress of the project and deepened my understanding in my research.
Rebecca Lowton	The approachability and friendliness of the staff at PNNL and the organization of the internship as a whole
Amir Saheb	The ability to work alongside experts in the various fields and yet have the flexibility to make independent decisions as to the direction of the project
Guanjun Wang	I know more friend from all kinds of science field
(name on file)	The ability to utilize different analytical techniques at the lab, the openness to collaboration and mentorship provided. Also it was very beneficial to the entire SRI program to meet other graduate students and SRI participants. I really appreciated the welcome BBQ
(name on file)	1) The orientation - completion of appropriate training courses, office set-up, knowing whom to ask about issues that may arise, etc. 2) Outside the lab activities (i.e. BBQ and the lecture series)

Visitor	III.2. What can we do to improve the program?
Jeremy Cain	Make it abundantly clear how the e-mail system works. I was unable to check my e-mail because of the difficulty of it (and the short time I was there)
Luis A. Cuadra-Rodriguez	Maybe have seminars every 2 weeks with program participants where the students may present what they are proposing to do, why and how. Also when they have some data they might present that as well. Is always good to have people from different disciplines to look at what your doing and vice versa
Jun Cui	N/A
Diego Gomes	I would really enjoy attending more seminars in the specific area I was here to work.
Rodrigo González Abraham	Promote a final presentation to the participants in order to discuss the results or to inform the research realized.
Matteo Guglielmi	Do it more than once a year.
Rebecca J Hopkins	Possibly cut down the amount of training needed. A lot of this training seemed irrelevant.
Ngor Wai Lam	More outdoor activities for the participants to communicate with each other
Chan-Woo Lee	Housing problem…may be.
Suiqiong Li	N/A
Rebecca Lowton	Ensure that applicants know who to approach with specific issues IE for housing contact ……, for travel / visa information contact………. etc
Amir Saheb	More social gatherings
Guanjun Wang	Provide more information of adviser scientist on web
(name on file)	There were some initial delays as part of setting up computer accounts and orientation. Specifically we could not use the Igor analysis software for 2-3 weeks due to the need to set up a different PNL user account. I understand the paperwork involved, however. Also better coffee at the cafeteria would be wonderful and very welcome!
(name on file)	1) Ensure that contacts are made between mentors and students before arriving at PNNL. 2) Hold other SRI participant activities - i.e. lunch round tables - some other means of meeting the other participants in the program and learning about their respective projects.

Visitor	III.3. What difficulties did you encounter coming here or during your stay?
Jeremy Cain	N/A
Luis A. Cuadra-Rodriguez	So far none
Jun Cui	None
Diego Gomes	In the beginning transportation was an issue, but once you get used to the taxi feeder service everything works fine
Rodrigo González Abraham	None
Matteo Guglielmi	None
Rebecca J Hopkins	None
Ngor Wai Lam	No difficulties
Chan-Woo Lee	Nothing
Suiqiong Li	I just felt a little inconvenient to do grocery shopping during my stay since the guesthouse is far from downtown and I did not have a car.
Rebecca Lowton	It was quite isolated at the guesthouse without access to a car and difficult organizing supermarket trips etc. A weekly minibus trip to the supermarket for all interns without access to a car would have been useful
Amir Saheb	Other than transportation, not many.
Guanjun Wang	No
(name on file)	The computer account problems mentioned above. Also I was shifted around several times for workspace. This was probably because there were two of us on the same project and limited desk space at EMSL
(name on file)	1) Not having regular, effective contact with my mentor. 2) Finding inexpensive transportation for evenings and weekends.

Visitor	IV General comments
Jeremy Cain	No additional comments.
Luis A. Cuadra-Rodriguez	N/A
Jun Cui	N/A
Diego Gomes	N/A
Rodrigo González Abraham	It was one of the most interesting and exiting experience in mi life. It was a great opportunity and means a big step in my research career.
Matteo Guglielmi	Vale di piu' un uovo oggi che una gallina domani!
Rebecca J Hopkins	N/A
Ngor Wai Lam	N/A
Chan-Woo Lee	The opportunity allowed me to have great turning point as a researcher. I won't forget what I learned from SRI. I will also strongly recommend the program if someone asks about the SRI. I also want to thank Mrs. Barlow for great parties.
Suiqiong Li	N/A
Rebecca Lowton	Generally, thank you to all who worked so hard to bring me over to PNNL and were so helpful when I arrived. It was a wonderful to experience work in a government based lab and to see how research works outside of academia. It was a privilege to work with Tom Autrey and the rest of the Molecular Interactions group.
Amir Saheb	N/A
Guanjun Wang	N/A
(name on file)	Everyone was very welcoming and overall it was a good experience
(name on file)	There were too many summer program participants (total 3) working in my lab, especially with only two and a half "regular" group employees. One of the summer program participants never should have been chosen for his respective program (not SRI). He was extremely immature and always disruptive to the group. Therefore, focus and time were often taken away from the tasks at hand with my project.

[1] A. Owens, A. Peacock, Nucl. Instr. Meth. A 531 (2004) 18.

[2] A. Lo Giudice, F. Fizzott, C. Manfredotti, E. Vittone, F. Nava, Appl. Phys. Lett. 87 (2005) 222105.

[3] Y. Zhang, G. Possnert, W.J. Weber, Appl. Phys. Lett. 80 (2002) 466

[4] Y. Zhang, W.J. Weber, H.J. Whitlow, Nucl. Instr. and Meth. B 215 (2004) 48.

Stephan E. Barlow
Director
ICPCPSRI
(509) 376-2642
cpsi@pnl.gov
http://www.pnl.gov/si